# The Late Quaternary Northwest Pacific: Palaeoenvironmental change and development of regional marine chronostratigraphy

**Ambrose Peter McCarron**

**A thesis submitted for the degree of Doctor of Philosophy**

**The Department of Geography**
**The University of Sheffield**

**June 2021**

# Abstract

The Northwest (NW) Pacific contains a significant, but poorly constrained and poorly understood ice-rafted debris (IRD) belt extending from the subarctic to the mid-latitudes. While these deposits point to substantial glacial ice in the Kamchatka-Koryak region during the last glacial period, the timing and dynamics of glacial change are not well constrained. This thesis updates the Late Quaternary marine core record with a high resolution and multi-faceted study of environmental change. The thesis begins with a review of the state of knowledge relating to Late Quaternary glacial and climatic change in the NW Pacific. I present a high resolution, ~175 kyr study of site ODP 1207A (37.79ºN, 162.75ºE), encompassing IRD, $^{14}$C dating, benthic $\delta^{18}$O, tephrochronology and planktic foraminifera counts. The southern limit of ice-rafting is revealed to be further south than previously thought. This discovery, in conjunction with a new high resolution age model reveals new information about the scale and timing of large magnitude ice-rafting events from NE Siberia. Ice-rafting does not show synchronicity with other major Northern Hemisphere ice sheets. A second IRD analysis is presented for DSDP 580 (41.37ºN, 153.59ºE) where icebergs are known to have reached. I present an updated age model for DSDP 580 derived from both pre-existing age tie points and new tephrochronological data. Together, these new IRD records reveal periods of widespread glacial collapse and possible synchronous collapse of NE Siberian glacial ice ~40 ka BP. Chapter 6 presents a comprehensive analysis of XRF core scanning data of Late Quaternary sections of nine North Pacific cores. This analysis extracts palaeoenvironmental signals from element intensities and log ratios, which identify episodes of palaeoproductivity change and terrigenous input. The palaeoproductivity indicators Ba and Ca are used to identify inter-core stratigraphic tie-points at multiple N Pacific sites, particularly around the last deglaciation. Chapter 7 presents the results and analysis of coupled climate-iceberg model experiments, which explores the most likely source points for icebergs into the N Pacific. The model experiments are important indicators of IRD provenance and provide a foundation for future geochemical provenance studies.

# Contents

## List of Figures

# List of Tables

# Acknowledgements

I would firstly like to thank my principal supervisor, Professor Grant Bigg, who has been approachable and supportive at every stage of this research project. His optimism, encouragement, and inspirational suggestions have been invaluable. I would also like to thank my co-supervisors Mike Rogerson and Jim Marshall, who have been enthusiastic supporters of this project and have always been on hand to read drafts and to offer their advice. Jim's expert guidance on oxygen isotope analysis, and Mike's in-depth knowledge of XRF have helped me enormously. Thanks also to Mike for providing me with most of the ODP and DSDP core material for this project.

Special thanks to Harriet Brooks in the Department of Geography, University of Sheffield, who tirelessly and enthusiastically carried out counts on planktic foraminifera for this research. Thanks also to Melanie Leng at the BGS for her collaboration on the NERC isotope project, the results of which form an important part of the chronostratigraphy of ODP 1207A. I am also grateful to Vera Ponomareva at the Institute of Volcanology and Seismology, Petropavlovsk-Kamchatsky, and Maxim Portnyagin at GEOMAR, for their work on tephra geochemistry which was highly valuable for developing the age models for ODP 1207A and DSDP 580. Thank you to Paula Reimer at the 14CHRONO Centre at Queen's University Belfast for providing radiocarbon dates and technical support with calibration. Thanks to all of the above for their patient collaboration on a submitted manuscript based on the work of Chapter 4.

I am immensely grateful to the friendly staff in the Physical Geography Laboratory, Department of Geography, University of Sheffield, where almost all of my lab time was spent. Special thanks to Rob Ashurst, Alan Smalley, Joe Hufton and David Finlayson for providing me with space, equipment, and time to work on my core samples. I am also grateful to Le Ma at the Sorby Centre for Electron Microscopy at the University of Sheffield for her support with SEM imaging and EDS analysis.

I would like to thank Phil Rumford and Brian LeVay at the International Ocean Discovery Program, College Station, Texas for hosting me for a week in August 2017 where I acquired my XRF data. It was an unforgettable experience to carry out research in such an important repository for palaeoenvironmental science.

I would like to thank all of my friends at the University of Sheffield. A special mention goes to my friends in the A Floor office in the Department of Geography, who have been a supportive presence during the past four years. Thanks to Lad and Lady the cats, who were a help in times of stress. Thanks go to my family, with special thanks to my father, who passed away before this work was completed, and to my daughter Caitlin, who was born in February 2020. A final thanks goes to my wife, Sarah, for her patience, love and support.

## Note on Funding

This research was mainly funded by a NERC ACCE PhD studentship. The stable isotope analysis was funded by a NERC Isotope Geoscience Facilities Steering Committee (NIGFSC) award. The foraminifera counts were funded by the Sheffield Undergraduate Research Experience (SURE) Scheme. Samples were provided by the Integrated Ocean Drilling Program (IODP). Tephra geochemical analysis was supported by the Russian Science Foundation grant #16-17-10035.

# Chapter 1: Introduction, Aims and Objectives

## 1.1: Introduction to this thesis

The research presented in this thesis addresses an area of study which is routinely omitted from discussions of Quaternary environmental change. This situation continues despite the emergence twelve years ago, of evidence in the ice-rafted debris (IRD) record of intriguing episodes of dynamic glacial change on the NW Pacific rim (Bigg et al., 2008). The widespread existence of NW Pacific IRD has been documented as early as Conolly and Ewing, (1970), yet there have been very few high-resolution studies of these deposits. Even following the exciting discovery of Bigg et al., (2008), subsequent work has been slow on unveiling the Late Quaternary marine sediment archive of glacial and climatic change, with work confined mainly to the Sea of Okhotsk (e.g. Nürnberg et al., 2011).

While the opportunity has so far not been fully grasped by the Quaternary science community, it is not altogether surprising. The deep-sea Northwest (NW) Pacific is a complex and challenging zone for chronostratigraphy and palaeo-environmental reconstruction. Its great depth (mostly exceeding 5,000 m) largely excludes the possibility of radiocarbon dating, which consequently makes the establishment of regional chronostratigraphy very difficult. Additionally, this region's Late Quaternary glacial history is not viewed as holding the same significance as, for example, the North Atlantic, because the ice sheets of Northeast Siberia were substantially smaller than the Laurentide ice sheet.

This thesis attempts to add significant data to the Late Quaternary marine stratigraphy of the NW Pacific. I begin in Chapter 2 by presenting a detailed overview of the published work so far carried out on the Late Quaternary marine and terrestrial deposits of the region. In Chapter 3 I present the scope of this thesis, providing an overview of the general structure of the writing. Chapter 4 then presents a detailed analysis of core ODP 1207A, on the northern Shatsky Rise, NW Pacific. This is the keystone site of this thesis, and the IRD and chronostratigraphic data produced from this core is key to the narrative and conclusions of this thesis. The IRD record of ODP 1207A reveals significant information about the scale and extent of Late Quaternary ice-rafting into the NW Pacific, particularly during the “40 ka” ice-rafting event (see Bigg et al., 2008 and Chapter 4).

Chapter 5 presents an analysis of DSDP 580, which is to the northwest of ODP 1207A, and during the Late Quaternary was within the known IRD belt. The high resolution IRD record and improved age model is used to reinforce and strengthen the conclusions of Chapter 4, and also improves the marine tephrostratigraphy.

Chapter 6 presents a study of X-ray fluorescence (XRF) data from nine NW and Northeast (NE) Pacific cores. This analysis attempts to identify key elemental signals which may indicate biological productivity and terrigenous sediment flux for the purposes of seeking possible stratigraphic correlations which may be used to improve the marine stratigraphy of the region. The XRF data will also be used to identify important climate signals such as stadials and interstadials, and Marine Isotope Stage (MIS) boundaries.

Chapter 7 continues the analysis of sediment provenance by presenting results of the Fine Resolution Greenland and Labrador Sea (FRUGAL) intermediate complexity coupled climate-ocean-iceberg model (Levine and Bigg, 2008). These innovative ocean-iceberg modelling experiments attempt to model the most likely sources of IRD in the NW Pacific, and reveal exciting information about the range of possible sources along the Kamchatka-Koryak-Sea of Okhotsk coast, and where the expected distribution from each local source is likely to be found at deep sea sites. This modelling work uncovers multiple possibilities for exciting future model verification research on IRD provenance in the region.

The final chapter (8) presents a summary of the key findings of this thesis. A discussion of the major environmental changes in the Late Quaternary NW Pacific then follows. This chapter also includes a discussion of the limitations of this research, and offers suggestions for future work which can build on the foundations laid here.

Below, I outline the main aims and objectives of this thesis.

## 1.2: Aims

**1**.To produce new records of ice-rafted debris in the NW Pacific.

**2**. Search for inter-core evidence of widespread glacial change through comparison of regional ice-rafted debris records.

**3**. To improve the age control in the NW Pacific through the production of high resolution chronostratigraphic records.

**4**. Identify major Late Quaternary sources and entrainment mechanisms of terrigenous sediments, including ice-rafted debris, to the deep-sea NW Pacific.

## 1.3: Objectives

1. Identify changes in ice-rafting in the NW Pacific over at least the last ~45 ka (for $^{14}$C dates) and up to ~100 ka (for tephrochronology and stable isotope analysis).
2. Identify discrete tephra layers and dispersed ash zones.
3. Use a variety of dating methods including $^{14}$C, $\delta^{18}$O, and tephrochronology and biostratigraphy on at least one marine core to contribute towards a robust regional marine stratigraphy of the last glacial period in the NW Pacific and to resolve the lack of data surrounding the age of Late Quaternary deposits in the NW Pacific. Improved dating will also be used to explore the temporal, as well as regional, changes in ice-rafting across the region.
4. Carry out XRF analysis and ocean-iceberg computer modelling to identify the sources regions of marine sediments. Computer modelling is used to explore how sources of NE Siberian icebergs may have varied between sites in the NW Pacific, for example, between

subarctic and mid-latitude sites. XRF is used to explore broader patterns of sediment supply and different possible transport mechanisms.

# Chapter 2: The Late Quaternary NW Pacific: the current state of knowledge

## 2.1: Introduction

This chapter reviews the current data regarding the glacial, climatic and oceanographic conditions of the Late Quaternary north-west (NW) Pacific. Where appropriate, research from the north-east (NE) Pacific will also be reviewed here. The review is divided between publications which are primarily concerned with the terrestrial evidence of Late Quaternary glaciation, and those which are concerned with marine core data, the latter of which encompass not only information on glaciation, but also on oceanography. A further section reviews the stratigraphic uncertainties in NW Pacific datasets, and outlines the importance of constructing robust, regionally correlative stratigraphic records.

## 2.2: Definition of the Late Quaternary

The term "Late Quaternary", although not used in the literature to span a definite period of geological time, is used in this thesis to refer to the period beginning in the penultimate glaciation in MIS 6, through to the Holocene. Data from earlier regional Quaternary glaciations is also described in Section 2.3. to provide context to Late Quaternary changes.

## 2.3: The onset of Quaternary glaciation on the North Pacific rim

The NW Pacific coast was occupied by marine-terminating glaciers from at least c. 2.67 Ma BP, in congruence with the onset of large-scale Eurasian and North American glaciation (Shackleton et al. 1984). Glacial advance is marked by the appearance of coarse terrigenous sediments and increases in magnetic susceptibility values in both NW Pacific in the Meiji Drift deposits (to the east of the Kamchatka peninsula) and in central and NE Pacific marine cores (Kent et al, 1971; Prueher and Rea, 2001). The glacial intensification appears to be synchronous across the subarctic North Pacific and is also preceded-and accompanied by an intensification of explosive volcanism from the Kamchatka-Kurile and Aleutian arcs, as shown by the sudden increase in volcanic glass within the same marine cores. This finding led Prueher and Rea, (2001) to suggest that the Late Pliocene/early Pleistocene volcanism may have triggered glacial intensification in the subarctic north Pacific. The onset of glacial-interglacial cycles is reflected in the large fluctuations in $\delta^{18}O_{diatom}$ in NW Pacific core ODP 882, attributed to large influxes of freshwater from the subarctic North Pacific/Bering Sea region during the Late Pliocene (Swann, 2010). This freshwater signal points to the existence of substantial glacial ice masses around the north Pacific rim from the Kamchatka-Koryak Pacific/Bering coast to the Gulf of Alaska from at least 2.73 Ma BP. A combination of moisture supply driven by the Aleutian low pressure system and cold air supply from Siberia may have created the conditions for glacial expansion originating in the highland areas of the Sredinny range of Kamchatka, the Koryak Highlands and the Verkhoyansk mountains (Pickart et al., 2009), generating glaciers of several hundred km in length (Barr and Clark, 2012a). An intensification of glaciation is apparent in the mid-Quaternary around 1.2 Ma BP as shown by enhanced IRD in multiple cores across the north Pacific basin (Kent et al., 1971).

While there is a general long-term increase in IRD concentrations over the entire north Pacific basin at the onset of the Quaternary and around the 1.2 Ma BP glacial intensification, the exact timings, geographical patterns and geological composition of IRD vary widely from west to east, and from the northernmost subarctic sites to the southern limits of glacio-marine deposits (St. John and Krissek, 1999). Consequently, when investigating the glacio-climatic trends of the Quaternary, it is important to consider multiple sources of IRD into the North Pacific, and the temporally and spatially varying climatic and oceanographic influences of this wide region. This therefore not only requires a detailed review of the marine record of glacial change, but also a close examination of the terrestrial evidence of the stages and spatial extent of north Pacific glaciation.

## 2.4: Quaternary ice masses on the north Pacific rim

Due to the deleterious effects of weathering and erosional processes of successive glaciations and fluvial activity on the terrestrial signal of earlier glaciations (Barr, 2009), it is difficult to derive estimates of the extent and chronology of glacial ice for the early-and mid-Quaternary from terrestrial evidence alone (Glushkova, 2001). However as discussed in Section 2.3 it is assumed that from the Plio-Pleistocene transition marine-terminating glaciers or ice shelves occupied the Russian Pacific coast for prolonged periods, as shown in the IRD record (Fig. 2.1; Section 2.3 and 2.7). Sections 2.5-2.10 and 2.12-2.14 are therefore concerned with the Late Quaternary timescale described in Section 2.1. and begins with a discussion of the controversy and uncertainty surrounding the extent of glaciation of NE Russia during the last glacial cycle.

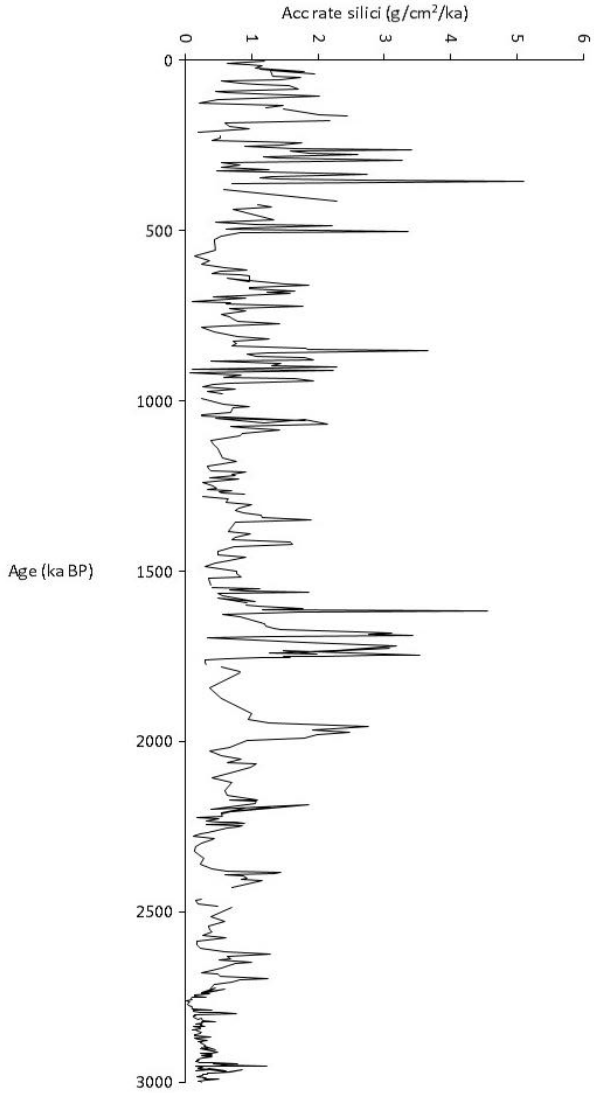

**Figure 2.1:** Long term siliciclastic accumulation rate record from ODP 882 in the NW Pacific at 50.2°N, 167.4° (Haug et al., 1995) Data downloaded from Pangaea.de. Data points have been removed where the age-depth profile is inconsistent.

## 2.5: The Late Quaternary glaciation of NE Russia: Part of a pan-Arctic ice sheet or limited mountain-centred glaciation?

Research on the Late Quaternary glaciation of NE Russia is divided into two broad hypotheses. The first hypothesis asserts that the entirety of NE Russia was occupied by a vast ice sheet as late as the Last Glacial Maximum (LGM). The key proponents, who have remained consistent in their support of this theory are Grosswald (1980), Grosswald and Hughes (1995, 1999, 2002, 2005), Grosswald (1998, 2003), Hughes et al. (1977). Other publications which support the ‘maximalist’ view of Late Quaternary glacial extent include Grosswald and Spektor (1993) and Kotilainen and Shackleton (1995). Polyak et al. (2001) and Grosswald and Hughes (2005) use geomorphic and bathymetric mapping and ice-sheet-climate modelling to argue that an LGM marine ice sheet formed multiple mega-scale u-shaped channels, hills and hummocks in the Sea of Okhotsk. They also suggest that the Bering Strait was glaciated during the LGM. These hypotheses could explain the variations in abundance and the heterogenous composition of NW Pacific IRD (St. John and Krissek, 1999; Bigg et al. 2008), which could be a consequence of a large ice sheet draining from regional ice streams, with IRD derived from both the Okhotsk region and the eastern Kamchatka-Koryak coast.

However, the Arctic/NW Pacific ice sheet hypothesis is largely theoretical, and a second, more observation-based hypothesis proposes that the evidence points to much less extensive glaciation in Beringia (Glushkova 2001), Chukotka (Gualtieri et al. 2000), the Koryak Highlands (Stauch and Gualtieri 2008), the Verkhoyansk mountains (Stauch and Lehmkuhl 2010) and Kamchatka (Barr and Clark, 2009) during the Late Quaternary. More recently however, bathymetric data and ice sheet modelling have somewhat revitalised support for the possibility of multiple coalescing ice sheets spanning the Arctic Ocean (Niessen et al. 2013), Beringia, the Pacific Russian coast and the Sea of Okhotsk (Colleoni et al. 2016). However, as discussed below, recent extensive investigations of moraine sequences have made a compelling case for an intermediate-scale glaciation with two key phases during the Late Quaternary.

Strong evidence exists for an intermediate-sized ice-mass in the Kamchatka-Koryak region (Zamoruyev, 2004). This hypothesis argues that moraine complexes point to the existence of extensive montane-centred glaciation characterised by radially-flowing glaciers extending >100km in length into the lowlands, and is supported by the extensive geomorphic evidence gathered by Barr (2009) and Barr and Clark (2009, 2012a, 2012b) adding further weight to the idea of a montane glacial system during the last glacial cycle with large glaciers emanating from the key mountain ranges of the Sredinny Range on Kamchatka, the Koryak Highlands and the Kolyma Highlands. Barr and Clark (2012a) present compelling evidence from 8414 moraines in NE Russia that the largest glaciers in the Kamchatka-Koryak and Kolyma regions may have reached the glacial shoreline and contributed to the iceberg flux into the NW Pacific. It is also important to note that even those reconstructions which point to limited-scale glaciation suggest that both the Pacific and Sea of Okhotsk coasts were potential iceberg source regions (Gualtieri et al. 2000; Zamoruyev, 2004; Barr and Clark, 2009, 2012a, 2012b; Figure 2.2). However, only a single confirmed moraine has been discovered beyond the present-day coastline to the east of the central Koryak Highlands (Barr, 2009). Further high-resolution study of bathymetric data is required to identify other off-shore moraines, as it is unlikely that NW Pacific IRD originated from a single outlet glacier.

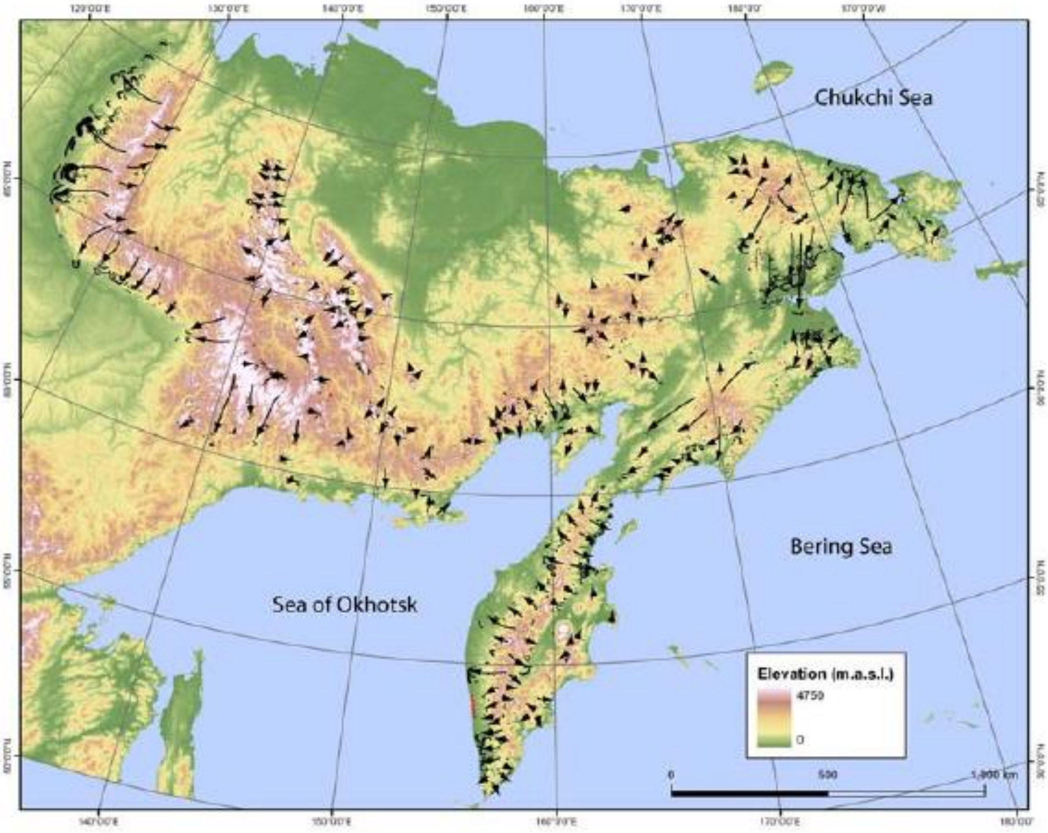

**Figure 2.2:** Ice flow directions from moraine orientations in NE Russia (Barr and Clark 2009). Moraine patterns suggest radially flowing ice masses centred on highland regions, with evidence of some glaciers reaching the coast including on Kamchatka, the Koryak Highlands and the northern coast of the Sea of Okhotsk

### 2.6: Age estimates of terrestrial glacial landforms

The moraine sequences centred around upland areas reflect two Late Quaternary glacial stages described in the Russian literature consisting of older, more advanced sequences attributed to the Zyryan glaciation (MIS-5 to early MIS 3), and younger, less advanced sequences of Sartan age, roughly equivalent to the global last glacial maximum (Glushkova, 2001). A limited number of glacial samples from NE Russia have been dated using a range of techniques including lichenometry (Solomina and Calkin 2003), and $^{14}$C dating (Glushkova, 2001; Braitseva et al. 2005). The best-preserved deposits are thought to have been formed during the Zyryan and Sartan stages of glaciation (Barr and Solomina 2014) and efforts are ongoing to generate Pleistocene-Holocene tephrochronological datasets for the Kamchatka peninsula, which can provide minimum ages for glacial landforms and deposits (Braitseva et al. 1995; Ponomareva et al. 2013). These dates support the hypothesis of a regional glacial maximum occurring at least 20 ka prior to the global Last Glacial Maximum (gLGM). Despite these efforts, most moraines on the Pacific Russian coast have no absolute chronological control, therefore previous work on ice-mass reconstructions have relied on extrapolations from the limited number of absolute dates and relative dating points derived from moraine configurations. Consequently, there remains a great deal of uncertainty about the timing of Late Quaternary glaciation in the region.

### 2.7: The marine record of Late Quaternary glacial change in the north Pacific

Notwithstanding a small number of important exceptions discussed in the following sections, the glaciomarine deposits of the NW Pacific remain largely unexplored and provide a potentially highly significant opportunity to address these uncertainties surrounding the timing, scale, and rate of change of Late Quaternary Kamchatka-Koryak glaciation, and interactions with climate and oceanography. This section begins with a discussion of the general oceanography of the region and the key oceanographic changes that have occurred during the Late Quaternary, while Section 2.9

goes on to review the marine data of the Late Quaternary north Pacific. The latter section has significant emphasis on the NW Pacific, and presents data on IRD including distribution and magnitude, age estimates and possible sources. The sites referred to in this review are shown in Fig. 2.3.

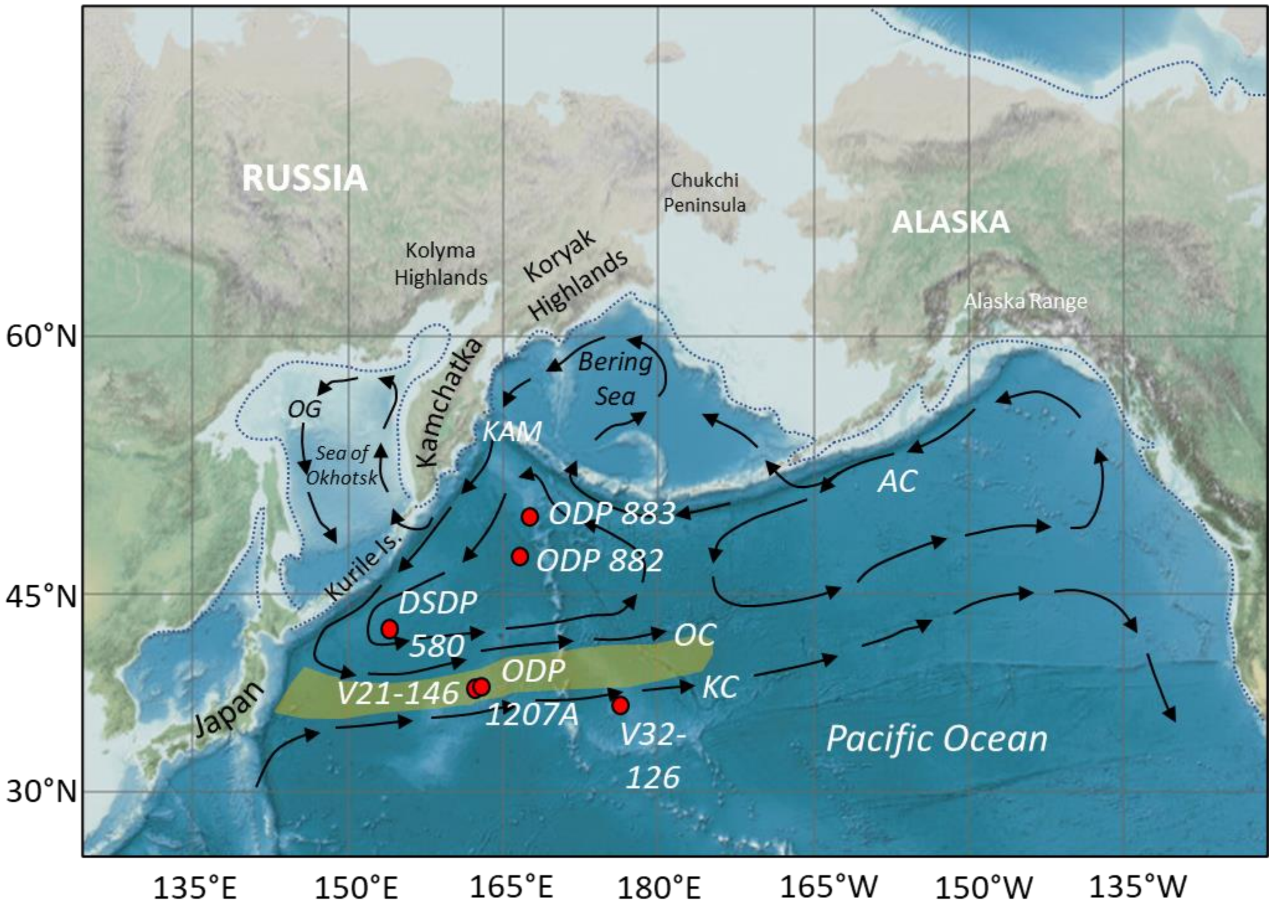

**Figure 2.3:** Locations of the cores mentioned in this review. Major surface ocean currents are shown by the arrows. AC=Alaska Current. OC=Oyashio current. KC=Kuroshio Current. OG=Okhotsk Gyre. Yellow shaded area denotes the subarctic-subtropical transition region in the NW Pacific.

## 2.8: The Late Quaternary oceanography of the NW Pacific

### ***The NW Pacific Basin***

The North Pacific is the end-point of the global ocean circulation (Keigwin, 1998). Its surface structure is dominated by the climatically important subarctic gyre, delimited by the western boundary currents of the cold, subarctic Oyashio current which is an extension of the southward flowing Kamchatka current, and the warm, subtropical Kuroshio current,. These currents converge ~35°N, east of northern Japan, forming the SW-NE-flowing Kuroshio-Oyashio Extension (Itoh and Yasuda, 2009; Fig. 2.3). This convergence zone marks the approximate known southern limit of ice-rafting in the NW Pacific. The Kuroshio-Oyashio Extension is often referred to as the Kuroshio-Oyashio transition zone and is considered to mark the subarctic front (SAF) between cold and warm surface water masses (Yasuda, 2003; Vanin, 2013). During the Late Quaternary the SAF shifted latitudinally, both to the north and south of its modern position, as shown by nannofossil and planktic foraminiferal assemblages (Thompson and Shackleton, 1980; Thompson, 1981; Harada et al. 2004; Seo et al. 2018).

Significant influxes of cold waters southward of 35°N are inferred by Thompson and Shackleton (1980) during MIS 6 and MIS 2 as shown by both coiling ratios of *N. pachyderma* and planktic $\delta^{18}O$ at core V21-146 (37.41°N, 163.02°E) and V32-126 (35.19°N, 177.55°E) This is corroborated by Yamane (2003) who observe the highest ratios of left/right-coiling *N. pachyderma* during MIS 6 and 2 at Site S-2 (33.22°N, 159.08°E). Seo et al. (2018) argue that species abundances and $\delta^{18}O$ of planktic foraminifera species have not varied significantly at Site NPGM 1302-1B (32.16°N, 158.13°E), suggesting that subarctic surface waters did not reach this latitude from at least the LGM to the present day. Nevertheless, there may have been periodic influxes of transition zone waters causing the observed abundance changes. These studies suggest that the southernmost extent of significant subarctic water influx between MIS 6 and MIS 1 in the NW Pacific is around 33°N. No IRD is recorded at the sites described above, either due to very low concentrations or due to complete absence of IRD. No research has been carried out on the relationship between latitudinal shifts in the SAF and IRD distribution in the NW Pacific. Future research on this question would be valuable for investigating palaeo-ocean-iceberg interactions and may prove useful for reconstructing the history of NE Asia Late Quaternary glaciation.

In a key study from the subarctic NW Pacific, Kiefer et al. (2001) observe millennial-scale planktic $\delta^{18}$O shifts at ODP 883 which show abrupt SST maxima during MIS 3, which may be related to North Atlantic Dansgaard-Oeschger stadials.

### *The Sea of Okhotsk*

The surface waters of the Sea of Okhotsk are dominated by the cyclonic Okhotsk Gyre (Figure 1.3). Inflowing waters from the East Kamchatka current flow northward, forming the West Kamchatka current, and outflowing waters flow through the narrow Bussol Strait in the south-central Kurile chain (Nürnberg et al., 2011). The Sea of Okhotsk is covered by seasonal sea ice (Nürnberg and Tiedemann, 2004) which contributes to the ventilation of the low-salinity NW Pacific Intermediate Water (NPIW) (Talley, 1991; Barash et al., 2006). Nürnberg and Tiedemann (2004) argue that a combination of periodic freshwater discharge from the Amur River and Kamchatkan glacier-melt, especially during the last interglacial (Temination 2 and MIS 5) may have caused freshening and weakening of the West Kamchatka current during the last glacial cycle (Nürnberg and Tiedemann, 2004; Nürnberg et al., 2011). However, the current Amur River delta drains into the Tartar Strait and into the outflowing water of the Sea of Okhotsk (Simizu and Ohshima, 2006), therefore the freshwater discharges observed in the Central Basin could be primarily the result of glacier-melt.

### *The Bering Sea*

Like the Sea of Okhotsk, the Bering Sea plays an important role in the formation of NPIW, and during the Late Quaternary, as during the present day, it was extensively covered by sea ice (Katsuki and Takahashi, 2005). Its surface circulation is formed by the inflow of warm water from the Alaskan Stream, which is cooled and flows out through the Kamchatka Strait, forming the East Kamchatka current (Gorbarenko et al., 2010; Figure 1.3). During the last glacial cycle, millennial-scale changes in the abundances of IRD (argued to be sea-ice-transported) and the radiolarian species *C. davisiana*, are thought to be related to intermediate Bering Sea water ventilation, particularly during MIS 3 and 2 (Gorbarenko et al., 2010). The authors argue that these changes correspond with Heinrich events 5-3 and Dansgaard-Oeschger stadials. These millennial-scale changes could be related to those observed in the NW Pacific at ODP 883 by Kiefer et al. (2001), but further work is required to establish clear links between millennial-scale events in the Bering Sea and NW Pacific.

### 2.9: Geographical distribution of IRD across the north Pacific basin

Iceberg-derived IRD has been recorded in an almost continuous band above 42°N across the North Pacific from the Sea of Okhotsk in the west (Gorbarenko et al., 2002; Nürnberg et al., 2011) to the central-north Pacific (but with significantly lower concentrations in this region) (Kent et al., 1971), and the Gulf of Alaska in the east (Hewitt et al., 1997; Prueher and Rea, 2001; Fig. 2.4). The highest concentrations of IRD occur in the Gulf of Alaska (Hewitt et al. 1997) and in the Meiji Drift sediments to the east of Kamchatka (Bigg et al. 2008). Those deposits in the Gulf of Alaska are clearly derived from marine-terminating glaciers in south-eastern Alaska (Von Huene et al., 1976; McKelvey et al., 1995), while the Meiji Drift sediments and those of the Sea of Okhotsk are compositionally more similar to the Kamchatka-Koryak region (McKelvey et al., 1995), and in some cases are mixed with dispersed tephras geochemically fingerprinted to Kamchatkan eruptive centres, which are likely to have been at least partially iceberg-rafted (Bigg et al. 2008) with non-tephra IRD. There is no evidence that at certain longitudes in the central north Pacific, Kamchatka-Koryak and Alaskan-sourced IRD are both present at the same site. Further in-depth analysis of the mineralogical composition of central north Pacific sediments is needed to determine the respective east-west limits of IRD from these two main sources.

### 2.10: Broad Geographical Patterns and timing of IRD flux in The NW Pacific

Connolly and Ewing (1970) observed variable concentrations of feldspar, quartz, schist and gneiss, along with abundant volcanic glass and pumice, in the sand sized (>62µm) fraction of seventeen NW Pacific cores between 56°N in the SW Bering Sea and 40°N. The highest concentrations occur in a NE-SW band extending from the coast of eastern Kamchatka. Another significant SW-NE band of high IRD concentrations occurs approximately just north of the trajectory of the subarctic front. To the south of 40°N, no IRD was recorded by Connolly and Ewing. However, Okada (1980) observes exotic terrigenous pebbles less than 400km east of northern Honshu. It is possible that the two westernmost cores in this latter study may have been subject to downslope slumping, which would explain the presence of exotic pebbles at this site. However, the easternmost core, DSDP 436 (39°N, 146°E) is unlikely to have been subject to slumping.

### 2.11: Onset of Quaternary Ice-Rafting

As discussed in Section 2.3, IRD flux to the North Pacific intensified between 2.73 and 2.2 Ma (Connolly and Ewing, 1970; Kent, 1971; Prueher and Rea, 2001). This is concurrent with an abrupt increase in magnetic susceptibility values which reflect a mix of volcanic ash deposition, aeolian sedimentation and IRD, and is observed vividly in ODP 882 on the Meiji Drift (50.2°N, 167.36°E) (Haug et al., 1995; Haug et al., 1999; Maslin et al., 1996; Prueher and Rea, 2001; Bailey et al., 2011). However, Okada (1980) identifies the earliest occurrence of exotic pebbles at DSDP 436 east of Japan around the mid-Miocene suggesting that these early occurrences are not IRD.NW Pacific IRD flux significantly increases ~1.2 Ma BP concurrent with the Northern Hemisphere glacial intensification (Krissek et al., 1985).

### 2.12: Enhanced ice-rafting during Marine Isotope Stages 6-5e glacial termination

The eastern Sea of Okhotsk and western Bering Sea show evidence of greatly increased iceberg activity during MIS 6 into glacial termination 2 and MIS 5e (~130-115 ka BP) from counts of lithic sediments and magnetic susceptibility values (Nürnberg and Teidemann, 2004; Nürnberg et al., 2011; Levitan et al., 2013). Towards the southern limits of ice-rafting in the open NW Pacific at DSDP 580 (~41°N), IRD counts increase in late MIS 6 compared to low levels during the previous ~40 ka (St. John and Krissek, 1999). In the same study, higher IRD counts are observed during MIS 6 further north at ODP 882, but there is no clear peak during MIS 5e at this site. This lack of synchronicity could be due to the low resolution of the study (sampling interval of ~20cm), consequently diluting any millennial-scale peaks. Alternatively, DSDP 580 may be influenced to a greater degree by IRD influx into the NW Pacific from the Sea of Okhotsk, whereas the Koryak Highlands and eastern Kamchatka are the most likely sources of IRD at ODP 882. The open NW Pacific lacks any other high-resolution studies of the MIS 6-5e period, therefore it is not possible to make any further regional comparisons. Significant oceanographic changes occur during MIS 6-5e around the southern limits of ice-rafting (Section 2.8). There is substantial scope to investigate the IRD flux at southern locations including DSDP 580 and another unexplored core, ODP 1207A in relation to the last significant southward incursion of the Kuroshio-Oyashio transition zone around MIS 6-5e.

## 2.13: Ice-Rafting during the last glacial cycle

The NW Pacific has very few high-resolution, millennial and sub-millennial-scale IRD records spanning the climatic changes of the last glacial cycle. Key Quaternary NW Pacific IRD records (e.g. Connolly and Ewing, 1970 and St. John and Krissek, 1999) sample at intervals of approximately one sample per 20-150cm, which is far too coarse to identify short-term changes associated with Heinrich stadials, Dansgaard-Oeschger events or glacial advance and retreat. There are some high-resolution IRD series in the Bering Sea and Sea of Okhtosk (e.g. Gorbarenko et al., 2010; Nürnberg et al., 2011; see this section), however these marginal basins are extensively influenced by sea-ice, which can be a significant transport mechanism of IRD (St. John et al., 2015). Consequently, it can be difficult to separate the iceberg-rafted component from the sea-ice rafted component in these seas.

The highest resolution Late Quaternary IRD records of the NW Pacific are concentrated on the Meiji Drift to the east of Kamchatka (Keigwin et al., 1992; Haug et al., 1995; Kiefer et al., 2001; Bigg et al., 2008). Kiefer et al. (2001) constructed an IRD series (>150μm weight %) of the past ~60 ka at ODP 883 (51°N) and identified significant peaks around 60-57 ka close to the MIS 4-3 boundary, two peaks at 46 and 40 ka BP in MIS 3, and during the LGM. Bigg et al. (2008) later investigated the same sections of ODP 883, calculating the lithic content by using the grains/g method, and discovered that the 40 ka BP peak was not only an abrupt, millennial scale event, but was also significantly higher than the subsequent LGM IRD discharge. This finding supports the geomorphological data outlined in Section 2.6, which suggests a Late Quaternary ice maximum on the Kamchatka-Koryak region some time prior to the global Last Glacial Maximum (gLGM) and significantly depleted gLGM ice cover. The sudden nature of the IRD deposition up to concentrations of over 2000 grains/g during the ~40 ka BP event also suggests abrupt and massive glacial change. This peak in lithic grains is also accompanied by a sudden peak in volcanic ash. Bigg et al. argue that this could indicate a large-scale ice-volcano feedback process on the Kamchatka peninsula. The iceberg trajectory model accompanying the IRD counts show that iceberg trajectories in three different glacial ocean states appear to be significantly influenced by the Kamchatka/Oyashio current. Additionally, iceberg seeding locations in the model show that both eastern Kamchatka and the Koryak Highlands could potentially be the sources of icebergs to ODP 883. The model results corroborate moraine evidence from these regions (e.g. Zamoruyev, 2004, Barr and Clark, 2012a; Barr and Clark, 2012b).

Due to the large scale of the 40 ka BP event, it is likely that this signal is present elsewhere in the NW Pacific. At ODP 882 (50.2°N) in relatively close proximity to ODP 883 there is an increase in the siliciclastic fraction (>2μm weight %) from late MIS 4 (~63 ka BP) to mid MIS 3 (~41 ka BP) (Haug et al. 1995). This period of increased terrigenous flux may include the 40 ka BP event recorded by Bigg et al. (2008). However, the low temporal resolution sampled by Haug et al. makes it difficult to identify millennial-scale events.

Enhanced IRD is also observed in MIS 3 sediments of the Bering Sea. Ovsepyan et al. (2017) observed peaks in the weight % of the 125-2000µm fraction at ~40 and 35 ka BP in the western Bering Sea, in addition to other peaks which approximately correspond to Heinrich events 6-2. Wang et al. (2017) identify a large peak in exotic terrigenous minerals in the southern Sea of Okhtosk from ~45-41 ka BP. Both of these studies argue that the IRD was supplied by sea ice, but the abrupt nature and timing in relation to the 40 ka event described by Bigg et al. (2008) suggest that these signals may at least be partly due to sudden iceberg activity. Nürnberg et al. (2011) attempt to distinguish iceberg-derived IRD from sea-ice-derived IRD in the Sea of Okhotsk by examining the morphology of quartz grains and their relationships to the downcore presence of dark minerals. Angular quartz grains and dark minerals both indicate a glacial origin. They conclude that during MIS 3 there was heightened iceberg flux from western Kamchatka into the Sea of Okhotsk, particularly at ~60, 51, 42, 38, 36 and 31 ka BP. Nürnberg et al. conclude that the metamorphic minerals including amphibolite-grade paragneisses which are a significant component of the Okhotsk IRD, were transported by glaciers draining from the Sredinny Massif on southwest Kamchatka. The geology of this region is described by Bindemann et al. (2002). The enhanced IRD flux to the Sea of Okhotsk and NW Pacific between ~41 and 31 ka BP may indicate a degree of east-west synchronicity between east-and west-draining glaciers on the Kamchatka peninsula. The periods of increased iceberg activity in the Sea of Okhotsk appear to correspond to Heinrich events H6, H4, H3 and H2 (Hemming et al. 2004). Bigg et al. (2008) also identify short term peaks of IRD above background levels approximately corresponding with H3 and H2. Other Heinrich events do not appear to be represented. In ODP 882, there is also enhanced IRD during mid-MIS 6 and MIS 2, with the highest % ~23 ka BP (St. John and Krissek, 1999). Additionally, St. John and Krissek do not observe the 40 ka BP event further south at DSDP 580, but do observe enhanced IRD during mid-MIS 3. At this site, the highest concentrations occur during the deglacial late MIS 2 (~14 ka BP). As observed with the regional disparities in IRD concentrations during MIS 6-5e, the apparent lack of regional synchronicity may be due to regionally varying iceberg sources and trajectories, or due to lower-resolution sampling intervals compared to Bigg et al. (2008). Higher resolution sampling of NW Pacific cores is therefore necessary to resolve this issue.

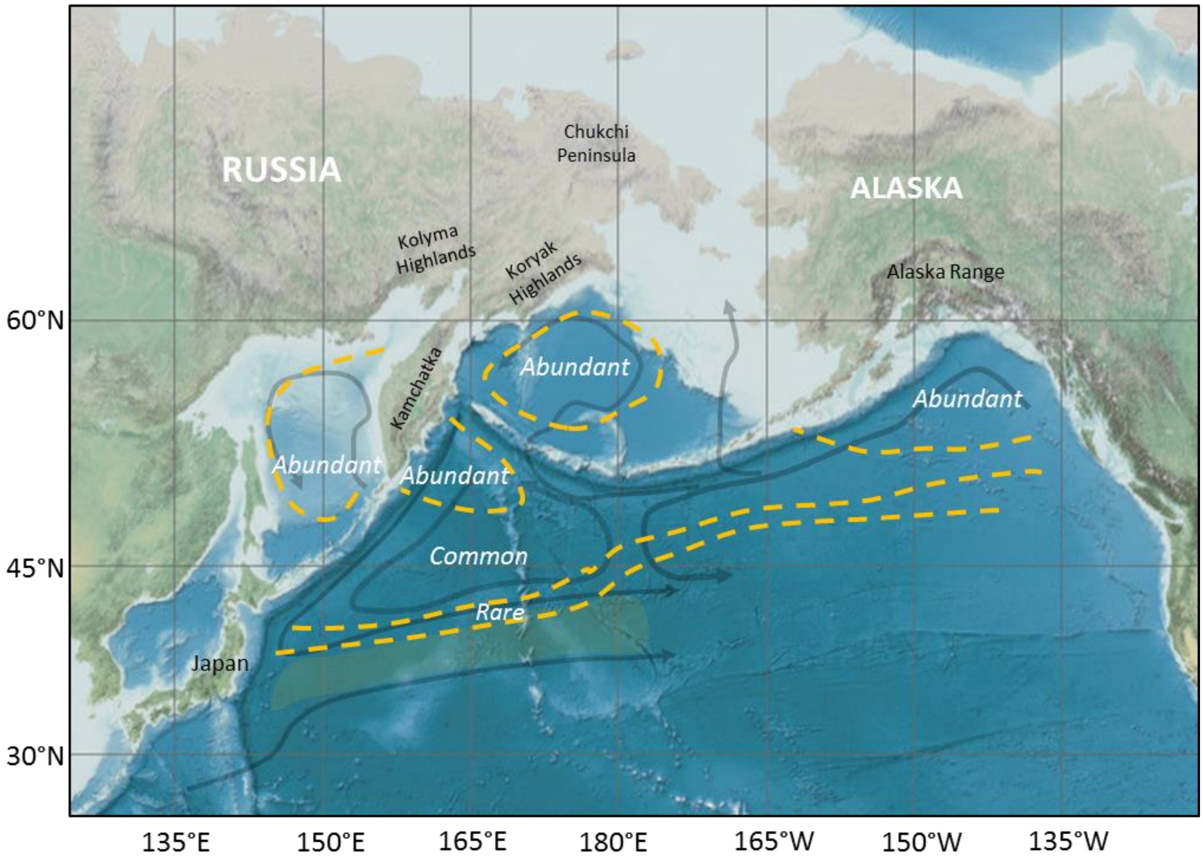

**Figure 2.4:** Known distribution of IRD in the north Pacific superimposed on regional ocean circulation (arrows). Distributions are drawn from publications discussed in this chapter. Note, a large proportion of the abundant IRD in the Sea of Okhotsk and Bering Sea are likely to be derived from sea ice.

## 2.14: Age control and stratigraphic uncertainty in the NW Pacific

Marine cores are highly useful as palaeoclimate/palaeoceanographic tools due to the long and continuous sedimentation in the marine environment, and due to the presence of planktic foraminifera which can be used for $^{14}$C dating and SST determination, and in the case of the NW Pacific, the presence of IRD which can be used to understand palaeo-ice sheet dynamics and climate change. Other dating techniques rely on the marine isotope stage stratigraphy generated from $\delta^{18}O$ analysis of benthic foraminifera (e.g. Lisieki and Raymo, 2005). A multitude of other environmental proxies can be used to generate age models from marine sediments including magnetostratigraphy, GRAPE density, colour changes and tephrochronology (outlined in Borreggine et al., 2017). However, while there is an increasing number of high-resolution stratigraphies in the Bering and Okhotsk seas (e.g. Gorbarenko et al., 2010; Nürnberg et al., 2011; Ovsepyan et al., 2017), facilitating basin-wide comparisons of Late Quaternary environmental changes and stratigraphic tie points, there continues to be a distinct lack of robust, high-resolution Late Quaternary stratigraphies in the open NW Pacific. This is partially due to the great depth of much of the NW Pacific basin (predominantly >5000m), causing the dissolution of dateable $CaCO_3$. The majority of $^{14}C$ dates and $\delta^{18}O$ records in the NW Pacific basin are therefore concentrated on the topographic highs of the Meiji Drift (Kiefer et al., 2001; Bigg et al., 2008), Emperor Seamounts (Kiegwin, 1998; Harada et al., 2004) and the Shatsky Rise (Seo et al., 2018).

In the NW Pacific, the use of non-carbonate-based proxy methods is particularly important in this mostly carbonate-poor region (Korff et al., 2016). Due to the proximity of the NW Pacific basin to the Kurile/Kamchatka and Japanese volcanic provinces, there is substantial scope to construct a regional stratigraphy using marine tephrochronology to identify discrete ash layers in addition to the analysis of dispersed tephra zones and ice-rafted debris in several cores. It is anticipated that this approach will provide valuable insight into the major sources of terrigenous sediment, their transport modes, and their variations throughout the last glacial period. Other potential approaches include the use of X-ray fluorescence scanning (XRF) which measures downcore chemical element changes and can provide information on sediment provenance (Monien et al., 2012), and has been used to identify glacial-interglacial signals through variations in elements which are derived from terrigenous geological sources (Ovsepyan et al. ,2017).

## 2.15: Conclusion

The NW Pacific provides a unique challenge to Quaternary science as a consequence of the dearth of high-resolution age models and regional stratigraphic tie-points across the basin, particularly in relation to the IRD record and regional oceanographic change. It is clear that the full potential of the Late Quaternary marine sediment record as a tool to understand glacial-ocean interactions of the NW Pacific rim, has not yet been taken advantage of. This research attempts to create a basin-wide stratigraphic framework equivalent to the records of the N. Atlantic, which addresses questions of glacial change, sedimentation patterns, climate and oceanographic change in the Late Quaternary NW Pacific. The key questions which this thesis attempts to address are outlined in the next chapter.

# Chapter 3: Research Scope: Key Areas of Inquiry

## 3.1: Introduction

The previous chapter outlines the state of knowledge regarding to Late Quaternary climatic, oceanographic and glacial change in the NW Pacific. It also outlines the research areas which require further in-depth study in order to explore the uncertainties which remain around the timing, extent and glacial-climate interactions during the Late Quaternary. This chapter focuses on these remaining questions and uncertainties and outlines how this thesis attempts to address them.

## 3.2: The timing of Late Quaternary glaciation in the NW Pacific

The terrestrial record of glaciation in the Kamchatka/Koryak region is limited to a small number of absolute dates (e.g. Stauch and Gualtieri, 2008) and relative dating based on moraine sequences (e.g. Barr and Clark, 2012), which suggest two phases of Late Quaternary glaciation characterised by an earlier and more extensive Zyryan phase and a less extensive Sartan phase. The terrestrial evidence is largely supported by key marine datasets which infer intensive iceberg activity during MIS 6 and 3, which is much reduced during the LGM (Bigg et al., 2008; Nürnberg et al., 2011).

The research described in this thesis attempts to expand on these studies by sampling multiple NW Pacific cores across a wide geographical region, producing age models which can be correlated with the aim of constructing a regionally correlative stratigraphy. This will be achieved by using a multi-proxy approach. This approach is necessary due to the inconsistent level of carbonate preservation across the NW Pacific basin which renders radiocarbon dating and foraminiferal $\delta^{18}$O impossible for most deep-sea sites away from the bathymetric highs of the marginal seas,the Meiji Drift, Emperor Seamounts and the Shatsky Rise. The age-depth models described in this thesis use both newly-acquired and existing data. The newly-acquired data includes radiocarbon dates, benthic $\delta^{18}$O, planktic foraminiferal species counts, tephrochronological control and an IRD series for ODP 1207A, and an IRD series and tephrochronological control for DSDP 580. A newly-acquired suite of XRF data obtained from nine cores from the NW, central-north, and NE Pacific is also included as a means of chronological control. Existing data includes radiocarbon dates from ODP 883 and ODP 887 and other sites, tephrochronology, biostratigraphy, IRD and stable isotope stratigraphy from multiple sites across the basin. These records will provide a region-wide picture of the timing of glaciation by placing ages on key IRD pulses. They will also identify the timing of changes in the supply of icebergs and their transport routes through observed spatial and temporal variations in IRD supply through the Late Quaternary.

### 3.3: Oceanographic controls on IRD distribution

As shown in Figure 2.3 (Chapter 2), the major surface currents broadly govern the trajectories of Late Quaternary icebergs in the NW Pacific, as seen elsewhere (e.g. Collares et al., 2018). The southern limit of ice-rafting is broadly demarcated by the Kuroshio-Oyashio transition zone, as inferred by Connolly and Ewing, (1970). Throughout the Late Quaternary, the subarctic front (the approximate southern limit of subarctic waters in the NW Pacific located at the northern boundary of the Kuroshio-Oyashio transition zone) has moved both north and south of its modern location at ~42°N (e.g. Chiyonobu et al., 2012). Through counts of calcareous nannofossil and foraminiferal assemblages significant southward excursions of subarctic surface waters have been identified during MIS 6 and MIS 2 to as far south as 33°N (e.g. Thompson and Shackleton, 1980; Chiyonubu et al., 2012; Seo et al., 2018). However, none of these counts have been accompanied by IRD counts, suggesting that either IRD has been overlooked due to low concentrations, or due to absence of IRD at these relatively low latitudes. Consequently, the relationship between southward excursions of the subarctic front and the southward transport of icebergs is unclear.

This research attempts to examine the degree of synchronicity between southward movements of subarctic waters and the southward extent of iceberg transport by carrying out counts of planktonic foraminifera assemblages and IRD at ODP 1207A. This core is ideally situated to address this question within the Kuroshio-Oyashio transition zone and currently to the south of the subarctic front. IRD counts to the north-west of ODP 1207A at the carbonate-poor site DSDP 580 (41.6°N, 153.9°E) are also presented in this thesis. This core is situated at the approximate latitude of the subarctic front and is therefore well-situated for an examination of the influence of the surface ocean circulation and IRD supply to relatively low-latitude sites. The age-depth model constructed for ODP 1207A and the tephrochronological framework established for DSDP 580 are used to compare the timing of IRD flux at these two sites.

### 3.4: Regional patterns of millennial-scale oceanographic changes

As discussed in the previous chapter, millennial-scale oceanographic changes occurred on multiple occasions during the Late Quaternary in the NW Pacific, Bering Sea and Sea of Okhotsk which bear resemblances in their character, abruptness and timing to N. Atlantic Heinrich events (e.g. Kiefer et al., 2001; Gorbarenko et al., 2010; Nürnberg et al., 2011). At this time, it is unknown whether these changes have a regional signal. It is also unclear whether glacial changes in the Kamchatka/Koryak region are related to these millennial-scale changes, thus the connection to IRD flux is uncertain. This research attempts to address this problem through high-resolution counts of planktic foraminiferal assemblages on core ODP 1207A and IRD counts on ODP 1207A and DSDP 580. Additionally, in Chapter 6 analysis of the X-ray fluorescence (XRF) core scanning data from nine north Pacific cores attempts to ascertain the degree of regional synchronicity in the environmental signal across the basin on millennial- and longer timescales. Element signals will be explored to examine regional signals of biological productivity and terrigenous flux in an attempt to identify wider environmental signals and patterns which can be used for stratigraphic correlation.

### 3.5: Regional sources of IRD and other sediments

The previous chapter describes the most likely source regions of IRD in the north Pacific. In the west these include the Kolyma Highlands on the northern coast of the Sea of Okhotsk, SW Kamchatka on the eastern coast of the Sea of Okhotsk, the Koryak Highlands and northern Sredinny Range on the Bering Sea coast, and SE and central East Kamchatka on the NW Pacific coast. In the east, the dominant sources are the mountain ranges along the Alaskan coast.

The research presented in Chapter 7 attempts to explore how these sources vary by carrying out ocean-iceberg modelling experiments. This analysis will be assisted by comparisons with key IRD records. The model experiments use similar configurations as Bigg et al., (2008) which explores the trajectories of icebergs in an LGM ocean state, seeded at the most likely locations on the north Pacific coast based on the geomorphic evidence presented in Chapter 2.

In addition to IRD, aeolian material makes up a significant proportion of the terrigenous component of north Pacific marine sediments (e.g. Hovan and Pisias, 1989). NW Pacific marine cores also contain a significant volcanogenic (e.g. Korff et al. 2016) and biological component (see Chapters 4 and 5). Using XRF data, I attempt to distinguish between multiple modes of sediment transport through examination of a variety of element signals. Both the $\delta^{18}O$ and aeolian signal can be used as proxies for Marine Isotope Stages (e.g. Serno et al., 2014). Therefore, non-destructive identification of the aeolian signal is used here in combination with the benthic $\delta^{18}O$ signal to identify the glacial-interglacial cycles, thus strengthening confidence in the regional chronological control. The XRF technique is highly useful for identifying discrete volcanic ash layers, as the volcanogenic signal is often highly pronounced against the background signal (e.g. McCanta et al., 2015). Elemental signals from XRF may therefore be able to detect hitherto undocumented tephras.

# Chapter 4: Late Quaternary Chronostratigraphy and Glacial Deposits of ODP 1207A

## 4.1. Introduction

This chapter presents the results of a detailed study of the Late Quaternary section of NW Pacific site Ocean Drilling Program (ODP) 1207A. This site was drilled on Leg 198 of the Ocean Drilling Program in 2001. The core was drilled through Holocene-Valanginian sediments in the NW Pacific at 37.79°N, 162.75°E at a water depth of 3103m on the Northern High of the Shatsky Rise (Fig. 4.1), a large marine Jurassic-Cretaceous igneous plateau (Yasuhara et al., 2017). The oceanographic conditions above the Shatsky Rise, and sedimentology of ODP 1207A are described in this chapter. The justification for choosing this site to investigate Late Quaternary NW Pacific glacial and climatic change will follow from these descriptions. The results of the investigations of ODP 1207A are presented in Section 4.6 and this chapter will conclude with a discussion of the implications for Late Quaternary climate, oceanographic and glacial change.

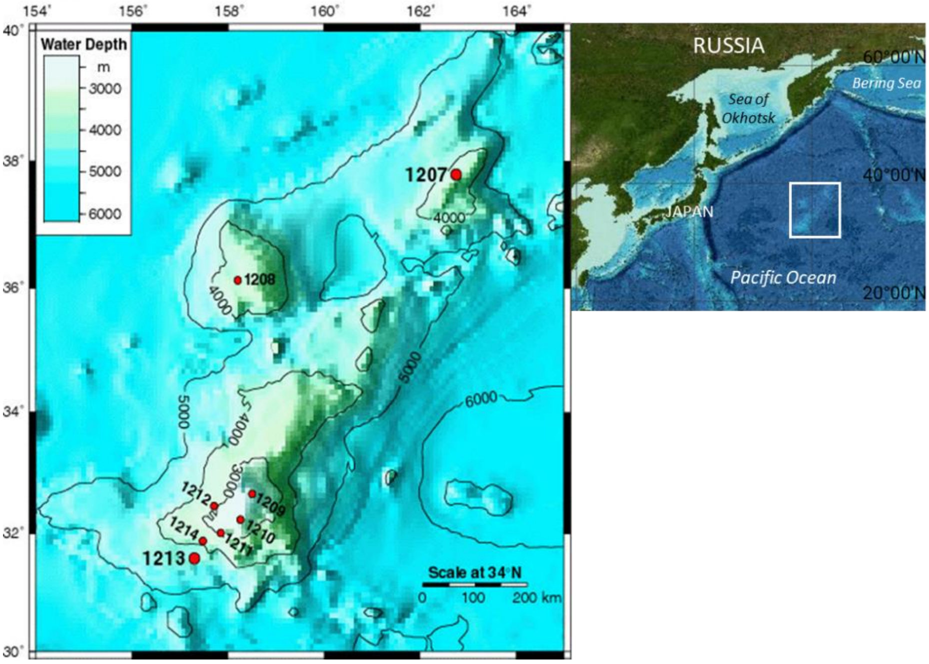

**Figure 4.1:** Bathymetry of the Shatsky Rise showing the location of ODP 1207 and other ODP Leg 198 sites (Lamont Doherty Earth Observatory). Inset: Location of the Shatsky Rise in the NW Pacific.

## 4.2. Oceanographic setting

ODP 1207A presently sits in a subtropical water mass to the south of the Kuroshio-Oyashio Extension zone where the subpolar and subtropical water masses form a transition zone referred to as the subarctic front (SAF; Bralower et al. 2002; Vanin, 2013; see Chapter 1, Section 2.8). During the past 200,000 years of the Quaternary, planktic $\delta^{18}$O ratios (Thompson and Shackleton, 1980; Thompson, 1981) and changes in the relative abundances of planktic foraminifera species in cores recovered from the Shatsky Rise as far south as 32ºN (Yamane, 2003; Seo et al., 2018) record at least two significant southward migrations of the SAF during MIS 6 and 2. Due to its location at the boundary of the subpolar and subtropical water masses, ODP 1207A may contain a detailed record of oceanographic change during the Late Quaternary.

## 4.3. Shipboard Description of ODP 1207A

The shipboard visual description of the major lithologies of ODP 1207A (from 0-300cm) from Bralower (2002) are shown in Fig. 4.2. In this study the upper 300cm of ODP 1207A were judged to be an appropriate age for study of late Pleistocene-Holocene sediments from the preliminary biostratigraphy of Bralower et al., (2002). Other sites local to ODP 1207A located on-or close to-the Shatsky Rise including SO202-39-3 (38°N, 164.3°E; Korff et al., 2016) and S-2 (33.3°N; 159.1°E; Yamane, 2003) span from up to 200 ka BP at 300cm below sea floor (bsf) to <10 ka BP at 0cm bsf. It was therefore expected that ODP 1207A would have a similar accumulation rate to other Shatsky Rise sites and would contain a sedimentary record spanning at least the last glacial cycle.

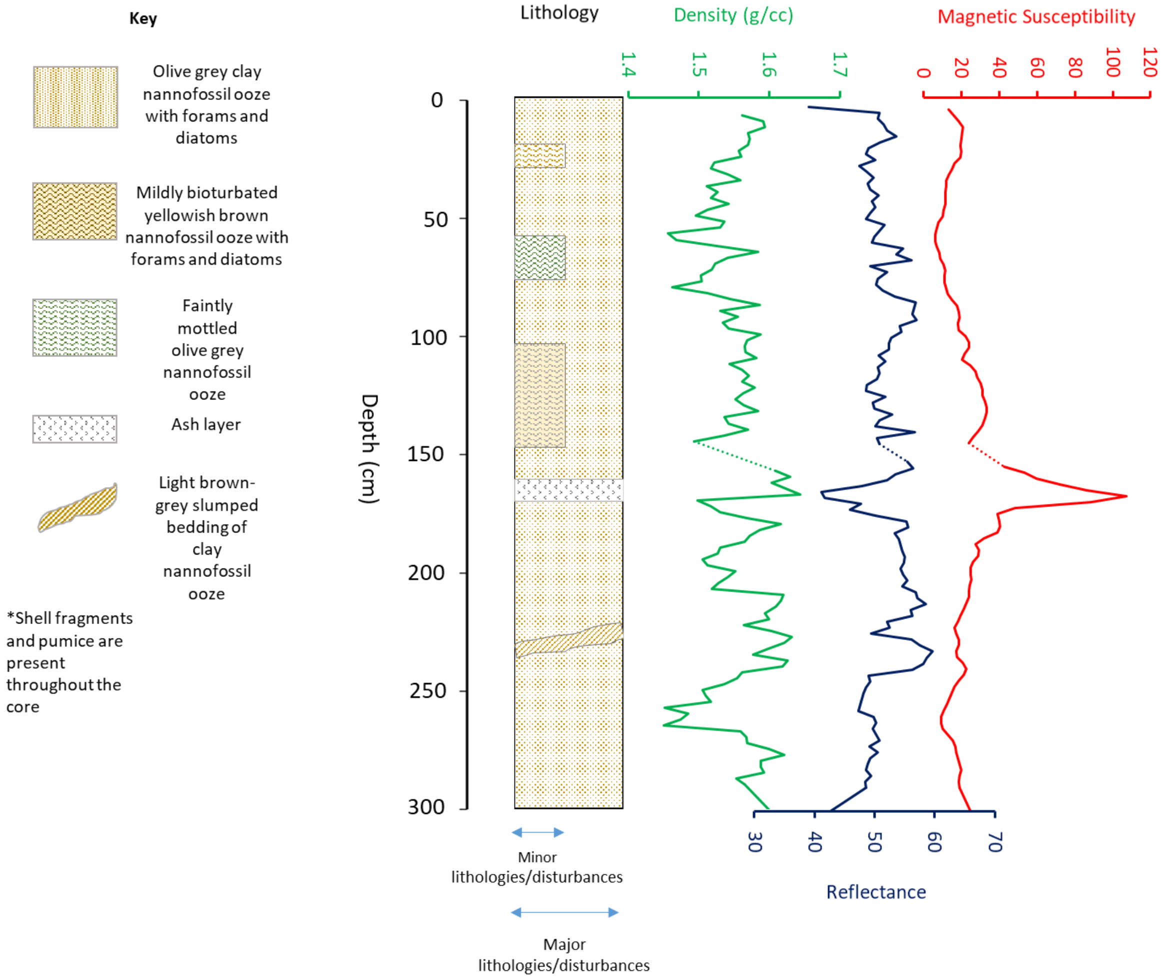

**Figure 4.2:** Lithology of 0-300cm in ODP 1207A shown alongside GRAPE density, reflectance and magnetic susceptibility. Dotted lines denote a gap in the sediment. All data was obtained from the IODP Janus database (web.iodp.tamu.edu/) and redrawn for this thesis.

### *4.3.1 Sediment properties*

The major lithology (Fig. 4.2) consists of olive grey calcareous clay nannofossil ooze with abundant forams and diatoms. Minor lithologies include volcanic ash, pumice and yellowish-brown calcareous clay nannofossil ooze. Bioturbation is mild throughout the 300cm section, and contacts between most lithologies are mildly bioturbated or gradational. The basal contact of the volcanic ash layer is sharp, and the top contact is mildly bioturbated. GRAPE density measurements show density between ~1.45 and ~1.64 g/cc, with a peak in the ash layer at 167cm. A reflectance maximum occurs at 232cm, and the minimum occurs within the ash layer at 165cm. The magnetic susceptibility signal is dominated by the ash signal at 167cm.

## 4.4: Site Justification

ODP 1207A was chosen as a suitable site for investigating Late Quaternary glacial and climatic change in the NW Pacific region for the reasons described below.

### *4.4.1: Core recovery*

From the shipboard scientific report of Bralower et al., (2002), the accumulation rate over the Quaternary appears to have been constant with no evidence of hiatuses in sedimentation at the site, and few coring gaps. The only significant gap was a 13cm interval between 137 and 150cm, which may have been lost during the drilling process.

### *4.4.2: Topographic setting*

ODP 1207A, close to the highest point on the northern Shatsky Rise (Fig. 4.1) is far from the influence of turbidite flows or river discharge. This reduces the complications that can arise when attempting to distinguish between fluvial, turbidite and ice-rafted sediments in marine environments (Hemming, 2004). Therefore, at this distal location, the most likely sources of coarse (>150µm) terrigenous sediments are icebergs and volcanism (Ruddiman and Glover, 1972).

### *4.4.3: Key oceanographic location*

As described in Section 4.2, ODP 1207A is located in an important oceanographic zone at the boundary between NW Pacific water masses, which have been known to fluctuate northwards and southwards of the site on millennial timescales. ODP 1207A was therefore chosen as a potentially important site for investigating oceanographic change.

### *4.4.4: Absence of existing data*

The Late Quaternary sections of ODP 1207A have not previously been studied. This research therefore provides new data from a previously unexplored site. Additionally, previous research has identified the modern SAF as the approximate southern limit of NW Pacific IRD (Conolly and Ewing, 1970). There are no published IRD records from the northern Shatsky Rise. However, at similar latitudes in the N Atlantic, the IRD signal of Heinrich Events can be found in very low concentrations of <1grain/g (Llave et al., 2006; Eynaud et al., 2009). Such low concentrations may be easily overlooked, particularly at latitudes thought to be beyond the IRD belt. Therefore, if IRD is present on the northern Shatsky Rise, this may explain the absence of any records in previous studies from this region (e.g. investigations on site V21-146 [37.68°; 163.03°E] by Thompson and Shackleton, 1980; Hovan et al., 1991).

### *4.4.5: Possibility of multiple IRD sources*

Previous modelling by Bigg et al., (2008) demonstrates that icebergs calved from both the east Kamchatka/Koryak region and the Sea of Okhotsk could reach a wide region of the NW Pacific, possibly as far south as ODP 1207A. This site may therefore contain ice-rafted material from more than one geological province, and may be useful for examining the provenance of NW Pacific IRD.

### *4.4.6: Carbonate content*

A key factor in the uncertainty surrounding NE Siberian glaciation is the unsuitability of Late Quaternary NW Pacific marine sediments for radiocarbon dating in this carbonate-poor basin (Korff et al., 2016), where the sea floor is predominantly below the calcite compensation depth (CCD; Berger et al., 1976). However, the initial report of Bralower et al., (2002) confirms the presence of foraminifera in the upper 300cm of ODP 1207A and further inspection in my study confirms abundant foraminifera. Therefore, this core is suitable for radiocarbon dating and other age model construction and palaeoclimatology tools including $\delta^{18}O$ and biostratigraphic analysis. This contrasts with other cores in the deep NW Pacific basin, where foraminifera are absent or rare (e.g. D'Agostino, 1985; Winter et al., 2005).

## 4.5. Methodology

Unless otherwise stated, the analyses described below were carried out by A.P. McCarron in the Department of Geography, University of Sheffield.

### *4.5.1: Sample preparation*

Prior to delivery and analysis, the core was cut into 1cm sections by staff at the International Ocean Discovery Program (IODP). Each 1cm sample weighed between 2 and 5g (Appendix 1). The bulk sediment was wet-sieved into three size fractions of >150μm, >63μm, and <63μm (Figure 4.3) by A.P. McCarron at The University of Sheffield. Some samples were divided into only two size fractions of >150μm and <150μm (Figure 4.3), due to limited drying space and time constraints. Samples were dried at 40°C until there was no further change in weight. Final sample weights were then recorded in grams (g).

### *4.5.2: Ice-rafted debris*

There are various size criteria for ensuring correct identification of IRD, e.g. the percentage (%) of lithogenic fraction in the 180-3000μm (Heinrich, 1988), grains/g of the total sample in the >62μm fraction (Ruddiman and Glover, 1972), or grains/g of the >250μm fraction (Hendy and Cosma, 2008). At open ocean sites, the lithogenic component in size fractions >63μm can generally be regarded as IRD, while lithic grains in the >150μm fraction can be confidently classified as IRD (Hemming, 2004). Therefore, following the quantification method of the key NW Pacific study by Bigg et al., (2008) the >150μm fraction was closely inspected for IRD at 1cm resolution using a standard reflected light binocular microscope by A.P. McCarron. Due to the expected low concentrations of IRD at this mid-latitude site, the samples were not split into aliquots. Grains with the character of lithic material were categorised as IRD. The absolute number of grains were then converted to grains/g of the entire bulk sample.

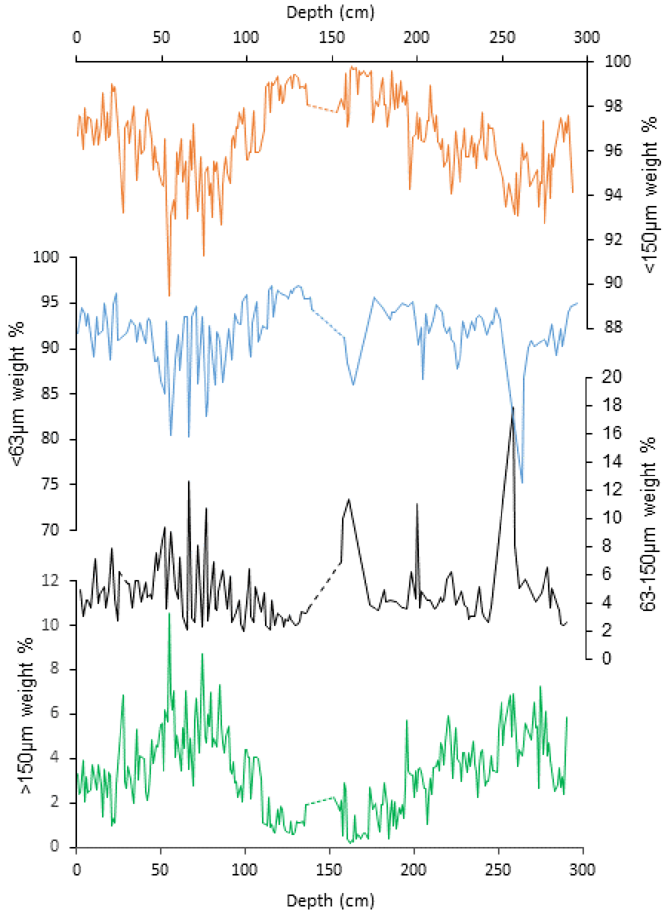

**Figure 4.3:** Size fractions by weight % (g). Note the different scales for each size fraction. Dashed lines show where there is a 13cm sediment gap between 137 and 150cm.

Selected grains were analysed further using a scanning electron microscope (SEM) from which high-resolution images were obtained to identify morphological features indicative of IRD such as conchoidal fractures, scour marks and degree of angularity (Immonen et al., 2014). Electron-dispersive spectroscopy (EDS) was carried out on selected grains to confirm their bulk chemistry as a means of inferring mineralogy, which was required to ensure that the grains being observed were terrigenous in origin.

### *4.5.3: Volcanic glass counts and tephrochronology*

Counts of volcanic glass were carried out in the >150μm fraction by A.P. McCarron alongside IRD counts to search for evidence of other potentially dateable tephra layers. The initial report of Bralower et al., (2002) identifies a ~9cm ash layer at 160-169cm in ODP 1207A. Shards from this layer were selected for geochemical fingerprinting by electron microprobe analysis and laser ablation inductively coupled mass-spectrometry (LA-ICP-MS) of single glass shards. Major and selected volatile elements (including S, F and Cl) in glass shards from ODP 1207A (166-167cm) were analysed in 2015 by V. Ponomareva and M. Portnyagin at GEOMAR Helmholtz Centre for Ocean Research Kiel, using a JEOL JXA 8200 electron microprobe. All analyses were performed at 15 kV accelerating voltage with a beam diameter of 5 μm and a beam current of 6 nA current. A detailed account of analytical conditions is described in Ponomareva et al. (2017), including internal standards and settings for spectrometers and subsequent data reduction. For comparison with literature data, the analyses were normalized to an anhydrous basis (i.e. 100 % total oxides). Trace element analyses were performed using laser ablation inductively coupled mass-spectrometry (LA-ICP-MS) at the Institute of Geosciences, Christian-Albrecht University of Kiel, Germany. The analyses were performed in 2019 using a quadrupole-based (QP) ICP-MS (Agilent 7900) and a Coherent GeoLas ArF 193 nm Excimer LA system. The data on glass from ODP 1207A and reference materials used for EMP and LA-ICP-MS analyses are provided in Appendix 2. The obtained glass composition was compared to those from known marker tephras (Aoki, 2008; Kimura et al., 2015; Albert et al., 2019) using bi-plots and spidergrams.

### *4.5.4: Accelerator mass spectrometry $^{14}C$ dating*

Around 20mg of the planktic foraminifera species *Neogloboquadrina (N) pachyderma* were picked from the >150μm size fraction by A.P. McCarron. Samples were cleaned by sonication in deionised water, followed by sonication in methanol. Pre-treatment and analysis were carried out by P.J. Reimer at the $^{14}$CHRONO Centre, Queen's University Belfast, UK. Pre-treatment of the foraminifera specimens followed the approach by Nadeau et al., (2001). Foram samples were weighed into septa seal vials and cleaned by adding 2 ml of 15% hydrogen peroxide and placed in an ultrasonic bath for 3 minutes. The peroxide was removed with a syringe, the forams rinsed with Milli-Q® water and then most of the water removed again with a syringe. While the forams were still damp, the septa seal vial was evacuated. A quantity of 1-2 mil of 85% phosphoric acid was added (depending on sample size) to hydrolyse the samples to $CO_2$. The vials were placed on a heating block at 70°C until the forams were completely dissolved.

The $CO_2$ was converted to graphite on an iron catalyst using the hydrogen reduction method (Vogel et al., 1987) and the $^{14}C/^{12}C$ ratio and $^{13}C/^{12}C$ were measured by accelerator mass spectrometry (AMS). The sample $^{14}C/^{12}C$ ratio was background-corrected and normalised to the HOXII standard (SRM 4990C; National Institute of Standards and Technology). The radiocarbon ages were corrected for isotope fractionation using the AMS measured $\delta^{13}C$, which accounts for both natural and machine fractionation. The radiocarbon age and one standard deviation were calculated using the Libby half-life of 5568 years following the conventions of Stuiver and Polach (1977).  The background sample used for samples UBA-28906 and 28907 was Icelandic spar calcite. For UBA-26539 the $^{14}C/^{12}C$ ratio of forams was used and processed at the same time from a depth expected to correspond to >60ka BP. The CALIB8.2 Radiocarbon Calibration Program (Stuiver et al., 2020) with the Marine20 curve (Heaton et al., 2020) was used to calibrate the dates, and includes a global offset and a regional correction (ΔR) of 328 $^{14}$C years (Yoneda et al., 2007).

### *4.5.5: Benthic $\delta^{18}O$ and $\delta^{13}C$ stratigraphy*

Samples were chosen from the benthic foraminifera species Cibicidoides wuellerstorfi for construction of benthic $\delta^{18}O$ and $\delta^{13}C$ curves. Samples were picked from the >150µm size fraction, of a consistent diameter of ~500µm by A.P. McCarron. Samples were cleaned by sonication in deionised water, and then sonicated again in methanol. Three different sampling methods were trialled: twelve individuals per cm, one individual per cm, and the mean of three individuals per cm. The mean $\delta^{18}O$ value of three individuals per cm was chosen as the most appropriate sampling method, as it yielded the lowest standard deviation between samples. Samples were analysed at the Centre for Isotope Geochemistry, British Geological Survey, UK by M.J. Leng. Approximately 60-100 micrograms of carbonate were used for isotope analysis using an IsoPrime dual inlet mass spectrometer plus Multiprep device. Samples were loaded into glass vials and sealed with septa. The automated system evacuated vials and delivered anhydrous phosphoric acid to the carbonate at 90°C. The evolved $CO_2$ was collected for 15 minutes, cryogenically cleaned and passed to the mass spectrometer. Isotope values ($\delta^{13}C$, $\delta^{18}O$) were reported as per mille (‰) deviations of the isotopic ratios ($^{13}C/^{12}C$, $^{18}O/^{16}O$) calculated to the VPDB scale using a within-run laboratory standard calibrated against NBS-19. The Calcite-acid fractionation factor applied to the gas values was 1.00798. Due to the long run time of 21 hours a drift correction was applied across the run, calculated using the standards that bracket the samples. The Craig correction was also applied to account for $\delta^{17}O$. The average analytical reproducibility of the standard calcite (KCM) was 0.05‰ for $\delta^{13}C$ and $\delta^{18}O$.

### *4.5.6: Planktic foraminifera counts*

The relationship between IRD and sea-surface oceanographic shifts was investigated through high-resolution counts of planktic foraminifera. Following wet sieving, the >150µm size fraction was split using a sample micro-splitter until a sample of approximately 300 grains was obtained. Counts of all planktic foraminiferal species were then carried out in the split sample by H. Brooks, with help in identification by A.P. McCarron. The absolute abundances of each species were converted to relative abundances by calculating the percentage contribution of each species to the total planktic foram count. Relative abundances were analysed for evidence of oceanographic change, particularly SST change.

### *4.5.7: Age model construction*

The age model for ODP 1207A was derived from a synthesis of the dating techniques described in this section. Sedimentation rates were calculated from each radiocarbon, tephra and MIS boundary age point, the latter being derived from the benthic $\delta^{18}O$ curve. The MIS boundaries were determined by visually comparing the $\delta^{18}O$ signal with other NW Pacific curves (Thompson and Shackleton, 1980; Kiefer et al., 2001), deriving the ages of MIS boundaries from the LR04 global benthic stack of Lisiecki and Raymo (2005). A further age-tie point was derived from the *N. pachyderma* (sinistral) counts, where a known (Thompson and Shackleton, 1980; Yamane, 2003) NW Pacific temperature change occurs shown by a rapid reduction in the abundance of this cold water species. This temperature change coincides with the boundary between the penultimate glacial period (MIS 6) and the last interglacial (MIS 5E), thus serving as a useful age marker for the MIS 6-5E boundary in the Shatsky Rise region.

## 4.6: Results

This section presents the data produced to construct the age model for ODP 1207A, followed by the results of IRD analysis. In the discussion, these data components are analysed alongside the planktic foraminifera counts and then synthesised into an analysis of iceberg flux, climatic and oceanographic change throughout the Late Quaternary.

### *4.6.1: Chronostratigraphic framework*

The volcanic ash component was dominated by bubble wall glass shards ~150-500µm diameter, with isolated pumice stones up to 1000µm diameter. The ash in ODP 1207A was deemed to be a primary airfall deposit due to the homogenous geochemical population of the tephra and counts showing a distinct single shard peak (Fig. 4.4; Griggs et al., 2014), and was therefore considered suitable for tephrochronological analysis.

The glass composition obtained permitted the explicit identification of the ODP 1207A ash as the geochemically unique Aso-4 marker tephra layer from the Aso caldera on Kyushu, Japan (Fig. 4.4; Aoki, 2008; Kimura et al., 2015; Derkachev et al., 2016; Albert et al., 2019). The Aso-4 tephra has been found in numerous cores in the Sea of Japan, Okhotsk Sea and NW Pacific as well as in the Lake Suigetsu sedimentary record, and was independently dated at 86.8-87.3 ka based on the oxygen isotopic stratigraphy of core MD01-2421 (off central Japan; Aoki, 2008) and at 86.4±1.1 ka ($^{40}$Ar/$^{39}$Ar; Albert et al., 2019). The age model for ODP 1207A uses the median date of 87.05 ka from Aoki (2008), which is also within the range calculated by Albert et al. (2019).

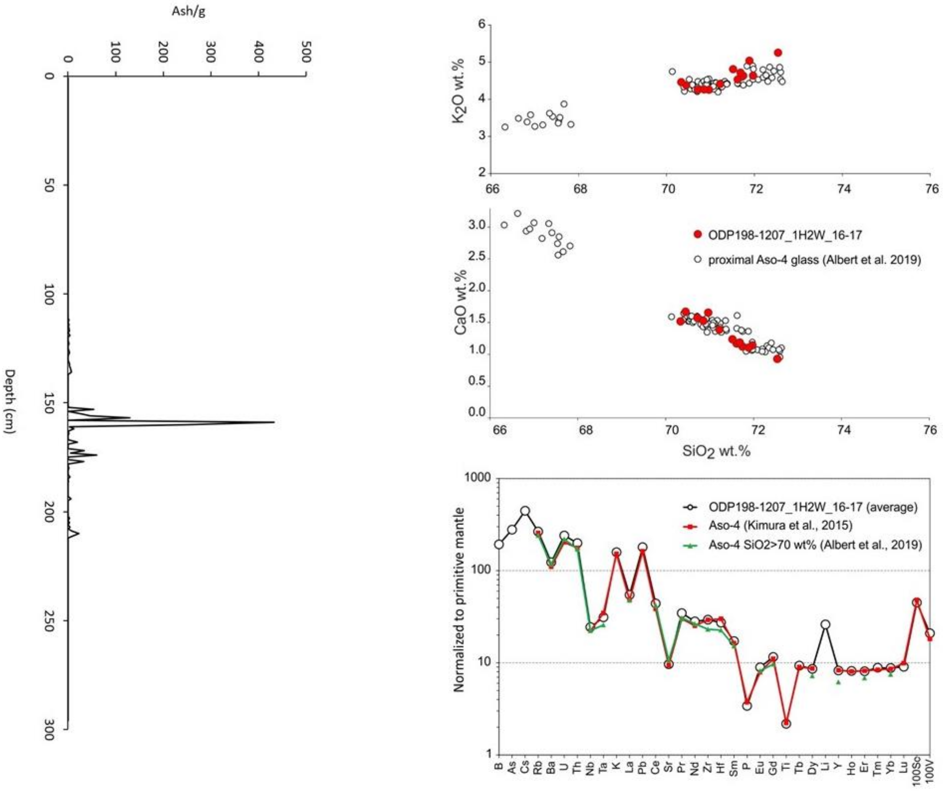

**Figure 4.4:** Left: Volcanic glass shards/g in the >150µm fraction of the upper 300cm of ODP 1207A, showing a distinct glass peak between 160 and 169cm. Right: Composition of glass from tephra sample ODP198 core 1207A, section 1H2W, interval of 16-17 cm (166-167cm below sea floor) and proximal Aso-4 samples (Kimura et al., 2015; Albert et al., 2019). Albert et al., (2019) analyzed pumice from three levels: base, middle and upper). Low-Si glass occurs only in the upper level. Note, sample depth is recorded as

1H2W- 16-17. This refers to the original ODP labelling methodology, which splits cores into 150cm sections. The absolute depth from the core-top is 166-167cm.

Data for the five $^{14}C$ dates are shown in Table 4.1. These dates suggest that most of the Holocene sediments are not present in ODP 1207A, and may possibly have been lost during drilling. The four younger dates shown in Table 4.1 were used in the final chronology from ODP 1207A. These dates were obtained from depths between 9 and 51cm. Most of the core deeper than 51cm was deemed to be beyond the age range of $^{14}C$ analysis (Reimer et al., 2013). The oldest date of 47,495 cal. years BP at 150-151cm, was not included in the final chronology because it was inconsistent with the age of the Aso-4 tephra by >40 ka. This may be because a mix of foram species were used in the analysis of this sample, including both planktics and benthics, due to the low foram abundance at this depth. The sample may also have been contaminated as a result of the sediment hiatus described in Section 4.4.2.

| **Depth (cm)** | **Lab ID** | **$^{14}C$ BP** | **14C 1 sd.** | **Cal BP Age Range (95.4%)** | **Median Cal BP Age (95.4%)** |
|---|---|---|---|---|---|
| **9-10** | UBA-28907 | 13445 | 68 | 14791 – 15089 | 14925 |
| **34-35** | UBA-40785 | 28919 | 218 | 31497 - 32107 | 31826 |
| **38-39** | UBA-28906 | 27836 | 282 | 30545 - 31078 | 30799 |
| **50-51** | UBA-40786 | 32920 | 350 | 35844 - 36632 | 36231 |
| **150-151** | UBA-26539 | 43747 | 1285 | 44108 - 46303 | 47495* |

**Table 4.1: $^{14}C$ and calibrated calendar dates from ODP 1207A.** The CALIB Radiocarbon Calibration Program was used to calibrate the dates, which assumes a hypothetical Reservoir Correction of around 200 $^{14}C$ years, however, this is likely to be an underestimate of the actual local Reservoir Age by over 600 $^{14}C$ years (Kiefer et al., 2001; Reimer et al., 2013; Yoneda et al., 2007). *The oldest sample (150-151) was not used for the age model, as it conflicted with the age of the Aso-4 tephra and the $\delta^{18}O$.

Marine Isotope Stage (MIS) boundaries were identified from the benthic $\delta^{18}O$ curve, extending from 0 to 263cm (Fig. 4.5). The $\delta^{18}O$ chronostratigraphy shows that the upper 300cm of ODP 1207A extends from ~175 ka BP, in the penultimate glacial MIS 6 to ~11 ka BP in the early Holocene. The benthic $\delta^{18}O$ curve fits well with the LR04 benthic stack of Lisiecki and Raymo, (2005), as shown in Fig. 4.5.

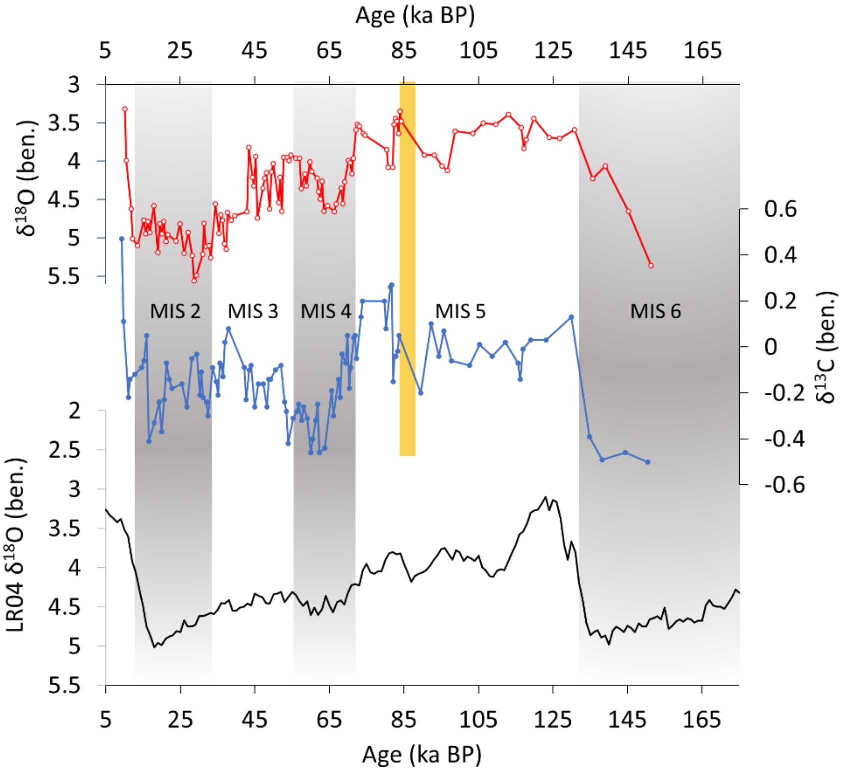

**Figure 4.5:** Chronostratigraphy of ODP 1207A based on the benthic $\delta^{18}O$ curve (red line), $^{14}C$ dates and the dated Aso-4 tephra (yellow bar). The $\delta^{13}C$ curve from ODP 1207A is also shown (blue line). Dates are extrapolated from the sedimentation rate calculated from the $\delta^{18}O$, $^{14}C$ and tephra analyses. Alternating grey and white bars denote Marine Isotope Stages 1-6. The LR04 benthic $\delta^{18}O$ stack of Lisiecki and Raymo, (2005) is shown for comparison on the bottom axis.

### *4.6.2: Composition of IRD in ODP 1207A*

Analysis by SEM and EDS confirmed the majority of lithic grains in ODP 1207A as quartz (Fig. 4.6). Two dark dropstones were also identified. Some quartz grains exhibited high relief and high angularity (e.g. Images A and B), while others were rounded (e.g. Images D and E). Rounded grains (Images D and E) may have been transported supraglacially, thus avoiding intense glacial weathering. The morphology of quartz grains at Site 1207 is similar to those previously described as having a glacial origin at Site 580 (41.6°N, 154°E; St. John and Krissek, 1999; Fig 4.6, Images G-I; Chapter 5). Both sites contain populations of rounded and angular grains, demonstrating that glacially-derived quartz does not necessarily require an angular or fractured morphology to be categorized as glacial in origin. Rather, grain size could be regarded as the more important criteria to be definitely regarded as ice-rafted (Hemming, 2004).

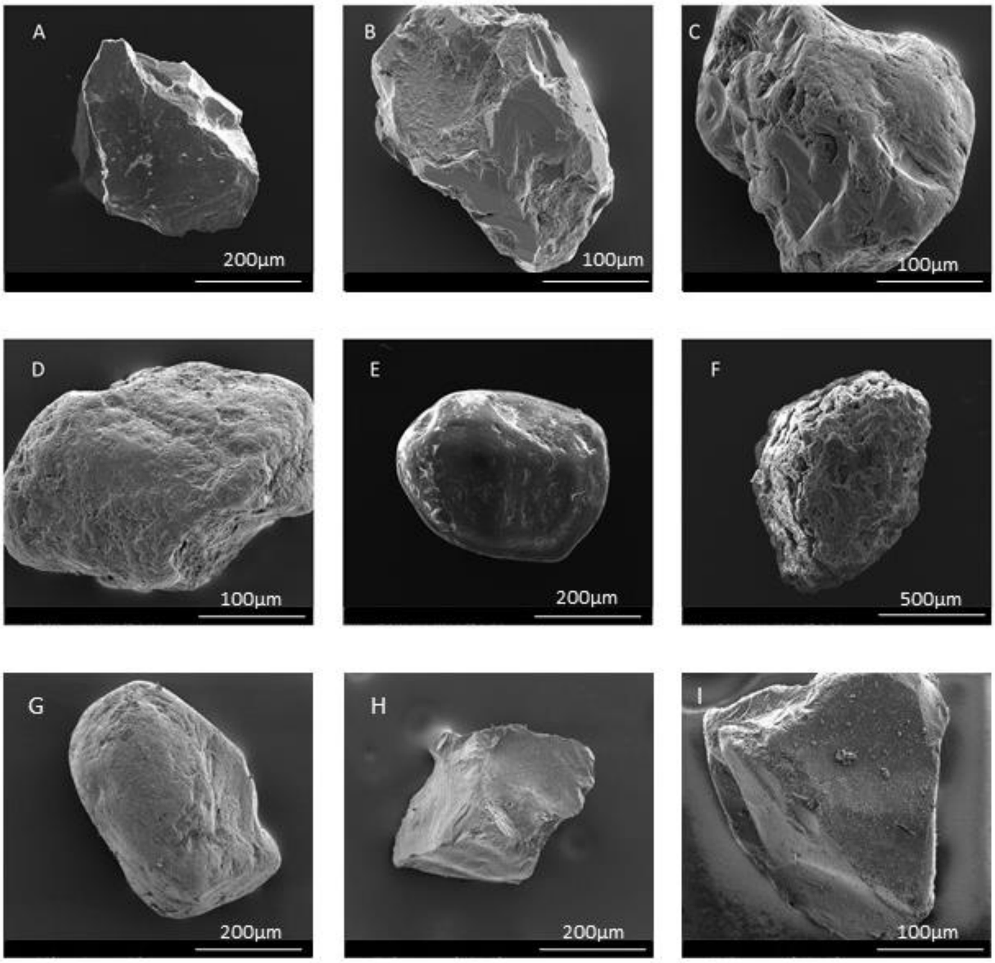

**Figure 4.6: SEM Images of Quartz grains and dropstone.** Grains A-F were found at ODP Site 1207A, and grains G-I were found at DSDP Site 580. Grains were confirmed as quartz (A-E and G-I) and mafic rock fragment (F) from Electron Dispersive Spectroscopy (EDS). Scale bars in the bottom right of each image.

Note: Scale is not consistent in all images. A: Angular grain 104cm depth. B: Angular grain, 55cm depth. C: Sub-angular grain, 55cm depth. D: Sub-rounded grain, 55cm depth. E: Rounded grain, 152cm depth. F: Dark dropstone, 32cm depth. Grains G-I from DSDP 580 with a known IRD component, show similar morphologies to those in ODP 1207A, with sub-rounded to angular grains present. Grains with higher angularity (A-C and H-1) show hallmarks of glacial scouring and crushing.

### *4.6.3: Late Quaternary iceberg flux to ODP 1207A*

The IRD flux to ODP 1207A is characterised by low-level supply of <3 grains/g of the bulk sample (Fig. 4.7). The temporal pattern of IRD is distinctly episodic, with multi-millennial periods of no ice rafting, preceding and following short periods of IRD deposition. The highest concentrations of IRD occur in late MIS 3, with three peaks of similar magnitude (Fig. 4.7). These peak IRD concentrations align approximately in time with the large Heinrich-style IRD layer in ODP 883 further north (Bigg et al., 2008), and are likely to derive from the same period of significantly heightened iceberg flux. There are slightly enhanced levels of IRD around the depth of the Aso-4 tephra (~87,000 years ago). IRD counts at this depth reveal quartz and a small number of dark lithic fragments, distinct from the layer of volcanic glass shards and pumice, suggesting a glacial, rather than volcanic origin. All other glacial stages between MIS 2 and the MIS 6-5 transition are characterised by similarly low levels of episodic IRD flux. However, IRD is absent for most of MIS 6, with ice-rafting to Site 1207 during this glacial period only occurring towards the termination and transition to interglacial MIS 5e.

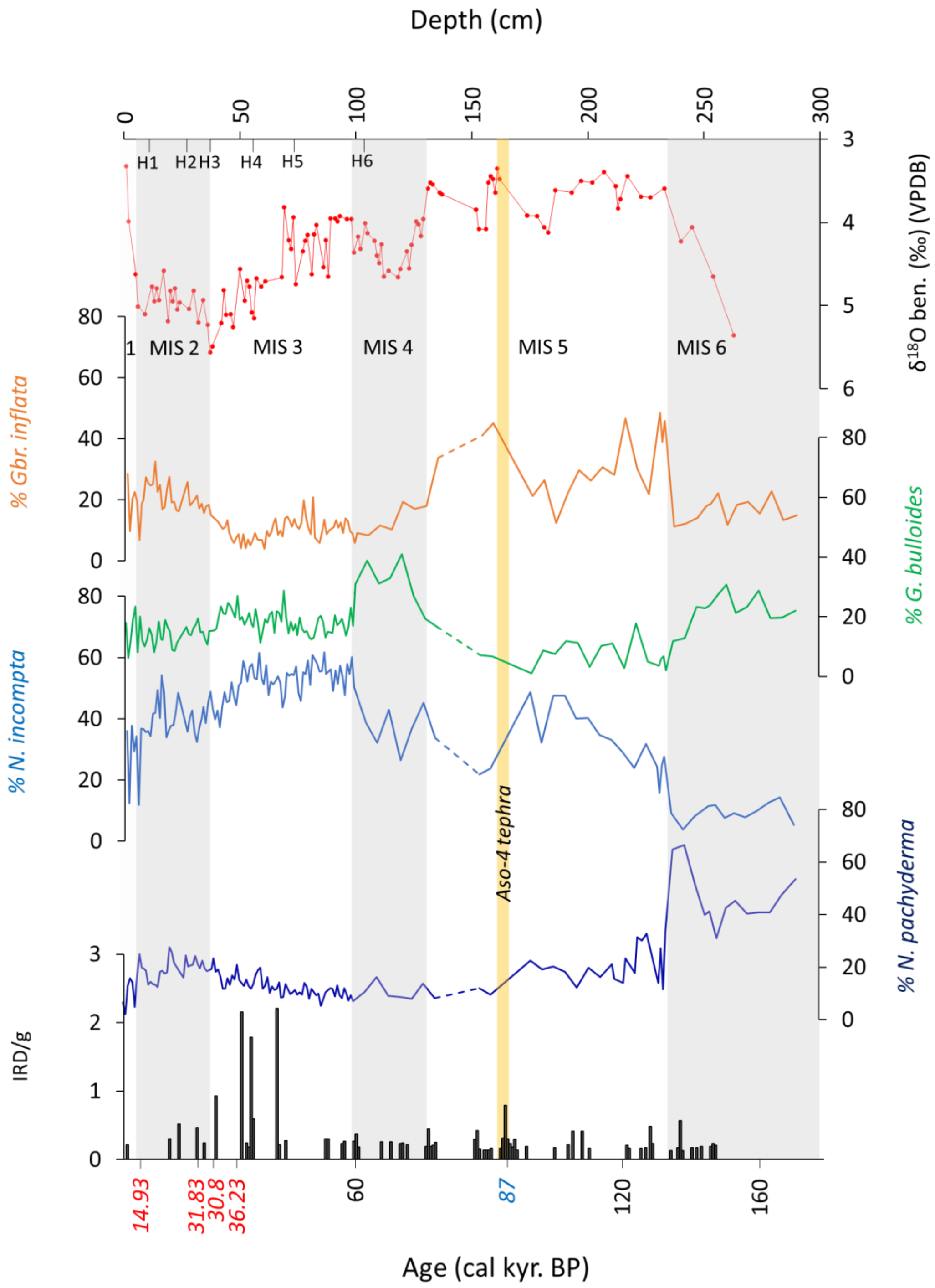

**Figure 4.7: % Abundances of the four most common planktic foraminifera species, δ$^{18}$O and IRD in ODP 1207A.** Note: the sample density is higher in the upper 100cm than in the lower 200cm as the highest IRD concentrations occur in this section (late MIS 3 to early MIS 2), therefore a higher sampling resolution was used in an attempt to identify abrupt oceanographic changes during this period. Dates in red are calibrated median probability $^{14}$C dates (see Table 4.1). The blue date and the yellow bar denote the Aso-4 tephra. Dates in black were extrapolated from the δ$^{18}$O stratigraphy, $^{14}$C and tephra ages. Marine Isotope Stages are marked by

alternating grey bars. Approximate timings of Atlantic Heinrich Events are shown by H1-H6. Note that the absence of IRD older than ~150,000 years ago is a zero count, as IRD recording extended to 300 cm. Note also that the three largest IRD peaks occur in mid-late MIS 3, and the age model shows that the oldest of these aligns approximately with the 40 ka event in ODP 883 (Bigg et al., 2008).

### *4.6.4: Planktic foraminifera*

Four planktic foraminifera species dominate the Late Quaternary assemblage and account for ~80-99% of the total abundance in ODP 1207A (Figs. 4.7 and 4.8). A maximum in *Neogloboquadrina (N.) pachyderma* occurs during MIS 6 (>65% of the total population). This is in contrast to a minimum in *N. incompta* during the same period. *N. pachyderma* and *Globigerina (G.) bulloides* both decline at the MIS 6-5 boundary while *N. incompta* and *Globorotalia (Gbr.) inflata* rapidly increase. A maximum in *G. bulloides* occurs during MIS 4, concurrent with decreases in *Gbr. inflata* and *N. incompta*. *N. incompta* dominates and reaches a maximum during MIS 3. *Gbr. inflata* and *N. pachyderma* both increase in MIS 2 (33% and 26% respectively) while there are slight decreases in *N. incompta* and *G. bulloides.* There are variable decreases in all four species at the MIS 2-1 boundary.

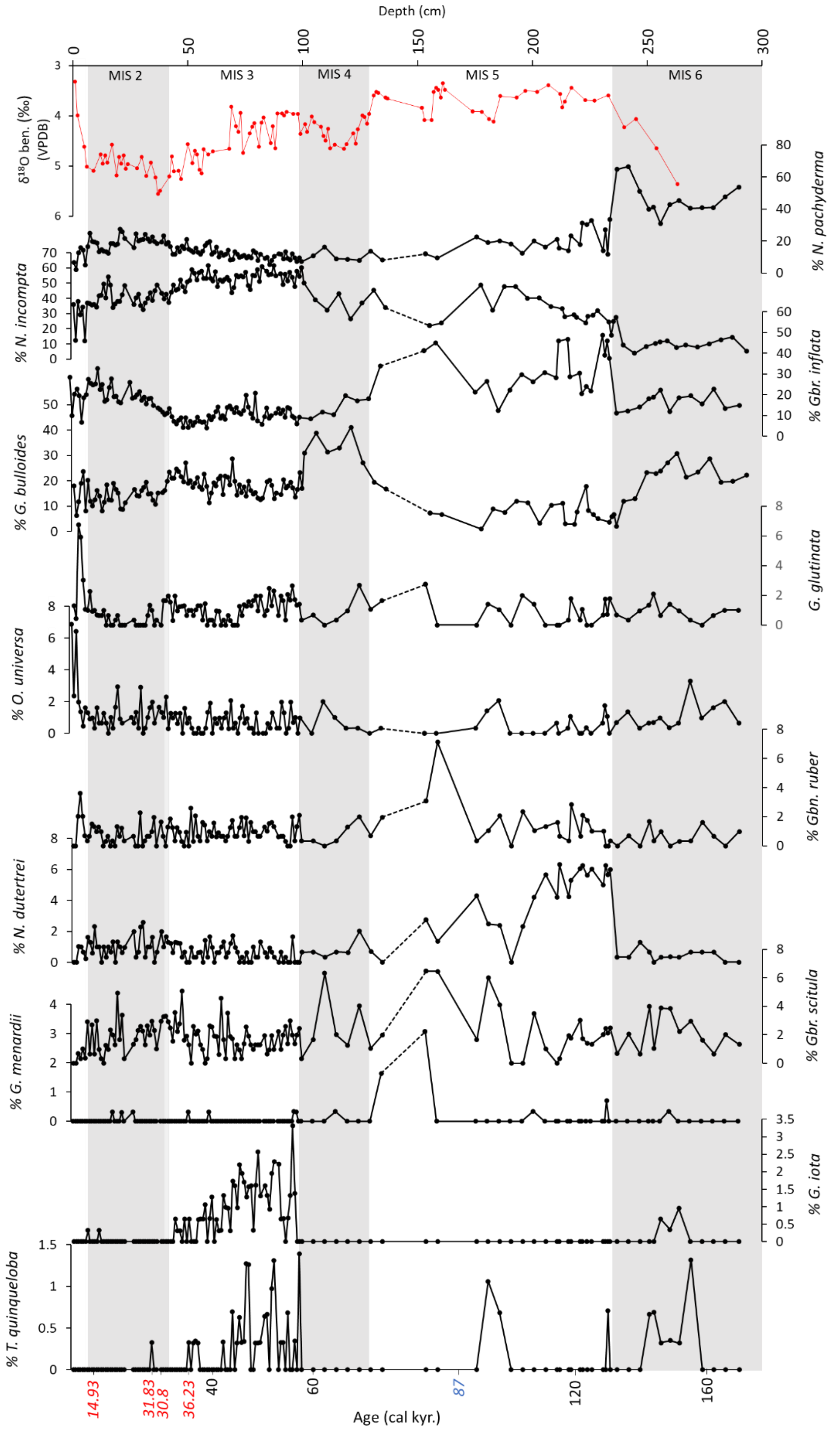

**Figure 4.8: % abundances of planktic foraminifera species in ODP 1207A:** All species with abundances >1% in at least one sample are shown. Note: Y-axis is different for some species. The least abundant species are at the bottom of the chart and the most abundant are at the top. Abundances are plotted against the

benthic δ$^{18}$O curve in red. MIS are shown by the grey and white bars. Dates are on the bottom x-axis. Dashed lines denote a sediment gap between 137 and 150cm.

## 4.7: Discussion

### *4.7.1: Late Quaternary oceanography on the northern Shatsky Rise*

Table 4.2 outlines the geographic and depth preferences for the planktic foraminifera found in ODP 1207A. Out of the four most common planktic foraminifera species shown in Fig. 4.7, *N. pachyderma* shows a strong preference for cold sea surface temperatures (SST), while *N. incompta* shows a preference for temperate waters (Chiyonubu et al., 2012). Together these two species are indicators of SST (Thompson and Shackleton, 1980; Chiyonubu et al., 2012).

| **Species** | **Geographical Distribution** | **Depth Preference** |
|---|---|---|
| *N. incompta* | temperate-transitional | 0-500m |
| *N. pachyderma (s)* | polar-subpolar | 0-500m |
| *Gbr. inflata* | transitional-subtropical | >200-1000m |
| *G. bulloides* | Broad tolerance. Slight preference for subpolar or cold upwelling | 0-100m |
| *Gbr. scitula* | subtropical | >200m |
| *N. dutertrei* | tropical-subtropical | >25m. Abundant at the depth of the chlorophyll maximum (Fairbanks and Weibe, 1980). |
| *G. truncatulinoides* | subtropical | >200m, ascending to shallower depths during winter. |
| *Gbn. ruber* | tropical-subtropical | 0-50m |
| *G. falconensis* | temperate-subpolar | 0-1000m |
| *G. menardii* | tropical-subtropical | 200-400m |
| *G. bilobata* | broad tolerance | >200-1000m |
| *O. universa* | broad tolerance | >200-1000m |
| *G. glutinata* | broad tolerance | 0-10m |
| *T. quinqueloba* | transitional to polar | 0-200m |
| *G. iota* | subtropical-transitional | 0-200m |

**Table 4.2:** Planktic foraminifera species found at 0-300cm in ODP 1207A and general geographical preferences. Geographical distribution and depth data obtained from ngdc.noaa.gov/.

The different temperature preferences between *N. pachyderma* and *N. incompta* are apparent in Figs. 4.7 and 4.8. This is particularly clear during MIS 6 when *N. pachyderma* dominates the assemblage, suggesting cold SST, but also during MIS 5, 3 and 2 when *N. incompta* is dominant, suggesting more temperate SST.

Changes in the relative abundance of the subpolar *N. pachyderma* are likely to be linked to latitudinal shifts in the position of the SAF relative to Site 1207. As observed in other cores situated in the Shatsky Rise region of the NW Pacific (Thompson and Shackleton, 1980; Yamane, 2003), peak abundances of *N. pachyderma* at Site 1207 occurred during MIS 6 (>65% of total planktonic foram population) and to a lesser extent during mid-late MIS 2 (~26% of total planktonic foram population). The widely observed decline in *N. pachyderma* is a useful marker for verifying the depth of the MIS 6-5 boundary inferred from the benthic $\delta^{18}O$ curve (Figs. 4.7 and 4.8). During these periods, and particularly MIS 6, the SAF was likely further south than its present-day position, and cold subpolar waters were dominant. This corroborates the lipid palaeothermometer study of Jonas et al., (2017) who argue that reduced SST in the Kuroshio-Oyashio interfrontal zone during MIS 6 and MIS 2 are related to weakening of the subtropical gyre, thus permitting the southward influx of polar and subpolar waters as far south as the coast of southern Japan. This oceanographic change marked by abundance shifts in *N. pachyderma* may also serve as a useful age tie-point for future inter-core correlation of sites around the Kuroshio-Oyashio transition zone.

The abundances of *G. bulloides,* a mixed-layer-dwelling species (<10m below sea surface), and *Gbr. inflata,* which prefers conditions at the base of the thermocline (~1000m) are largely dependent on nutrient supply at these two respective depths (Channell et al., 2013). *G. bulloides* is most abundant during MIS 6 and MIS 4, suggesting a productive environment during these periods, which may be due to increased upwelling and possible influx of subarctic waters, the latter of which was likely the case during MIS 6 as recorded in the proliferation of *N. pachyderma*. *Gbr. inflata* increases in abundance during early MIS 5 (interglacial MIS 5e) which may be due to increased nutrient supply at depth.

During MIS 5, peaks of subtropical species *Neogloboquadrina (N.) dutertrei*, accompanied by a gradual increase in transitional species *N. incompta*, point towards the dominance of transitional waters during this time. Mid-MIS 5 (around MIS 5c) shows evidence of subtropical water influx with peaks in the subtropical species *Globigerinoides (Gbn.) ruber* and *Gbr. scitula* and the transitional species *Gbr. inflata*, and a minimum in cold water species *N. pachyderma*. *N. incompta* reaches a maximum of >61% of the total assemblage during MIS 3, when transitional waters appear to have been dominant. The significant appearance of the scarce species *Globigerinita (G.) iota* and *Turborotalia (T.) quinqueloba* and a rapid decrease in *G. bulloides* at the MIS 4-3 boundary appears to confirm a distinction in SST between MIS 4 and MIS 3, and adds confidence to the depth-estimate of MIS 3 from the benthic $\delta^{18}$O chronostratigraphy. Slight increases in *N. pachyderma* during MIS 2 confirms earlier observations of cooler waters during the LGM (Thompson and Shackleton, 1980; Yamane, 2003). However, with relative abundances of *N. pachyderma* no greater than ~ 26%, migration of the SAF south of ODP, 1207A during this period cannot be inferred, but the site may have been towards the northern edge of the transition zone. Planktic foraminiferal assemblages during the past ~175 ka suggest that temperate surface waters were dominant at ODP 1207A, except during MIS 6 when there was an influx of subpolar waters, consistent with a notable increase in *N. pachyderma*.

### ***4.7.2: The relationship between planktic foraminifera and IRD***

During late MIS 6 when there was maximal abundance of *N. pachyderma*, there was a concurrent onset of ice-rafting to ODP 1207A, suggesting that there may have been a relationship between colder SST and iceberg activity on the NE Siberian coast. However, prior to late MIS 6, *N. pachyderma* abundance was relatively high, between ~40 and 65% of total planktic foraminifera, but IRD was absent for a prolonged period during this time. During more recent MIS the relationship between the position of the SAF inferred from *N. pachyderma* and the flux of Siberian icebergs to Site 1207 is weak, as the largest IRD flux occurred in late MIS 3 when warmer transitional waters were dominant. The palaeoceanographic data therefore shows no strong correlation between the timing of iceberg events and large-scale NW Pacific surface oceanographic variability during most glacial and interglacial stages throughout the Late Quaternary. Indeed, the colder climate, consistent with the high abundance of *N. pachyderma* found in most of MIS 6 contrasts with the absence of IRD at Site 1207, except towards the MIS 6-5 boundary (Fig. 4.7). This discrepancy is discussed further in Section 4.7.3.

### *4.7.3: Implications for Late Quaternary NE Siberian glaciation and climate*

The new IRD series at ODP 1207A represents the most southerly recorded occurrence of IRD in the NW Pacific. This finding adds compelling evidence to support the hypothesis that during the Late Quaternary, glaciation in NW Siberia was significant enough to deposit an IRD belt ranging from the Kamchatkan coast to the Shatsky Rise in the deep-sea NW Pacific, >1500 km from the nearest possible source of icebergs. The IRD belt is similar in scale to the ‘Ruddiman Belt’ of the N Atlantic, and the approximate southern limit of ice-rafting in the NW Pacific is shown here to be significantly further south than previously thought, with episodic iceberg drift southward of the SAF. The low IRD concentrations of <3 grains/g are similar to IRD concentrations at some sites at the same latitude in the Gulf of Cadiz in the N Atlantic during Heinrich Events 1 and 4 (Llave et al., 2006; Eynaud et al., 2009).

The episodic supply of icebergs to ODP 1207A, preceding and following multi-millennial periods of no iceberg supply, suggests that only the largest iceberg flux events were capable of generating sufficient bergs to reach this distal site. Therefore, ODP 1207A’s IRD record serves as an important indicator of episodic large-scale glacial change or collapse on the east Siberian margin during the last-and-penultimate glacial periods. Maximum ice-rafting during MIS 3 around 40 ka BP in the 883 and 1207 IRD records supports the hypothesis that the maximum glacial ice extent in eastern Siberia occurred ~20,000 years earlier than the global LGM, but could also mean that MIS 3 was the period of peak ice sheet instability. It is likely that the abrupt intensification of ice-rafting to ODP 1207A around 40ka BP is the same ice-rafting signal observed in the dramatic Heinrich-style

IRD peak in ODP 883 (Bigg et al., 2008). Therefore, this event has a basin-wide expression and can be considered a key event in the Late Quaternary history of NE Siberian glaciation. Inter-core comparisons of IRD and other climatic proxies are explored in detail in Chapters 5 and 6.

With the confirmation of an extensive IRD belt in the NW Pacific, and heightened IRD flux during late MIS 3, this study strengthens the argument that a large glacial ice mass existed in NE Siberia during the last glacial period. Its collapse from its maximal state provides at least a partial explanation for the ~ 20 m anomalous rise in global sea level around 40ka BP (Siddall et al., 2003). Additionally, large-scale iceberg discharge into the NW Pacific, similar in magnitude to the N. Atlantic Heinrich Events, would have injected large volumes of freshwater into the ocean. As observed in the N. Atlantic (Hemming, 2004) and NE Pacific (Maier et al., 2018), such changes have the potential to significantly alter the regional and global climate, and further work should be carried out to investigate the climatic impact of sudden freshwater influx to the NW Pacific.

The palaeoenvironmental data from ODP 1207A shows very little evidence of temporal coupling between the NW Pacific and cold N Atlantic climatic events (marked by Heinrich Events H1-H6 in Fig. 4.7), unlike in the NE Pacific (Maier et al. 2018). However, it is important to note that the data presented in this chapter does not rule out this possibility. It may be hypothesised that glacial change in NE Siberia occurs with different rhythms to those around the North Atlantic, but this is not conclusive from this study.

The size and behaviour of NE Siberian ice masses appear to differ significantly between glacial periods. The longest period of no ice-rafting over the past >160,000 years occurs in MIS 6. According to the age model, this prolonged period of IRD absence lasts at least 30,000 years. Reduced IRD supply to the NW Pacific during mid-late MIS 6 is also observed to the north-west of ODP 1207A at DSDP 580 (41.6°N, 154°E; St. John and Krissek, 1999). IRD absence at ODP 1207A is followed by a period of ice-rafting towards the Termination of MIS 6 which coincides with the coldest SST. Nürnberg et al., (2011) also observe an increase in ice-rafting in late MIS 6 from W Kamchatka into the Sea of Okhotsk, suggesting that icebergs reaching ODP 1207A during this time may have originated from the Sea of Okhotsk coast. Alternatively, late MIS 6 ice-rafting may have been regionally synchronous. The dominance of quartz in the IRD record suggests that IRD deposited at site 1207A may have originated from geological provinces in the Koryak Highlands (Fedorov et al., 2011) or western Kamchatka (Nürnberg et al., 2011). The most likely sources of IRD to the NW Pacific are investigated in Chapters 6 and 7.

Whilst ice-rafting is absent for much of MIS 6, the MIS 6 planktic foraminifera counts in ODP 1207A show strong evidence of colder SST. In contrast to MIS 6, cold MIS 2 and the LGM exhibit an ice-rafting pattern typical of the last glacial period at ODP 1207A, with low, episodic supply of icebergs. The contrast in ice-rafting patterns between the LGM and MIS 6 suggests differing glacial dynamics from one glacial period to another. While there is evidence of iceberg supply to other sites during earlier MIS 6 (St. John and Krissek, 1999; Nürnberg et al., 2011), the absence of IRD at ODP 1207A suggests that ice-rafting was not of sufficient intensity to transport bergs to this distal site. This theme will be discussed further in Chapter 8.

## 4.8. Summary

The new ice-rafting record presented in this chapter demonstrates that NE Siberian icebergs were episodically transported further south than previously recorded over the past ~160 ka. It is likely that IRD levels ~40 ka BP, present in both ODP 883 and ODP 1207A originate from the same glacial collapse event, or series of events. The discovery of IRD in the mid-latitude NW Pacific suggests the need for a re-evaluation of the scale and importance of Late Quaternary regional NE Asian iceberg input.

Planktic foraminifera populations appear to show little correlation between ice-rafting and SST change. Furthermore, ice-rafting events which reached ODP 1207A appear to be independent of N Atlantic Heinrich Events and NE Pacific climatic changes, but this observation requires further investigation given that the data does not resolve this question. The mechanisms associated with periods of heightened glacial change and ice-rafting on the NE Siberian coast remains uncertain.

Whilst it is accepted that NW Pacific IRD, including that found at ODP 1207A originated from icebergs calving from the Kamchatka-Koryak coast, and possibly the northern Sea of Okhotsk (see Chapter 2), further work is required to understand the spatial and temporal variation in Late Quaternary ice-rafting and glacial change. Furthermore, despite focused efforts in the Bering Sea and Sea of Okhotsk (e.g. Nürnberg et al., 2011; Ovsepyan et al., 2017), detailed open NW Pacific inter-core comparisons exploring Late Quaternary NE Siberian glaciation have not been attempted. The remainder of this thesis addresses these problems.

# Chapter 5: Late Quaternary Chronostratigraphy and Glacial Deposits of DSDP 580

## 5.1. Introduction

This chapter presents the results of the analysis of Late Quaternary sediments in the NW Pacific site Deep Sea Drilling Program (DSDP) 580. This site was drilled on Leg 86 of the DSDP in 1982. A 155.3m series of cores of late Pliocene-Holocene age was drilled at 41.37°N, 153.59°E at a water depth of 5375m on the NW Pacific abyssal plain (Figure 5.1). The chronostratigraphy and results of the analysis of the glacial sediments at this site are presented in the following sections. The discussion section examines the significance of the IRD record at DSDP 580 in the upper 3m for our understanding of glacial change in NE Asia, compares the conditions at DSDP 580 with those at ODP 1207A (see Chapter 4), and discusses the implications for spatial and temporal variations in glacial change, iceberg flux and climatic change in the NW Pacific during the Late Quaternary.

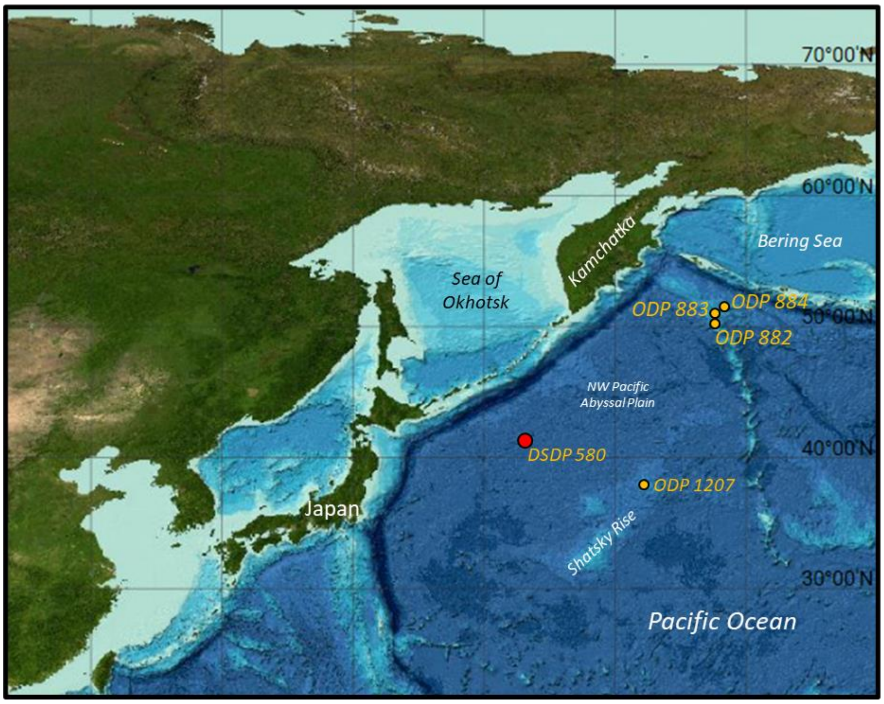

**Figure 5.1:** Map of the NW Pacific Ocean showing the location of DSDP 580. The location of other cores mentioned in this chapter are also shown.

## 5.2. Oceanographic Setting

DSDP 580 is situated close to the present-day Subarctic Front (SAF) which is located at approximately 42°N (Heath et al., 1985). However, as demonstrated by planktic foraminiferal assemblages in Chapter 4, and in Thompson and Shackleton (1980) and Chiyonubu et al. (2012), the SAF was south of DSDP 580 throughout the Quaternary, with polar-subpolar conditions dominating at this latitude. The North Pacific Intermediate Water (NPIW) is ventilated by the dense outflowing Okhotsk Intermediate Water where it meets the Oyashio-Kuroshio convergence at the approximate latitude of DSDP 580 (Shcherbina et al., 2003; Ohkushi et al., 2016). This zone of intermediate water formation is therefore crucial to the overturning circulation in the Pacific.

## 5.3. Existing Chronology and Shipboard Description of DSDP 580

### *5.3.1. Existing Chronology*

The major lithologies of the upper 300cm of DSDP 580 are shown in Fig.5.2. Koizumi (1994) established an age model derived from diatom assemblage temperature values and magnetostratigraphic intensity age tie points, and St. John and Krissek (1999) used magnetostratigraphic intensity age tie points only; both determined that the upper 300cm spanned approximately the last ~50 kyr (Table 5.1). The accumulation rate at DSDP 580 is similar to the rate observed further north at ODP 883 (51.2°N, 167.8°E). There are a number of dating offsets between Koizumi (1994) and St. John and Krissek (1999) which increase deeper down the core (Table 5.1). The dating method described in this chapter attempts to resolve these offsets through the production of an updated age-depth model (Section 5.5.3).

| Depth (cm) | Age (ka BP) |
|---|---|
| 18 | 3.509 |
| 25 | 4 |
| 41 | 7.992 |
| 55 | 10.721 |
| 74 | 14.425 |
| 130 | 22 |
| 134 | 26.121 |
| 153 | 29.825 |
| 170 | 33.138 |
| 181 | 31 |
| 191 | 37.232 |
| 210 | 40.936 |
| 242 | 47.174 |
| 257 | 50.098 |
| 280 | 48 |
| 301 | 58.674 |
| 302 | 52 |

**Table 5.1:** Published age estimates (ka BP) for DSDP 580 derived from magnetostratigraphy and diatom temperature values. Dates in red are from Koizumi (1994) and dates in black are from St. John and Krissek (1999). See Section 5.3 for description of dating methodologies. Note: Koizumi, (1994) does not state which dates were obtained through magnetostratigraphy and which were obtained through diatom temperature values.

### *5.3.2. Sediment properties*

The major lithology of 0-300cm described in the shipboard description (Heath et al., 1985) consists of dark brown-black and dark grey siliceous clay, with local patches and thin layers of greenish-grey and very dark grey clay (Fig. 5.2). Diatoms and radiolaria are common. Carbonate content is very low and foraminifera are very rare to absent. Four ash layers are visible in this interval. The shipboard core description identifies two ash layers at 43-50cm and 57-66cm. However, the core photograph shows substantial mixing between these layers, and the description suggests that the sediments are deformed between 50 and 65cm (Heath et al., 1985). Ash layers between 0 and 150cm are brown-grey. Ash layers between 150 and 300cm are light grey. Section 5.6.1 presents the results of geochemical analysis of these ash layers. In addition to the discrete ash layers, dispersed volcanic glass shards and pumice are present throughout the core. Gamma Ray Attenuation Porosity Evaluator (GRAPE) density values (Fig. 5.2; Heath et al., 2004) range between 1.14 g/cm$^3$ and 1.74g/cm$^3$. The highest GRAPE values occur within the ash layers.

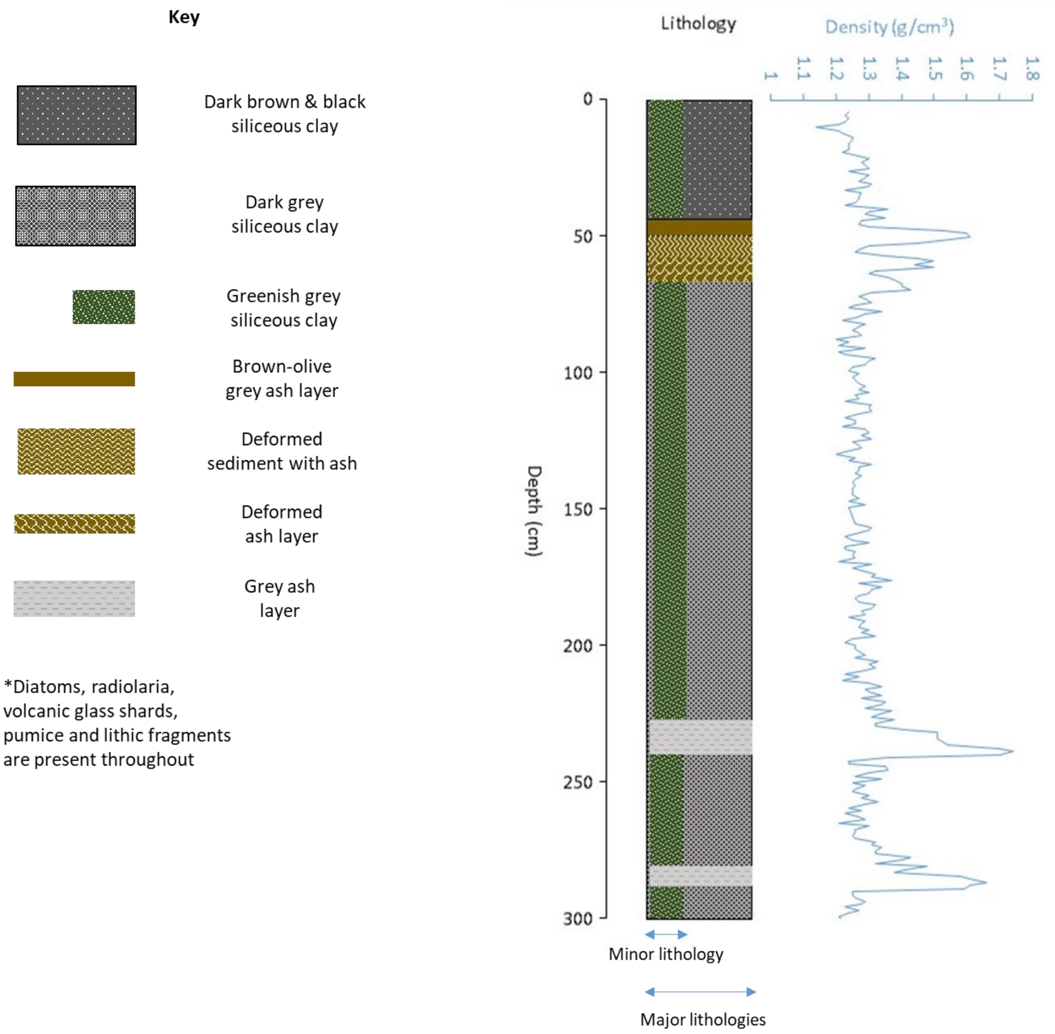

**Figure 5.2:** Lithology of 0-300cm in DSDP 580 shown alongside GRAPE density. Lithological data was obtained from Heath et al. (1985) and redrawn for this thesis. GRAPE data (Heath et al., 2004) was obtained from pangaea.de.

## 5.4: Site Justification

DSDP 580 was chosen as a suitable site for investigating Late Quaternary glacial and climatic change in the NW Pacific for the reasons described below.

### *5.4.1: Core location: possibility of multiple IRD sources*

DSDP 580 is situated in the region where ocean currents emanating from both the Bering Sea and the Sea of Okhotsk meet (Section 5.2; Fig. 5.1). The paths of these ocean currents were both iceberg routes during the Late Quaternary (e.g. Nürnberg and Teidemann, 2004; Bigg et al., 2008), and therefore it is possible that IRD from both the Sea of Okhotsk and eastern Kamchatka-Koryak regions may have reached DSDP 580. This site is therefore suitably placed to investigate temporal and spatial variations in IRD sources and can be compared to other NW Pacific sites where a single iceberg source region was likely to be dominant.

### *5.4.2: Existing IRD records*

IRD counts were carried out on DSDP 580 by St. John and Krissek (1999; Fig. 5.3), who quantified IRD fluctuations by calculating the accumulation rate (g/cm$^2$/ka). While this IRD record is of low temporal resolution of one sample every 3-8 kyr, it confirms the presence of IRD in this core, setting a foundation for higher resolution studies. The highest concentrations counted by St. John and Krissek (1999) in the upper 300cm occur around 14 ka BP, according to their tentative chronology. Due to the low resolution of St. John and Krissek’s study, it is possible that some key IRD peaks were not counted, particularly if short-lived peaks such as the 40 ka event in ODP 883 (Bigg et al., 2008), and those observed in ODP 1207A (Chapter 4) are present in DSDP 580.

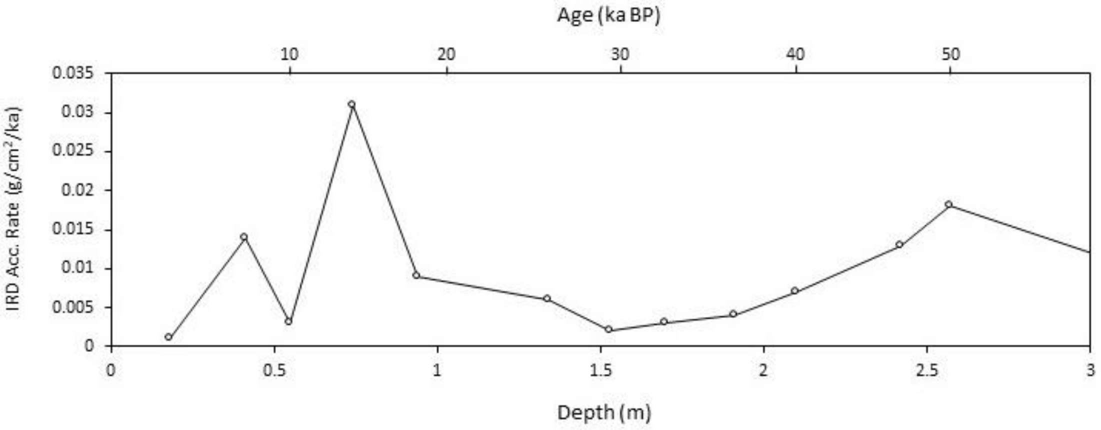

**Figure 5.3:** IRD accumulation rates (g/cm$^2$/ka) for the upper 3m of DSDP 580 (St. John and Krissek, 1999). Data was acquired from pangaea.de and redrawn for this thesis. The age scale used here follows that of St. John and Krissek (1999); detailed age tie points can be found in Table 5.1.

### *5.4.3: Potential tephrochronological age tie points*

The upper 300cm of DSDP 580 contains abundant volcanic glass as reported in the Shipboard Initial Report (Heath et al., 1985). Four discrete ash layers were documented (Section 5.3.2; Fig. 5.2). These layers have not been previously geochemically analysed, therefore their eruptive origins and ages were unknown prior to this study. Ascertaining their geochemical fingerprint would add confidence to the existing age model and would add data to the scarce Late Quaternary tephrostratigraphy of the open NW Pacific. This approach is particularly important at this site and other sites in the abyssal NW Pacific where carbonate content is very low (Section 5.3.2 of this chapter; Chapter 4, Section 4.4.7).

## 5.5: Methodology

Unless otherwise stated, the analyses described below were carried out by A.P. McCarron in the Department of Geography, University of Sheffield.

### *5.5.1: Sample preparation*

As described in Section 4.5.1 of Chapter 4, 1cm samples were provided by staff at the IODP. The 1cm samples weighed between 1.4 and 9.5g (Appendix 3). Sieving followed the same procedure as in Chapter 4, Section 4.5.1, producing three size fraction of >150µm, >63-150µm, and <63µm. As with ODP 1207A, some samples were divided into only two size fractions of >150µm and <150µm due to limited drying space and time constraints. Samples were dried at 40°C until there was no further change in weight. Final sample weights were then recorded in grams (g).

### *5.5.2: Ice-rafted debris*

Following the quantification method used to count IRD at ODP 1207A (Chapter 4), the >150µm fraction was closely inspected for IRD at a resolution of ~5cm using a reflected light binocular microscope. Samples were split into aliquots of approximately 300 grains. Grains with the character of lithic material were categorised as IRD. The absolute number of grains were then converted to grains/g of the entire bulk sample. The IRD counts for 0-300cm were added to a previous unpublished MSc study of 150-300cm by Hayes (2014) who used the same quantification method described in this thesis.

### *5.5.3: Volcanic glass counts and tephrochronology*

Counts of volcanic glass were carried out in the >150µm fraction alongside IRD counts to quantify background ash concentrations and ash in the discrete tephra layers described in Section 5.3.2. Counts from the split samples were converted to shards/g of the total sample. Shards from the four discrete tephra layers were selected for geochemical fingerprinting by electron microprobe analysis and laser ablation inductively coupled mass-spectrometry (LA-ICP-MS) of single glass shards and were analysed in 2015 and 2019 by V. Ponomareva and M. Portnyagin at GEOMAR Helmholtz Centre for Ocean Research, Kiel, using a JEOL JXA 8200 electron microprobe. Samples from the two ash layers located at 227-238cm and 281-288cm were picked for microprobe analysis by M. Rogerson at the University of Hull in 2015 while samples from the two ash layers at 43-50cm and

57-66cm were picked by A. McCarron at the University of Sheffield. Sampling depths are shown in Table 5.2. Analytical conditions and methodology were the same as described in Chapter 4, Section 4.5.3. The data on glass from DSDP 580 for EMP and LA-ICP-MS analyses are provided in Appendix 4. The obtained glass composition was compared to those from known marker tephras (Matsu'ura et al., 2018; Albert et al., 2019).

| Ash layer depth | Sampling depth |
|---|---|
| 43-50cm | 49-50cm |
| 57-66cm | 64-65cm |
| 227-238cm | 234-235cm |
| 281-288cm | 290-291cm |

**Table 5.2:** Ash layer depth intervals and sampling depths for electron microprobe analysis.

### *5.5.4: Siliceous microfossil abundance*

Diatoms and radiolaria in the >150µm size fraction were counted alongside IRD and volcanic ash. Counts from the split samples were converted to specimens/g of the total sample.

### *5.5.5: Age model construction*

The updated age model for DSDP 580 was derived from the existing dates of Koizumi (1994) and St. John and Krissek (1999) and the tephrochronological framework established in this study. The siliceous microfossil assemblage was also used to identify key oceanographic changes which may be related to climatic changes associated with MIS boundaries.

## 5.6: Results

This section begins with presenting the updated age model derived from the addition of the tephrochronology to the dates established by Koizumi (1994) and St. John and Krissek (1999). This is followed by the results of the IRD and microfossil counts. These results are then discussed in Section 5.7 where DSDP 580 is compared to ODP 1207A and other NW Pacific IRD records. The discussion is concluded by examining the implications for variations in the timing and sources of NW Pacific IRD flux.

### *5.6.1: Volcanic ash content and tephrochronological control*

Volcanic ash was common to abundant throughout the upper 300cm of DSDP 580 (Fig 5.4). A continuous background population of volcanic glass shards and pumice was identified throughout the core between 0 and 300cm at concentrations of between ~9 and ~700 shards/g in the >150µm size fraction. Concentrations within tephra layers were between ~90 and ~5000 shards/g in the >150µm fraction. The concentrations in the <150µm fraction are likely to be higher than in the >150µm fraction (Wiesner et al., 2004). However, due to time constraints size fractions finer than 150µm were not counted in this study. As discussed later in this section, there appears to have been significant vertical mixing of tephra layers, resulting in mixed geochemical populations within ash layers.

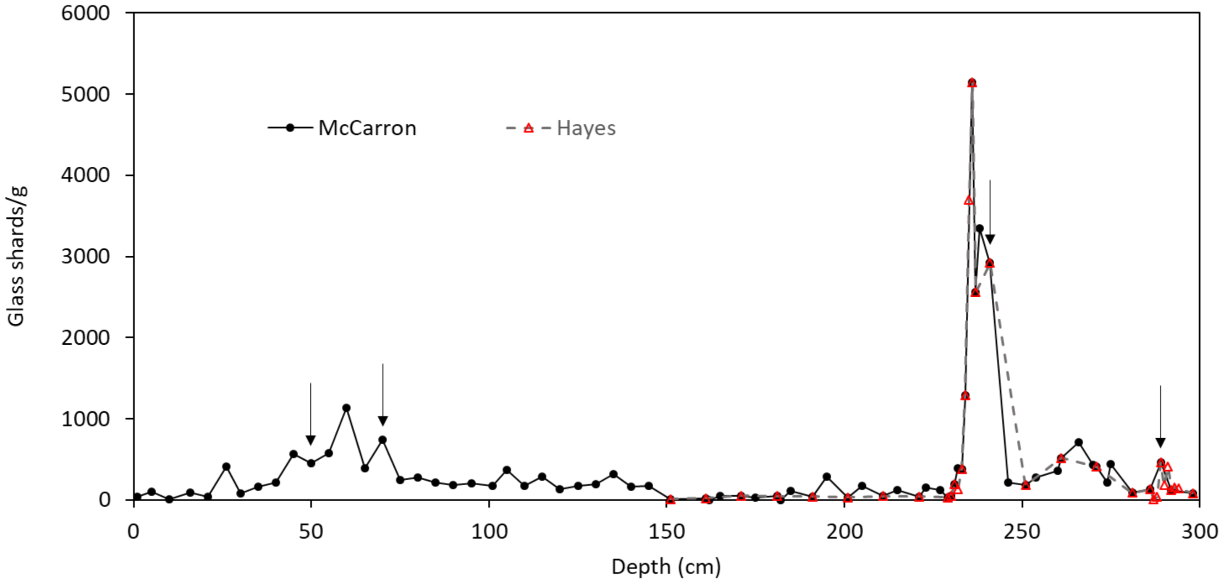

**Figure 5.4:** Volcanic glass shards/g (>150µm) of total sample in DSDP 580. Solid line with filled circles show samples counted for this thesis, while dashed line with red triangles show samples counted in Hayes

(2014). Counts carried out by Hayes were checked for this thesis and found to be accurate. Arrows mark the bases of ash layers.

The glass composition obtained from electron microprobe analysis of single shards from the four identified ash layers show close geochemical similarities to Late Quaternary Japanese tephras. The glass shards from the two ash layers at 49-50cm and at 64-65cm (Table 5.2) both contained a geochemical population found by V. Ponomareva and M. Portnyagin to be similar to the major elemental composition of the Towada Hachinohe (TO-H) tephra from the Towada volcano in northern Honshu, Japan (40.47°N, 140.92°E ;Matsu'ura et al., 2018). This tephra was dated to 15.7± 0.2 b2k (before Year 2000) in the Greenland ice core (Bourne et al., 2016). This date is in good agreement with the existing chronology of Koizumi, (1994) but is ~5 ka older than the age predicted by St. John and Krissek, (1999) (Table 5.1). Figure 5.5 plots $SiO_2$ against CaO and $K_2O$ for shards from DSDP 580: 49-50 and 64-65cm alongside shards from the proximal TO-H tephras (Albert et al., 2018; Matsu'ura et al., 2018). DSDP 49-50cm also contains a second high-$SiO_2$, high-$K_2O$ population, which may be derived from a different eruptive source, possibly an undated Kurile tephra (Ponomareva, *pers. comm.*, 2019). However, further analysis is required to establish the date and eruptive source of this glass.

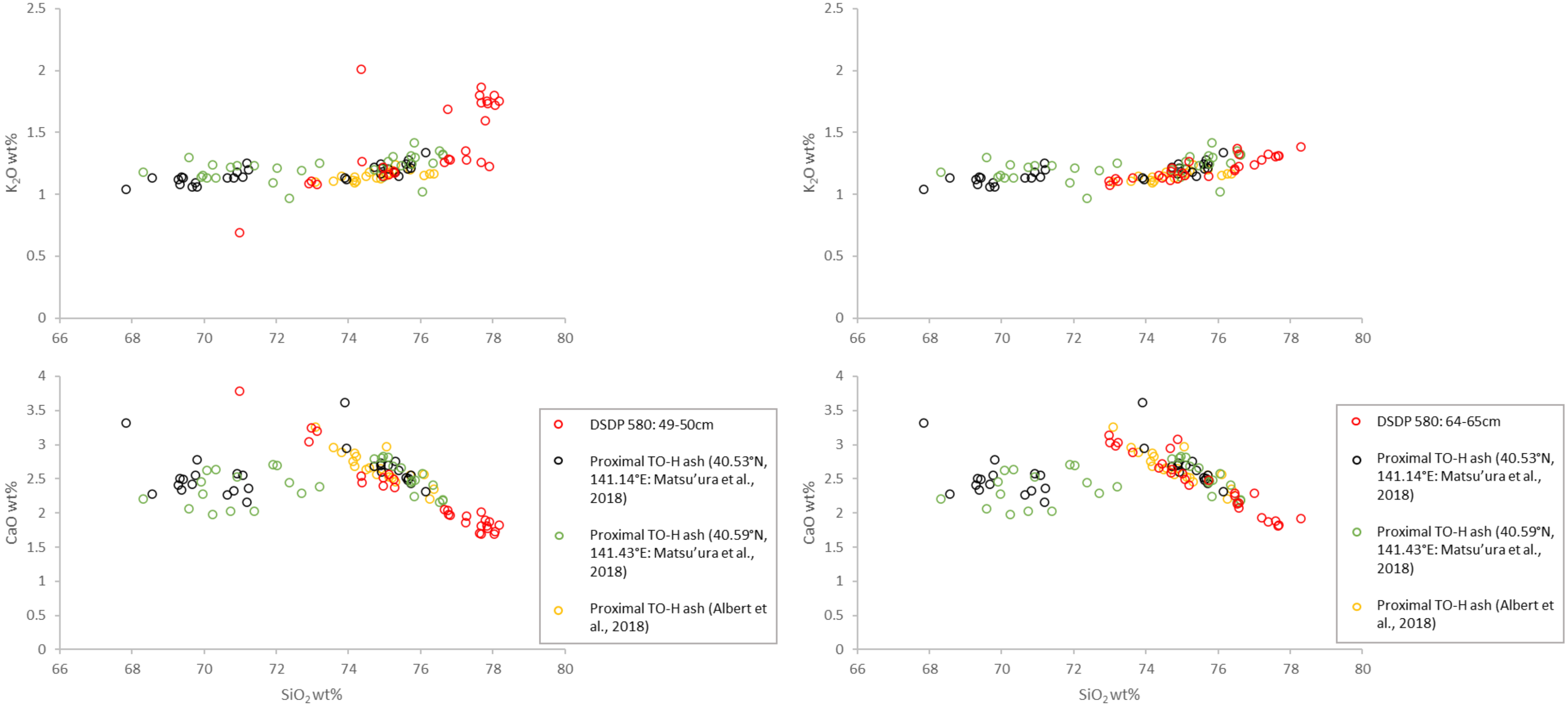

**Figure 5.5:** Bi-plots of $SiO_2$ against CaO and $K_2O$ in glass shards from two ash layers at 49-50cm (left) and 64-65cm (right) in DSDP 580. Shards are plotted alongside proximal TO-H ash samples from Albert et al., (2019) and Matsu'ura et al., (2018). DSDP 580 data are from unpublished measurements by V. Ponomareva and M. Portnyagin in 2019. Diagrams were drawn for this thesis by A. McCarron.

The two ash layers deeper in the core at 227-238cm and 281-288cm also contain glass shards which are geochemically identical (Fig. 5.6). The composition of these shards closely resemble the Kutcharo Shoro (Kc-Sr) eruption from the Kutcharo volcano on Hokkaido, northern Japan.

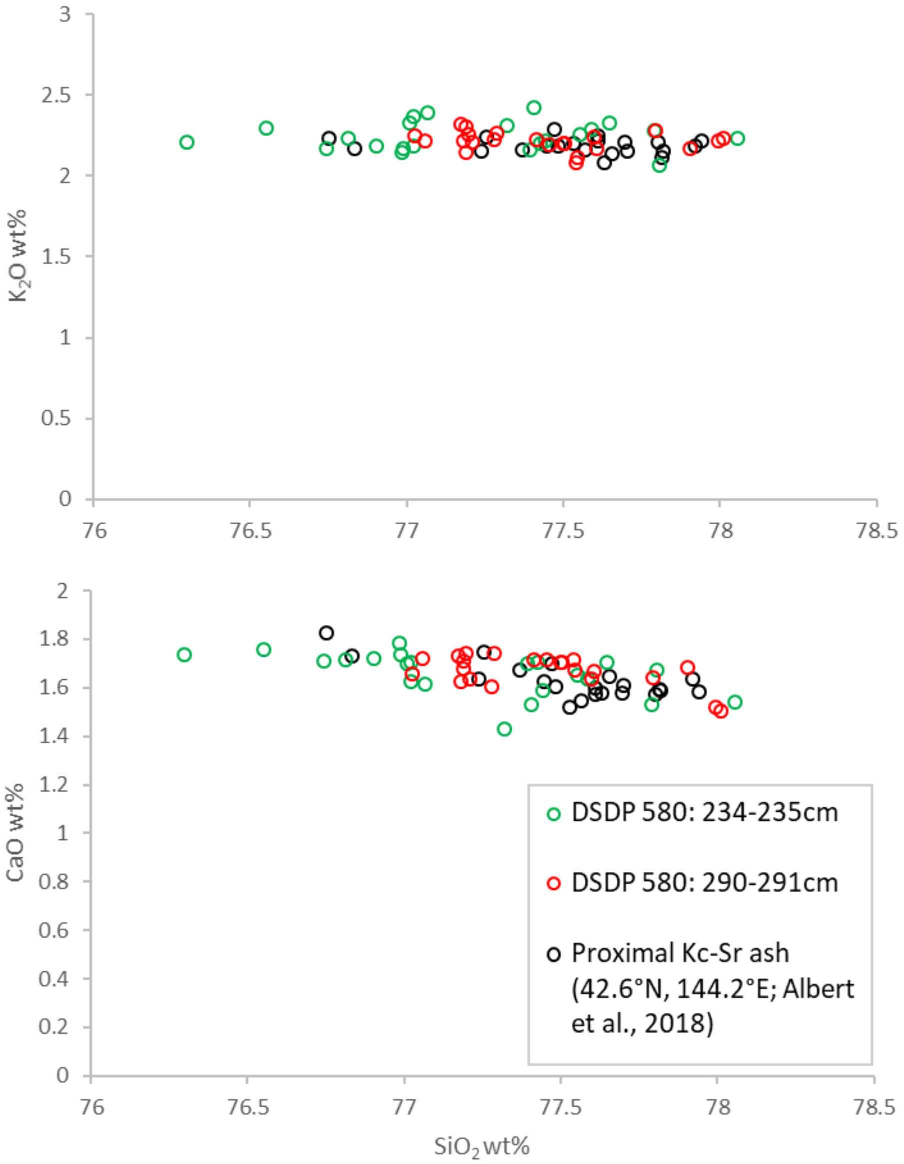

**Figure 5.6:** Bi-plots of SiO2 against CaO and K2O in glass shards from two ash layers at 234-235cm and 290-291cm in DSDP 580. Shards are plotted alongside proximal Kc-Sr ash from Albert et al. (2018). DSDP 580 data are from unpublished measurements by V. Ponomareva and M. Portnyagin in 2015. Glass shards were picked by M. Rogerson in 2015. Diagrams were drawn for this thesis by A. McCarron.

The Kc-Sr eruption was dated to 39,265-45,070 ka BP (Machida and Arai, 2003). The existing chronostratigraphic framework combining dates from Koizumi, (1994) and St. John and Krissek, (1999; Table 5.1) suggests that the depth of the upper ash layer at 227-238cm is closer to the age of this eruption than the lower ash layer at 281-288cm, while the lower ash layer is likely to be between 48 and 58 ka BP. However, the near-identical geochemistry of the two discrete layers at 227-238cm and 281-288cm leaves some uncertainty as to the identity and age of these tephras. These chronostratigraphic problems are discussed further in Section 5.7, where an updated age model is presented.

### *5.6.2: IRD concentrations*

Fig. 5.7 shows the total IRD counts (grains/g) at 0-300cm in DSDP 580. The maximum concentration between 0 and 300cm was 546 grains/g at 261cm, while the lowest concentration was 3 grains/g at 234cm. The rock fragment IRD component was largely composed of dark, possibly basaltic fragments, while the crystal component was composed of detrital quartz, feldspar and mica. Other minerals were likely to be present, however specific identification was not possible. The rock fragment component was larger than the crystal component in most samples (Fig. 5.7).

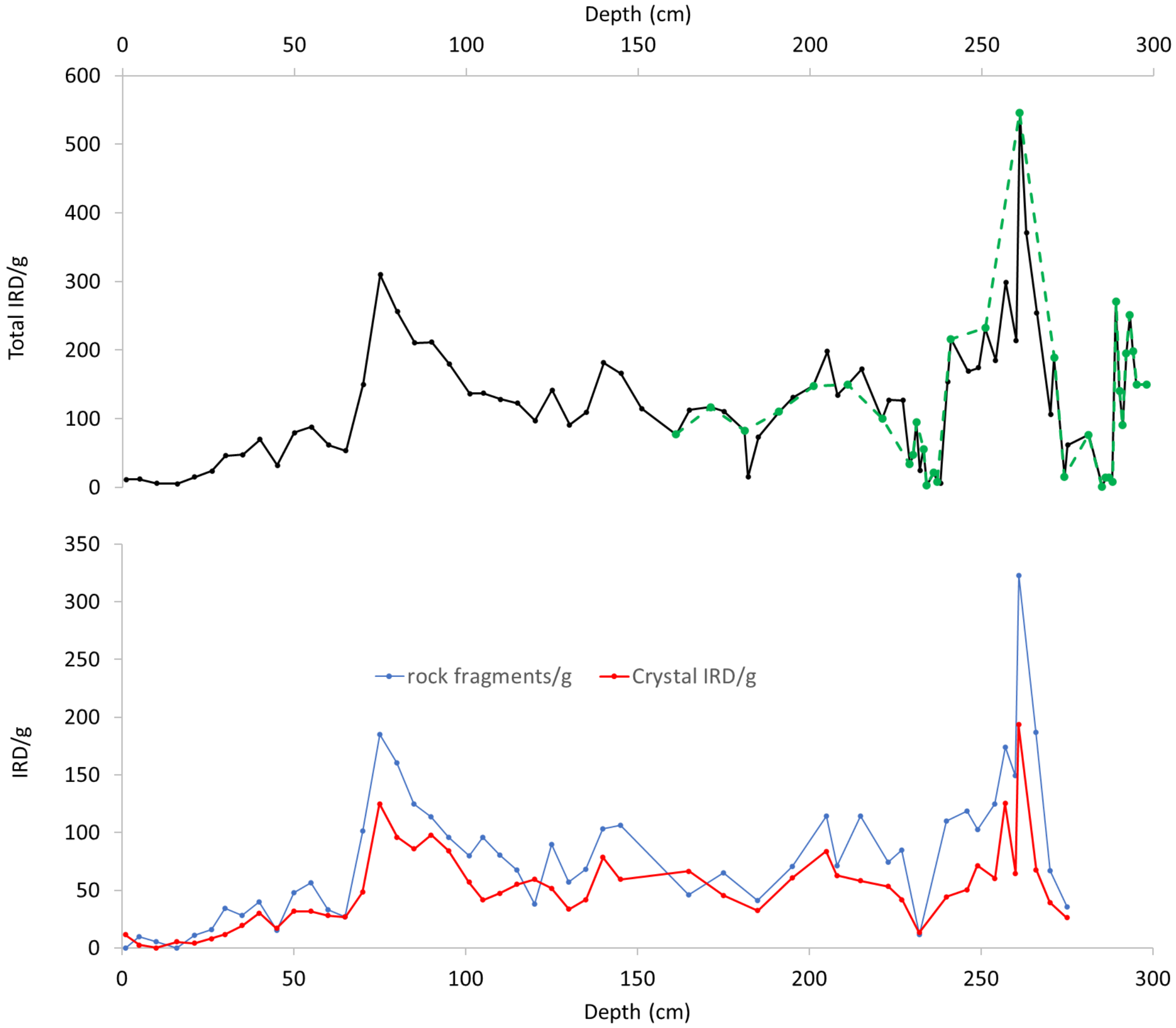

**Figure 5.7:** IRD counts (grains/g) in DSDP 580 against depth (cm). The top diagram shows total IRD/g. The black line and markers show counts carried out by A.P. McCarron. The green dashed line and green markers show counts carried out by N. Hayes which were checked for accuracy by A.P. McCarron for this study. The bottom diagram shows rock fragments/g and crystal IRD grains/g.

### *5.6.3: Diatoms and Radiolaria*

Fig. 5.8 shows counts of radiolaria and diatoms/g of total bulk sediment, plotted against IRD and age. Radiolaria abundances range from a maximum of 449.8 specimens/g at 16cm, to a minimum of 11 specimens/g at 246cm. Diatom abundances range from a maximum of 278.4 specimens/g at

5cm, to a minimum of 0 specimens/g at 65 and 70cm. It was not possible to identify individual species of radiolaria and diatoms. There were at least two species of diatom and radiolaria present in the core.

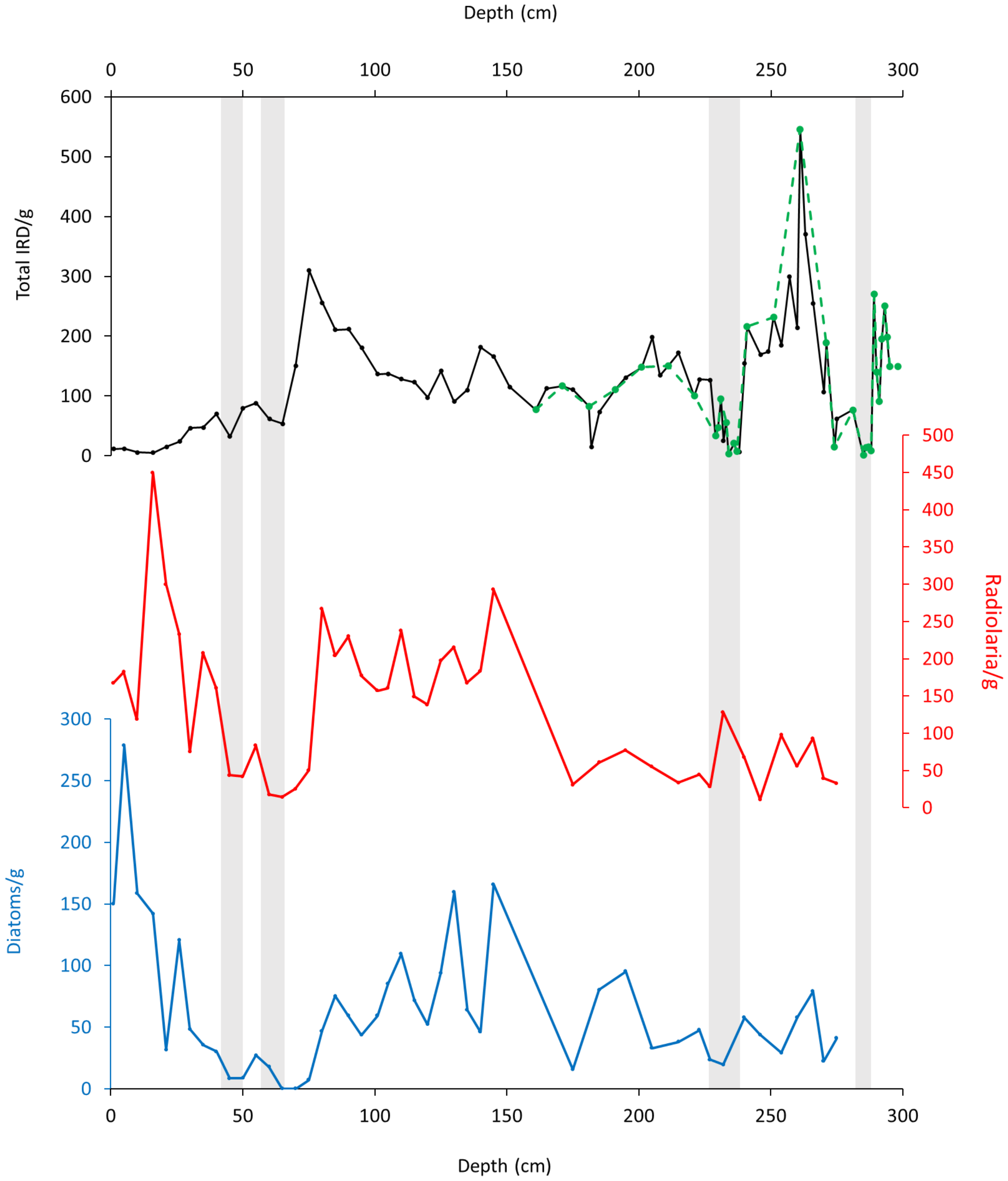

**Figure 5.8:** Diatoms/g and radiolaria/g plotted alongside IRD, age and depth. Grey bars mark volcanic ash layers.

## 5.7: Discussion

### *5.7.1: Tephrochronology and ash geochemistry*

As mentioned in Section 5.3.2, up to two ash layers are present between 43 and 66cm. Samples from within both ash layers contain an identical geochemical population matched to the TO-H eruption dated to 15.7 ± 0.2 b2k (Section 5.6.1; Fig. 5.5). A second, undated population is present in the upper layer at 49-50cm. The visible deformation and vertical mixing of sediments between ~45 and 70cm can explain the presence of the TO-H tephra in both ash layers (Fig. 5.9).

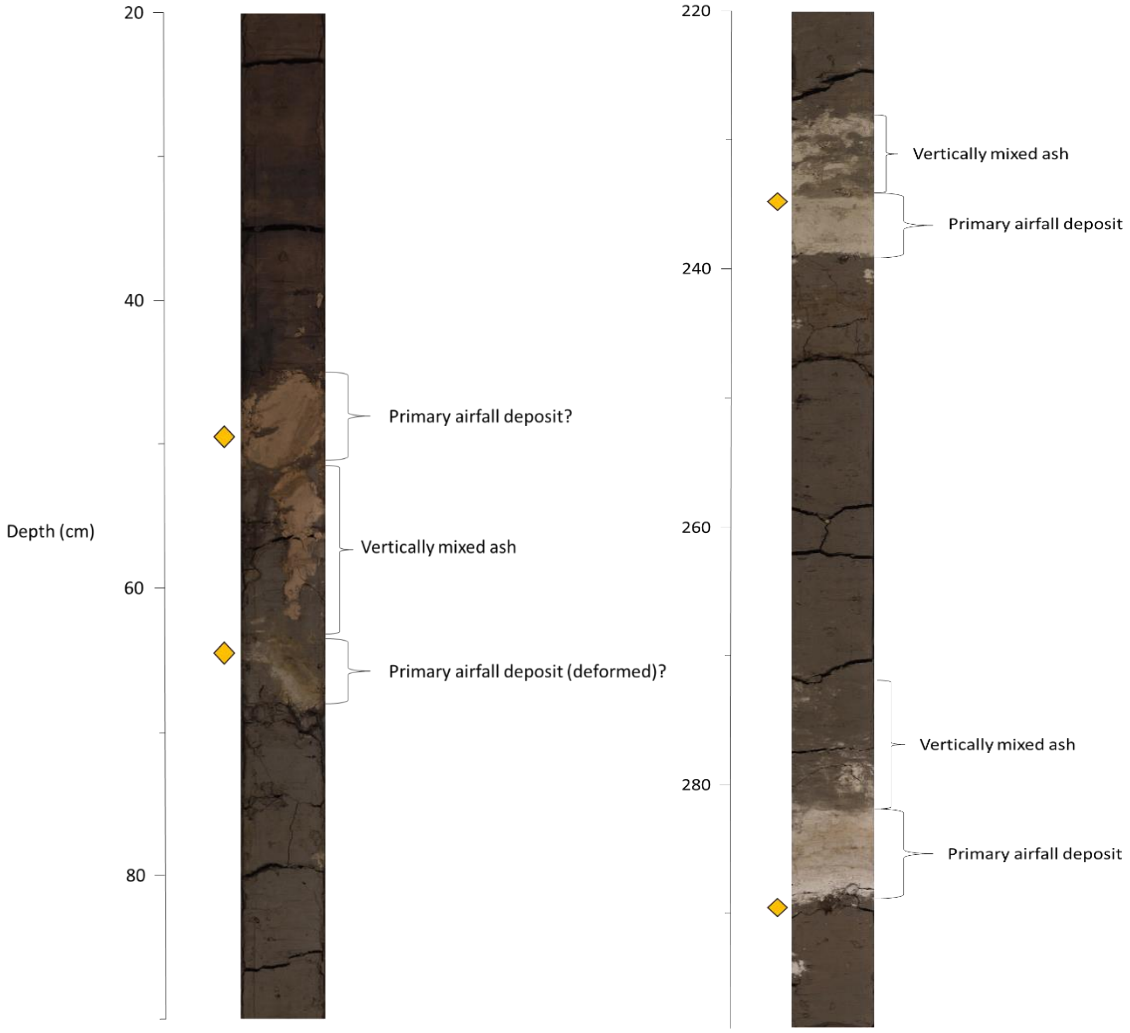

**Figure 5.9:** Core photographs of 20-90cm and 220-290cm of DSDP 580. Ashy deposits are clearly visible. The probable primary airfall deposits and vertically mixed ashy sediments are annotated. Yellow markers denote the depths sampled for geochemistry. Sediment gaps and cracks are a result of the natural drying process. The core photographs were taken at the IODP, Texas in 2017.

The two ash layers at 227-238cm and 281-288cm both contain a geochemical population matched to the Kc-Sr eruption (39,265-45,070 BP), despite these layers being separated by ~40cm. Both layers are characterised by a sharp basal boundary (Fig. 5.9), and single shard peak (Fig. 5.4) which are strong indicators of a primary airfall deposit (Griggs et al., 2014). These characteristics suggest that it is unlikely that the two layers were separated vertically by bottom current redistribution or bioturbation. However, closely separated eruptions from the same eruptive centre could produce tephras with very similar geochemistry (Brendryden et al., 2010; Griggs et al., 2014). The upper ash layer (227-238cm) fits within the age range of the Kc-Sr eruption, while the lower layer is >7 kyr older than the oldest age estimate of the Kc-Sr tephra according to the combined dates of Koizumi, (1994) and St. John and Krissek, (1999; Table 5.1). However, apart from Kc-Sr, there are no other published tephras from the Kutcharo caldera dated to within ~30 kyr of the 281-288cm layer. The Kc-Hb tephra (~120,000 BP; Hasegawa et al., 2009) and the Kc-2/3 tephra (~85,000 BP; Smith et al., 2013) are similarly medium to high $SiO_2$ and medium-K (Fig. 5.11A). Although these tephras are similar in composition to the DSDP 580 tephras, the Kc-Sr tephra is notably compositionally closer.

The only other prominent tephra of similar age and composition to Kc-Sr is the Shikotsu-1 (Spfa-1) originating from southern Hokkaido, dated to 45,105-46,560 BP (Uesawa et al., 2016). This tephra is slightly higher in $K_2O$ than the 580 ashes and the Kc-Sr proximal tephra (Fig. 5.10A). The geochemical variation between the tephras discussed above is made clearer when viewing the mean wt% of $SiO_2$ plotted against CaO and $K_2O$ (Fig. 5.10B). 580:234-235, 580:290-291 and Kc-Sr have very similar mean values and significant overlap in standard deviations. The mean of 580:290-291 is slightly closer to the mean of Kc-Sr than 580:234-235, therefore although the 227-238cm tephra fits with the existing combined chronology, the 281-288cm tephra is slightly closer geochemically to Kc-Sr. Therefore, 580: 281-288cm may be the Kc-Sr tephra while 580: 227-238cm may have originated from a later unidentified eruption from the Kutcharo caldera with very similar geochemistry to Kc-Sr, albeit slightly lower mean $SiO_2$ levels. This hypothesis is supported when correlating IRD peaks in DSDP 580 with other peaks in the NW Pacific (discussion presented in Section 5.7.3).

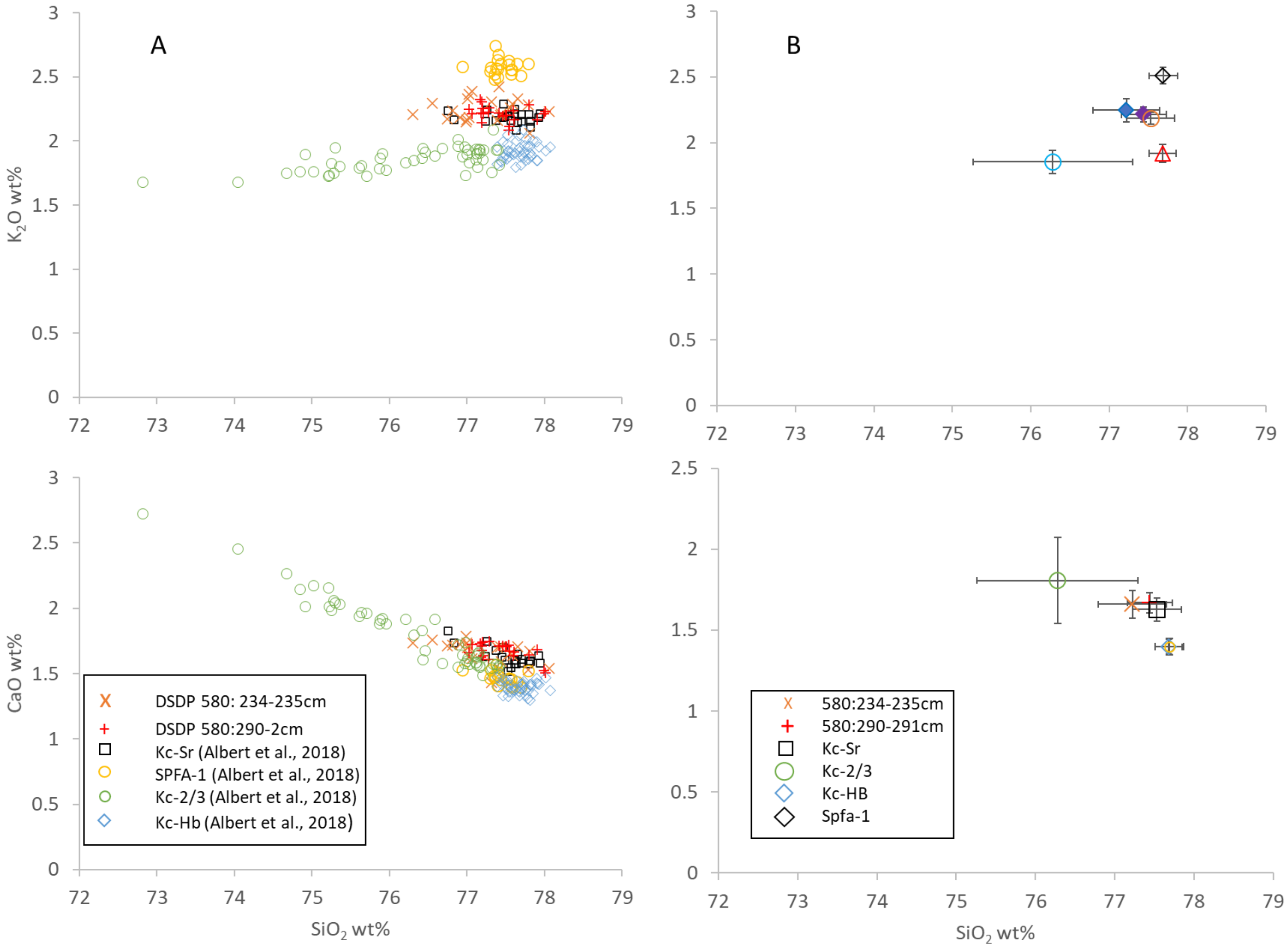

**Figure 5.10: A:** Bi-plots of $SiO_2$ wt% against CaO and $K_2O$ wt% in glass shards from DSDP 580 ash layer samples 234-235cm and 290-291cm plotted alongside selected Japanese Late Quaternary proximal tephras of a similar age to the Kc-Sr tephra, or tephras from the Kutcharo caldera. **B:** Mean wt% $SiO_2$/CaO and $K_2O$ of all sampled shards from DSDP 580 ashes and proximal Japanese tephras. Error bars denote standard deviations.

### *5.7.2: An updated age model for DSDP 580*

Following the identification of the TO-H (~15.7 ka BP) and the Kc-Sr (~39-45 ka BP), four different age-depth models were produced (Fig. 5.11) with the following conditions:

A)

- all age tie points of Koizumi, (1994) and St. John and Krissek, (1999).
- the TO-H tephra age tie point at 64-65cm.
- the Kc-Sr tephra age tie point at 234-235cm.

B)

- all age tie points of Koizumi, (1994) and St. John and Krissek, (1999).
- the TO-H tephra age tie point at 64-65cm.
- the Kc-Sr tephra age tie point at 288cm (see Section 5.7.1 for justification).

C)

- All age tie points of Koizumi, (1994) and St. John and Krissek, (1999) shallower than 210cm (as all published dates deeper than this depth and shallower than 288cm contradict the Kc-Sr age tie point at 288cm; Fig. 5.11C).
- The TO-H tephra age tie point at 65cm.
- The Kc-Sr tephra age tie point at 288cm.

D)

- Age tie points of Koizumi, (1994) shallower than 182cm (see C above for justification).
- The TO-H tephra age tie point at 65cm.
- The Kc-Sr tephra age tie point at 288cm.

A line of best fit was produced for each age-depth model, and the resulting regression equation was used to calculate an age model which assumed a linear sedimentation rate. The age models were then compared to the published dates and the new absolute dates derived from tephrochronology in this chapter. Age model D, which removes the age model of St. John and Krissek and places Kc-Sr at 281-288cm was deemed the most reliable age model, as the regression line age model is closely aligned to the Kc-Sr tephra. The reliability of this age model is further strengthened when considering the regional timing of IRD peaks in the NW Pacific, as discussed below in Section 5.7.3.

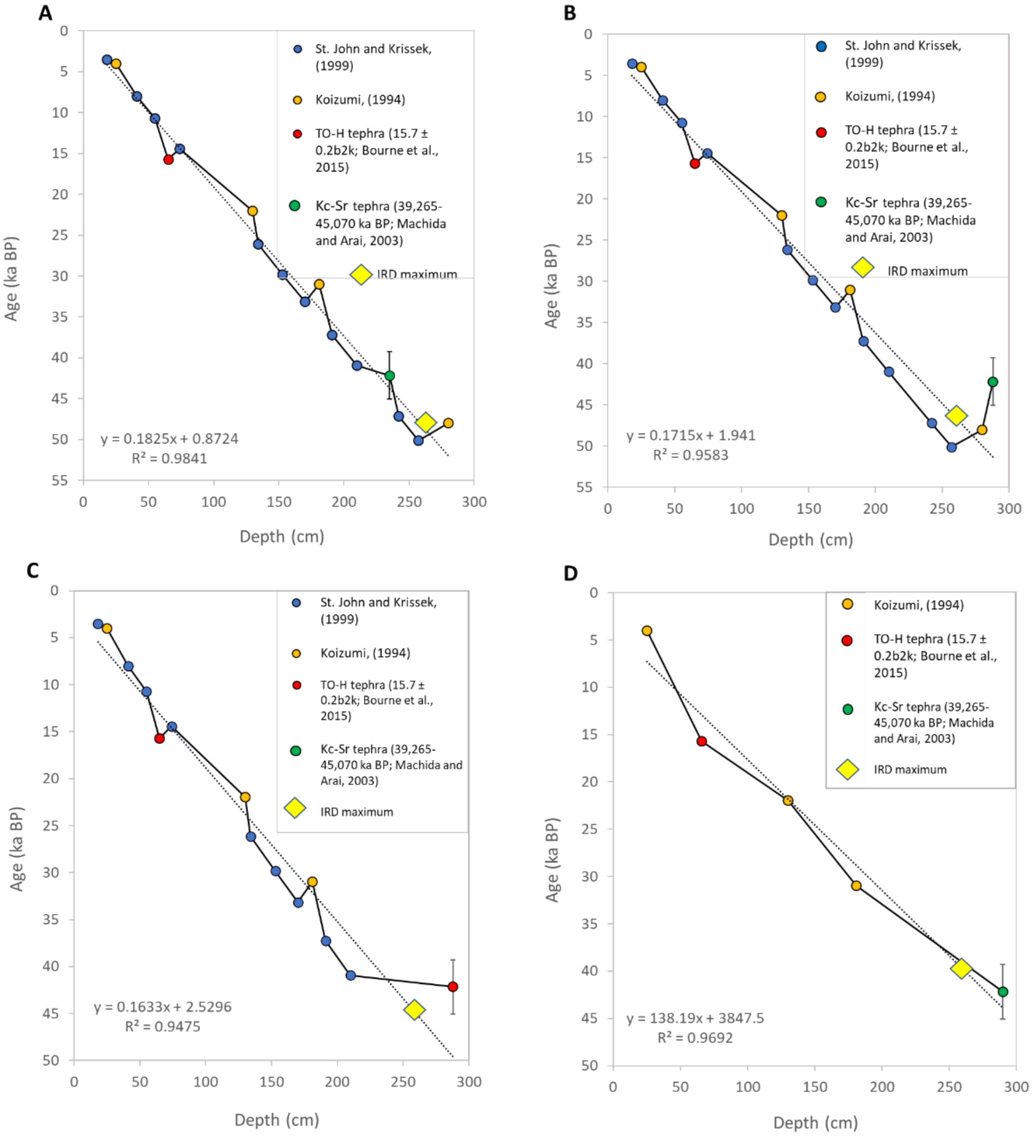

**Figure 5.11:** Possible age models for DSDP 580 derived from various combinations of age tie points (see this section for details of Age Models A-D). The marker with the error bar denotes the median value from the 39,265-45,070 ka age range for the Kc-Sr tephra (Machida and Arai, 2003). The error bars denote the minimum and maximum age estimates. The age error of 0.2 b2k on the ~ 50 cm TO-H tephra is too small to be shown on this diagram. Line of best fit and corresponding equation denote the updated age-depth model (see Appendix 5).

### *5.7.3: Ice-rafted debris at DSDP 580, regional comparisons and implications for chronosratigraphy*

IRD deposition at DSDP 580 was near-continuous during much of the Late Quaternary, with a significant decline ~14 ka BP around the MIS 2-1 boundary when glacial ice no longer reached the coast of NE Asia. The short-lived spike in IRD concentrations of 546 grains/g, at 261cm, occurred around 40 ka BP ka BP according to the newly developed age model in this chapter. This IRD spike shares similar characteristics with the spike in ODP 883, dated to ~39 ka BP in Bigg et al., (2008). The 39-41 ka BP peak in ODP 883 marks the maximum ice-rafting period during the Late Quaternary at this site, and may be related to substantial collapse of glacial ice from the Kamchatka-Koryak region (Bigg et al., 2008).

The largest DSDP 580 and ODP 883 spikes beginning around 40 ka BP display a similar duration with a gradual increase lasting ~3-2 kyr followed by a short-lived peak of <1 kyr and a rapid decrease to near-background levels (Fig. 5.12). As discussed in Section 5.7.1, the tephrochronological framework is unresolved due to the identical chemistry of the two ash layers at 227-238cm and 281-288cm, which matches the Kc-Sr eruption of 39,265-45,070 BP (Section 5.6.1). The age model presented in this chapter places the Kc-Sr tephra at 281-288cm as this depth produces a better fit with other NW Pacific IRD peaks, assuming a linear sedimentation rate. If the Kc-Sr tephra date is placed at the 281-288cm ash layer, the IRD maximum in DSDP 580 is dated to ~39.9 ka BP, within 1 kyr of the ODP 883 peak as dated by Bigg et al., (2008). This scenario would explain the similar shape and durations of the main MIS 3 IRD peaks in ODP 883 and DSDP 580. Moreover, the likely presence of the 39-41 ka BP IRD peak in DSDP 580 in addition to ODP 883, ODP 882 and ODP 1207 (Figure 5.11; Chapter 4) adds further evidence to the hypothesis that during mid-MIS 3 an abrupt collapse of glacial ice occurred on the Kamchatka-Koryak coast which released icebergs over a wide region of the NW Pacific, leaving a widespread IRD signal across the basin. Further inter-core comparisons and correlations are described in Chapter 6.

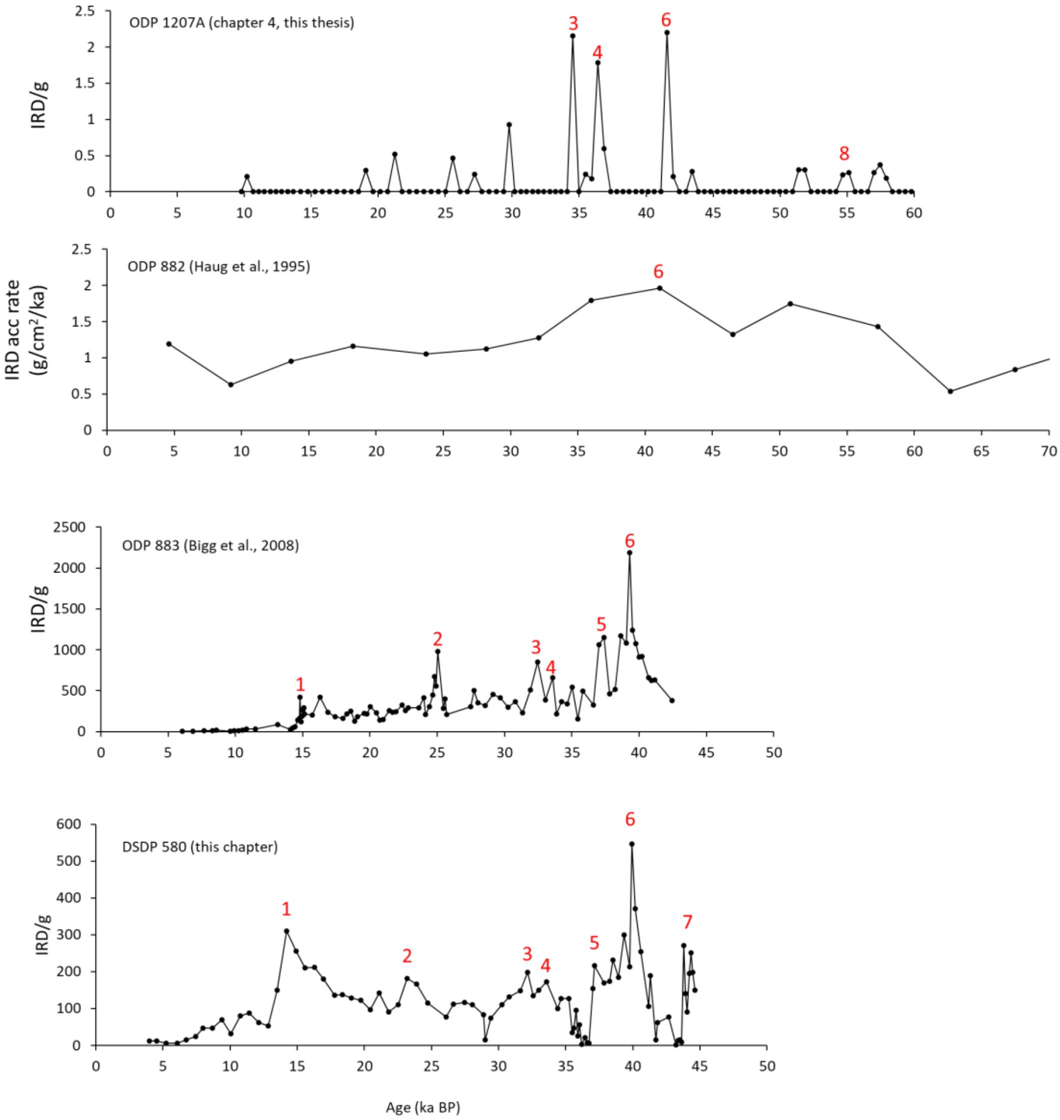

**Figure 5.12:** Late Quaternary IRD/g at NW Pacific sites 580, 883, 882 and 1207. Red numbers show possible correlations between IRD peaks at more than one site/dataset likely to have been derived from the same period of ice-rafting. Each dataset is plotted against the age model used in each individual study, which may explain the offset between some corresponding peaks. The age model used for DSDP 580 is derived from the line of best fit from dates in Koizumi, (1994) and the tephra ages (with Kc-Sr placed at 281-288cm) given in this chapter (see Figure 5.11 for age-depth model D). Note IRD at ODP 883, 1207 and DSDP 580 is calculated using grains >150µm/g, whereas IRD at ODP 882 is calculated using an accumulation rate in g/cm$^2$/ka.

### *5.7.4: Holocene IRD*

As mentioned in 5.7.3, IRD is near-continuous in DSDP 580 in the upper 300cm (~5-55 ka BP). IRD concentrations significantly reduce to ~1 grain/g in tephra layers, where rapid deposition of ash diluted the IRD record. A further significant decrease occurred ~14 ka BP following a deglacial IRD spike when glacier termini rapidly broke up and retreated from the coast (Peak 1 in Figure 5.11), as observed in IRD records of the N Atlantic (e.g. Ng et al., 2018). Background levels persisted at levels of between ~90 and 5 grains/g during the Holocene. ODP 883 also contains a background Holocene population of IRD. Geomorphological evidence does not support the existence of marine terminating glaciers in NE Siberia later than deglaciation ~14-15 ka BP (Gualtieri et al., 2000; Stauch and Gualtieri, 2008; Barr and Clark, 2012a and b). Therefore it is unlikely that the IRD signal at these two sites is a genuine indicator of Holocene ice-rafting. It is possible that bioturbation or drilling disturbances caused contamination of the Holocene sediments with deeper, glacial sediments. The position of the Holocene sediments near the top of the core increases the likelihood of disturbances during the core-drilling process. Furthermore, as discussed in 5.7.1, the ash layers in the upper 70cm of DSDP 580 were deformed, possibly due to drilling disturbance. This deformation may have been responsible for the upward mixing of older glacial sediments into the Holocene deposits. It is unlikely that sea ice was responsible for transporting Holocene IRD to DSDP 580. Sea ice formation was largely limited to the Okhotsk and Bering seas or the eastern Kamchatka-Koryak coasts throughout the Holocene (Harada et al., 2014), and several models also suggest that sea ice was largely limited to the coasts during the LGM (Gong et al., 2019).

### *5.7.5: Radiolaria and diatom abundance changes*

The radiolaria and diatom abundance fluctuations follow somewhat similar patterns throughout the upper 300cm of DSDP 580 (Fig. 5.8). Both diatoms and radiolarians increase in abundance during MIS 2. There is a clear decline in abundance in both during the deglaciation. However, this is unlikely to be a true climatological signal, and appears to be a dilution effect caused by the TO tephras at this depth (see Section 5.6.1 for a discussion of these tephras). During the Holocene, both diatoms and radiolarians increase in abundance. Individual species of diatoms and radiolarians exhibit strong sea surface temperature preferences (e,g. Barron, 1992). Productivity changes in response to glacial-interglacial (Lüer et al., 2009) and stadial-interstadial cycles (Nave et al., 2007) . However, as mentioned in Section 5.6.3, it was not possible to identify individual species, therefore it was not possible to conclude whether the observed assemblages were cold- or warm- preferring species. The MIS 2 peaks suggest an increase in cold water species, while the clear Holocene spikes suggest increases in warm water species. However, in the absence of species identification, I hypothesise that the abundance changes in diatoms and radiolarians reflect climate-driven productivity changes, but more research on species identification is needed to confirm this.

## 5.8: Summary

The data presented in this chapter provides an updated Late Quaternary chronology with new information about the sources and ages of tephra layers in DSDP 580. This chapter addresses the occurrence of discrete tephra layers with closely resembling geochemistry. An IRD record is also presented at a higher resolution than in previous studies. Some ice-rafting peaks in other NW Pacific cores, notably ODP 883 and ODP 1207A (see Chapter 4) correspond temporally with some of the largest peaks in DSDP 580 (Figure 5.11), notably the ~39-41 ka BP peak, and the deglacial peak. The apparently near-simultaneous occurrence of IRD peaks at widely separated sites strengthens the argument proposed in Chapter 4 that iceberg releases from the Kamchatka-Koryak coast were often large enough to produce a basin-wide IRD signal, similar in scale to that observed in Heinrich layers.

The following chapter presents a basin-wide analysis of the glacial sediments of the NW Pacific, and integrates the findings of the previous two chapters into a wider analysis which explores the regional and sub-regional climatic, oceanographic and glacial connections between multiple North Pacific sites using existing data and newly acquired X-ray fluorescence data.

# Chapter 6: Late Quaternary climate and sediment provenance in North Pacific cores from X-ray fluorescence core-scanner data

## 6.1: The Northwest Pacific stratigraphy problem

Understanding Late Quaternary fluctuations in NW Pacific climate and glaciation requires a reliable regional stratigraphy. As mentioned in Chapter 2, this is lacking in the NW Pacific due to low resolution or absent sampling and very sparse chronostratigraphic records. This problem has greatly limited the potential for cross-correlation of marine cores. Furthermore, many different sources, both terrestrial and marine have contributed to Late Quaternary sedimentation in the NW Pacific. The identification of the key sediment sources, and how they changed throughout the Late Quaternary can assist in the interpretation of climatic conditions in the region, and how these sources have varied between sites. X-ray fluorescence (XRF) is a popular method of extracting palaeoenvironmental interpretations from major and trace elemental intensities in marine sediments (e.g. Haug et al., 2001; Jaccard et al., 2005). The popularity of XRF is due to its rapid, non-destructive ability to obtain large datasets of downcore changes in approximate element abundances. While the NW Pacific sediments are unsuitable for some approaches to regional chronostratigraphy and palaeoenvironmental analysis due to the lack of dateable carbonate (see Chapters 3, 4 and 5 for discussion of this issue), XRF offers a different method for obtaining high-resolution data which can be used to identify common stratigraphic signals on a basin-wide scale. This chapter presents, and discusses the implications of, X-Ray fluorescence (XRF) data from multiple sites across the North Pacific.

## 6.2: X-ray fluorescence analysis

XRF is a rapid, non-destructive analytical technique for measuring the approximate chemical composition of an analysed material (Weltje and Tjallingii., 2008). XRF works through the ejection of an electron from the inner shell of an atom through the influence of X-ray radiation. The vacancy created by the ejection of the electron is then filled by an electron from the outer shell. The difference in energy between the two shells is emitted as electromagnetic radiation. Each element produces a characteristic wavelength of emitted radiation, and the peak amplitudes in the XRF spectrum are proportional to the concentration of the elements in the sample (Richter et al., 2006).

### *6.2.1: XRF core scanning*

XRF core scanners are specifically designed for rapid, non-destructive scanning of split sediment cores. The Avaatech core scanner can be programmed to scan cores at high spatial resolution down to 1mm, and spans the atomic mass range between Al and U (Avaatech XRF Core Scanner user manual version 2.0, 2007). A detailed technical description of the Avaatech core scanner is given in Richter et al., (2006) and a schematic diagram of the core scanner operation is shown in Fig. 6.1.

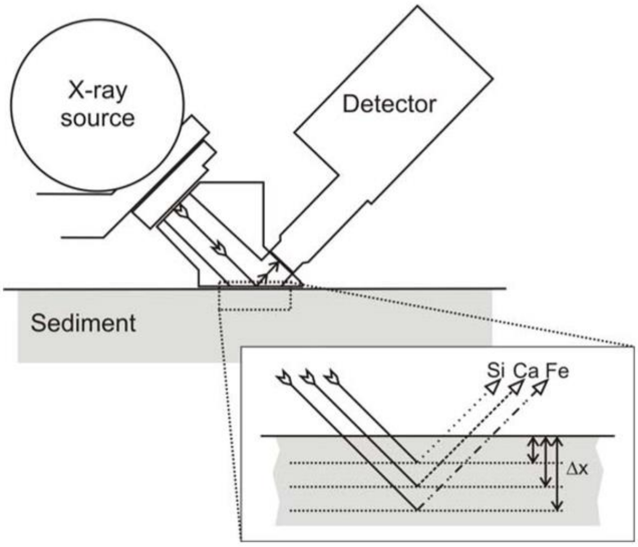

**Figure 6.1:** Schematic diagram showing the excitation geometry of an XRF core scanner (Tjallingii, 2006). $\Delta x$ = the critical depth of elements Si, Ca and Fe (not to scale). $\Delta x$ is governed by the fluorescence energies emitted by individual elements, with heavier elements requiring a greater $\Delta x$.

## 6.3: Aims of using XRF data on North Pacific sediment cores

The main aims of this chapter are as follows:

**1:** To identify element intensity signals which may represent key environmental and lithological signatures downcore at the nine chosen sites. These signatures include:

- terrigenous sediment input (non-volcanic) including IRD, aeolian input and riverine input.
- biogenic sediment input.
- volcanic ash layers.
- stratigraphic indicators of major global or local climatic and oceanographic changes including MIS transitions and changes in ocean circulation (the latter of which may be reflected in biogenic sediment input, e.g. Seo et al., 2018).

**2:** To compare the above element signal interpretations with existing data acquired in Chapters 4 and 5, including IRD and volcanic ash counts, foraminifera assemblages. Existing age models (where present) will be applied to the combined datasets for each core to assist with the interpretation of the intensity signals.

**3:** To carry out an inter-core comparison of the XRF signal in order to discern whether wider environmental signals can be observed at multiple sites in the N Pacific.

## 6.4: Methods

### *6.4.1: XRF scanning of North Pacific sediment cores*

Nine North Pacific ODP and DSDP sediment cores were selected for XRF scanning (Fig. 6.2; Table 6.1). Cores were selected to provide a wide geographical spread of sites including those within the subarctic water mass known to contain high concentrations of IRD (see Chapter 2), and those in transitional zones and at more distal sites with either lower or unknown concentrations of IRD. Other cores with very little or very low resolution Late Quaternary data were also sampled including ODP 1179 and DSDP 433. XRF data from ODP 1207A and DSDP 580 was compared against the IRD, tephra, biostratigraphy and chronostratigraphy presented in Chapters 4 and 5. A high IRD (e.g. Hewitt et al., 1997) NE Pacific site, ODP 887 was also scanned to assess the extent to which the XRF data varies in comparison to the NW Pacific where the geological sources of terrigenous sediment differ.

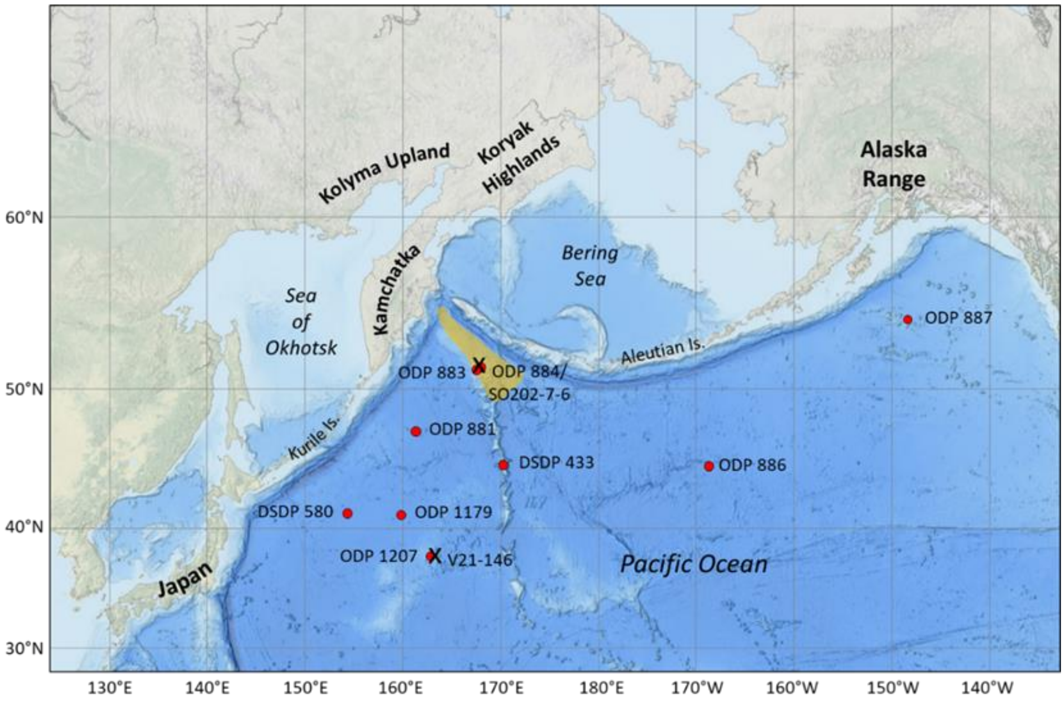

**Figure 6.2:** North Pacific ODP and DSDP core locations from which XRF core scanning data was obtained (red markers), and additional cores mentioned in this chapter (marked by a black ‘**X**’). Shaded orange area marks the Meiji Drift.

| Site | Latitude | Longitude | Depth (mbsf) | Age model? |
|---|---|---|---|---|
| ODP 1207A | 37.79ºN | 162.75ºE | 3103 | ✓ |
| DSDP 580 | 41.62ºN | 153.98ºE | 5375 | ✓ |
| ODP 883B | 51.12ºN | 167.46ºE | 2384 | ✓ |
| ODP884A | 51.27ºN | 168.2ºE | 3826.6 | ✓ |
| ODP 881B | 47.61ºN | 161.29ºE | 5530.8 | × |
| ODP 1179A | 41.08ºN | 159.96ºE | 5563.9 | × |
| DSDP 433 | 44.47ºN | 170.01ºE | 1874 | × |
| ODP 886A | 44.41ºN | 168.14W | 5713.4 | × |
| ODP 887A | 55.22ºN | 148.27W | 3631.2 | ✓ |

**Table 6.1:** Locations and water depths of cores which were XRF scanned for this study. The presence or absence of a Late Quaternary age model is also recorded.

All archive halves of the split cores are stored at the International Ocean Discovery Program (IODP) Gulf Coast Repository, College Station, Texas, USA. Archive cores were scanned at the IODP XRF Core Scanning facility in August 2017 using a third generation Avaatech Core Scanner (Fig. 6.3). The upper 300cm of all selected cores were scanned at a resolution of 1cm. All cores were scanned at three separate excitation energies of 10 kV (for detecting lighter major and minor elements including Al, Si, Ca, Ti, Mn, Fe, Cr, K, P, S and Mg), 30 kV (for heavier major and minor, and most trace elements including Ca, Ti, Mn, Fe, Ni, Sr, Rb, Zr, and Zn) and 50 kV (for heavier elements including Rb, Sr, Zr, Ag, and Ba). Initial data adjustment was carried out before analysis by removing data points with intensities of Ar greater than -915. High Ar counts result from poor contact between the scanner and sediment surface which causes contamination of the signal by air (Gross, 2014). Data-gaps were present in all nine cores where cracks and missing sediment sections had created cavities in the core.

**Figure 6.3:** Third generation Avaatech XRF core scanner and data-processing station with scan in progress, at the IODP, Texas.

Several major elements are commonly used to extract palaeoenvironmental signals from XRF intensities, with distinctions between elements indicative of terrestrial sources, e.g. Fe, Ti, K, Si, Al, Zr (e.g. Monien et al., 2012; Bahr et al., 2014), and elements indicative of biological sources, especially Ca (e.g. Hanslik et al., 2013) and Ba (e.g. Klump et al., 2000). In all nine cores, most of the key terrestrial elements have strong positive correlations (Table 6.2-6.9. Where correlations between terrestrial elements are weak (e.g. the correlation between Al and Ti in DSDP 580 is 0.14), this is due to the effects of individual tephra layers which are enriched or depleted in different terrestrial elements. Due to the predominantly strong correlations between terrestrial elements, only Fe, Ti, and Zr are displayed in the results to represent terrigenous sediment flux. Zr was chosen due to its usefulness in identifying tephra layers (Westerhold et al., 2009), and Fe is a common indicator of terrigenous flux (Nizou et al., 2010), although Fe can be susceptible to diagenetic effects (Rothwell and Croudace, 2015).

### *6.4.2: Log ratios of XRF intensities*

Although absolute counts of element intensities can reveal environmental information about changing sedimentation in relation to climate and other environmental change, intensities of a single element are influenced by the unit-sum constraint on proportions, where intensities of a single element are influenced by changes in other elements, in addition to environmental factors, resulting in noise (Weltje and Tjallingii, (2008). Therefore any interpretation of absolute element intensities alone must be treated cautiously. Noise resulting from interactions between elements is reduced when element intensities are converted to log ratios. Using log ratios of two elements has been shown to be an effective way of analysing elemental abundance change, and Weltje and Tjallingii, (2008) demonstrate that log ratios, when calibrated, are closely correlated with quantitative element or oxide concentrations measured by conventional chemical analysis.

Log ratios of a suite of elements are commonly normalised to a single, usually relatively immobile element which is less susceptible to alteration through chemical weathering or diagenetic effects (Johansson, 2017). Intensities of Ba, Ca, Fe, and Zr were converted to log-ratios over Ti, which is a relatively immobile element and is abundant in terrestrial minerals and occurs only in low concentrations in seawater and is scarce in organic systems (Wei et al., 2003). Log ratios of Ti/Al were also presented, to represent relative changes in Ti and Al. Al, like Ti, is a commonly used denominator in element ratios (e.g. Itambi et al., 2009).

Ti/Al has also been found to reflect climatically modulated terrigenous flux (Zeigler et al., 2009).

Intensities of Ca are used in marine sediments as an indicator of marine carbonate content, and may identify periods of productivity change (Richter et al., 2006). In the cores which have high calcium carbonate content (those at depths above the CCD, i.e. 1207, 883, 433 and 887), Ca is negatively correlated with terrestrial elements (Table 6.2-6.10). Therefore log ratios of Ca/Ti are shown in Figs. 6.4-6.13. Barium intensities may be used as a proxy for palaeoproductivity in cores which have low carbonate content, as this element has been found to reflect the abundance of biological debris in addition to solely carbonate productivity (Liguori et al., 2016). Therefore, Ba/Ti is also shown for all sites as a possible palaeoproductivity indicator.

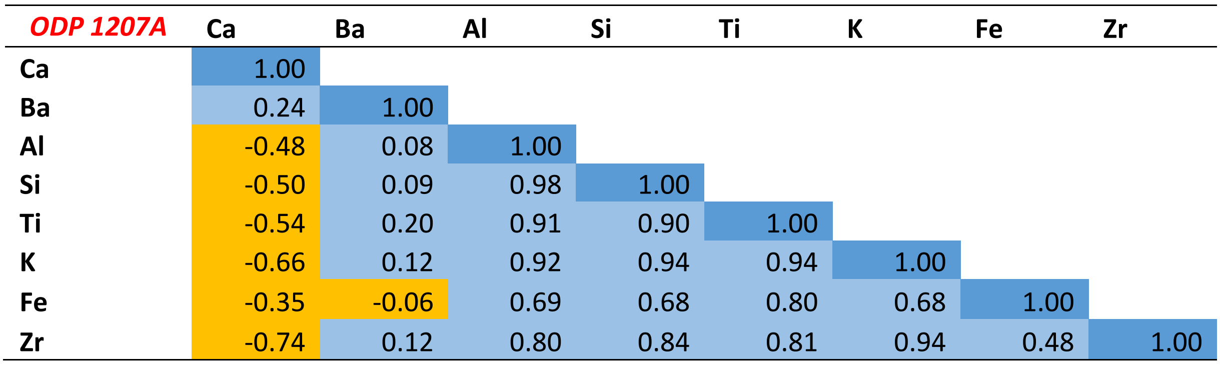

| *ODP 1207A* | Ca | Ba | Al | Si | Ti | K | Fe | Zr |
|---|---|---|---|---|---|---|---|---|
| **Ca** | 1.00 | | | | | | | |
| **Ba** | 0.24 | 1.00 | | | | | | |
| **Al** | -0.48 | 0.08 | 1.00 | | | | | |
| **Si** | -0.50 | 0.09 | 0.98 | 1.00 | | | | |
| **Ti** | -0.54 | 0.20 | 0.91 | 0.90 | 1.00 | | | |
| **K** | -0.66 | 0.12 | 0.92 | 0.94 | 0.94 | 1.00 | | |
| **Fe** | -0.35 | -0.06 | 0.69 | 0.68 | 0.80 | 0.68 | 1.00 | |
| **Zr** | -0.74 | 0.12 | 0.80 | 0.84 | 0.81 | 0.94 | 0.48 | 1.00 |

**Table 6.2:** Correlation matrix for a selection of elements representing predominantly biological processes (Ca, Ba) and predominantly terrestrial material (Al, Si, Ti, K, Fe and Zr) for ODP 1207A. Blue highlights positive correlations and yellow highlights negative correlations.

| DSDP 580 | Ca | Ba | Al | Si | Ti | K | Fe | Zr |
|---|---|---|---|---|---|---|---|---|
| Ca | 1.00 | | | | | | | |
| Ba | 0.01 | 1.00 | | | | | | |
| Al | 0.60 | 0.09 | 1.00 | | | | | |
| Si | 0.57 | 0.10 | 0.95 | 1.00 | | | | |
| Ti | 0.20 | 0.02 | 0.14 | -0.07 | 1.00 | | | |
| K | 0.15 | 0.11 | 0.68 | 0.64 | 0.34 | 1.00 | | |
| Fe | 0.05 | -0.02 | -0.02 | -0.16 | 0.87 | 0.28 | 1.00 | |
| Zr | 0.28 | 0.06 | 0.63 | 0.73 | -0.50 | 0.27 | -0.63 | 1.00 |

**Table 6.3:** Correlation matrix for a selection of elements at DSDP 580.

| ODP 883B | Ca | Ba | Al | Si | Ti | K | Fe | Zr |
|---|---|---|---|---|---|---|---|---|
| Ca | 1.00 | | | | | | | |
| Ba | 0.32 | 1.00 | | | | | | |
| Al | -0.57 | 0.32 | 1.00 | | | | | |
| Si | -0.24 | 0.41 | 0.83 | 1.00 | | | | |
| Ti | -0.67 | 0.19 | 0.96 | 0.74 | 1.00 | | | |
| K | -0.67 | 0.23 | 0.92 | 0.72 | 0.92 | 1.00 | | |
| Fe | -0.63 | 0.05 | 0.86 | 0.63 | 0.94 | 0.80 | 1.00 | |
| Zr | -0.41 | 0.18 | 0.42 | 0.30 | 0.36 | 0.67 | 0.17 | 1.00 |

**Table6.4:** Correlation matrix for a selection of elements at ODP 883B.

| ODP 884A | Ca | Ba | Al | Si | Ti | K | Fe | Zr |
|---|---|---|---|---|---|---|---|---|
| Ca | 1.00 | | | | | | | |
| Ba | 0.02 | 1.00 | | | | | | |
| Al | 0.29 | 0.25 | 1.00 | | | | | |
| Si | 0.29 | 0.28 | 0.84 | 1.00 | | | | |
| Ti | 0.18 | 0.33 | 0.92 | 0.77 | 1.00 | | | |
| K | 0.02 | 0.29 | 0.85 | 0.73 | 0.86 | 1.00 | | |
| Fe | 0.06 | 0.16 | 0.72 | 0.58 | 0.86 | 0.67 | 1.00 | |
| Zr | 0.10 | 0.02 | 0.19 | 0.13 | 0.09 | 0.42 | -0.18 | 1.00 |

**Table 6.5:** Correlation matrix for a selection of elements at ODP 884A.

| ***ODP 881B*** | ***Ca*** | ***Ba*** | ***Al*** | ***Si*** | ***Ti*** | ***K*** | ***Fe*** | ***Zr*** |
|---|---|---|---|---|---|---|---|---|
| ***Ca*** | 1.00 | | | | | | | |
| ***Ba*** | -0.27 | 1.00 | | | | | | |
| ***Al*** | 0.22 | 0.38 | 1.00 | | | | | |
| ***Si*** | 0.35 | 0.36 | 0.80 | 1.00 | | | | |
| ***Ti*** | 0.02 | 0.50 | 0.77 | 0.47 | 1.00 | | | |
| ***K*** | -0.39 | 0.72 | 0.74 | 0.47 | 0.82 | 1.00 | | |
| ***Fe*** | 0.32 | 0.34 | 0.65 | 0.45 | 0.88 | 0.55 | 1.00 | |
| ***Zr*** | -0.08 | 0.07 | 0.64 | 0.54 | 0.26 | 0.52 | 0.08 | 1.00 |

**Table 6.6:** Correlation matrix for a selection of elements at ODP 881B.

| ***ODP 1179A*** | ***Ca*** | ***Ba*** | ***Al*** | ***Si*** | ***Ti*** | ***K*** | ***Fe*** | ***Zr*** |
|---|---|---|---|---|---|---|---|---|
| ***Ca*** | 1.00 | | | | | | | |
| ***Ba*** | 0.04 | 1.00 | | | | | | |
| ***Al*** | 0.48 | 0.01 | 1.00 | | | | | |
| ***Si*** | 0.63 | 0.07 | 0.95 | 1.00 | | | | |
| ***Ti*** | 0.08 | 0.33 | 0.71 | 0.62 | 1.00 | | | |
| ***K*** | 0.22 | 0.10 | 0.85 | 0.77 | 0.69 | 1.00 | | |
| ***Fe*** | -0.07 | 0.14 | 0.24 | 0.22 | 0.66 | 0.21 | 1.00 | |
| ***Zr*** | 0.42 | -0.04 | 0.57 | 0.56 | 0.09 | 0.74 | -0.34 | 1.00 |

**Table 6.7:** Correlation matrix for a selection of elements at ODP 1179A.

| ***DSDP 433*** | ***Ca*** | ***Ba*** | ***Al*** | ***Si*** | ***Ti*** | ***K*** | ***Fe*** | ***Zr*** |
|---|---|---|---|---|---|---|---|---|
| ***Ca*** | 1.00 | | | | | | | |
| ***Ba*** | -0.14 | 1.00 | | | | | | |
| ***Al*** | -0.52 | -0.06 | 1.00 | | | | | |
| ***Si*** | 0.34 | 0.31 | -0.03 | 1.00 | | | | |
| ***Ti*** | -0.71 | 0.12 | 0.95 | -0.08 | 1.00 | | | |
| ***K*** | -0.63 | 0.06 | 0.97 | -0.11 | 0.96 | 1.00 | | |
| ***Fe*** | -0.75 | 0.16 | 0.89 | -0.16 | 0.97 | 0.94 | 1.00 | |
| ***Zr*** | -0.77 | 0.10 | 0.88 | -0.20 | 0.95 | 0.92 | 0.95 | 1.00 |

**Table 6.8:** Correlation matrix for a selection of elements at DSDP 433.

| ODP 886A | Ca | Ba | Al | Si | Ti | K | Fe | Zr |
|---|---|---|---|---|---|---|---|---|
| **Ca** | 1.00 | | | | | | | |
| **Ba** | 0.36 | 1.00 | | | | | | |
| **Al** | 0.31 | -0.08 | 1.00 | | | | | |
| **Si** | 0.46 | 0.18 | 0.94 | 1.00 | | | | |
| **Ti** | 0.65 | 0.25 | 0.84 | 0.92 | 1.00 | | | |
| **K** | 0.26 | -0.10 | 0.97 | 0.91 | 0.85 | 1.00 | | |
| **Fe** | 0.57 | 0.01 | 0.91 | 0.92 | 0.95 | 0.92 | 1.00 | |
| **Zr** | 0.23 | 0.02 | 0.84 | 0.79 | 0.74 | 0.83 | 0.76 | 1.00 |

**Table 6.9:** Correlation matrix for a selection of elements at ODP 886A.

| ODP 887A | Ca | Ba | Al | Si | Ti | K | Fe | Zr |
|---|---|---|---|---|---|---|---|---|
| **Ca** | 1.00 | | | | | | | |
| **Ba** | 0.33 | 1.00 | | | | | | |
| **Al** | -0.41 | 0.24 | 1.00 | | | | | |
| **Si** | -0.16 | 0.33 | 0.89 | 1.00 | | | | |
| **Ti** | -0.43 | 0.41 | 0.88 | 0.75 | 1.00 | | | |
| **K** | -0.57 | 0.03 | 0.91 | 0.81 | 0.74 | 1.00 | | |
| **Fe** | -0.44 | 0.30 | 0.86 | 0.74 | 0.95 | 0.74 | 1.00 | |
| **Zr** | -0.53 | -0.02 | 0.42 | 0.38 | 0.28 | 0.67 | 0.17 | 1.00 |

**Table 6.10:** Correlation matrix for a selection of elements at ODP 887A.

Of the nine cores studied in this chapter, all except ODP 881B, ODP 1179A, DSDP 433 and ODP 886A have existing Late Quaternary chronostratigraphic frameworks. Sites with an existing chronology were plotted against Ca, Ti, Fe and Zr intensities and analysed within the context of Late Quaternary Marine Isotope Stages (MIS), considering the likely change in flux of terrigenous material or changes in productivity during periods of climatic change. Sites with no existing chronology were analysed for changing elemental intensities and log ratios, and compared against sites with existing chronologies. Speculation about possible climate or source signals at these sites is presented in Section 6.6.

In the results section (6.5), elemental intensities of Ba, Ca, Fe, Ti and Zr in the upper 300cm of each site are presented first. Log ratios are plotted alongside raw intensities. Where present, intensities are plotted against other key sedimentary signals including IRD, ash and $\delta^{18}O$. Where possible, Marine Isotope Stages are also indicated. The interpretation of the XRF signals is found in Section 6.6. A discussion of possible palaeoenvironmental signals in the element intensities is presented in Section 6.6.1, 6.6.2 and 6.6.3, in addition to a discussion of the advantages and limitations of this approach to using XRF core scanner data in 6.7. Finally, a discussion of desirable future work to develop the research carried out in this chapter is presented at the end of this section.

## 6.5: Results

### *6.5.1: Element intensities and log ratios: ODP 1207A*

Intensities of Ba, Ca, Ti, Fe, and Zr were plotted against the age model for 0-300cm in ODP 1207A presented in Chapter 4 (Fig. 6.4). Log ratios of elements/Ti and Ti/Al were overlaid on raw element intensities. The benthic $\delta^{18}O$, IRD and ash counts were also plotted alongside the XRF data. The intensity signal is dominated by a large trough in Ca and to a lesser extent, Ba, and peaks in Ti, Fe, and Zr, at the depth of the Aso-4 tephra dated to ~87 ka BP. Periods of higher counts of Ti, Fe and, to a lesser extent, Zr occur in late MIS 3 until mid-MIS 2. MIS 6 is also characterised by higher counts of these elements, which decrease at the MIS 6-5 boundary. Notably, the increase in counts of Fe at the depth of the Aso-4 tephra is less pronounced than Ti. However, two notable peaks in Fe occur in MIS 6, ~170 ka BP and ~155 ka BP. Peaks of Zr are absent at these times. There are no clearly correlated responses in element intensities to IRD supply, except a concurrent short-lived peak in Ti and Fe with the largest IRD peak at ~40 ka BP. Ba intensities are lowest during MIS 6 and MIS 2, with low intensities also occurring during early MIS 4. Peaks in Ba and to a lesser extent, Ca, occur in MIS 5e, and there is a notable increase in Ba following the LGM and into the deglacial period of late MIS 2.

Fe/Ti and Ti/Al display notable fluctuations throughout the Late Quaternary. However, peaks generally occur in log ratios at the same depths as the peaks in raw intensities. whereas Ba/Ti, Ca/Ti, and Zr/Ti show visibly similar patterns of change as the raw element intensities of Ba, Ca, and Zr.

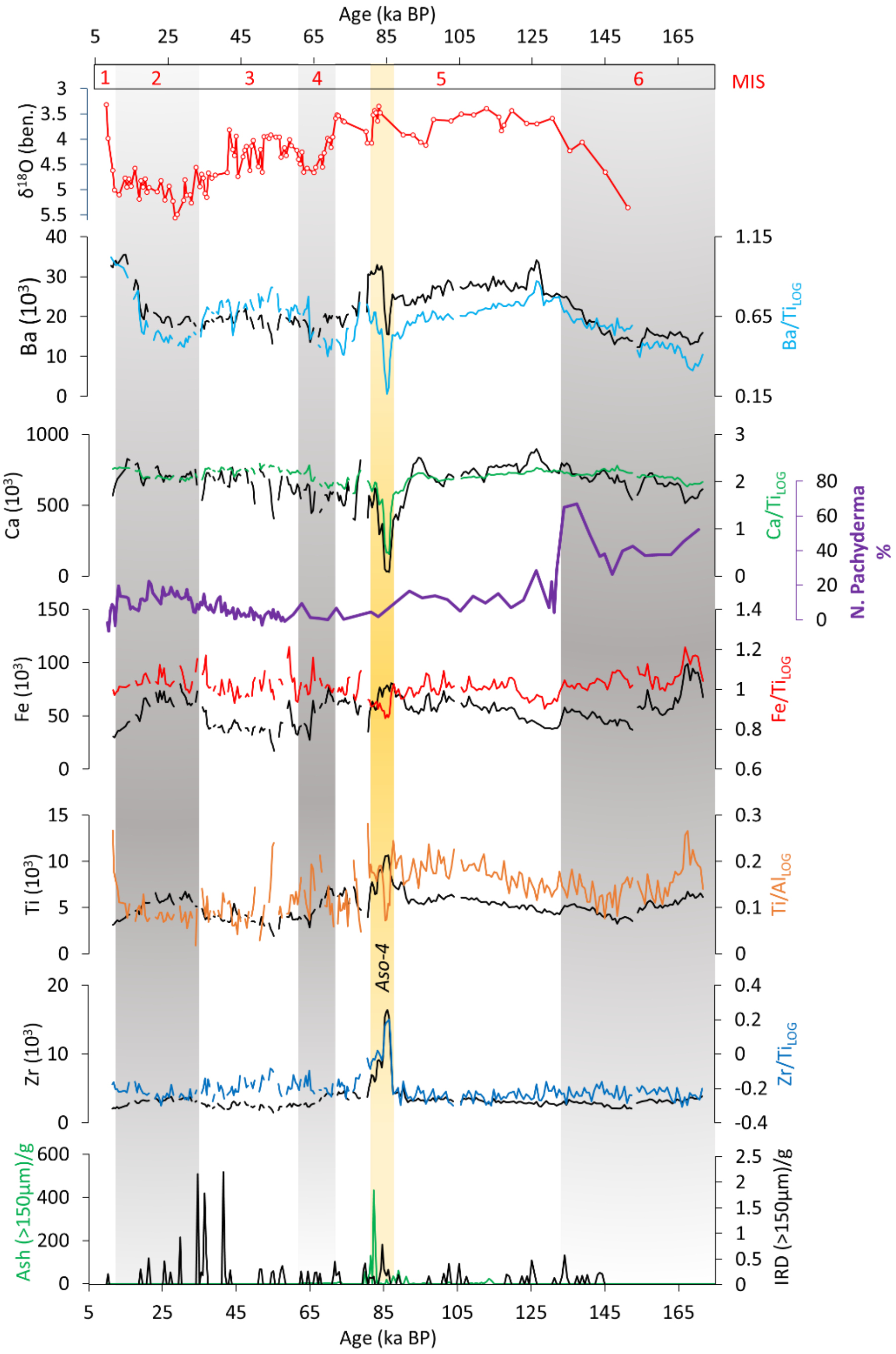

**Figure 6.4:** Elemental intensities of selected major elements in total counts ($10^3$) at ODP 1207A, plotted against the benthic $\delta^{18}O$ curve, % *N. pachyderma*, IRD and ash concentrations, (see Chapter 4) and element log ratios. Data gaps are due to cracks or gaps in the sediment. Alternating grey and white bars denote Marine Isotope Stages (labelled by red numbers), and the yellow bar denotes the Aso-4 tephra.

### *6.5.2: Element intensities and log ratios: DSDP 580*

The four tephra layers in the upper 300cm of DSDP 580 are visible in peaks in intensities of Zr (Fig. 6.5). Peaks in Ca are visible at the depth of the upper two ash layers, but less evident in the lower two ash layers (see Chapter 5 for a discussion of these tephras). Troughs of Fe and Ti are concurrent with all four tephra layers. Outside of tephra layers, a Ba peak occurs around 8 ka BP, and peaks in Ca occur ~40, 30, and 18 ka BP. No clear IRD signal is evident in the element intensity signal.

Ba/Ti, Ca/Ti and Zr/Ti exhibit peaks within ash layers. Ba/Ti also exhibits peaks between the two younger ash layers and around 9 ka BP. Generally, log ratios display a similar shape to raw intensities, with some deviations within the ash layers which appear to be low in Ti.

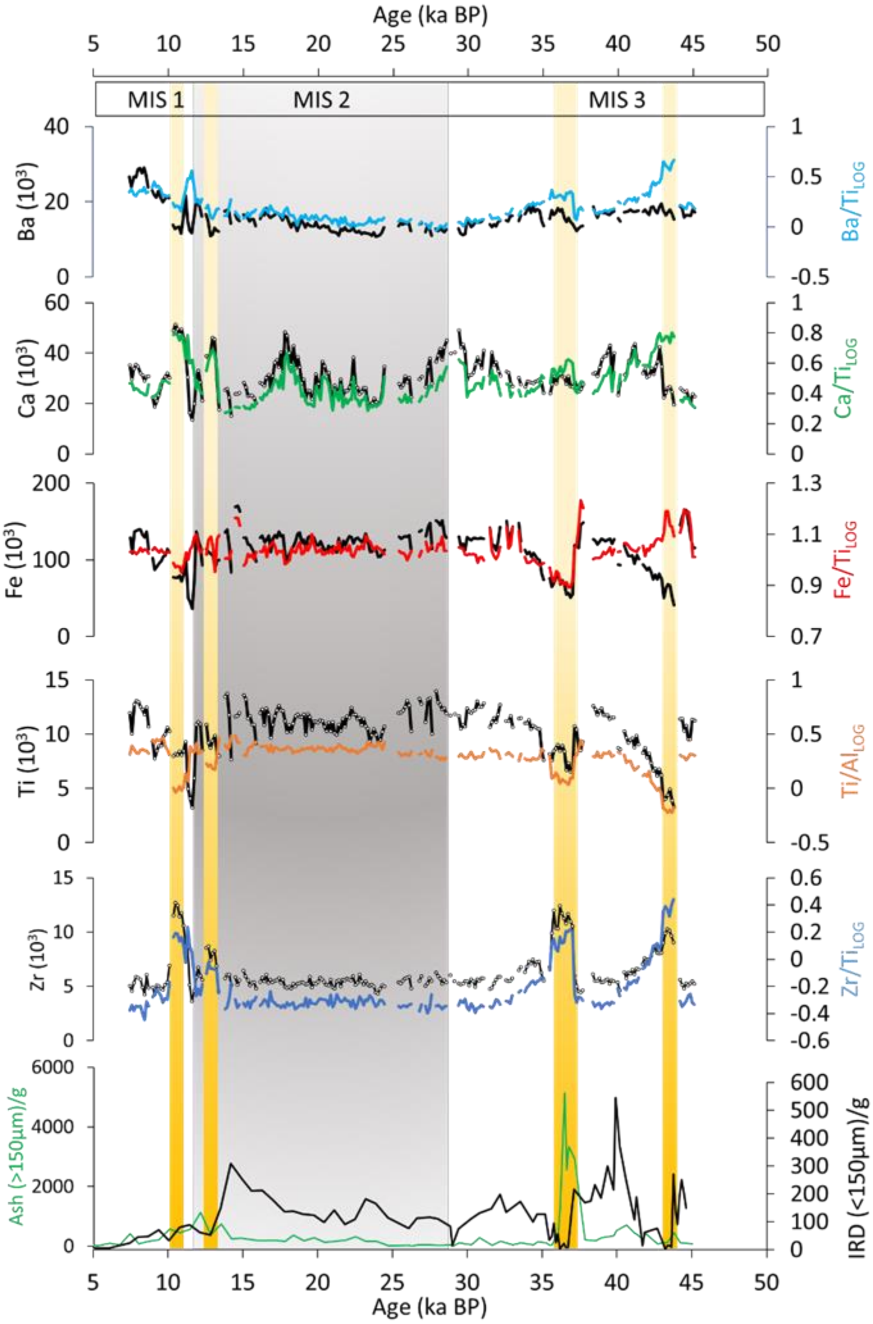

**Figure 6.5:** Elemental intensities of selected major elements in total counts ($10^3$) at DSDP 580, plotted against IRD/g and volcanic ash/g in the >150µm fraction (see Chapter 5) and element log ratios. Alternating grey and white bars denote Marine Isotope Stages and red bars denote tephra layers.

### *6.5.3: Element intensities and log ratios: ODP 883B*

A clear peak in Zr is visible at the depth of the tephra layer dated to ~39 ka BP (Bigg et al., 2008; Fig. 6.6). This tephra has been geochemically matched to the Gorely eruption on southern Kamchatka (Ponomareva, 2016, *pers. comm.).* The other elements show either smaller peaks or troughs concurrent with the tephra layer. Multiple simultaneous troughs in Ti and Fe occur in MIS 3, however, due to sediment gaps the signal here is somewhat unclear. Large and abrupt increases in Ba and Ca occurs prior to the MIS 2-1 boundary, accompanied by reductions in Ti and Fe. Further increases in Ba and Ca occur in early MIS 1.

Ba/Ti and Ca/Ti exhibit strong increases during late MIS 2, with abrupt fluctuations around 15 ka BP. Ba/Ti continues to rise, reaching a peak in early MIS 1, whereas Ca/Ti increases less steeply into MIS 1. Fe/Ti and Ti/Al exhibit somewhat less pronounced peaks and troughs than raw intensities of Fe and Ti. Zr/Ti appears similar to Zr, with an additional pronounced peak in Zr/Ti around 10 ka BP, concurrent with low Ti intensities.

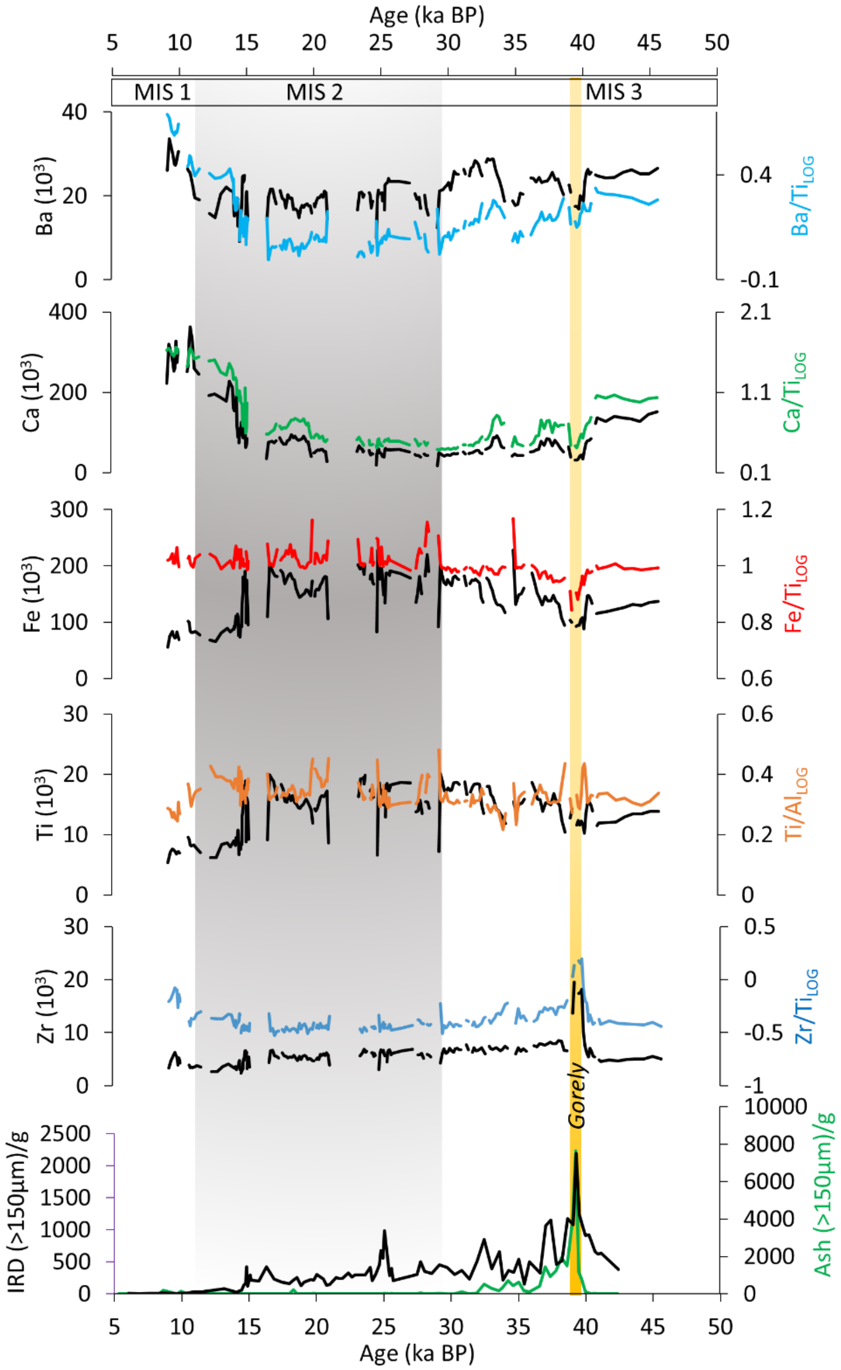

**Figure 6.6:** Elemental intensities of selected major elements in total counts ($10^3$) at ODP 883B, plotted against IRD/g and volcanic ash/g in the >150µm fraction, and element log ratios. Alternating grey and white bars denote Marine Isotope Stages and red bar denotes the Gorely tephra. IRD and ash data was redrawn from Bigg et al. (2008).

### *6.5.4: Element intensities and log ratios: ODP 884A*

Four ash layers are present in the upper 300cm of ODP 884A (Fig. 6.7), including the Gorely tephra ~39 ka BP (Ponomareva, 2019, *pers. comm.*). The Gorely tephra is less visibly defined in ODP 884A than in ODP 884B, and is most visible in ODP 884A in a peak of Fe, while all other element counts reduce at this depth. Around 31 ka BP there is a poorly defined ashy layer which, after electron microprobe analysis at GEOMAR, Kiel by M. Portnyagin, and tephra identification by V. Ponomareva, was found to contain a wide scatter of geochemically dissimilar glass shards, although it included shards from both the ~39ka BP Gorely eruption and the Opala ~40 ka BP eruption (V. Ponomareva, *pers. comm.*). This mix of sources suggests that it may be an IRD layer from SE Kamchatka. This ashy layer along with a defined tephra layer at ~25 ka BP are characterised by peaks in Ca, but reductions in the other elements. The tephra at ~16 ka BP is characterised by a prominent peak in Zr, but a reduction in all other elements. Ba exhibits somewhat elevated intensity counts at the MIS 3-2 boundary, and counts are generally higher during MIS 2 than MIS 3, with periods of higher counts interspersed with short-lived troughs. No clear relationship between element intensities and MIS are visible here.

Ba/Ti exhibits visible variations and a somewhat different shape to Ba, with a pronounced trough between around 37 and 32 ka BP. Troughs in Ba/Ti are also more pronounced than in Ba during MIS 2. While Ba stays relatively stable during deglaciation and into MIS 1, Ba/Ti decreases during this period. Ca/Ti exhibits a number of sharp peaks with slightly extended reductions during late MIS 3 and MIS 2, but exhibits less change than Ca during MIS 3 and during deglaciation and into MIS 1. Fe/Ti exhibits less fluctuation than Fe, with a peak within the Gorely tephra, and apparent peaks around 25 and 17 ka BP.

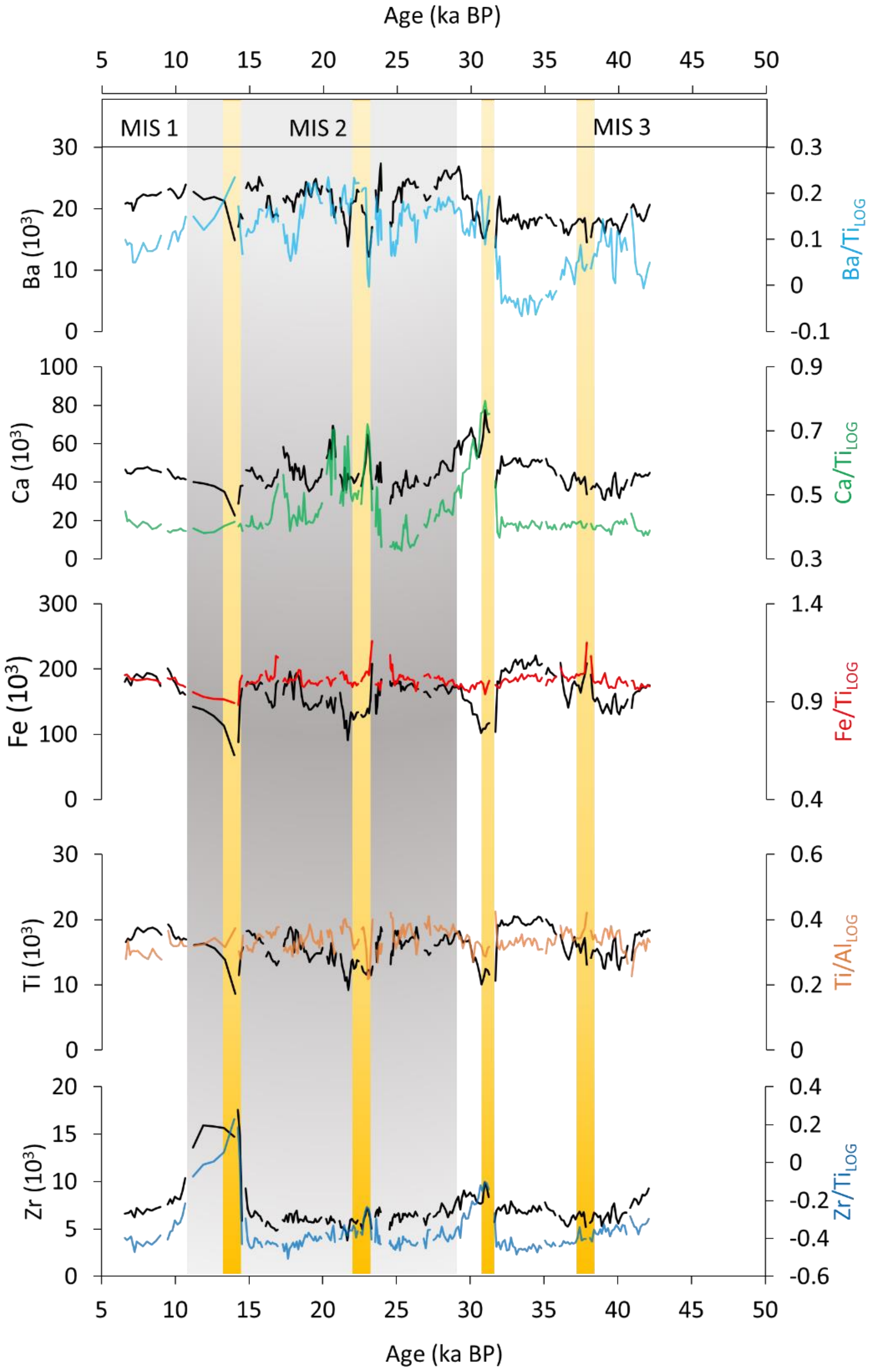

**Figure 6.7:** Elemental intensities of selected major elements in total counts ($10^3$) at ODP 884A, plotted against the age model of VanLaningham et al. (2009). Yellow bars mark the depths of tephra layers or ash-rich horizons. Alternating grey and white bars denote Marine Isotope Stages.

### *6.5.5: Element intensities and log ratios: ODP 881B*

No age model exists for ODP 881B (Table 6.1), therefore XRF intensities were plotted against depth (Fig. 6.8). Only one ash layer is clearly visible in the upper 300cm, at ~215cm. This ash layer is characterised in the element intensities by a peak in Zr and troughs in all other elements. Troughs in counts of Zr and Fe occur ~50cm, while peaks in Ca occur ~59cm, between 20and 35cm, and between 160 and 170cm where visible ashy pockets are present.

Element log ratios exhibit a number of positive and negative excursions, and peaks are particularly pronounced in Ca/Ti around 293cm, 222cm (ash layer), 168cm (ashy pockets), 139cm, 59cm and 33cm. Fe/Ti does not mimic the shape of Fe, and a peak is visible at the depths of the ashy pockets around 168cm. The amplitude of Fe/Ti peaks and troughs markedly increases between 120cm and around 36cm. These fluctuations become much smaller between around 35cm and the core-top.

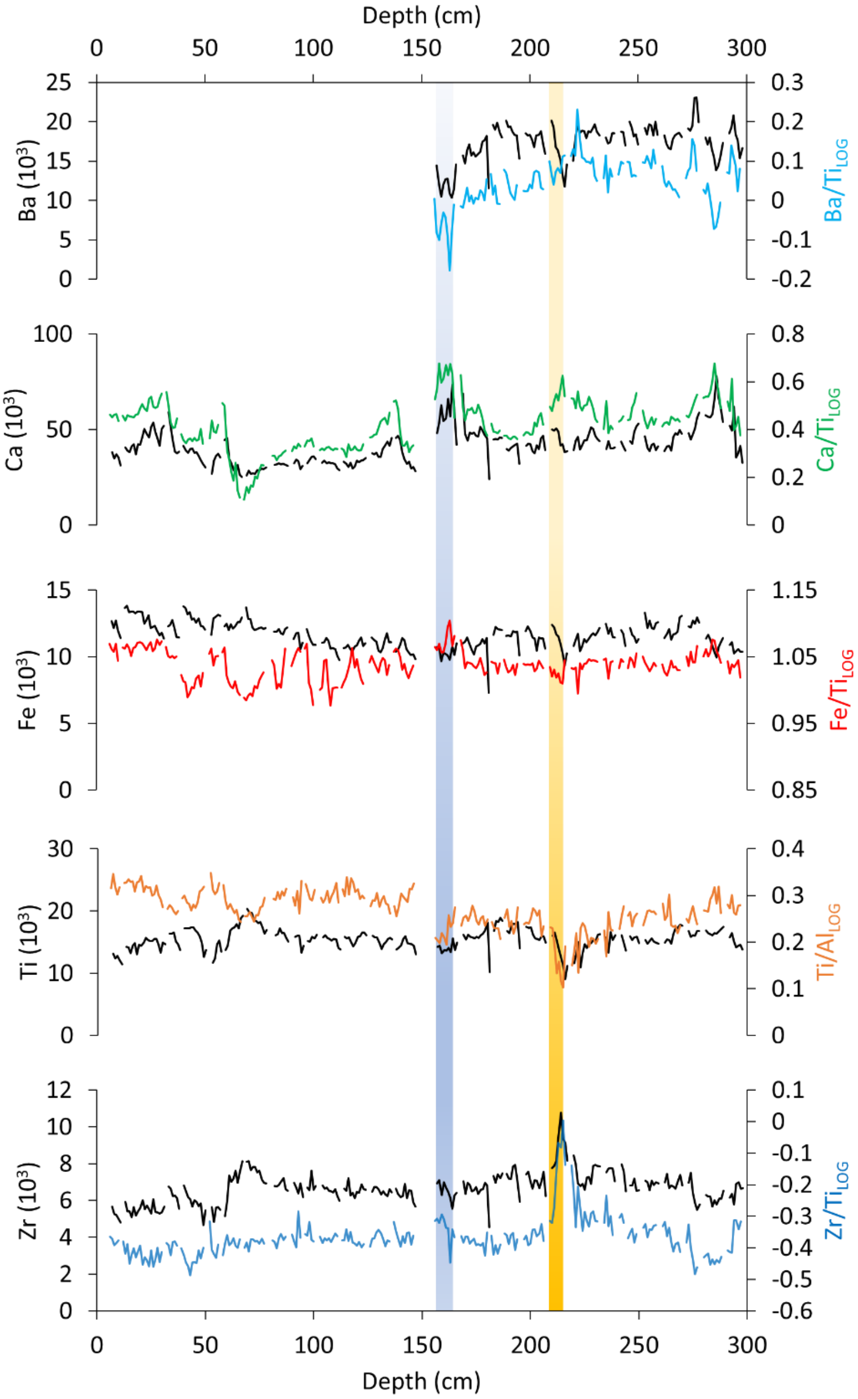

**Figure 6.8:** Elemental intensities of selected major elements in total counts ($10^3$) at ODP 881B, plotted against depth (cm). The yellow bar marks the visible tephra layer, and blue bar marks the depth of ashy pockets. Note: Ba intensities between 0-150cm is missing due to a data processing error.

### *6.5.6: Element intensities and log ratios: ODP 1179A*

As with ODP 881B, no age model exists for ODP 1179A (Table 6.1), therefore element intensities are plotted against depth (Fig. 6.9). Two ash layers are visible in ODP 1179A at 199-205cm and 215-223cm. Between these closely-spaced ash layers is an interval with high counts of Zr and Ti. This may be due to vertically mixed ash between the discrete tephra layers. Significant troughs in intensities of all elements occur at 40, 60, 80, 254 and 278cm.

Fluctuations in Ba/Ti are more pronounced than in Ba, and a prolonged minimum is visible between around 170 and 65cm, followed by an abrupt increase and higher Ba/Ti between around 64cm and the core-top. Fe/Ti largely mimics the shape of Fe intensities, while Ti/Al exhibits major short-lived peaks at 255cm and 40cm, which are absent in Ti intensities.

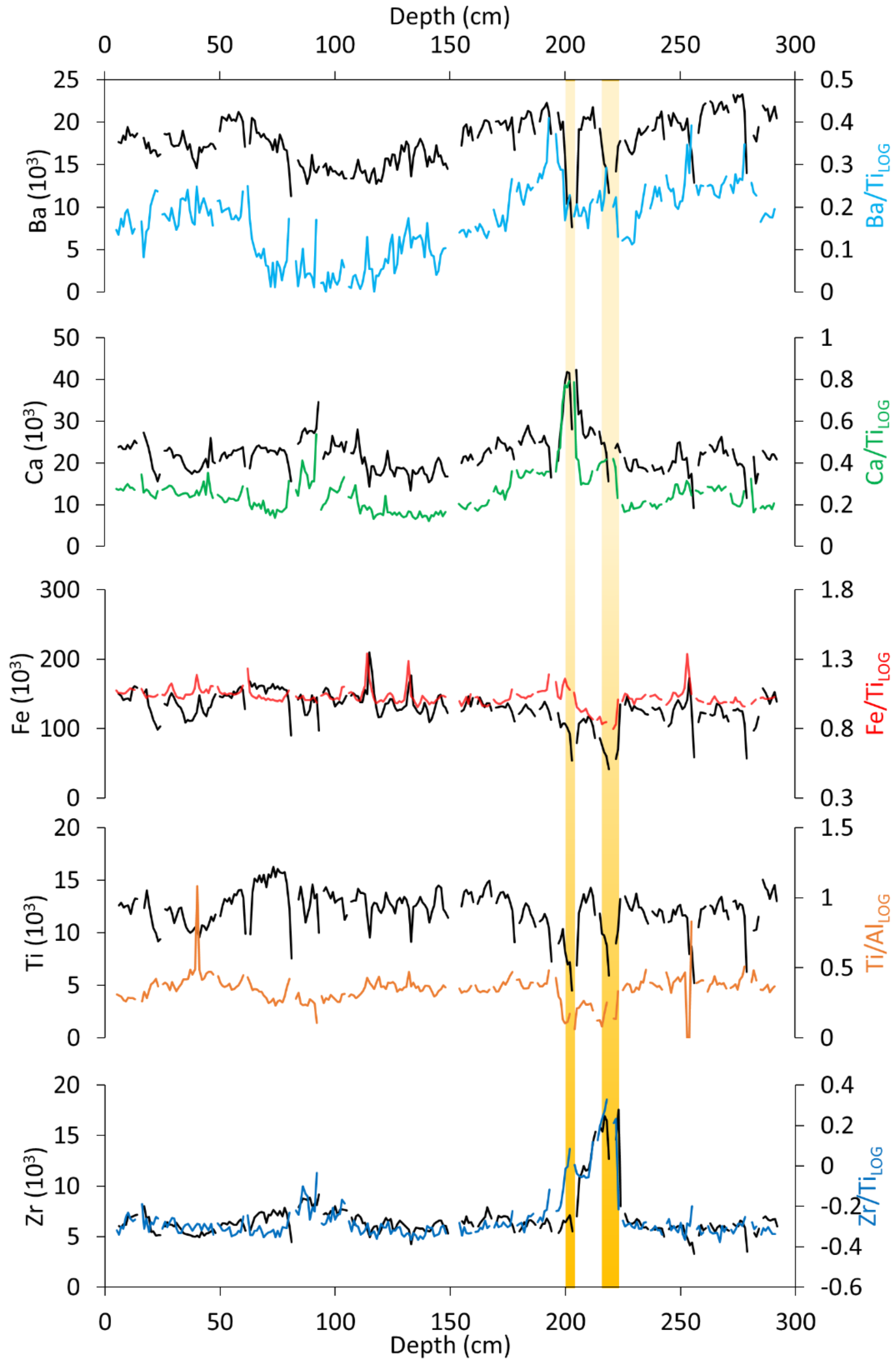

**Figure 6.9:** Elemental intensities of selected major elements in total counts ($10^3$) at ODP 1179A, plotted against depth (cm). Yellow bars mark visible tephra layers.

### *6.5.7: Element intensities and log ratios: DSDP 433*

No age model exists for DSDP 433, therefore XRF intensities were plotted against depth. This core contains many large dropstones up to 2cm in diameter (Fig. 6.10). The dropstones were composed of dark rock fragments and pumice. Dropstones were temporarily removed from the core surface for XRF scanning due to their uneven surfaces which can cause inaccurate measurements. Their depths were recorded and they were placed back in the sediment at the correct depth after the core was scanned.

Dropstone depths were plotted against element intensities (Fig. 6.11). Significant fluctuations in Ca intensities occur between 0 and 300cm. In general, peaks in Ca are accompanied by troughs in Fe, Ti, and Zr. Ba behaves differently to the other elements, no visible major concurrent peaks or troughs. Ash layers are not clearly visible in this core.

Log ratios of Ba/Ti and Ca/Ti exhibit similar behaviour. Fe/Ti exhibits a much flatter signal than Fe, particularly between 215cm and the core-top. Ti/Al exhibits a signal dissimilar to the other log ratios or element intensities, however the ratio change is slight (between 0.2 and 0.5). Zr/Ti exhibits similar behaviour to Fe/Ti, however the signal is slightly noisier.

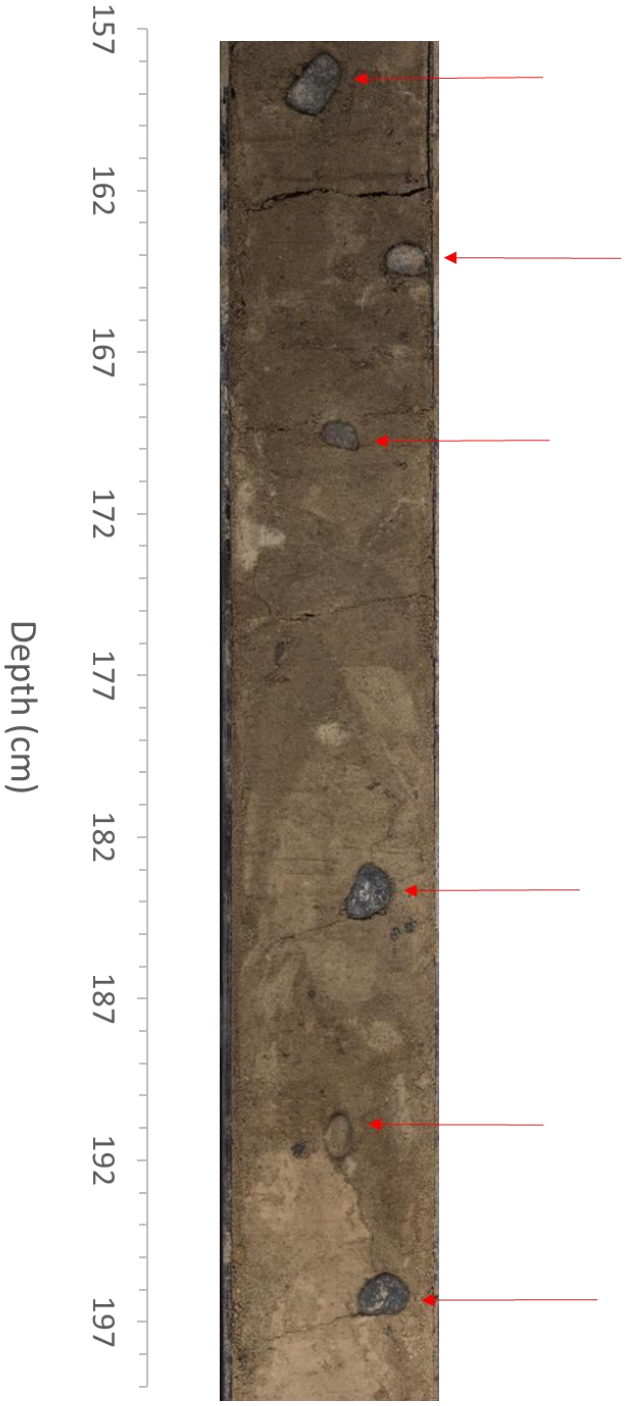

**Figure 6.10:** Photograph of DSDP 433 (157.5cm-199.5cm). Arrows point to large dropstones, which were removed during scanning to prevent scanner errors on the uneven dropstone surfaces.

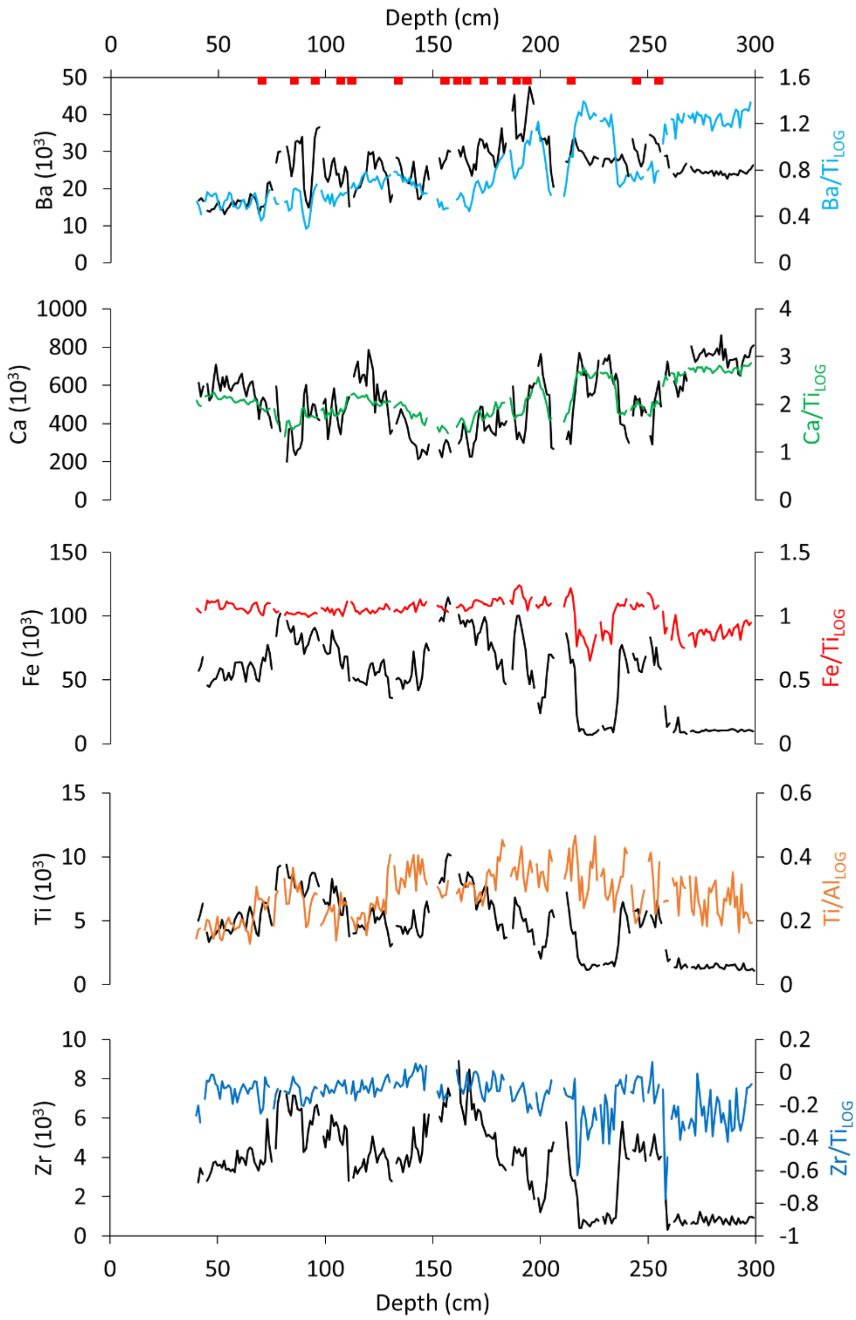

**Figure 6.11:** Elemental intensities of selected major elements in total counts ($10^3$) at DSDP 433, plotted against depth (cm). Depths of dropstones are shown by red markers. Marker length varies with dropstone spacing (longer marker = higher concentration of dropstones).

### *6.5.8: Element intensities and log ratios: ODP 886A*

No high-resolution Late Quaternary age model exists for ODP 886A, therefore element intensities were plotted against depth (Fig. 6.12). However, The Bruhnes-Matuyama reversal (0.78 ma) was identified in the magnetostratigraphy at ~350cm depth in the shipboard scientific study (Rea et al., 1993). Additionally, a late Pleistocene diatom assemblage is also present. The resulting low resolution chronostratigraphy infers that the upper 300cm of this site spans ~0.6 Ma due to a low accumulation rate at this distal deep ocean site. All elements show similar patterns with significant peaks occurring ~60cm, 120cm, and between 160cm and 200cm. However, unlike the other elements, Ba declines gradually between around 270cm and 193cm.

Log ratios of Ba/Ti, Ca/Ti and Zr/Ti exhibit similar behaviour to the corresponding raw intensities of Ba, Ca, and Zr. Fe/Ti displays a visible signal with greater fluctuation than Fe. Ti/Al also displays different behaviour to Ti, with peaks (i.e. 130cm and 109cm) and troughs (i.e. 193-165cm and 129-111cm) in log ratios which do not occur in the raw intensities.

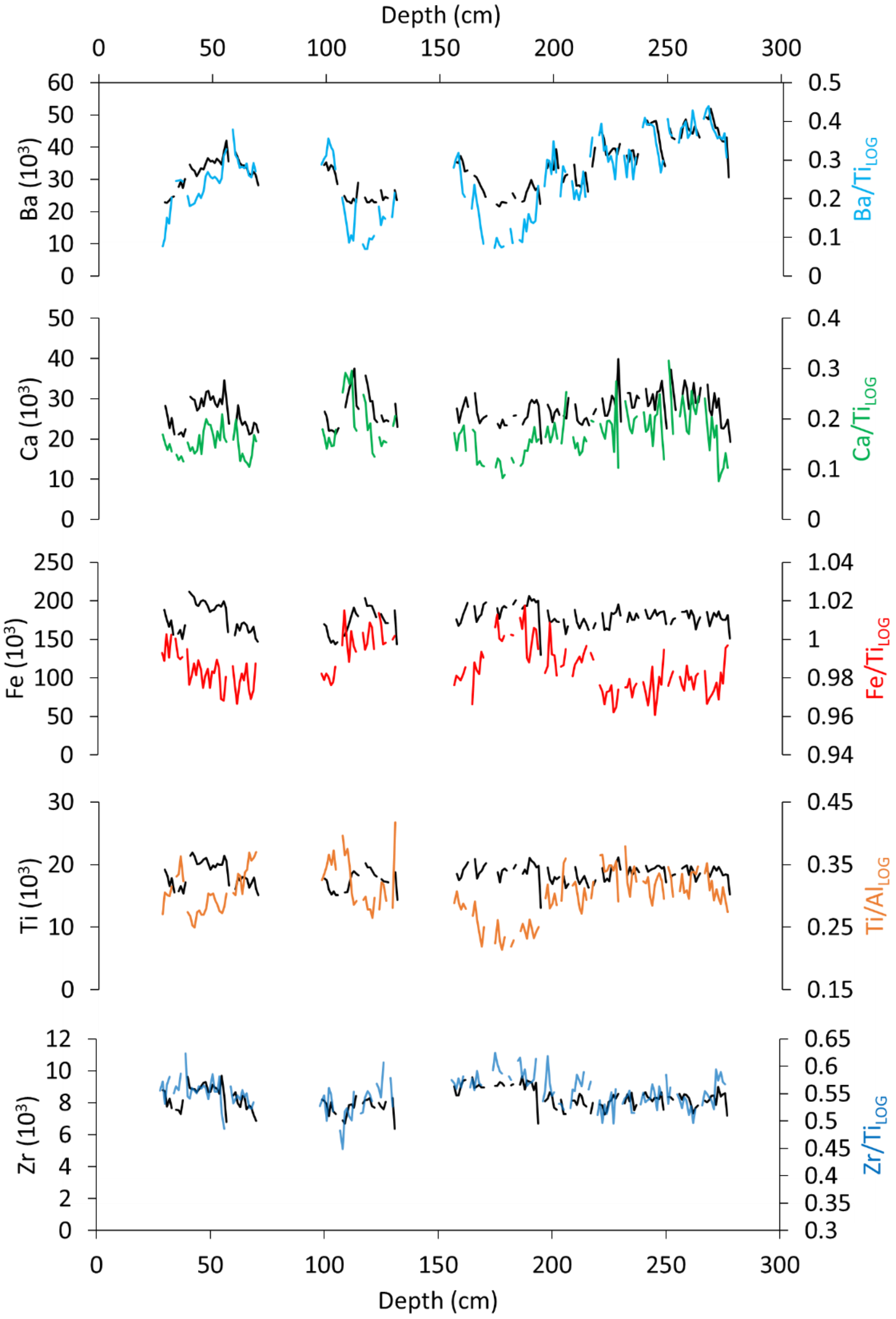

**Figure 6.12:** Elemental intensities of selected major elements in total counts ($10^3$) at ODP 886A, plotted against depth (cm).

### *6.5.9: Element intensities and log ratios: ODP 887A*

The age model for ODP 887A was constructed from the $^{14}$C stratigraphy of ODP 887B (McDonald et al., 1999; Fig. 6.13). Both 887A and 887B recovered the same sections of sediment between 0 and 300cm, therefore the age model from 887B can be applied to both holes. The IRD record for ODP 887A was constructed by St. John and Krissek, (1999) and was plotted against element intensities (Fig. 6.13). Two ash layers are visible in the upper 300cm at ~42 ka BP and ~26 ka BP. The older of these ash layers coincides with peaks in Zr, Fe, and Ti, but coincides with a trough in Ca and Ba. The younger ash layer coincides with a distinct peak in Zr, and troughs in Fe and Ti. There is little change in Ca associated with this ash layer, but a sharp increase in Ba. Peak counts of Ca occur abruptly around 15 ka BP, concurrent with abrupt reductions in Zr, Fe, and Ti, while two smaller peaks in Ca occur during MIS 3. Ba does not exhibit the MIS 3 peaks seen in Ca, but due to the troughs in Ti during MIS 3, the log ratio of Ba/Ti does produce peaks corresponding with those in Ca and Ca/Ti. An abrupt spike in Ba/Ti occurs around 15 ka BP, corresponding with a sharp decrease in Ti, while raw counts of Ba increase less rapidly around the MIS 2-1 boundary, reaching peak counts around 6 ka BP.

Log ratios of Ba/Ti and Ca/Ti exhibit similar behaviour. An abrupt spike in Ba/Ti occurs around 14.5 ka BP, concurrently with a spike in Ca/Ti, around 2 ka earlier than the increase in raw Ba counts. Fe/Ti exhibits a relatively constant signal in comparison to Fe. However, a notable spike occurs around 13.8 ka BP. Peaks and troughs in Ti/Al are suppressed in comparison to Ti.

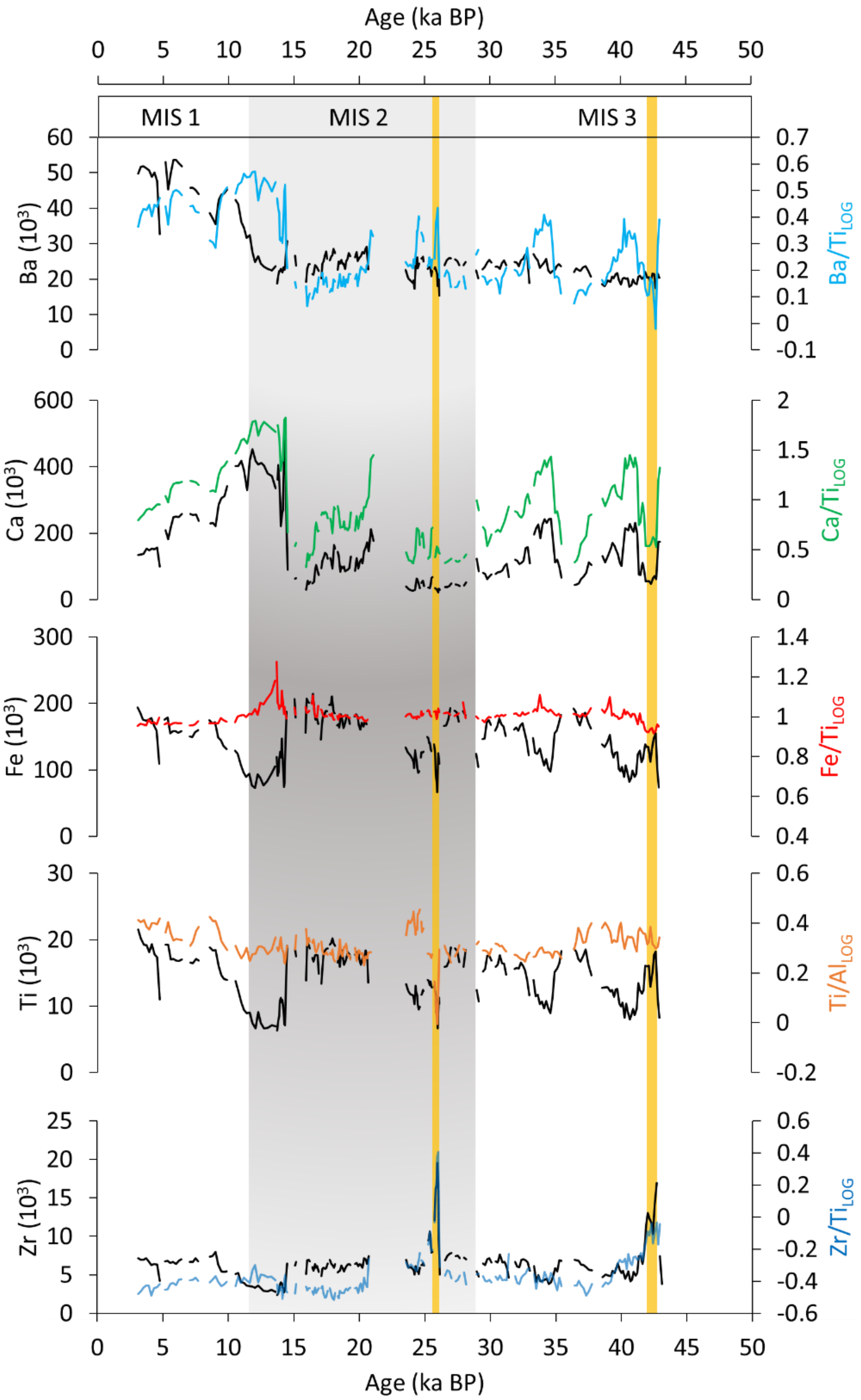

**Fig. 6.13:** Elemental intensities of selected major elements in total counts ($10^3$) at ODP 887A, plotted against the age model of McDonald et al. (1999). The IRD mass accumulation rates of St. John and Krissek (1999) are also shown. Yellow bars mark tephra layers.

## 6.6: Discussion: Extraction of palaeoenvironmental signals from XRF data in the N Pacific

Section 6.5 demonstrates the existence of downcore and inter-site variation in the XRF signal across the N Pacific. The major signals interpreted from the XRF data in this section which are significant for developing greater understanding of regional stratigraphy here and in future studies are tephra layers, biological productivity maxima and minima, and terrestrial sediment flux maxima and minima. Each of these signals will be treated in turn in this section.

### *6.6.1: Ba/Ti and Ca/Ti as indicators of biological productivity*

As previously stated in Section 6.4.1, Ca and Ba can be used as proxies for biological productivity. The XRF log ratios of Ca/Ti and Ba/Ti exhibit common maxima and minima across several sites which may serve as regional stratigraphic tie points and may reveal or reinforce information about N Pacific productivity relative to flux from terrigenous sources during the Late Quaternary.

At ODP 1207A, the Ba/Ti generally exhibits peaks during warm periods, especially MIS 5e, MIS 3, and during deglaciation following the LGM (Fig. 6.4). This pattern suggests enhanced productivity during warm periods. Conversely, low Ba/Ti occurs during MIS 6, MIS 5a and into MIS 4, and during MIS 2 prior to deglaciation when productivity was weaker. A Ba/Ti minima occurs at the depth of the Aso-4 tephra, due to dilution of biogenic signals as a result of rapid deposition of ash shards. In contrast, Ca/Ti does not show as pronounced changes as Ba/Ti, with no clear minima or maxima, with the exception of the dilution effect within the Aso-4 tephra. These findings suggest that Ba/Ti is more sensitive to productivity changes than Ca/Ti at ODP 1207A, possibly because it responds to both calcareous and noncalcareous biogenic debris flux, whereas Ca primarily reflects the deposition of calcareous organisms.

Figure 6.14 displays Ca/Ti and Ba/Ti for ODP 1207A, ODP 883B, ODP 887A, ODP 881B and ODP 1179A between 50 and 5 ka BP. All dated cores (1207A, 883B, 887A) exhibit a strong deglacial increase in log ratios which corresponds to the onset of the Bølling Allerød warming (Grey et al., 2018), although the increase at ODP 1207A occurs earlier than at the other sites.

At site 883 this increase is associated with proliferation of planktic foraminifera, likely associated with increased productivity (Hughes, 2004). The increase in Ba/Ti at sites 887, 883, 1179 and 881, which occurs simultaneously with the increase in Ca/Ti suggests that this peak is a signal of biological activity. An increase in measured $CaCO_3$ at Site 887 at the MIS 2-1 transition (McDonald, 1997), reflected in the peak in Ca (Fig. 6.13), may also signify an increase in surface productivity associated with glacial termination 1. Furthermore, there is convincing evidence for enhanced nutrient-rich upwelling in the subarctic N Pacific during the Bølling Allerød warming (14.7 ka BP-12.9 ka BP), which contributed to the productivity peak during this period (Gray et al., 2018).

Abrupt increases in Ca/Ti and Ba/Ti also occur at ODP 1179A and ODP 881B, and the depth and shape of this increase corresponds well with the deglacial increases at the dated sites. The “deglacial” signals at ODP 1179A and ODP 881B provide a possible marker which can be used to build a chronostratigraphic framework at these undated sites. ODP 881B exhibits a reduction in Ca/Ti, which corresponds with the timing of the Younger Dryas (assuming that the Ca/Ti peak here represents a deglacial productivity increase), although this possible Younger Dryas signal is not apparent at the other sites.

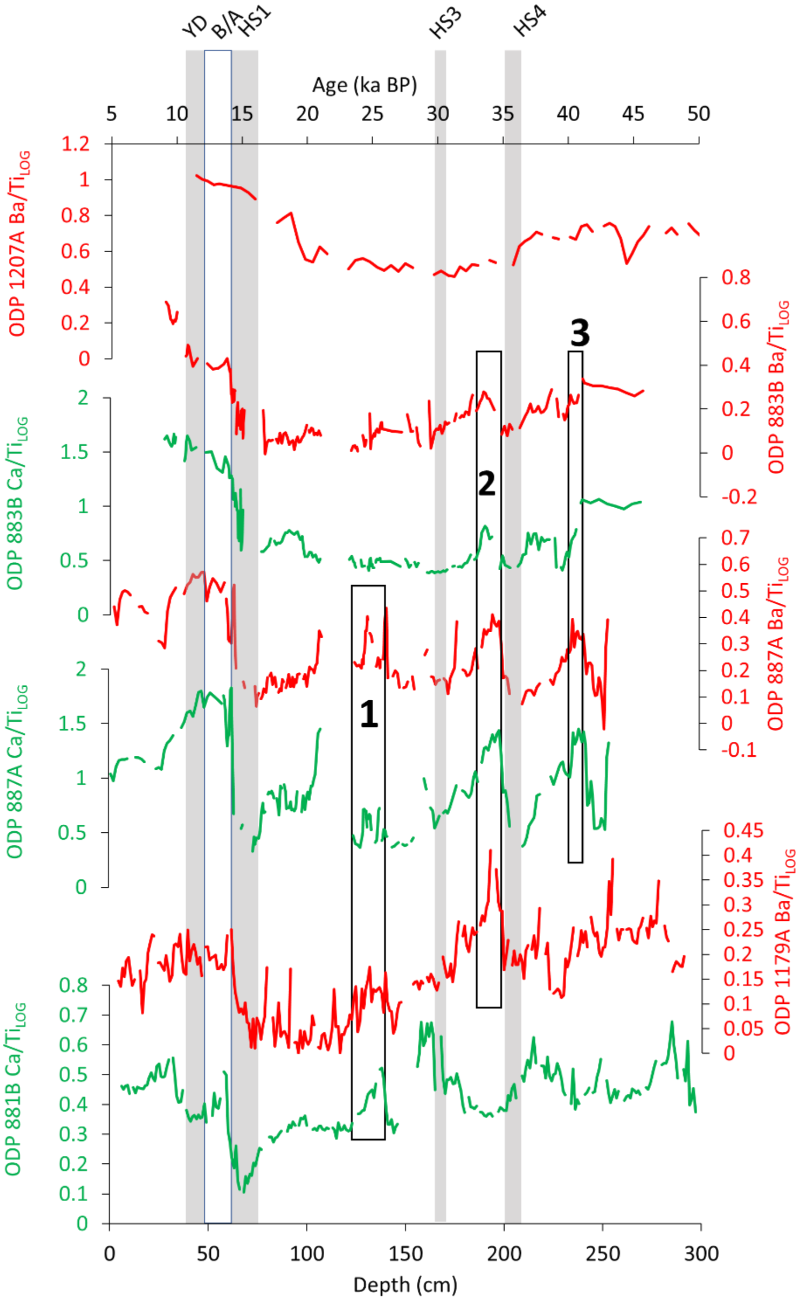

**Figure 6.14:** Ca/Ti and Ba/Ti log ratios between 5 and 50 ka BP at ODP 1207A (Ba/Ti only), ODP 883B and ODP 887A, and between 0 and 300cm at ODP 1179A (Ba/Ti only) and ODP 881B (Ca/Ti only). Boxes labelled 1, 2 and 3 mark possible corresponding inter-core peaks which may be used for stratigraphic correlation. Grey boxes labelled HS3 and HS4 mark the age and possible signals of Heinrich Stadials 3 and 4, respectively. Dates for HS3 and HS4 taken from Sánchez Gońi and Harrison, (2010). Also marked are ages and possible signals of Heinrich Stadial 1 (HS1), the Bølling Allerød warming (BA), and Younger Dryas (YD). Dates of these events are taken from Grey et al., (2018). The depth scale on the bottom axis refers only to ODP 881B and ODP 1179A.

Further downcore, minima in log ratios of Ca/Ti and Ba/Ti correspond with Heinrich Stadial 4 (HS4) at ODP 883B, ODP 887A and ODP 1179A. A slight reduction in Ba/Ti occurs at ODP 1207A during HS4. A corresponding minimum at ODP 881B is not apparent. However, all sites except ODP 1207A exhibit minima during HS1. A productivity minimum is expected during HS4 and HS1 at ODP 887A, as Maier et al., (2018) demonstrate that freshwater injections from the Cordilleran Ice Sheet are believed to have caused surface freshening and cooling, and subsurface warming of the NE Pacific. The hosing experiments carried out by the researchers also demonstrate how these conditions also occur, albeit less intensely, in the subarctic NW Pacific when freshwater is injected into both the N Atlantic and NE Pacific. The extent to which the drop in Ba/Ti and Ca/Ti in the NW Pacific is related to NE Pacific cooling and freshening should be explored through further experiments.

The HS1 minima can be interpreted as a basin-wide productivity minimum due to enhanced stratification between the North Pacific Intermediate Water (NPIW) and North Pacific Deep Water (NPDW) during HS1 (Gong et al., 2019). An additional, although less pronounced, minimum in Ca/Ti and Ba/Ti corresponds with Heinrich Stadial 3 (HS3) at ODP 887A. This minimum is most pronounced in Ca/Ti. The HS3 signal may be present in Ca/Ti at ODP 883B, but is not apparent in Ba/Ti at this site. HS3 minima do not appear to occur at ODP 881B and ODP 1179A. The less apparent signal during HS3 is also in agreement with Maier et al., (2018), who do not find evidence for cooling and freshening of the N Pacific during HS3.

Boxes 1, 2 and 3 in Fig. 6.14 represent maxima in Ca/Ti and Ba/Ti which display good inter-site correspondence. The abrupt ratio increases and subsequent gradual decreases, particularly in Box 3 ODP 887A, Box 2 at ODP 887A and ODP 1179A, and Box 1 at ODP 881B mimic the characteristics of Dansgaard-Oeschger events (Boers, 2018).

The other sites for which XRF data was obtained (DSDP 580, ODP 884A, DSDP 433 and ODP 886A) do not exhibit signals in Ca/Ti and Ba/Ti which appear to be present in the stratigraphy of the sites discussed above (see Figs. 6.5, 6.7, 6.11 and 6.12). There is a noticeable increase in Ba and Ba/Ti at DSDP 580 during MIS 1, however, there is no concurrent peak in Ca or Ca/Ti. While increases in Ba and Ba/Ti may represent enhanced productivity during MIS 1, the absence of a clear deglacial rise in Ca and Ca/Ti can largely be explained by the great depth of DSDP 580 resulting in high carbonate dissolution. Furthermore, the two deglacial peaks in Ca and Ca/Ti are strongly associated with the two tephra layers marked in Fig. 6.5.

ODP 884A exhibits several fluctuations in Ca/Ti and Ba/Ti, which do not show discernible patterns which could suggest productivity changes. Ca/Ti in particular appears to be more influenced by volcanic ash, notably in the ash layers around 32 ka BP and 23 ka BP, which also exhibit peaks in Zr/Ti, suggesting the deposition of high Ca ash (Fig. 6.7; see Section 6.6.3 for further discussion of the XRF signal of tephra layers).

At DSDP 433, where calcareous ooze is the major lithology (Jackson et al., 1980), a productivity signal may be present in counts of Ca and Ba, and their associated ratios/Ti (Fig. 6.11), but due to the absence of an age model and possible coring disturbances during core acquisition, it is not possible to align any peaks or troughs in Ca and Ba with wider environmental signals such as MIS boundaries. However, multiple peaks and troughs are visible, which appear to have an inverse relationship with the occurrence of dropstones (Figs. 6.10 and 6.11), which could suggest that periods of higher Ca and Ba are related to enhanced productivity. The concurrent peaks in Ca and Ba, and troughs in Zr, Fe, and Ti in addition to the lower occurrence of dropstones may indicate warm interstadial or interglacial periods and reduced ice-rafting from NE Siberia.

The wide data gaps in ODP 886A make identification of possible productivity signals difficult (Fig. 6.12). However, there are multiple apparent peaks in Ba/Ti and Ca/Ti, notably at ~270cm, (Ba/Ti), 250 and 228cm (Ca/Ti), 223, 200 and 159cm (Ba/Ti), 110cm (Ca/Ti), 103cm (Ba/Ti) and 60cm (Ba/Ti and Ca/Ti). While these peaks may represent productivity maxima, they cannot be reliably correlated with peaks at other sites because the low resolution age model and diatom assemblages within the upper 300cm suggest that these sediments are a mix of mid-Pleistocene and late Pleistocene material (see Section 6.5.7 for further description).

### ***6.6.2: Terrestrial flux in XRF signals: the last glacial cycle at ODP 1207A***

Terrigenous sediment flux to the N Pacific appears to vary considerably between sites, with numerous fluctuations throughout the Late Quaternary. The longer term record at ODP 1207A spanning the last glacial cycle and the penultimate glacial period (MIS 6) exhibits a cyclical terrigenous sediment signal, with enhanced terrigenous flux during MIS 6, as shown by high Fe/Ti and Ti/Al, particularly around 165 ka BP. The absence of IRD during the earlier part of MIS 6 (see Chapter 4 and Fig. 6.4) suggests that the terrigenous XRF signal here reflects enhanced aeolian dust flux, as observed at other mid-latitude NW Pacific sites during this period (Hovan et al., 1991).

As discussed in Chapter 4, for most of the Late Quaternary, site 1207 is largely uninfluenced by glacially derived sediments, as IRD, although present, is rare and occurs in low concentrations (Fig. 6.4; Chapter 4). Consequently, it is reasonable to assume that the terrigenous fraction here is aeolian in origin. N Pacific aeolian dust deposited at distal sites is present in the clay-silt size fractions of <20µm (Leinen et al., 1994). However, no direct analysis of the <150µm size fraction was carried out in this study, therefore the XRF signal is the only new method used here which can detect the dust component. The visible change in Fe and Fe/Ti at the MIS 6-5e boundary, coeval with a distinct positive excursion in Ba and Ba/Ti and an abrupt decrease in *N. pachyderma* (see Chapter 4), suggests that the changes in terrigenous element intensities and log ratios during MIS 6-5e are climatically driven changes in dust flux, with influence from climatically driven productivity changes associated with a northward shift of the Subarctic Front (see Chapter 4). Furthermore, Fe, Fe/Ti and Ti are enhanced during MIS 2, and Ba/Ti is suppressed until deglaciation. Therefore, it may be assumed that these signals are glacial dust signals.

The predominant source of dust to the Shatsky Rise, and by extension Site 1207, during the Late Quaternary was the Chinese loess plateau, as shown by the mineralogy of the fine-grained fraction at site V21-146 (Hovan et al., 1991; Fig. 6.2 for location). Both the Chinese loess plateau and the Shatsky Rise are situated under the pathway of the Asian/N Pacific westerlies (Serno et al., 2014), and modelled LGM 850hPa winds over the N Pacific show that conditions over E Asia were conducive to enhanced transport of dust to the Shatsky Rise region in glacial conditions (Wang et al., 2018), as confirmed by the enhanced Fe in ODP 1207A and V21-146 during cold phases of the Late Quaternary (Fig. 6.4). Several geochemical provenance studies highlight East Asia as the dominant Quaternary source of dust found across the entire N Pacific basin (Hovan et al., 1991; Pettke et al., 2000; Nagashima et al., 2011; Serno et al., 2014). Furthermore, the observed (Serno et al., 2014) and modelled (Wang et al., 2018) dominant LGM storm tracks support the mass transport of fine-grained material from east Asian sources across much of the N. Pacific.

At DSDP 433 on the Emperor Seamounts (Fig. 6.2), a distinctive XRF signal with clear cycles of high terrigenous element intensities alternating with periods of high biogenic element intensities suggests glacial-interglacial or stadial-interstadial cycles. No age model exists for the upper 300cm at this site, therefore it is not possible to attempt a chronostratigraphy based on these signals, which do not clearly correspond with those shown in Fig 6.14, for example.

The prolonged period of low Fe, Ti and Zr counts and absence of dropstones between ~260 and 300cm at DSDP 433 may indicate an interstadial or even possibly an interglacial period such as MIS 5e. The low terrigenous sedimentation during this period may reflect reduced regional ice cover and an absence of ice rafting. The fluctuations in element intensities at site 433 may therefore be useful chronostratigraphic markers that could be used in future studies, alongside other dating methods including biostratigraphy and IRD analysis, to establish a time series and climate record at this location.

Significant variations in biogenic signals are present at different sites across the N Pacific, even during the same time periods and when located in relatively close proximity (e.g. ODP 883B and ODP 884A; Figs. 6.2, 6.6 and 6.7). The disparity between these two closely situated sites can be partially explained by the local depositional environment, largely controlled by the water depth at the drill site (Table 6.1). Sites 883, 1207, 433 and 887 are relatively shallow sites (<3700mbsf). Due to these sites being above the carbonate compensation depth (CCD) (Chen et al., 1988), a major lithology at these sites is calcareous ooze, resulting in higher intensities of Ca than at the deeper north Pacific sites. At other sites, changes in Ca are less visible. ODP 884A does not show a visible deglacial/termination1 peak in Ca, Ba or their corresponding log ratios, despite being <45km to the NE of site 883. This disparity is likely to be due to the greater depth of site 884 (Table 6.1) resulting in greater carbonate dissolution.

### *6.6.3: Terrigenous flux in XRF signals: Subarctic N Pacific*

Volcanic material from explosive eruptions evidently comprises a major portion of the subarctic and mid-latitude N Pacific lithology in the form of volcanic ash from the nearby Kamchatka-Kurile, Japanese, Aleutian-Alaskan arcs from direct eruption airfall events (e.g. Gorbarenko et al., 2002), from wind-blown transport of fine-grained volcanic ash deposits (e.g. Bailey, 1993) and ice-rafted ash (Bigg et al., 2008). However, other important terrestrial sources to these subarctic sites include riverine and hemipelagic sediments (Jones, 2000; VanLaningham et al., 2009), and as previously discussed aeolian sediment also contributes a substantial percentage of the lithogenic fraction in the N. Pacific. Serno et al. (2014) measured aeolian dust proxies $^{4}$He, $^{232}$Th and a range of rare earth elements in subarctic Pacific core tops and found that the lithogenic fraction in the open ocean of the NW Pacific (e.g. the Shatsky Rise) consists of 80-100% aeolian dust (and thus supporting the argument that the MIS 6 and MIS 2 peaks at ODP 1207A are aeolian in origin). However, close to the margins in the subarctic NW and NE Pacific, the aeolian contribution declines to <50%. This percentage may have been higher during glacial periods.

The contribution of aeolian dust to the terrigenous XRF signal was examined by visually comparing the dust proxy terrestrial Helium-4 ($^{4}He_{terr}$) from a location close to sites 883/884, site SO202-7-6 in the NW Pacific (51.3ºN, 167.7ºE, 2345 mbsf; data from Serno et al., 2015) against Fe, Ti, Zr and log ratios of Fe/Ti, Ti/Al and Zr/Ti at ODP 883B for the period 28-0 ka BP (Fig. 6.15). Additionally, the log ratio of Ca/Ti and Ba/Ti was analysed to examine the relative contribution of dust and biological productivity.

The Fe and Ti signals show some similarities with the dust signal at SO202-7-6, particularly in the abrupt change at the onset of the Bølling Allerød warming (Fig. 6.15). Zr also decreases during this warming event, but Zr/Ti increases due to a larger decrease in Ti than

Zr. However, the increase in $^{4}He_{terr}$ during the Younger Dryas at SO202-7-6 is not present in the Fe and Ti intensities at site 883 or in the log ratios. There is however, a decrease in Ba during this cold phase. Consequently, the Fe and Ti signals may have been influenced to some extent by aeolian dust flux, but other factors, such as flux from other sources of terrigenous sediment and biological productivity, may control the terrigenous XRF signal to a greater degree at site 883. The Ca/Ti log ratio is in good agreement with Ca counts and appears to show that the Bølling Allerød increase in Ca is a genuine climate-related productivity signal.

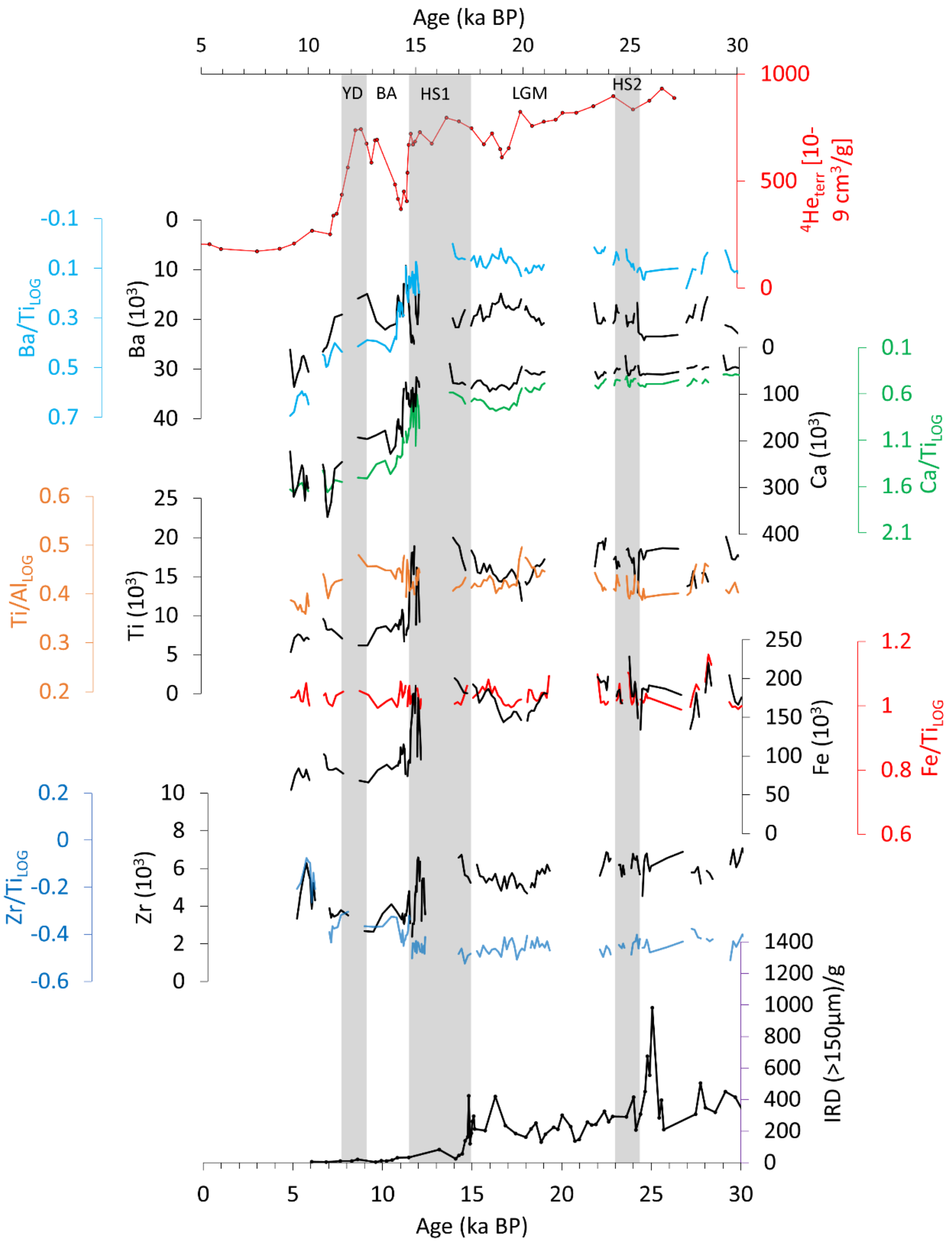

**Figure 6.15:** Comparison of $^4$He$_{terr}$ at SO202-7-6 against log ratios of Ca/Ti, Ba/Ti, Ti/Al, Fe/Ti, Zr/Ti, and counts of Ba, Ca, Fe, Ti and Zr at ODP 883B, and IRD/g at ODP 883D (the latter from Bigg et al., 2008). Heinrich stadials 2 and 1 and the Younger Dryas are marked by the shaded grey boxes and the Bølling Allerød warm period is marked by the clear box. SO202-7-6 data is from Serno et al. (2015) and taken from Pangaea.de. Note: Some axes are reversed.

### *6.6.4: Tephra in the XRF signal*

An examination of the terrestrial XRF signal at other N Pacific sites reveals significant inter-site variation. One major factor influencing downcore changes in Fe, Ti, and Zr and the log ratios of these elements with Ti (Al in the case of Ti) is the presence of discrete tephra layers which dominate the XRF signal at multiple sites. The prominence of volcanic eruptive material makes disentangling this lithology from the non-volcanic terrigenous signal difficult. At sites 580 and 884, for instance, the tephra layers dominate the terrigenous signal (Figs. 6.5 and 6.7). Here, associations with MIS and other climatic stages are not possible within the scope of this study.

Prominent spikes in Zr and Zr/Ti occur in several visible N Pacific tephra layers (see Table 6.11 for a summary). Notably, these peaks occur in correspondence with the Aso-4 tephra in ODP 1207A, Gorely at ODP 883B (although less prominent in the Gorely tephra at ODP 884A). Spikes in Zr and Zr/Ti are also present at all four prominent tephra layers at DSDP 580. A major Zr and Zr/Ti peak occurs at the ~14 ka BP ash layer at ODP 884A, while the peaks for the ~23 ka BP and 32 ka BP tephras are present but subdued. At ODP 881B, Zr and Zr/Ti are elevated within the tephra layer at 215cm. In the NE Pacific at ODP 887A, Zr and Zr/Ti spikes occur within the visible tephra layers ~42 ka BP and ~26 ka BP.

Across the N Pacific, tephras with high Zr and Zr/Ti are not consistently accompanied by spikes in other terrigenous elements. Therefore, Zr may be a more reliable indicator of the presence of discrete tephra layers than Fe and Ti, although abrupt troughs in these elements may, as in the case of DSDP 580, indicate the presence of a tephra layer. Additionally, some tephra layers, notably the TO-H tephra at DSDP 580 (see Chapter 5) and the tephra ~204cm in ODP 1179A are characterised by high Ca and Ca/Ti. High Ca counts within tephra layers have been found to indicate the presence of Calcium oxide (CaO) in rhyolitic tephras (Peti et al., 2019). A clear peak in Ca and Ca/Ti, accompanied by peaks in Zr and Zr/Ti, also occurs ~93cm in ODP 1179A, again pointing to the presence of a rhyolitic calc-alkaline tephra.

While XRF intensities are semi-quantitative, variations in counts of Ca and other terrigenous elements (including K and Si, e.g. Peti et al., 2019), may provide a framework for comparing XRF data from N Pacific tephra layers with quantitative chemical analysis of tephra, which may, similar to the log ratio calibrations of Weltje and Tjallingii (2008) be used to calibrate XRF data from tephra layers with quantitative chemical data.

### *6.6.5: Limitations of XRF data and scope for future research*

While XRF scanning is rapid, non-destructive and has been shown to correlate well with element concentrations, especially when transformed to log ratios, there are factors which limit the ability of XRF scanner data to reveal true environmental signals. Some of these factors are due to the complex depositional environment of the N Pacific and the absence of age models at some sites which make interpretation problematic, while other factors relate to limitations inherent to the XRF method.

An important limitation in this study of XRF core scanner data is that due to resource constraints, it was not possible to compare the raw element counts and log ratio data with chemical analysis of discrete samples. Consequently it is not possible to conclude the extent to which matrix effects influenced the element data. Although the transformation of raw element counts to log ratios is known to improve the correlation with quantitative chemical composition data, a relative matrix effect still remains (Weltje and Tjallingii, 2008), and the extent to which matrix effects influence the XRF data in N Pacific cores currently remains undetermined. Despite the lack of information on matrix effects, visual comparison of key log ratios against raw element counts, in particular Ca/Ti and Ba/Ti reveals strong similarities at some sites (Fig. 6.14), suggesting that at these sites, matrix effects do not substantially affect differences between raw elements and log ratios in the palaeoproductivity signal. However, obvious deviations between Fe and Fe/Ti, and Ti and Ti/Al are clearly visible at most sites (Figs. 6.4-6.13). Here, matrix effects may be important in the element intensities produced. Further quantification and calibration against quantitative element concentration data is required to further examine terrigenous element change.

A further issue relates to potential problems arising from XRF scanning of sediment cores which have been held in storage for several decades (ODP 1207A was drilled in 2001, while DSDP 433 was drilled in 1977). Consequently, deterioration of the split core has occurred in all nine cores. The resultant data gaps, which are present in all nine cores, are in some cores not only numerous, but are, in the case of ODP 886A up to 27cm deep. These gaps complicate the interpretation of the XRF signal, by disrupting any recognisable millennial – or shorter timescale - environmental signals which may correspond with other proxies such as benthic $\delta^{18}O$, which could be used to begin constructing a stratigraphic framework in cores with no Late Quaternary age model.

Other issues which are known to influence XRF intensity data arise from changing sediment properties. Porosity (related to grain size and lithology) and water content are known to interfere with environmental signals in XRF data (Bönning et al., 2007; Löwermark et al., 2011; Hennekam and de Lange, 2012). However, not enough data on these properties are available for the nine N Pacific cores analysed in this chapter, therefore the effects of these sediment properties for now, remains unknown. However, it may be assumed that water content on the surface of split cores which have been in cold storage for at least twenty years is much lower, and therefore much less of a technical problem than cores which have been freshly drilled.

The further limitation of this XRF study is that it is not possible to compare the element intensities to data related to the origins of terrigenous material within sediment cores, such as Uranium series dating of IRD grains and discrete quantitative chemical analyses at depths of interest. As alluded to in Chapters 4 and 5, and reinforced in the next chapter, it is likely that there was more than one East Siberian source region feeding icebergs into the NW Pacific, which could be reflected in the chemical composition of IRD. The lack of information regarding chemical composition limits the conclusions drawn from the XRF data to more general statements about likely climatic signatures (such as MIS transitions) and when peaks in terrigenous elements relate to enhanced aeolian flux during glacial periods (only convincing in the case of ODP 1207A). The study by Monien et al., (2010) combines quantitative chemical analysis with principal component analysis of lithological facies and corresponding intensities of Fe, Ti and K in the Southern Ocean to identify regional IRD source terranes.

It is highly desirable to apply a technique similar to Monien et al. to Late Quaternary sections of N Pacific cores. While it may not be possible to group the last glacial cycle into discrete facies due to the N Pacific cores being predominantly pelagic, hence terrigenous components are relatively minor (Monien et al. analysed primarily glaciomarine lithologies on the continental shelf, which span a much longer period), it may be possible to reveal distinct terrigenous source signals through a combination of principal component analysis to identify groupings of element signals, and quantitative chemical analysis. If combined with a geological dating technique, e.g. Nd/Sr isotope analysis of IRD grains (e.g. North, 2015), an opportunity is presented for creating a tool for calibrating N Pacific semi-quantitative XRF data with chemical data which reveals information about IRD sources and other terrigenous sources. This would require substantial resources and would also depend on sufficient proximal geological data from the highly complex Kamchatka-Koryak, Kolyma regions and surrounding terranes to geologically “fingerprint” terrigenous populations in the N Pacific.

## 6.7. Conclusion

There exists a wealth of palaeodata within the XRF core scanner results presented in this Chapter. Table 6.11 summarises the key elements and element log ratios from which environmental signals have been extracted, and provides a description of the interpreted environmental signals.

This chapter presents one approach to deciphering Late Quaternary climate signals from the complex lithologies of the region, with some success in inter-core correlation at some sites (particularly during deglacial productivity spikes: Fig. 6.14 and 6.15) and identification of tephra layers. The first finding is significant as it provides tentative chronostratigraphic tie points for ODP 881B and 1179A (Fig. 6.14). The second finding related to tephra is significant, as it demonstrates the reliability of Zr as an indicator for the presence of tephra, although this chapter does not explore whether Zr was able to record cryptotephra. Further examination of the Zr signal coupled with tephra counts on discrete samples, and possibly a higher spatial scanning resolution may be required for very thin tephra layers (McCanta et al., 2015).

| **Environmental signal** | **XRF Indicators** | **Sites** | **Interpretation/tephra layer** |
|---|---|---|---|
| Enhanced biogenic carbonate production | High Ca; high Ca/Ti | ODP 883B, ODP 887A, ODP 881B | Interstadial and deglacial enhanced productivity and reduced terrigenous flux. |
| Calc-alkaline rhyolitic tephra layers | High Ca accompanied by high Ca/Ti, Zr, Zr/Ti, low Fe, low Ti | DSDP 580, ODP 881B, ODP 884A, ODP 1179A | TO-H tephra (~13 ka BP) and mixed ash (~11 ka BP) at DSDP 580; Tephras ~31 and 23 ka BP at ODP 884A; tephra 215cm at ODP 881B; tephra 205cm at ODP 1179A; |
| Tephra layers | High Zr (may or may not be accompanied by high Fe and/or Ti) | ODP 1207A, ODP 883B, ODP 887A | Aso-4 tephra (~87 ka BP), ODP 1207A; Gorely tephra (~39 ka BP), ODP 883B; unidentified tephras (~43 ka BP and ~26 ka BP), ODP 887A |
| Enhanced primary productivity | High Ba; high Ba/Ti | ODP 1207A, ODP 883B, ODP 887A, ODP 881B, ODP 1179A | Interglacial (MIS 5e at ODP 1207A), and interstadial peaks in primary productivity, and deglacial peaks in productivity. |
| Aeolian dust flux | High Fe, high Ti; high Fe/Ti and high Zr during glacial stages accompanied by low Ba and Ba/Ti | ODP 1207A | Enhanced aeolian dust flux from E Asia during MIS 6 and MIS 2. |

**Table 6.11:** Summary of key element intensities and log ratios in N Pacific sediment cores and descriptions of the environmental signals interpreted from the study of their occurrence patterns.

There remains extensive potential to develop this data beyond that presented here, especially if combined with additional palaeoenvironmental analyses. Chapter 7 lays a foundation for investigations into the provenance of N Pacific IRD through ocean-iceberg model experiments, which permits the generation of hypotheses related to inter-site variations in the expected origins of Late Quaternary icebergs, and by presenting data alluding to likely source regions of icebergs may prove valuable in the continued effort to reconstruct Late Quaternary ice cover in the NW Pacific.

# Chapter 7: Modelling Late Quaternary iceberg flux from the N Pacific rim

## 7.1: Sources of NW Pacific IRD: current knowledge

As discussed in previous chapters, there are multiple possible sources of NW Pacific Late Quaternary IRD on the NE Siberian coast. Glacial ice is known to have reached the present-day coastline in several locations, and in many instances evidently extended well beyond the coastline (e.g. Bigg et al., 2008; Barr and Clark, 2012a). The iceberg flux throughout the Late Quaternary is known to be substantial, as evidenced by the widespread IRD in the NW Pacific (see the previous chapters of this Thesis), and some initial mineralogical identification of grains has been carried out (e.g. Conolly and Ewing, 1970; St. John and Krissek, 1999; Hughes, 2004), which confirms the Kamchatka/Koryak region as the main source of IRD to the NW Pacific. More detailed provenance work has taken place on IRD in the Sea of Okhotsk (Nürnberg et al., 2011; Wang et al., 2017), showing that western (W) Kamchatka is the dominant source of IRD here. However, the limited nature of geological provenance studies in the open NW Pacific leaves a gap in our understanding of more localised IRD sources which may explain variable IRD supply at the deep sea sites investigated earlier in this Thesis. This chapter investigates the most likely sources of Late Quaternary icebergs in the NW Pacific through intermediate complexity coupled ocean iceberg modelling. The model results are compared against existing NW Pacific IRD data and XRF data from Chapter 6. The identification of the major IRD sources and the variable flux of sources to each site has important implications for understanding the dynamics of glacial ice in NE Siberia during the Late Quaternary.

## 7.2. Methods

### 7.2.1: Iceberg modelling

We investigate the range of likely iceberg sources for IRD in the NW Pacific using the Fine Resolution Greenland and Labrador Sea (FRUGAL) intermediate complexity coupled climate-ocean-iceberg model (Levine and Bigg, 2008). The nine cores analysed in Chapter 6 are used as reference points to discuss the spatial variations in iceberg flux in the N Pacific (Fig. 7.1). While the results of runs are presented and discussed for both the NW and NE Pacific, the emphasis of this chapter is mostly on the NW Pacific, as this region is more relevant to discussions of glacial change in NE Siberia. As new IRD records have been developed for sites 1207 and 580 in Chapters 4 and 5, some of the discussion will focus on simulated iceberg flux to these sites.

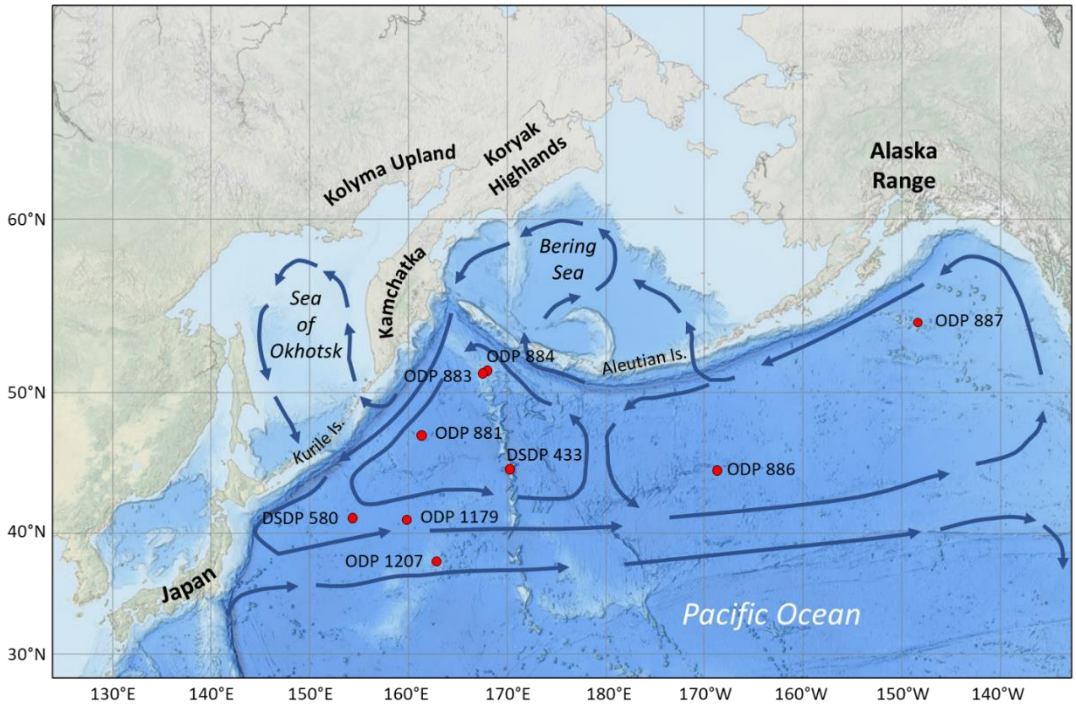

**Figure 7.1:** The North Pacific and surrounding landmasses, with key core locations discussed in Chapters 4, 5, and 6. These sites are plotted on the model output maps later in this chapter. Approximate LGM ocean surface currents are marked by blue arrows.

### *7.2.2: Model Specifications and Methodology*

The FRUGAL (Fine ResolUtion Greenland And Labrador) intermediate complexity global climate model includes coupling between ocean, radiative-advective atmospheric and advective-thermodynamic iceberg trajectory and sea-ice models (Levine and Bigg, 2008). FRUGAL has been used for a range of palaeoclimate studies, including for the last glacial period (Fedorov et al., 2011; Bigg et al., 2012), the penultimate glaciation (Green et al., 2010) and the Early Pleistocene (Rea et al., 2018). It uses a curvilinear grid with the North Pole displaced to Greenland, giving an enhanced resolution in the Arctic and North Atlantic (Wadley and Bigg, 2000). This study uses a fine resolution grid of 182 x 211 cells, which is equivalent to approximately 2° longitude by 1.5° latitude in the Southern Hemisphere, but with a resolution of 20 km around the Greenland coast. The sea-ice model configuration are given in detail in a similar resolution, but present day, study (Wilton et al., 2015) and consist of a thermodynamic model with simple advection. The atmospheric part of FRUGAL is a simple radiative-advective atmosphere, which is an adaptation of the energy and moisture balance model of the UViC Earth Systems Model (Fanning and Weaver, 1996) that allows for advection of water vapour. The atmospheric model uses a monthly varying glacial wind stress, which has no feedback from the sea surface temperature (SST) field (Levine and Bigg, 2008). The basic topography and bathymetry of the model has been previously described (Levine and Bigg, 2008), but here the finer resolution of the model grid is also taken into account in the shaping of local bathymetry for important global passages, shallow seas and the Kurile and Aleutian island chains in the North Pacific. The iceberg module has a range of both dynamic and thermodynamic components (Levine and Bigg, 2008), although in this study there is no feedback between the iceberg model and the rest of the FRUGAL system as interest focuses on the iceberg trajectories only. Icebergs may roll over (Wagner et al., 2017) and grounded icebergs are allowed to melt instantaneously (Levine and Bigg, 2008). Model icebergs are divided into ten different size classes (Levine and Bigg, 2008) ranging from 0.491 to 492 x $10^9$ kg in mass, based on observations of present day Arctic and Southern Ocean icebergs, excluding giant icebergs. Each model berg is assigned a scale factor appropriate to that size of berg from its specific seed site. Icebergs were seeded at locations where geomorphic evidence suggests that glaciers reached the coast during the Late Quaternary, including on the Koryak coast, the north-east Kamchatka coast, central-east Kamchatka, south-east Kamchatka, the south-west Kamchatka coast, the northern coast of the Sea of Okhotsk (Barr and Clark, 2012) and the main Kurile islands (Gorshkov, 1970), between Japan and Kamchatka (Fig. 7.2). For two of the simulations (Section 7.3.1), icebergs were also seeded on the Alaskan coast, as was done in the simulations of Levine and Bigg (2008), to observe the distribution of bergs in the NE Pacific.

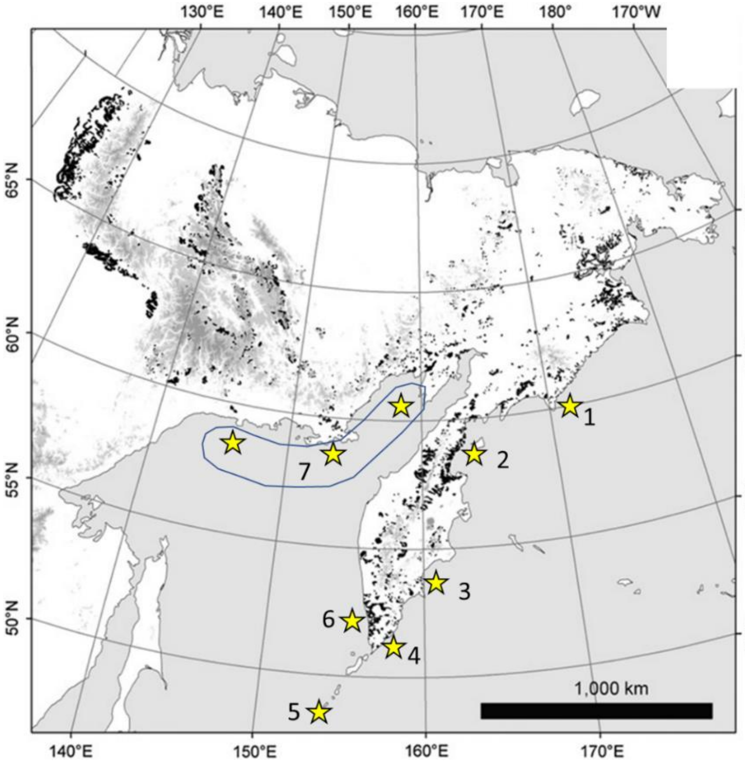

**Figure 7.2:** NE Siberia, showing Quaternary moraines in black (moraine map from Barr and Clark, 2012a, with stars and labels added for this Thesis). Yellow stars show the approximate locations of iceberg seed points for the FRUGAL simulations. 1: Southern Koryak Highlands. 2: NE Kamchatka. 3: Central-East Kamchatka. 4: SE Kamchatka. 5: Kurile Islands. 6: SW Kamchatka. 7: Northern Sea of Okhotsk coast (includes three stars inside the circled area).

In the base simulation, the number of icebergs seeded at each location is proportional to the width of the palaeo-ice stream termini (Appendix 6). Ice stream terminus widths were estimated by measuring geomorphological features on Google Earth which were identified by Barr and Clark, (2012) to be coastal end moraines. The terminus discharge sizes were then taken from Bigg et al., (2012) based on similar sized terminus widths on the British-Irish ice sheet. This simulation shows the maximal possible extent of iceberg distribution, whereas real-world iceberg calving would not occur simultaneously across the region at continuous maximum discharge. Note that as little is known about glaciation on the Kuriles, small, valley glacier-size fluxes were given to the Kurile seed points. Summing the mass of each berg, multiplied by its scale factor, gives the average ice discharge per quarter year expected from that seed site (Appendix 6).

## 7.3: Results

### *7.3.1: Maximal and "normal" flux from all possible iceberg sources*

An 1100 year spin-up simulation was run, using orbital parameter and atmospheric $CO_2$ levels from 21 kyr BP (as in previous glacial runs (Levine and Bigg, 2008; Bigg et al., 2012; Bigg, 2020)). By the end of this simulation, all large-scale ocean and atmospheric fields had reached an essential state of equilibrium.

To investigate these possible iceberg trajectories several decadal-long experiments were then carried out where icebergs were seeded quarterly around the North Pacific and their lifetimes followed. The two simulations shown here are: i) maximal discharges from all seed points; and ii) discharges restricted to just the five smallest size classes of icebergs (Levine and Bigg, 2008). The iceberg density fields for experiments i) – a maximal flux scenario – and ii) – a "normal" flux scenario – are shown in Fig. 7.3.

There is a significantly wider distribution of icebergs in the maximal than in the minimum flux simulation, with icebergs in the former simulation reaching south of 30ºN in both the NW and NE

Pacific. Icebergs reach all sites except ODP 886 in both simulations. In the maximal simulation i), the main modelled iceberg alley in the NW Pacific appears to originate on the E Kamchatkan and possibly SW Kamchatkan coast. Sites 881, 1179, 1207 and 433 are all within this zone. Sites 883, 884 and 580 are outside of this zone, but icebergs still reach these three sites less frequently.

In the more typical situation of simulation ii) relatively few icebergs reach the vicinity of 1207, 1179 and 433, consistent with the episodic nature of IRD presence at site 1207. The flux to sites 883, 884 and 580 is similar to the maximal simulation. The modelled iceberg flux to the NW Pacific is compared to the observed IRD record later in this chapter.

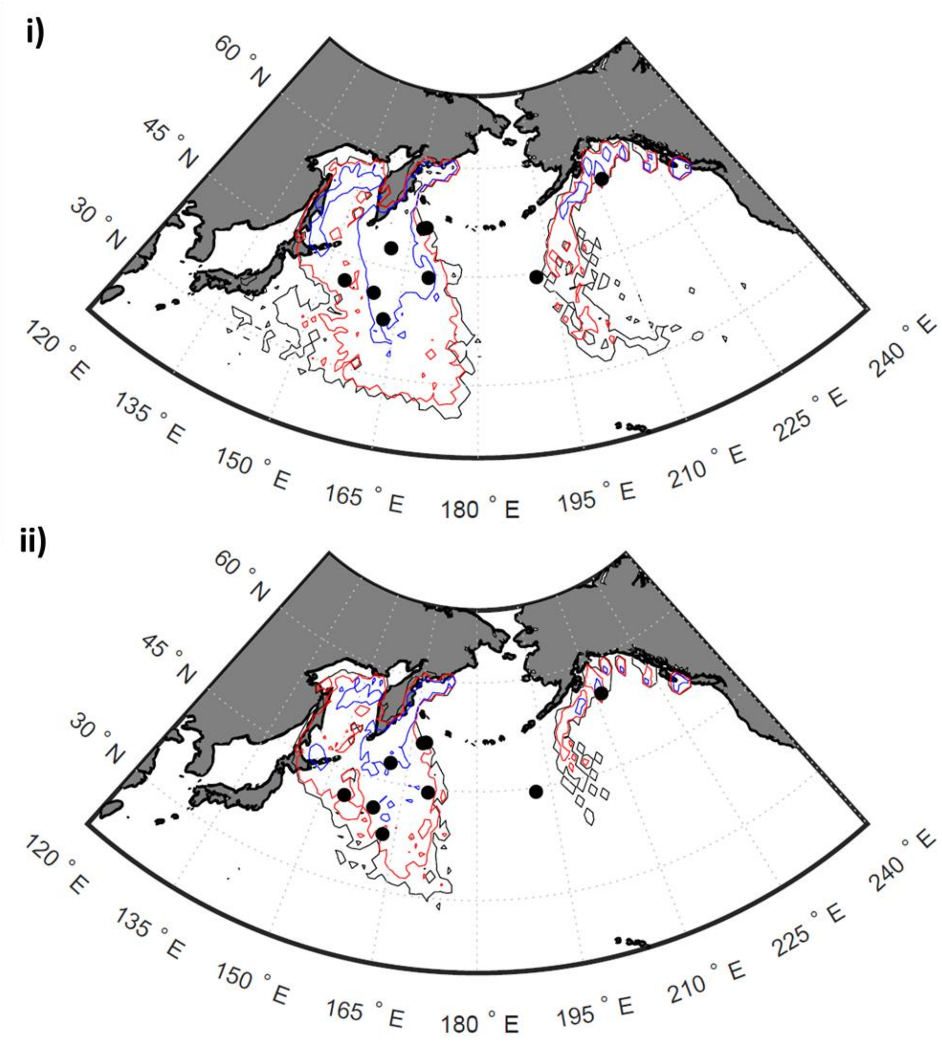

**Figure 7.3: Iceberg density maps for:** i) maximal flux simulation and ii) typical iceberg flux simulation. Contours are number of icebergs entering a 1x1° square in a 10 year period – 1 (black); 10 (red); 100 (blue);

1000 (black). ODP and DSDP sites are shown by black dots discussed in Chapters 4, 5 and 6, and shown again in Fig. 7.1.

The origin of the icebergs near ODP 1207, DSDP 580 and ODP 883 are shown in Fig. 7.4. These sites were selected for analysis of their iceberg sources because they have important Late Quaternary IRD records, and are widely spaced across the NW Pacific. Icebergs seeded on the eastern Kamchatka coast account for almost 50% of all model icebergs reaching Site 1207, which is consistent with geomorphological evidence showing that most Kamchatkan coastal end-moraines are on the eastern side of the peninsula, particularly in the northern Sredinny Range (Barr and Clark, 2012). However, the Koryak-and-west Kamchatka coasts account for 46% of icebergs reaching Site 1207, which is consistent with the prevalence of quartz IRD at this site (see Chapter 4, Fedorov et al., 2011, and Nürnberg et al., 2011). Over 50% of all icebergs reaching Site 883 are also calved from the E. Kamchatka coast. Icebergs reaching Site 580 originate exclusively from E. Kamchatka and W. Kamchatka, despite this site's relatively close proximity to the Kurile Islands. Model icebergs seeded from the N American coast are limited to the NE Pacific gyre and do not reach any NW Pacific sites (Fig. 7.3), consistent with previous mineralogical analyses of St. John and Krissek, (1999). The similar proportions of modelled iceberg origins to Sites 1207 and 883 support the hypotheses proposed in Chapters 4 and 5 that the enhanced late-MIS 3 iceberg flux to both sites is a marker of the same iceberg-flux events. The E and W Kamchatka origins of icebergs reaching site 580 suggests that the enhanced late-MIS 3 ice-rafting also seen here (Chapter 5) originated at one or both of these coasts. Iceberg flux from key NW Pacific coasts are explored further in Section 7.3.2.

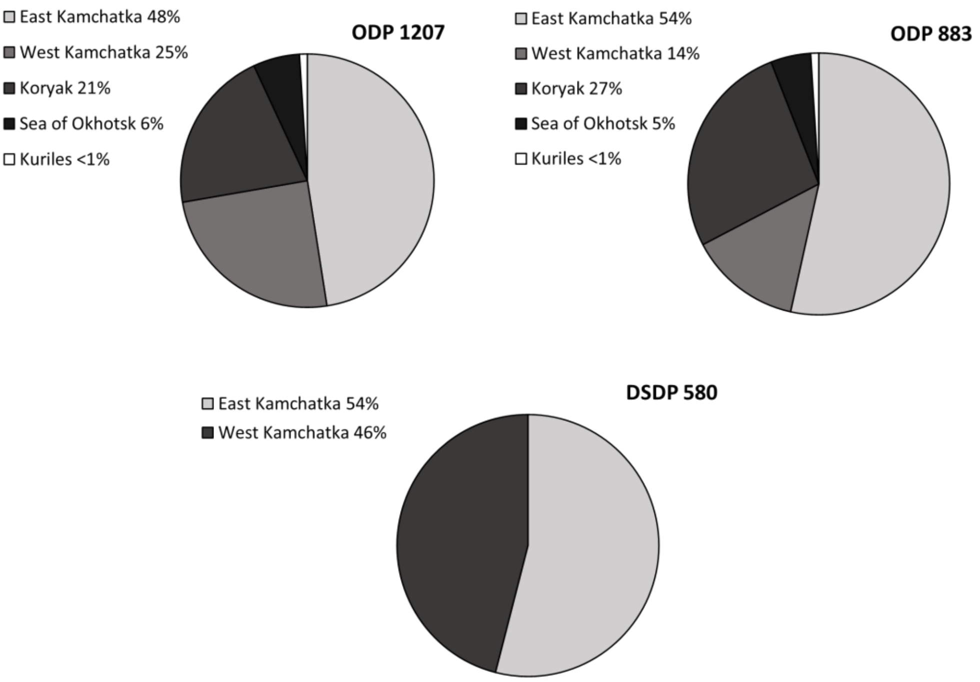

**Figure 7.4:** Origin pie charts for icebergs entering a 5x5° square around cores ODP 1207A, ODP 883 and DSDP 580, derived from the maximal FRUGAL climate-ocean-iceberg model simulation (see Fig. 1 for core locations).

### *7.3.2: Simulations of iceberg flux from possible key glacial termini on the NE Siberian coast*

The "maximal" and "normal" simulation results presented in Section 7.3.1 provide a useful picture of the overall flux of icebergs into the N Pacific during the Late Quaternary. However, they do not provide clear information on more localised sources of IRD, namely the key coastal zones shown in Fig. 7.2. To explore the most likely localised sources of IRD in the NW Pacific, further individual simulations were carried out in which icebergs were seeded from each of the coastal zones (Fig. 7.2; Table 7.1). Each zone was seeded with a specific number of seed points which varies between zones, due to the estimated flux based on the approximate size of the palaeo-ice stream termini. The estimated palaeo-ice stream termini and number of seed points are shown in Table 7.1. All localised simulation output maps are shown in Fig. 7.5, labelled A-H.

| **Iceberg seed zone** | **No. of seed points** |
|---|---|
| **Southern (S) Koryak Highlands** | 15 |
| **NE Kamchatka** | 25 |
| **Central E Kamchatka** | 10 |
| **SE Kamchatka** | 15 |
| **Kurile Islands** | 10 |
| **SW Kamchatka** | 10 |
| **Northern Sea of Okhotsk** | 10 |

**Table 7.1:** Coastal zones where icebergs were seeded in seven FRUGAL simulations. The number of seed points was determined by the estimated iceberg flux from each zone based on the size and number of coastal moraines and other glacial landforms taken from Barr and Clark, (2012; see Appendix 6 for seed zone coordinates and estimated palaeo-iceberg flux).

The density map of icebergs seeded purely from the S Koryak Highlands is shown in Fig. 7.5A. Icebergs seeded on this coast do not escape the Bering Sea, and do not travel far from the coast. The southward Kamchatka current prevents strong eastward flux, yet does not allow any significant transport through the Kamchatka Strait. Icebergs seeded on the S Koryak coast do not reach any of the NW Pacific core sites.

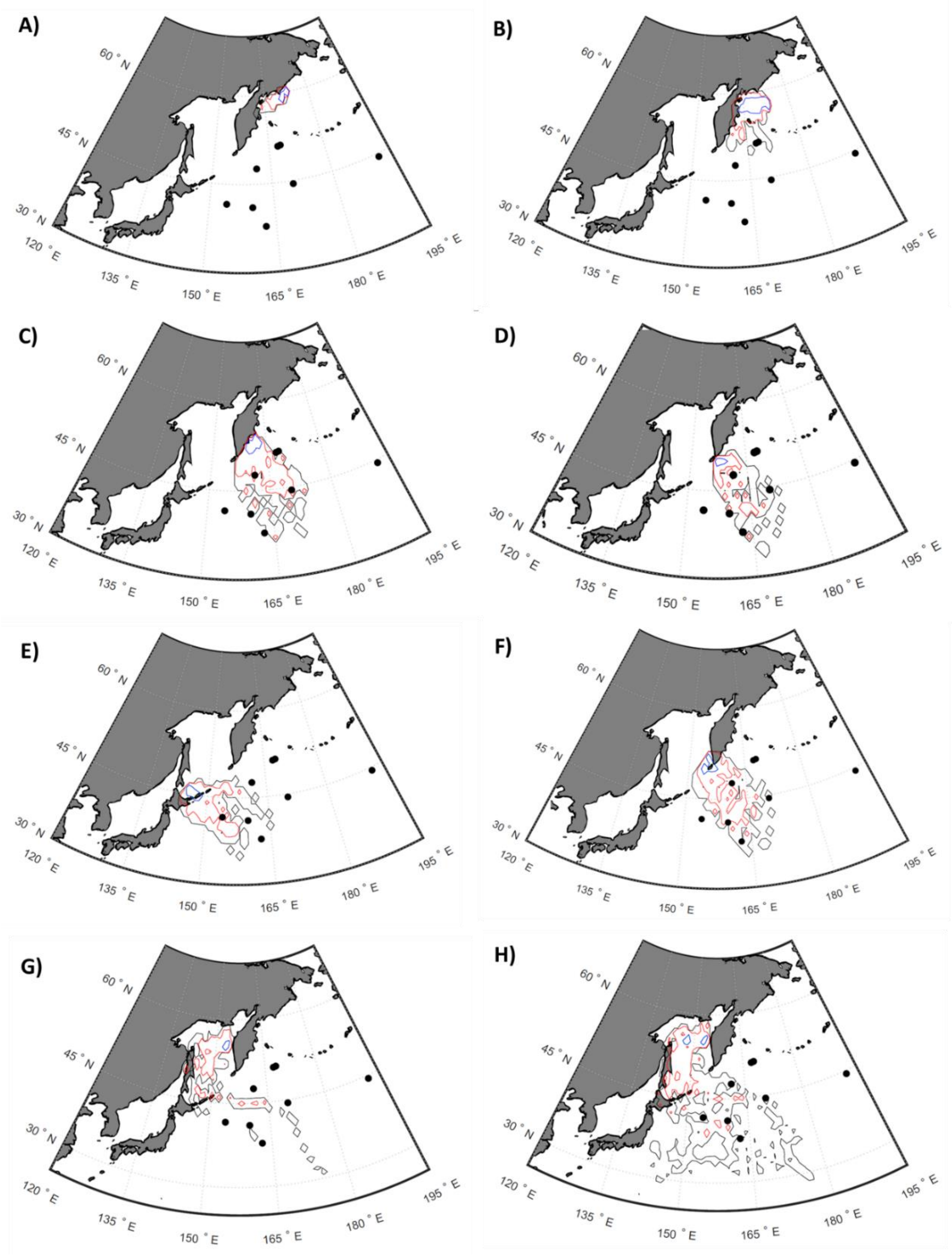

**Figure 7.5:** Iceberg density maps for all localised simulations A) Koryak Highlands. B) NE Kamchatka. C) CE Kamchatka. D) SE Kamchatka. E) Kurile Islands. F) SW Kamchatka. G)NE Sea of Okhotsk. H) General N Sea of Okhotsk. 1 (black); 10 (red); 100 (blue); 1000 (black)

Similarly to those seeded slightly further north on the Koryak coast, most icebergs seeded purely from NE Kamchatka (Fig. 7.5B) do not travel southward into the open NW Pacific, and remain within the Bering Sea. However, a lower but significant flux of icebergs does pass through the Kamchatka Strait and reaches SE Kamchatka, while another, lower density arm of icebergs extends south-eastward to a similar latitude. This arm reaches the vicinity of sites 883 and 884. Icebergs from NE Kamchatka do not reach other NW Pacific sites.

In contrast to the two previous runs in which icebergs were seeded on the Bering Sea coast of Kamchatka and the Koryak Highlands, in the third run (Fig. 7.5C) icebergs were seeded south of the Kamchatka Strait, on the central East Kamchatka coast. Consequently, icebergs calve directly into the NW Pacific currents, resulting in a much wider distribution of icebergs. While the higher density of bergs remains close to the Kamchatka coast, many are transported to the south-east in a broad, medium density path, reaching site 433. Site 881 is within this medium density path. To the north, sites 883 and 884 sit just outside this zone and few icebergs reach these sites from Central E Kamchatka. To the south, sites 1179 and 1207 sit just outside the low density zone, and very few icebergs will reach here. Site 580 is well outside of the iceberg zone.

The distribution of icebergs seeded from SE Kamchatka (Fig. 7.5D) is similar to the Central E Kamchatka simulation (Fig. 7.5C), with the same approximate eastward and southward extent. The key difference in this run is that icebergs do not come close to sites 883 and 884. Furthermore, site 433 sits within a lower density of bergs than in the Central E Kamchatka experiment, as the main axis is orientated in a more southerly direction. Again, icebergs do not travel close to site 580, while sites 1179 and 1207 sit on the edge of the low density contour line.

The density map for icebergs seeded from the Kurile Islands is shown in Fig. 7.5E. Here, icebergs were seeded off the coast of Urup, a southern island of the Kuriles where evidence of past glaciation is known to exist (C. Clark, *pers. comm.*). The iceberg flux is distributed in an easterly/south-easterly orientation. Site 580 is within the vicinity of many of the bergs calved from the Kurile

Islands, while to the north, site 881 sits just outside of the low density flux, and to the south and east, sites 1179 and 1207 are also rarely reached by bergs. No other NW Pacific sites are reached by the modelled Kurile icebergs.

The density map for icebergs seeded from SW Kamchatka is shown in Fig. 7.5F. While many icebergs stay near the coast of SW Kamchatka, not passing out of the Sea of Okhotsk, many are transported into the open NW Pacific and have a similar distribution to icebergs seeded on the SE Kamchatka coast (Fig. 7.5D). The main iceberg alley is oriented in a south-easterly direction, and passes south of site 881, and just north of 1179. However, these sites along with site 1207, sit in a low density field of icebergs. Site 433 sits at the eastward limit of SW Kamchatka bergs.

The density map for icebergs seeded from the northern Sea of Okhotsk is shown in Figs. 7.6G and 7.6H. Two simulations were performed: G) to investigate iceberg flux from the NE Sea of Okhotsk, where coastal or near-coastal moraines in W Kamchatka and the Kolyma Upland have been identified (Fig. 7.2), and H) to investigate generalised release from the N Sea of Okhotsk coast, including a second set of release points to the west, where glaciers may have reached the coast. There are substantial differences between these two runs. Icebergs seeded from the NE Sea of Okhotsk (G) largely stay within the Sea, however, an arm of icebergs are transported eastward into the open NW Pacific, and a small number are carried in a south-easterly direction. Some bergs may reach site 881, but do not appear to reach other sites.

In the generalised release experiment of H), as with G), most icebergs remain trapped within the Sea of Okhotsk, however, there is a much wider distribution of icebergs in the open NW Pacific, with significant, but low density southward and eastward flux. A small number of bergs reach south of 30$^{o}$N. Small numbers of icebergs reach the vicinity of sites 881, 1179, and 433 while sites 580 and 1207 sit on the edge of the zone of low density iceberg transport.

Section 7.4 discusses the implications of the simulations presented in this chapter. The existing IRD (discussed in Chapters 2, 4, 5 and 6) is considered in the light of the simulated iceberg distributions from the various NW Pacific sources. The discussion concludes with an exploration of where IRD is likely to have originated at each of the NW Pacific sites featured in this thesis.

## 7.4: Discussion

### *7.4.1: NE vs NW Pacific IRD belts*

The simulated iceberg distributions demonstrate that there are likely to be multiple IRD sources for locations in the N Pacific, and that these sources may vary between sites. The modelling results shown in Fig. 7.3 demonstrate that there are two broad IRD belts in the N Pacific, which are derived from the two major ice masses on the N Pacific rim. The modelled iceberg distribution in the NE Pacific is derived exclusively from the Cordilleran ice sheet, and icebergs seeded on the NW American coast reach the vicinity of ODP 887 in both 'typical' and 'maximal' experiments, as expected by the high levels of IRD found here (Krissek, 1995). The modelled iceberg distribution in the NW Pacific is derived exclusively from the Siberian coast and the Kurile Islands. There is no mixing between NE and NW IRD sources.

### *7.4.2: Simulated iceberg distributions vs. expected IRD occurrences in the NW Pacific*

The simulations presented in Section 7.2 show that all seven NW Pacific sites featured here should contain a Late Quaternary IRD record. Simulated icebergs reach the vicinity of all sites where IRD has already been recorded (883, 884, 580, 1207 and 433). This sub-section focuses first on the two sites which have been the focus of Chapters 4 and 5 (ODP 1207 and DSDP 580), and then discusses the other dated sites, and then what may be expected in the undated sites.

Table 7.2 shows whether simulated icebergs from each NW and NE Pacific coastal source reach each of the nine N Pacific sites. It is important to note that Table 7.2 relates to the individual local runs, and therefore does not correspond to the results presented in the maximal runs of Figs. 7.4 and 7.5, where the flux rate is greater.

ODP 1207A, which contains low concentrations of Late Quaternary IRD possibly representing episodes of enhanced iceberg flux (Chapter 4) is unambiguously reached only by icebergs from SW Kamchatka in the ‘typical’ flux simulations. Icebergs from Central E Kamchatka, SE Kamchatka and the N Sea of Okhotsk drift close to site 1207, but only in very low densities. The low concentrations of observed IRD at site 1207 is likely to be the outcome of low densities of icebergs reaching the site, and therefore, the simulated iceberg distributions can be deemed to be sensible and in agreement with observed IRD at site 1207.

| | **KH** | **NEKam** | **CEKam** | **SEKam** | **KI** | **SWK** | **NESO** | **GNSO** | **A** |
|---|---|---|---|---|---|---|---|---|---|
| **ODP 883** | ✗ | ~ | ✓ | ✗ | ✗ | ✗ | ✗ | ✗ | ✗ |
| **ODP 884** | ✗ | ~ | ✓ | ✗ | ✗ | ✗ | ✗ | ✗ | ✗ |
| **ODP 881** | ✗ | ✗ | ✓ | ✓ | ✗ | ✓ | ✗ | ✓ | ✗ |
| **DSDP 580** | ✗ | ✗ | ✗ | ✗ | ✓ | ✗ | ✗ | ~ | ✗ |
| **ODP 1179** | ✗ | ✗ | ~ | ✓ | ~ | ✓ | ~ | ✓ | ✗ |
| **DSDP 433** | ✗ | ✗ | ✓ | ✓ | ✗ | ~ | ✗ | ~ | ✗ |
| **ODP 1207** | ✗ | ✗ | ~ | ~ | ✗ | ✓ | ✗ | ~ | ✗ |
| **ODP 886** | ✗ | ✗ | ✗ | ✗ | ✗ | ✗ | ✗ | ✗ | ✗ |
| **ODP 887** | ✗ | ✗ | ✗ | ✗ | ✗ | ✗ | ✗ | ✗ | ✓ |

**Table 7.2:** N Pacific iceberg seeding locations against N Pacific sites. Green ticks indicate that modelled icebergs reach the site. Red x indicates that modelled icebergs do not reach the site. ~ indicates that modelled icebergs travel close to the site, but the site remains on the periphery of iceberg transport, and it is likely that

few icebergs will reach the site. KH = Koryak Highlands. NEKam = NE Kamchatka. CEKam = Central E Kamchatka. SEKam = SE Kamchatka. KI = Kurile Islands. SWK = SW Kamchatka. NESO = NE Se of Okhotsk. GNSO = General N Sea of Okhotsk. A = Alaska.

Simulated icebergs at DSDP 580 to the NW, differ in their sources to site 1207. Notably, the primary source of icebergs here are the Kurile Islands. A Kurile source may explain the high concentrations of volcanic rock fragments at site 580 (Chapter 5). Seemingly, very few icebergs reach site 580 from E Kamchatka, however some icebergs from the N Sea of Okhotsk may enter the vicinity of this site. The Late Quaternary IRD flux to site 580 is relatively continuous in comparison to site 1207, and is also of much greater magnitude (Chapter 5). The IRD concentrations found here would require a stable supply of icebergs. Little is known about Late Quaternary glaciation on the Kurile Islands, but glacial growth is likely to have been limited here by the size of the landmasses.

In Kurile Islands run, icebergs commonly reach site 580. These results are different to the iceberg origin pie charts in Fig. 7.4, as Kurile icebergs from the maximal regionwide run do not reach site 580. This is because in the maximal run, Kurile icebergs were seeded slightly further to the west than in the individual Kurile Islands run, thus accounting for the NW Pacific output differences between these two runs.

Icebergs were commonly calved from W Kamchatka into the Sea of Okhotsk where high concentrations of IRD have been observed (e.g. Gorbarenko, 1996; Nürnberg et al., 2011). As the provenance of NW Pacific IRD has not been studied in detail, the extent to which icebergs from the Sea of Okhotsk entered the NW Pacific is unknown. However, it may be assumed that some icebergs did pass into the open ocean. The quartz fraction of IRD at site 580 (Chapter 5) may be derived from the sedimentary and metamorphic provinces of W Kamchatka.

While the Kurile Islands and Sea of Okhotsk appear to be highly feasible main sources for IRD at site 580, these simulations raise questions about a previous assumption made in Chapter 5, that the

~40 ka BP IRD spike observed at several NW Pacific sites including site 580, 1207 and 883 was derived from the same event, and possibly the same source. In the ‘typical’ simulations shown here, the iceberg flux to site 580 originates from a different source to sites 1207 and 883. This gives rise to two possible scenarios for the simultaneous IRD spike at these three widely separated sites:

1) The 40 ka BP spike does not represent ‘typical’ levels of iceberg flux, and instead was caused by a ‘maximal’ flux event from both E and W Kamchatka (as shown in Fig. 7.4). The 40 ka BP spike was caused by regionwide ice sheet collapse caused by wider climatic changes, resulting in a simultaneous increase in iceberg calving from Kamchatka, the Northern Sea of Okhotsk and the Kurile Islands.
2) The 40 ka BP spike is the result of a coincidental increase in iceberg flux from multiple locations on the Kamchatka-Kurile-Sea of Okhotsk coast which was not the result of changing regional climate.

The second scenario is unlikely, as IRD increases are widespread at 40 ka BP and during the broader MIS 3 period (e.g. Bigg et al., 2008; Nürnberg et al., 2011). The first scenario is feasible, and it suggests that the 40 ka IRD peak may be of different geological provenance to the background IRD at site 580. It also suggests that there was regional synchronicity in the dynamics of glacial ice in NE Siberia, and could lend support to the hypothesis of extensive NE Siberian glaciation with regional ice streams draining the Okhotsk and E Kamchatka regions. Further research into the provenance of the 40 ka peak, and background IRD at site 580 should be carried out to address these scenarios.

In the ‘typical’ flux simulations, only IRD from Central E Kamchatka reaches the vicinity of the subarctic sites 883 and 884. These results are unexpected due to the relatively high Late Quaternary IRD concentrations found at site 883 (Bigg et al., 2008; Chapter 5). The discrepancy between the simulations and observed IRD concentrations may be because the actual Late Quaternary flux from NE Siberia to site 883 was higher than the simulated flux in the ‘typical’ simulations. The actual iceberg flux may have been closer to the ‘maximal’ IRD flux shown in Fig. 7.3 Alternatively, the model ocean currents may have a weaker eastward component on the coast of Kamchatka than the real-world ocean currents.

Site 433 is well within the reach of simulated icebergs from Central E and SE Kamchatka, despite this site’s relatively distal location. Icebergs from SW Kamchatka and the N Sea of Okhotsk may also reach here, but in small numbers. The observed IRD at site 433, characterised by mineral grains, rock fragments and larger dropstones (Chapter 6) would support the picture generated by these simulations that this site was within the range of strong eastward iceberg flux from E Kamchatka. This eastward flux at this latitude would be expected as this site in the path of strong eastward surface current flow (e.g. Harada et al., 2004).

Site 881, which is known to contain Quaternary IRD (Krissek, 1995) although no high resolution Late Quaternary counts have been carried out, is well within the main alley of icebergs seeded from Central E Kamchatka, SE Kamchatka and SW Kamchatka (Fig. 7.13). Icebergs from the general N Sea of Okhotsk region also reach this site, although in lower concentrations. Site 881 is in the path of a strong modelled eastward surface current (Fig. 7.3), resulting in strong iceberg transport over this site. The modelled iceberg flux predicts that site 881 would have higher IRD concentrations than site 883 to the north. The low resolution counts of Krissek (1995) confirm that IRD wt% at site 881 is higher than at site 883 throughout the Quaternary. Higher IRD wt% at site 881 may thus be due to greater flux over this site due to the trajectories of Kamchatkan icebergs, although it must be remembered that there has been greater calcareous biological accumulation at the shallower site 883. Due to its position within the main axis of flux from Kamchatka, site 881 has potential for important future studies of Late Quaternary glacial change on Kamchatka, and may prove to be as important as site 883 for examining abrupt iceberg calving events.

To the south of site 881, icebergs reaching the vicinity of site 1179 originate on the coasts of SE Kamchatka and the general N Sea of Okhotsk region in low concentrations. However, the greatest number of icebergs reaching this site originate on the SW Kamchatka coast. IRD has been confirmed here by the identification of at least one dropstone (Chapter 6), but no in-depth study of this site's age or IRD concentrations has been carried out. Here, the expected concentrations would be lower than those observed at sites 881 and 883, but higher than at site 1207. The IRD geology is expected to be similar to that found at site 881.

### 7.5: Conclusion

The FRUGAL model simulations estimate the key iceberg release regions for Late Quaternary icebergs in the N Pacific. They confirm that there is no mixing between Alaskan and Siberian icebergs. In some instances, in particular with regard to the flux of icebergs to sites 883 and 884, the actual iceberg discharge is likely to have been higher than in the 'typical' simulations for much of the Late Quaternary, and especially during the 40 ka BP Heinrich-style event, which was more likely to be a 'maximal' scale event. The simulations also propose the hypothesis that there are several possible NE Siberian sources of IRD in the NW Pacific, and these sources vary geographically across the basin. Some sites are likely to have mixed, sometimes widely geographically spread sources. The resultant mixed geological composition of IRD at sites which have received material from multiple sites, should be used to analyse the regional dynamics and timing of NE Siberian glacial change. Such an analysis would also confirm the accuracy of the model simulations. Chapter 8 summarises the major findings and arguments of this thesis, and presents a basin-wide view of glacial and climatic change in the Late Quaternary NW, and more generally, N Pacific.

# Chapter 8: The Late Quaternary NW Pacific: summary, limitations and scope for future work

## 8.1: Introduction

In this final chapter, the key findings of this thesis, and their implications are summarised. Then, the key limitations of this research are discussed. Following this summary, desirable future follow-on work is discussed which would complement and enhance the work presented in this thesis.

## 8.2: Major findings of this research

### *8.2.1: New and updated age models at ODP 1207A and DSDP 580*

In this research, age models are generated or consolidated at two NW Pacific sites using multiple absolute and relative dating methods. These age models improve the chronostratigraphy of the open NW Pacific, which contains relatively few high resolution Late Quaternary dated cores. These age models provide crucial time markers for the interpretation of major environmental changes in the NW Pacific.

In Chapter 4, a new Late Quaternary age model was constructed for ODP 1207A on the Shatsky Rise. Four AMS $^{14}$C dates were acquired in the upper 51cm, and a high resolution benthic $\delta^{18}$O record was constructed using the foraminifera species *C. wuellerstorfi.* Through interpretation of the $\delta^{18}$O record, it was demonstrated that the upper 300cm of this core dates to mid-MIS 6 at its greatest depth. The depths of MIS 5-1 were also identified through the $\delta^{18}$O curve. There is good agreement between the $^{14}$C and $\delta^{18}$O ages. A further age tie point was added to the age model by the geochemical identification of the ~87 ka BP Aso-4 tephra. The MIS 6-5 transition was also visually identified in counts of the planktic foraminifera *N. pachyderma,* where an abrupt decline in the population of this species was noted. This event has previously been documented at other NW Pacific sites in the subarctic-subtropical transition zone and is interpreted to be a northward shift in the subarctic front during the penultimate deglaciation (Thompson and Shackleton, 1980; Yamane, 2003). This occurrence in the ODP 1207A core corroborates the depth assignment of the MIS 6-5 transition at ~230cm. A further tie point for the MIS 6-5e transition is visible in the Ba/Ti log ratio, which reaches a peak during MIS 5e, corresponding with a rapid decline in % of *N. pachyderma.* Fig. 8.1 presents selected key Late Quaternary stratigraphic records for ODP 1207A.

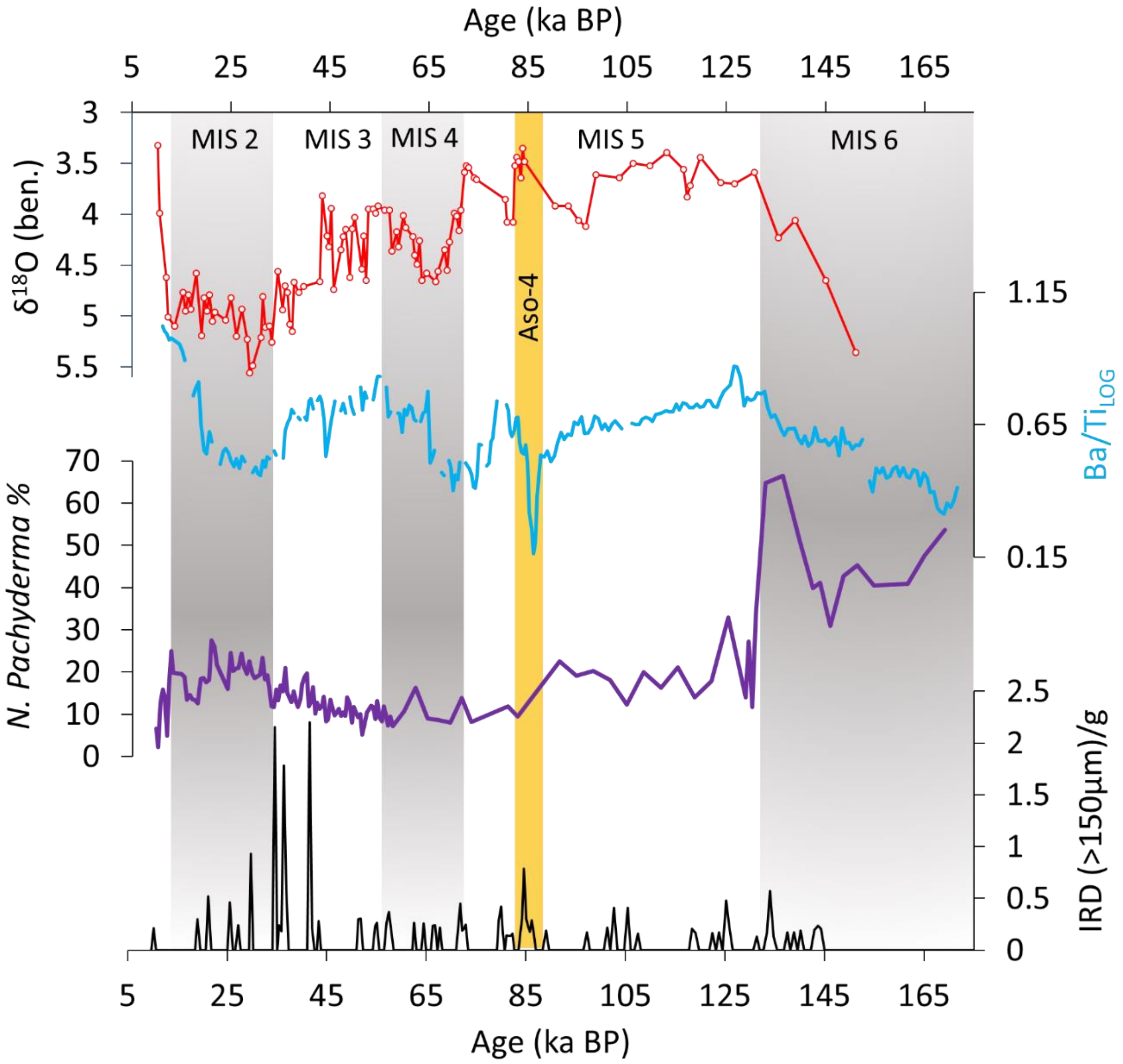

**Fig. 8.1:** Key stratigraphic data for ODP 1207A against the newly acquired age model presented in Chapter 4.

Prior to this research, DSDP 580's age model between 0 and 300cm consisted of 18 dates derived from diatom assemblage tie points (Koizumi, 1994) and magnetostratigraphy (St. John and Krissek, 1999). There were several dating offsets between these two models. A new composite age model was produced in Chapter 5 using tephrochronology on two tephra layers, which geochemically matched to Late Quaternary Japanese tephras. These dates were in agreement with the dates of Koizumi (1994), but aligned less well with St. John and Krissek (1999). Therefore an updated age model involving tephrochronology and the dates of Koizumi was constructed. Fig. 8.2 shows a reference stratigraphy for DSDP 580, ODP 883B, ODP 1179A and ODP 881B (~55 ka-5 ka BP), and includes the new age model for DSDP 580. Sites 883, 1179 and 881 are presented here because they display features within the Ba/Ti and Ca/Ti signals which have the potential for regional correlation, particularly if the deglacial and Holocene core sections of ODP 883B are compared to the upper sections of ODP 1179A and ODP 881B. Here there are productivity signals which show similarities with ODP 883B, and may be used to build chronostratigraphies at these sites.

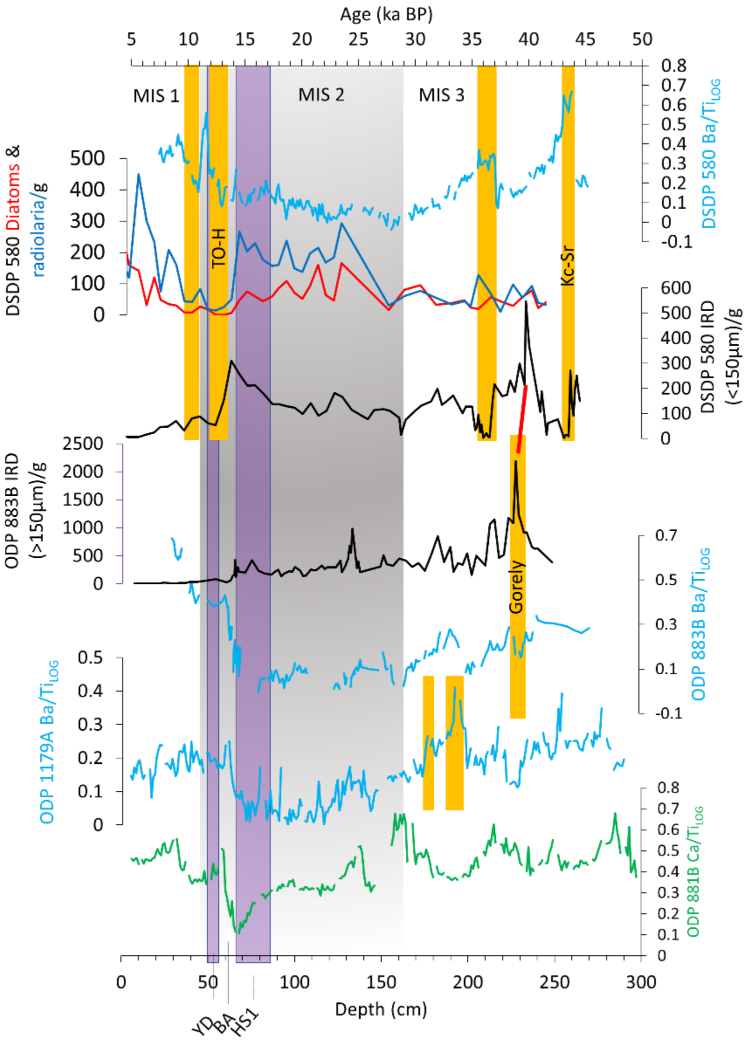

**Figure 8.2:** Selected climate proxy data from DSDP 580, ODP 883B, ODP 1179A and ODP 881B. Yellow bars represent tephra layers. Ash layers without labels have not been matched to proximal tephra. Red bar shows corresponding IRD peaks in DSDP 580 and ODP 883B. IRD data for ODP 883D is from Bigg et al., (2008).

### *8.2.2: Ice-rafted debris in the NW Pacific*

One of the major foci of this project has been the expansion of knowledge and coverage of Late Quaternary IRD in the NW Pacific. Chapters 4 and 5 are in large part devoted to developing the IRD record at sites 1207 and 580 respectively (see Figs. 8.1 and 8.2). The existing IRD record at site 883 (Fig. 8.2) is also used as an important reference site for understanding the magnitude, timing and other characteristics of iceberg flux in the NW Pacific, following the work of Bigg et al., (2008). IRD was described at site 433 (Chapter 6), where dropstones and an interesting XRF record hold potential for palaeoclimate investigations (see Sections 8.3 and 8.4 for further discussion).

### *8.2.3: Episodic iceberg flux to mid-latitude site ODP 1207A*

The newly constructed IRD series at ODP 1207A (Fig. 8.1 and Chapter 4) demonstrates that NE Siberian icebergs were transported further south than previously recorded since MIS 6, thus expanding southward the important IRD distribution map of Conolly and Ewing, (1970). Furthermore, ice-rafting events which reached ODP 1207A appear to be independent of North Atlantic Heinrich Events and NE Pacific climatic events. The discovery of IRD in the mid-latitude NW Pacific suggests the need for a re-evaluation of the scale and importance of Late Quaternary regional iceberg input. The scope for future work in this area is discussed in Section 8.4.

There is a strong contrast in ice-rafting between the LGM and MIS 6. This may be due to differing regional glacial dynamics from one glacial period to another. The absence of IRD at site 1207 for much of MIS 6, in contrast to elsewhere in the NW Pacific (see references in Chapter 4) suggests that the intensity of ice-rafting during this period was not sufficient for icebergs to reach site 1207, despite this period being colder, as can be inferred from its planktic foraminifera record (Fig. 8.1 and Chapter 4). These contrasts between MIS 6 and 2 may also mean that NE Siberian ice extent was very different during each of the last two glacial periods. The implications for future sea level palaeo-reconstructions are discussed in Section 8.4.5.

### *8.2.4: The 40 ka BP ice-rafting event and other basin-wide events: Implications for NE Siberian glacial scale and dynamics*

A ~40 ka BP spike in IRD is identified in both ODP 1207A and to the NW at DSDP 580, and is concluded to be a marker of the same glacial collapse event, or series of closely spaced events, recorded in the subarctic Pacific at ODP 883 (Bigg et al., 2008). The magnitude, basin-wide spread, and abrupt nature of this event is comparable to N Atlantic Heinrich Events. The FRUGAL simulations in Chapter 7 point strongly to this event being a widespread, rather than localised collapse of the glacial ice cover in NE Siberia, with several potential areas of collapse including E and W Kamchatka, the northern coast of the Sea of Okhotsk, and the Kurile Islands (Fig. 8.3).

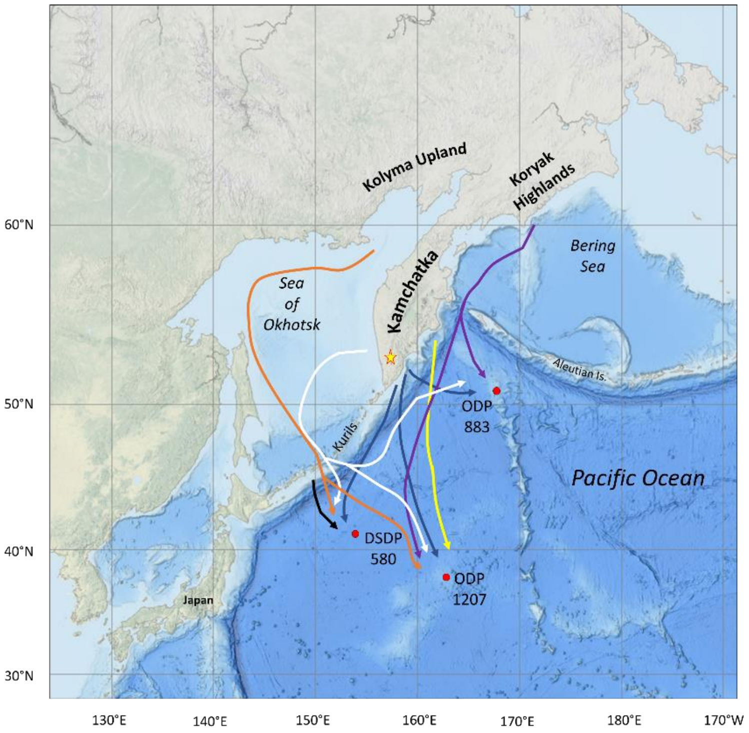

**Figure 8.3:** Likely approximate paths of icebergs in a 40 ka BP – type collapse of NE Siberian glacial ice, modelled by FRUGAL. Purple lines: Icebergs from the Koryak Highlands. Yellow lines: from central-east Kamchatka. Blue lines: from south-east Kamchatka. White lines: from south-west Kamchatka. Orange lines: from the northern Sea of Okhotsk. Black line: from the Kurile islands. Star marks location of terrestrial evidence of ice retreat after 40 ka BP (Baumler and Zech, 2000).

The apparently regional, rather than localised glacial collapse strongly suggests that prior to ~40 ka BP, there was extensive and possibly continuous glacial ice covering much of the NE Siberian region, which responded synchronously to climatic changes.

### *8.2.5: Key climate signals during the Late Quaternary*

Data from MIS 6 was acquired from ODP 1207A. E Asian dust dominated the supply of terrigenous sediment during this period, and icebergs did not reach the mid-latitudes until late MIS 6. The subarctic front was south of site 1207 during MIS 6, as demonstrated by counts of *N. pachyerma* (Chapter 4).

During MIS 3, as discussed earlier, ice-rafting from the Kamchatka-Koryak/Sea of Okhotsk regions is a key terrigenous signal in the NW Pacific (Figs. 8.1; 8.2; 8.3). Key tephrochronological layers are deposited between 45 and 38 ka BP at sites 883 (Gorely) and 580 (Kc-Sr), and provide important chronostratigraphic markers. During the LGM, ice-rafting continues in the NW and NE Pacific, but is reduced in intensity (Figs. 8.1 and 8.2). Abrupt productivity increases occur during deglaciation across the NW Pacific and NE Pacific as shown by intensities of Ba and Ca, and log ratios of Ba/Ti and Ca/Ti at multiple sites (Figs. 8.1; 8.2). During the Holocene, ice-rafting ceases in the NW Pacific. Productivity in the subarctic and subtropical N Pacific remains high.

## 8.3: Limitations of this research

While the research presented in this thesis improves the understanding of Late Quaternary environmental change in the NW Pacific, and adds to the regional stratigraphy, there are key limitations which are acknowledged here. One of the key limitations relates to the evidence for the provenance of IRD and other terrigenous sediments. Due to time limitations, the provenance analysis presented in Chapter 6 is largely a qualitative assessment which relies on visual correlation of data points of semi-quantitative XRF intensities to draw conclusions about regional environmental change. While the estimations made about IRD provenance by the FRUGAL simulations match observed IRD distributions, geological provenance analysis is an obvious missing piece of the puzzle (see Section 8.4 for further discussion).

A further limitation relates to the lack of chronological control in the N Pacific. This research has significantly improved age control at ODP 1207A and DSDP 580. However, of the nine ODP and

DSDP sites analysed in Chapter 6 using XRF, even after the age model work of this thesis only five had reliable Late Quaternary age tie points, although tentative stratigraphic correlations were made between ODP 1179A and ODP 881B and other dated cores (Fig. 8.2 and Chapter 6). Although the spread of dated cores over the region is reasonably good, there are several gaps in key areas, such as at ODP 881B, which may contain a significant ice-rafting record (see the modelling results in Chapter 7), but no confirmed age control. Elsewhere, DSDP 433 contains a potentially important Pleistocene stratigraphy. However, without age control, the major climatic changes interpreted through the XRF record, cannot at this stage be confidently attributed to key climate stages.

A further limitation is that the investigation into sea surface temperature (SST) was limited to planktic foraminiferal counts at ODP 1207A. It was also not possible to obtain planktic $\delta^{18}$O for ODP 1207A, as it was not possible to obtain funding for this analysis. Consequently, ocean surface changes here were reliant on visual interpretation of key species changes, especially *N. pachyderma*, and semi-quantitative inferences made from Ba/Ti and Ca/Ti. While these methods did reveal a key episode of SST change at the MIS 6-5 transition and changes during deglaciation, there is significant scope for SST studies to investigate these datasets further (see Section 8.4 for further discussion).

## 8.4: Scope for future work in the NW Pacific

This research leaves open many possible avenues of enquiry which would consolidate and expand on the work presented here. The following section presents those key avenues which logically follow on from this research, and which would strengthen understanding of the Late Quaternary NW Pacific

### *8.4.1: Sampling of previously unexplored Late Quaternary sections of NW Pacific cores*

Despite the addition of two new high resolution IRD datasets through this research, there remains numerous sites where IRD has not been counted, or even documented through direct sampling. Sites 881 and 1179 are potentially important sites for IRD, possibly being within-or close to-the main axis of iceberg transport during the Late Quaternary, as demonstrated by the early work of Conolly and Ewing, (1970) and the FRUGAL modelling of Chapter 7. New IRD datasets should search for evidence of abrupt ice-rafting events, including the 40 ka BP event. New IRD datasets at these locations would “fill in the gaps” between the major datasets at site 1207 in the south, 580 in the west, and 883 in the north. The spatial coverage of IRD records would then be very good in the NW Pacific, and comparable to the “Ruddiman Belt” of the N Atlantic. ODP 1179A contains at least two tephra layers in the upper 300cm (Chapter 6, Fig. 6.9), which could be geochemically analysed to identify their eruptive origins (as described in Chapter 5). The addition of age tie points through tephrochronology would be vital in establishing the timing of ice-rafting events in the NW Pacific where carbonate content is low, and $^{14}$C dating is not possible at many sites.

### *8.4.2: Geological provenance of NW Pacific IRD*

The potential for multiple NW Pacific IRD sources on the NE Siberian coast predicted by the FRUGAL simulations, lays a compelling framework for future quantitative geological provenance analysis on IRD in the NW Pacific. Provenance studies such as neodymium-strontium isotope analysis (e.g. Molina-Kescher et al., 2014; Maccali et al., 2014) from IRD samples at multiple NW Pacific sites have the exciting potential to map iceberg sources, and if combined with chronostratigraphy, could be used to improve the understanding of the timing of glacial change in NE Siberia. The results of these analyses could be used to inform future terrestrial investigations of Late Quaternary glaciation in the region.

Element concentration measurements can also be used to investigate sediment provenance, and provide a useful test of the accuracy of XRF data (Weltje and Tjallingii, 2008). This use of XRF data alongside chemical abundance data has been successfully used by Monien et al., 2012) to investigate sediment provenance in the Southern Ocean. Future work could focus on acquiring geochemical and lithological and grain size data for Late Quaternary sections of the NW Pacific. Published geological data from NE Siberia (e.g. Bindemann et al., 2012) and possibly from other regions including E Asia and Beringia could be incorporated into this approach, and may reveal distinct ice-rafting signals from different regions, and could challenge or add support to the XRF analysis of Chapter 6.

### *8.4.3: Further investigation of XRF core-scanning data*

The XRF data presented in Chapter 6 reveals some interesting signals, especially those related to productivity which have potential uses as chronostratigraphic tools as well as indicators of climatic and oceanographic change. This method made use of a select few major elements which are commonly used as environmental indicators. However, there are many potential future uses of this dataset, which contains several thousand data points and over 20 chemical elements per core.

Chapter 6 demonstrates that XRF core-scanning (especially Zr) is sensitive to the presence of visible tephra layers. The NW Pacific Late Quaternary stratigraphy is strongly influenced by volcanism (see Chapters 4, 5 and 6), therefore, it is highly likely that many more unidentified tephras or cryptotephras (non-visible ash layers; Lane et al., 2014) are present within the core sections studied in this thesis. XRF, along with validation by direct sampling has been found to be useful in identifying cryptotephras in ocean sediments (e.g. McCanta et al., 2015). Application of this approach to the N Pacific XRF data could drastically improve the regional chronostratigraphy.

### *8.4.4: Palaeo-sea level investigations*

The NE Siberian contribution to sea level is routinely omitted from most palaeo-sea level investigations. However, Batchelor et al., (2019) is an exception in palaeo-ice sheet and sea level reconstructions. They synthesise existing records of global ice sheet coverage and show that the “best estimates” of ice extent correlate well with sea level reconstructions. They acknowledge that significant glacial ice existed in the NW Pacific region during the Late Quaternary, and therefore should be factored into investigations of sea level change. However, their conclusions focus mainly on the effect of the Laurentide ice sheet. The potentially widespread effect of events such as the NW Pacific 40 ka event should be investigated for their specific effects on sea level and regional climate and oceanography. In this thesis, the 40 ka event is confirmed as an important episode of environmental change in the NW Pacific. Its magnitude and spatial fingerprint, comparable to the N Atlantic Heinrich layers, is found from the subarctic to the mid latitudes. Therefore, the possible effect on sea level should be investigated, and greater efforts should be carried out to search for evidence of similar Late Quaternary events in the region.

# References

Albert, P.G. et al. 2019. Geochemical characterisation of the Late Quaternary widespread Japanese tephrostratigraphic markers and correlations to the Lake Suigetsu sedimentary archive (SGO6 core). *Quat. Geochron.* 52: 103-131.

Aoki, K. 2008. Revised age and distribution of ca. 87 ka Aso-4 tephra based on new evidence from the northwest Pacific Ocean. *Quat. Int.* 178: 100-118.

Avdeiko, G.P., D.P. Savelyev, A.A. Palueva. S.V. Popruzhenko. 2007. Evolution of Kurile-Kamchatkan Volcanic Arcs and Dynamics of the Kamchatka-Aleutian Junction. Geophys. Monog. Ser. 172. DOI: 10:1029/172GM04.

Bailey, J.C. (1993). Geochemical history of sediments in the northwestern Pacific Ocean. *Journ. Geochem.* 27: 71-90.

Bailey, I., L. Qingsong, G.E.A. Swann et al. 2011. Iron fertilisation and biogeochemical cycles in the sub-Arctic northwest Pacific during the late Pliocene intensification of northern hemisphere glaciation. *Earth Plan. Sci. Lett.* 307: 253-265.

Barash, M.S., A.G. Matul, G.K. Kazarinaet al. 2006. Paleoceanography of the Central Sea of Okhotsk during the Middle Pleistocene (350-190 ka) as inferred from micropaleontological data. *Oceanology* 46: 501-512.

Barr, I.D. 2009. Constraining the extent, style and phases of glaciation to derive Late Quaternary snowline estimates in far NE Russia. *PhD Thesis, The University of Sheffield.*

Barr, I.D., C.D. Clark. 2009. Distribution and pattern of moraines in far NE Russia reveal former glacial extent. *J. of Maps* 5: 186-193.

Barr, I.D., C.D. Clark. 2012a. Late Quaternary glaciations in Far NE Russia; combining moraines, topography and chronology to assess regional and global glacial synchrony. *Quat. Sci. Rev.* 53: 72-87.

Barr, I.D., C.D. Clark. 2012b. An updated moraine map of far NE Russia. *J. of Maps* 8: 431-436.

Barr, I.D., O. Solomina. 2014. Pleistocene and Holocene glacier fluctuations upon the Kamchatka Peninsula. *Glob. Plan. Chge* 113: 110-120.

Barron, J.A. 1992. Pliocene paleoclimatic interpretation of DSDP Site 580 (NW Pacific) using diatoms. *Marine. Micropal.* 20: 23-44.

Batchelor, C.L. et al. 2019. The configuration of Northern Hemisphere ice sheets through the Quaternary. *Nature Comm.* 10: 3713.

Berger, W.H., C.G. Adelseck, JR., L.A. Mayer. 1976. Distribution of Carbonate in Surface Sediments of the Pacific Ocean. *J. Geophys. Res.* 81: 15.

Bigg. G.R. 2020. The impact of icebergs of sub-Antarctic origin on Southern Ocean ice-rafted debris distributions. *Quat. Sci. Rev.* 232: 106204.

Bigg, G.R., C.D. Clark, A.L.C. Hughes. 2008. A last glacial ice sheet on the Pacific Russian coast and catastrophic change arising from coupled ice-volcanic interaction. *E.P.S.L.* 265: 559-570.

Bigg, G. R. et al. 2012. Sensitivity of the North Atlantic circulation to break-up of the marine sectors of the NW European ice sheets during the last Glacial: a synthesis of modelling and palaeoceanography, *Glob. Planet. Change*, 98-99: 153-625.

Bindemann, I.N., V.I. Vinogradov, J.W. Valley et al. 2002. Archean protolith and accretion of crust in Kamchatka: SHRIMP dating of zircons from Sredinny and Ganal Massifs. *J. of Geol.* 110: 271-289.

Boers, N. 2018. Early-warning signals for Dansgaard-Oeschger events in a high-resolution ice-core record. *Nat Comm.* 9: 2556.

Bönning, P., E. Bard, J. Roe. 2007. Toward direct, micron-scale XRF elemental maps and quantitative profiles of wet marine sediments. *Geochem. Geophys. Geosyst.* 8: Q05004.

Borreggine, M., S.E. Myhre, K.A.S. Mislan et al. 2017. A database of paleoceanographic sediment cores from the north Pacific, 1951-2016. *Earth Syst. Sci. Dat.* 9: 739-749.

Bourne, A.J. et al. 2016. Underestimated risks of recurrent long-range ash dispersal from northern Pacific-Arc volcanoes. *Nature Scientific Reports* 6: 29837.

Braitseva, O.A., I.V. Melekestsev, V.V. Ponomareva, L.D. Sulerzhitsky. 1995. The ages of calderas, large explosive craters and active volcanoes in the Kuril-Kamchatka region, Russia. *Bull. of Volcanology* 57: 383-402.

Braitseva, O.A., I.V. Melekestsev, L.D. Sulerzhitskii. 2005. New data on the Pleistocene deposits age in the Central Kamchatka depression. *Stratig. & Geol. Correl.* 13: 99-107.

Bralower T.J, I. Premoli Silva, M.J. Malone et al., eds. 2002. Shipboard Scientific Party. Site 1207. Proceedings of the Ocean Drilling Program Initial Reports 198. College Station: Ocean Drilling Program.

Brendryen, J., H. Haflidason, H.P. Sejrup. 2010. Norwegian Sea tephrostratigraphy of marine isotope stages 4 and 5: Prospects and problems for tephrochronology in the North Atlantic region. *Quat. Sci. Rev.* 29: 847-864.

Channell, J.E.T. et al. 2013. Data report: oxygen isotopes and foraminifer abundance record for the last glacial–629 interglacial cycle and marine isotope Stage 6 at IODP Site U1313. *Proc. I.O.D.P.* 303/306.

Chiyonobu, S., Mori, Y., Oda, M. 2012. Reconstruction of paleoceanographic conditions in the northwestern 631 Pacific Ocean over the last 500 kyr based on calcareous nannofossil and planktic foraminiferal assemblages. 632 *Marine Micropal.* 96-97: 29-37.

Clark, P.U. et al. 2012. Global climate evolution during the last deglaciation. *P.N.A.S* 109:

Colleoni, F., N. Kirchner, F. Niessen et al. 2016. An East Siberian ice shelf during the late Pleistocene glaciations: Numerical reconstructions. *Quat. Sci. Rev.* 147: 148-163.

Conolly, J.R., M. Ewing. 1970. Ice-rafted detritus in Northwest Pacific deep-sea sediments. In Hays, J.D. (Ed). *Geological Investigations of the North Pacific.* The Geological Society of America, Inc. Memoir 126.

D-Agostino, A., ARCO Exploitation Company. 1985. Foraminifers and coarse detritus from five deep-water sites, Deep Sea Drilling Project Leg 86, Northwest Pacific. *Deep Sea Drilling Project Initial Reports* 86: 337-347.

Derkachev et al. 2016. Tephra layers of in the Quaternary deposits of the Sea of Okhotsk: Distribution, composition, age and volcanic sources. *Quat. Int.* 425: 248-272.

Eynaud, F., L. de Abreu, A. Voelker et al. 2009. Position of the Polar Front along the western Iberian margin during key cold episodes of the last 45 ka. *Geochem., Geophys. Geosyst.* 10: Q07U05.

Fanning, A.F., Weaver, A.J. 1996. An atmospheric energy moisture-balance model: climatology, interpentadal climate change and coupling to an OGCM. J. Geophys. Res. 101, 15111-15128.

Fedorov, P.I. et al. 2011. Western Kamchatka-Koryak continental-margin volcanogenic belt: Age, composition and 644 sources. *Geochem. Int.* 49: 813-838..

Glushkova, O.Y. 2001. Geomorphological correlation of late Pleistocene glacial complexes of Western and Eastern Beringia. *Quat. Sci. Rev.* 20: 405-417.

Gong, X. et al. 2019. Enhanced North Pacific deep=ocean stratification by stronger intermediate water formation during Heinrich Stadial 1. *Nature Comm.* 10: 656.

Gorbarenko, S.A. 1996. Stable Isotope and Lithologic Evidence of Late-Glacial and Holocene Oceanography of the Northwestern Pacific and its Marginal Seas. *Quat. Res.* 46: 230-250.

Gorbarenko, S.A., D. Nürnberg, A.N. Derkachev et al. 2002. Magnetostratigraphy and tephrochronology of the Upper Quaternary sediments in the Okhotsk Sea: implication of terrigenous, volcanogenic and biogenic matter supply. M*arine Geol.* 183: 107-129.

Gorbarenko, S.A., P. Wang, R. Wang, X. Cheng. 2010. Orbital and suborbital environmental changes in the southern Bering Sea during the last 50 kyr. *Palaeog., Palaeoclim., Palaeoecol.* 286: 97-106.

Gorshkov, G.S. 1970. Volcanism and the upper mantle: investigations in the Kurile Island Arc. Plenum Press, New York, doi:10.1007/978-1-4684-1767-8.

Gray, W.R., J.W.B. Rae, R.C.J. Wills et al. 2018. Deglacial upwelling, productivity and $CO_2$ outgassing in the North Pacific Ocean. *Nat. Geosci.* 11: 340-344.

Green, C.J., Bigg, G.R., Green, J.A.M. 2010. Deep draft icebergs from the Barents Ice Sheet during MIS 6 are consistent with erosional evidence from Lomonosov Ridge, central Arctic. *Geophys. Res. Lett*. 37, L23606.

Griggs, A.J. et al. 2014. Optimising the use of marine tephrochronology in the North Atlantic: a detailed investigation of the Faroe Marine Ash Zones II, III and IV. *Quat. Sci. Rev.* 106: 122-139.

Grosswald, M.G. 1980. Late Weichselian ice sheet of northern Eurasia. *Quat. Res.* 13: 1-32.

Grosswald, M.G. 1998. Late-Weichselian ice sheets in Arctic and Pacific Siberia. *Quat. Int.* 45/46: 3-18.

Grosswald, M.G. 2003. The Arctic center of Quaternary ice and flood spreading: A deductive model. *Russ. J. of Earth Sci.* 5: 203-217.

Grosswald, M.G., T.J. Hughes. 1995. Paleoglaciology’s grand unsolved problem. *J. of Glaciol.* 41: 313-332.

Grosswald, M.G., T.J. Hughes. 1999. The case for an ice shelf in the Pleistocene Arctic Ocean. *Polar Geog.* 23: 23-54.

Grosswald, M.G., T. Hughes. 2002. The Russian Component of an Arctic Ice Sheet during the Last Glacial Maximum. *Quat. Sci. Rev.* 21: 121-146.

Grosswald, M.G., T.J. Hughes. 2005. “Back-arc” marine ice sheet in the Sea of Okhotsk. *Russ. J. of Earth Sci.* 7: ES5004.

Grosswald, M.G., V.B. Spektor. 1993. The glacial relief of the Tiksi region (west shore of Buor-Khaya Inlet, Northern Yakutia). *Polar Geog & Geol.* 17: 154-166.

Gualtieri, L., O. Glushkova, J. Brigham-Grette. 2000. Evidence for restricted ice extent during the last glacial maximum in the Koryak Mountains of Chutkotka, far eastern Russia. *Geol. Soc. of America* 112: 1106-1118.

Hanslik, D. et al. 2013. Biogenic and detrital-rich intervals in central Arctic Ocean cores identified using x-ray fluorescence scanning. *Polar Research* 32: 18386.

Harada, N., N. Ahagon, M. Uchida, M. Murayama. 2004. Northward and southward migrations of the frontal zones during the past 40 kyr in the Kuroshio-Oyashio transition area. *G3* 5: Q09004.

Hasegawa, T., H. Kishimoto, M. Nakagawa, J.-I. Itoh, T. Yamamoto. 2009. Eruptive history of post-caldera volcanoes of Kutcharo caldera,  eastern Hokkaido, Japan, as inferred from tephrostratigraphy in the Konsen and Shari areas for the period 35-12 ka. *J. Geol Soc. Jap.* 115: 369-390.

Haug, G.H., M.A. Maslin, M. Sarnthein, et al. 1995. Evolution of northwest Pacific sedimentation patterns since 6 Ma (Site 882). In Rea, D.K., I.A. Basov, D.W. Scholl, J.F. Allan (Eds). *Proc. of the Ocean Drill. Prog.* 145: 293-314.

Haug, G.H., D.M. Sigman, R. Tiedemann et al. 1999. Onset of permanent stratification in the subarctic Pacific Ocean. *Nature* 401: 779-782.

Haug. G.H. et al. 2001. Southward migration of the Intertropical Convergence Zone Through the Holocene. *Science* 293: 1304-1308.

Hayes, N. 2014. An investigation of the Late Pleistocene ice-rafted debris and volcanic ash record of IODP core 580: implications for volcano/glacier interaction in Kamchatka. *MPhys Dissertation, The University of Hull.*

Heath, G.R. et al. 1985. Site 580: Shipboard Scientific Party. *Init. Rep. Deep Sea Dr. Proj.* 86: 209-239.

Heath, R.G., L.H. Burckle. 2004. Wet bulk density (GRAPE) of Hole 86-580. *Pangaea.*

https://doi.org/10.1594/PANGAEA.225203

Heinrich, H. 1988. Origin and consequences of cyclic ice rafting in the Northeast Atlantic during the past 130,000 years. *Quat. Res.* 29: 142-152.

Hemming, S.R. 2004. Heinrich events: Massive late Pleistocene detritus layers of the North Atlantic and their global climate imprint. *Rev. of Geophys.* 42: RG1005.

Hendy, I.L. T. Cosma. 2008. Vulnerability of the Cordilleran Ice Sheet to iceberg calving during Late Quaternary rapid climate change events. *Paleoceanography* 23: PA2101.

Hennekam, R., G de Lange. 2012. X-ray fluorescence core scanning of wet marine sediments: methods to improve quality and reproducibility of high-resolution paleoenvironmental records. *Limn. and Oceanog.: Methods* 10: 991-1003.

Hewitt, A.T., D. McDonald, B.D. Bornhold. 1997. Ice-rafted debris in the North Pacific and correlation to North Atlantic climatic events. *Geophys. Res. Lett.* 24: 3261-3264.

Hovan, S.A., N.G. Pisias. 1989. A Direct Link Between The China Loess and Marine Delta-o-18 Records – Aeolian Flux in the North Pacific. *Nature* 340: 296-298.

Hovan, S.A., D.K. Rea, N.G. Pisias. 1991. Late Pleistocene continental climate and oceanic variability recorded in northwest Pacific sediments. *Paleoceanography* 6: 349-370.

Hughes, T.J., G.H. Denton, M.G. Grosswald. 1977. Was there a late-Würm Arctic ice sheet? *Nature* 266: 596-602.

Hughes, A.L. 2004. The ice-rafted debris record of ODP Site 883, Northwest Pacific. *MSc Thesis, Royal Holloway, University of London.*

Immonen, N., K. Strand, A. Huusko, J. P. Lunkka. 2014. Imprint of late Pleistocene continental processes visible in ice-rafted grains from the central Arctic Ocean. *Quat. Sci. Rev.* 92: 133-139.

Itoh, S., I. Yasuda. 2009. Characteristics of mesoscale eddies in the Kuroshio-Oyashio Extension region detected from the distribution of the sea surface height anomaly. *J. of Phys. Oceanog.* 40: 1018-1034.

Jaccard, S.L. et al. 2005. Glacial/Interglacial Changes in Subarctic North Pacific Stratification. *Science* 308: 1003-1006.

Jackson, E.D et al. 1980. Site 433: Suiko Seamount. *Init. Rep. Deep Sea Drill. Proj.* 55: 127-282.

Jonas, A-S. et al. 2017. Late Quaternary water temperature variations of the Northwest Pacific based on the lipid 677 paleothermometers TEXH 86,UK´37 and LDI. *Deep-Sea Research* 125: 81-93.

Jones, C.E., A.N. Halliday, D.K. Rea, R.M. Owen. 2000. Eolian inputs of lead to the North Pacific. *Geochem. Cosmo. Act.* 64: 1405-1416.

Jordan, J.W. 2001. Late Quaternary sea level change in Southern Beringia: postglacial emergence of the Western Alaskan Peninsula. *Quat. Sci. Rev.* 20: 509-523.

Keigwin, L.D. 1998. Glacial-age hydrography of the far northwest Pacific. *Paleoceanography* 13: 323-339.

Keigwin, L.D., G.A. Jones, P.N. Froelich. 1992. A 15,000 year paleoenvironmental record from Meiji Seamount, far northwestern Pacific. *E.P.S.L.* 111: 425-440.

Kent, D., N.D. Opdyke, M. Ewing. 1971. Climate change in the North Pacific using ice-rafted detritus as a climatic indicator. *Geol. Soc. of America Bull.* 82: 2741-2754.

Kiefer, T., M. Sarnthein, H. Erlenkeuser et al. 2001. North Pacific response to millennial-scale changes in ocean circulation over the last 60 kyr. *Paleoceanography* 16: 179-189.

Kimura, J.I., Y. Nagahashi, Y Satoguchi, C. Qing. 2015. Origins of felsic magmas in Japanese subduction zone: Geochemical characterizations of tephra from caldera-forming eruptions <5 Ma. *Geochem. Geophys. Geosyst.* 16: 2147-2174.

Klump, J, D Hebbeln, G Wefer. 2000. The impact of sediment provenance on barium-based productivity estimates. *Mar. Geol.* 169: 259-271.

Koizumi, I. 1994. Spectral analysis of the diatom paleotemperature records at DSDP Sites 579 and 580 near the subarctic front in the western North Pacific. *Palaeogeog., palaeoclim., Palaeoeco.* 108: 475-485.

Korff, L., T. von Dobeneck, T. Frederichs et al. 2016. Cyclic magnetite dissolution in Pleistocene sediments of the abyssal northwest Pacific Ocean: Evidence for glacial oxygen depletion and carbon trapping. *Paleoceanography* 31: 600-624

Kotilainen, A.T., N.J. Shackleton. 1995. Rapid climate variability in the North Pacific Ocean during the past 95,000 years. *Nature* 377: 323-326.

Krissek, L.A., J.L. Morley, D.K. Lofland. 1985. The occurrence, abundance, and composition of ice-rafted detritus in sediments from Deep Sea Drilling Project sites 579 and 580, Northwest Pacific. In Turner, K.L. (Ed). *Init. Rep. of the Deep Sea Drill. Proj.* LXXXVI: 647-655.

Krissek, L.A. 1995. Late Cenozoic ice-rafting records from Leg 145 sites in the north Pacific: Late Miocene onset, late Pliocene intensification, and Plocene-Pleistocene events. *In* Rea, D.K., I.A. Basov, D.W. Scholl, J.F. Allan (eds). *Proc. Ocean. Drill. Prog. Sci. Res.* 145: 179-194.

Kujau et al. 2010. Mississippi River discharge over the last ~560,000 years. Indications from X-ray fluorescence core-scanning. *Palaeogeog., Palaeoclim., Palaeoeco.* 298: 311-318.

Lane. C.S. et al. 2014. Cryptotephra as a dating and correlation tool in archaeology. *J. Arch. Sci.* 42: 42-50.

Leinen, M., J.M. Prospero, E. Arnold, M. Blank. 1994. Mineralogy of aeolian dust reaching the North Pacific Ocean 1. Sampling and analysis. *Journ. Geophys. Res.* 99: 21,017-21-023.

Levine, R.C., G.R. Bigg. 2008. Sensitivity of the glacial ocean to Heinrich events from different iceberg sources, as modelled by a coupled atmosphere-iceberg-ocean model. *Paleoceanography* 23: PA4213.

Levitan, M.A., T.G. Kuzmina, V.L. Luksha et al. 2013. Late Pleistocene sedimentation history of the Shirshov Ridge, Bering Sea. *Geochem. Int.* 51: 173-204.

Liguori, B.T.P, M.G. De Almeida, C.E. De Rezende. 2016. Barium and its importance as an indicator of (Paleo)Productivity. *Ann. Braz. Ac. Sci.* 88 (4): 2093-2103.

Lisieki, L., M. Raymo. 2005. A Pliocene-Pleistocene stack of 57 globally distributed benthic $\delta^{18}$O records. *Paleoceanography* 20: PA1003.

Llave, E., J. Schönfeld, F.J. Hernández-Molina et al. 2006. High-resolution stratigraphy of the Mediterrranean outflow contourite system in the Gulf of Cadiz during the late Pleistocene: The impact of Heinrich events. *Marine Geology* 227: 241-262.

Löwermark, L. et al. 2011. Normalizing XRF-scanner data: A cautionary note on the interpretation of high-resolution records from organic-rich lakes. *Journ. As. Earth. Sci.* 40: 1250-1256.

Lüer, V. et al. 2009. Radiolarian-based sea surface temperatures and paleoceonographic changes during the Late Pleistocene-Holocene in the subantarctic southwest Pacific. *Marine Micropal.* 70: 151-165.

Maccali, J., C. Hillaire-Marcel, C. Not. 2018. Radiogenic isotope (Nd, Pb, Sr) signatures of surface and sea ice-transported sediments from the Arctic Ocean under the present interglacial conditions. *Polar Research* 37: 2018.

Machida, H., F. Arai. 2003. Atlas of Tephra in and around Japan. University of Tokyo Press, Tokyo.

Mahowald, N. et al. 1999. Dust sources and deposition during last glacial maximum and current climate: A comparison of model results with paleodata from ice cores and marine sediments. *Journ. Geophys. Res.* 104: 15,895-15,916.

Maier, E. et al. 2018. North Pacific freshwater events linked to changes in glacial ocean circulation. *Nature* 559: 241-245.

Maslin, M.A., G.H. Haug, M. Sarnthein, R. Tiedemann. 1996. The progressive intensification of northern hemisphere glaciation as seen from the north Pacific. *Geol Rundsch* 85: 452-465.

Matsu'ura, T, J. Komatsubara, N. Ahagon. 2018. Using Late and Middle Pleistocene tephrostratigraphy and cryptotephrastratigraphy to refine age models of Holes ODP 1150A and ODP 1151C, NW Pacific Ocean: A cross-check between tephrostratigraphy and biostratigraphy. *Quat. Geochron.* 47: 29-53.

McCanta, M.C. et al. 2015. Identifying cryptotephra units using correlated rapid, nondestructive methods: VSWIR spectroscopy, X-ray fluorescence, and magnetic susceptibility. *Geochem., Geophys., Geosyst.* 16: doi.org/10.1002/2015GC005913.

McDonald, D., T.F. Pederson, J. Crusius. 1999. Multiple Late Quaternary episodes of exceptional diatom production in the Gulf of Alaska. *Deep Sea Res. II. Trop. Stud. Oceanog.* 46: 2993-3017.

McKelvey, B.C., W. Chen, R.J. Arculus. 1995. Provenance of Pliocene-Pleistocene ice-rafted debris, Leg 145, northern Pacific Ocean. In Rea, D.K., I.A. Basov, D.W. Scholl, J.F. Allan (Eds). *Proc. of the Ocean Drill. Prog.* 145: 195-204.

Molina-Kescher, M. Frank, E.C. Hathorne. 2014. Nd and Sr isotope compositions of different phases of surface sediments in the South Pacific: Extraction of seawater signatures, boundary exchange, and detrital/dust provenance. *Geochem., Geophys., Geosyst.* 15: 3502-3520.

Monien, D., G. Kuhn, H. von Eynatten, F.M. Talarico. 2012. Geochemical provenance analysis of fine-grained sediment revealing Late Miocene to recent paleo-environmental changes in the western Ross Sea, Antarctica. *Glob. & Plan. Chg.* 96-97: 41-58.

Muhs, D.R. 2018. Origin of last-glacial loess in the western Yukon-Tanana Upland, central Alaska, USA. *Quat. Res.* 2018: 1-23.

Murton, J.B. et al. 2015. Palaeoenvironmental Interpretation of Yedoma Silt (Ice Complex) Deposition as Cold-Climate Loess, Duvanny Yar, Northeast Siberia. *Perm. Peri. Proc.* 26: 208-288.

Nadeau, M. J. et al. 2001. Carbonate C-14 background: Does it have multiple personalities? *Radiocarbon* 43: 169-176.

Nagashima, K. et al. 2011. Millennial-scale oscillations of the westerly jet path during the last glacial period. *Journ. Asian Earth Sci.* 40: 1214-1220.

Nave, S. et al. 2007. Primary productivity response to Heinrich events in the North Atlantic Ocean and Norwegian Sea. *Paleoceanography* 22: PA3216.

Niessen, F., J.K. Hong, A. Hegewald et al. 2013. Repeated Pleistocene glaciation of the East Siberian continental margin. *Nature Geoscience* 6: 842-846.

Nizou, J. et al. 2010. The Senegal River mud belt: A high resolution archive of paleoclimatic change and coastal evolution. *Marine Geology* 278: 150-164.

Ng, H.C., L.F. Robinson, J.F. McManus et al. 2018. Coherent deglacial changes in western Atlantic Ocean circulation. *Nat. Comm.* 9: 2947.

North, R.T. 2015. Deciphering the role of varying iceberg source in abrupt climate change. *PhD Thesis,* Cardiff University .

Nürnberg, D., D. Dethleff, R. Tiedemann et al. 2011. Okhotsk Sea ice coverage and Kamchatka glaciation over the last 350 ka – Evidence from ice-rafted debris and planktonic $\delta^{18}$O. *Palaeog., Palaeoclim., Palaeoeco.* 310: 191-205.

Nürnberg, D., R. Tiedemann. 2004. Environmental change on the Sea of Okhotsk during the last 1.1 million years. *Paleoceanography* 19: PA4011.

Ohkushi, K. et al. 2016. Intensification of North Pacific intermediate water ventilation during the Younger Dryas. *Geo-Mar Lett.* 36: 353-360.

Okada, H. 1980. Pebbles and carbonate nodules from Deep Sea Drilling Project Leg 56 cores. *Init. Rep. of the Deep Sea Drill. Proj.* 56: 1089. AGU, Washington DC.

Okamoto, T., E. Matsumoto, H. Kawabata. 2002. Fluctuations of aeolian dust over the past 200,000 years as seen from quartz in the deep-sea cores of the North Pacific Ocean. *Quat. Stud.* 41: 35-44.

Ovsepyan, E.A., E.V. Ivanova, L. Lembke-Jene et al. 2017. Penultimate and last glacial oceanographic variations in the Bering Sea on millennial timescales: links to North Atlantic climate. *Quat. Sci. Rev.* 163: 135-151.

Parfenov, L.M. 1991. Tectonics of the Verkhoyansk-Kolyma Mesozoides in the context of plate tectonics. *Tectonophysics* 199: 319-342.

Pettke, T., A.N. Halliday, C.M. Hall, D.K. Rea. 2000. Dust production and deposition in Asia and the north Pacific Ocean over the past 12 Myr. *Earth Plan. Sci. Lett.* 178: 397-413.

Pickart, R.S., G.W.K. Moore, A.M. Macdonald et al. 2009. Seasonal evolution of Aleutian low pressure systems: Implications for the North Pacific Subpolar Circulation. *J. of Phys. Oceanog.* 9: 1317-1339.

Polyak, L., M.H. Edwards, B.J. Coakley, M. Jackobsson. 2001. Ice shelves in the Pleistocene Arctic Ocean inferred from glacigenic deep-sea bedforms. *Nature* 410: 453-458.

Ponomareva, V., M. Portnyagin, A. Derkachev et al. 2013. Identification of a widespread Kamchatkan tephra: A middle Pleistocene tie-point between Arctic and Pacific paleoclimatic records. *Geophys. Res. Lett.* 40: 3538-3543.

Ponomareva, V. M. et al. 2017. A full Holocene tephrochronology for the Kamchatsky Peninsula region: Applications from Kamchatka to North America. *Quat. Sci. Rev.* 168: 101-122.

Prueher, L.M., D.K. Rea. 2001. Volcanic triggering of late Pliocene glaciation: evidence from the flux of volcanic glass and ice-rafted debris to the North Pacific Ocean. *Palaeogeog., Palaeoclim,, Palaeoeco.* 173: 215-2 30.

Rea, D.K. et al. 1995. Scientific results of drilling the north Pacific transect. *In* Rea et al. eds. *Proc. Ocean. Drill. Prog, Sci. Res.* 145: 577-596.

Rea, B et al. 2018. Extensive marine-terminating ice sheets in Europe from 2.5 million years ago, *Sci. Adv.* 4 (6).

Reimer, P.J. et al., 2013. IntCal13 and Marine13 Radiocarbon Age Calibration Curves 0-50,000 Years Cal BP. *Radiocarbon* 55: 1869-1887.

Richter, T.O. et al. 2006. The Avaatech XRF core scanner: Technical description and applications to NE Atlantic sediments. *Geol. Soc. Lond. Spec. Pub.* 267: 39-50.

Rothwell, R.G., I.W. Croudace. 2015. 20 Years of XRF Core Scanning Marine Sediments: What Do Geochemical Proxies Tell us? *In* Croudace, I.W., R.G. Rothwell eds. *Micro-XRF Studies of Sediment Cores: Applications of a non-destructive tool for the environmental sciences.* Springer.

Ruddiman, W.F., L.K. Glover. 1972. Vertical mixing of ice-rafted volcanic ash in North Atlantic sediments. *Geological Society of America Bulletin* 83: 2817-2836.

Sánchez-Gońi, M.F. S. Harrison. 2010. Millennial-scale climate variability and vegetation changes during the Last Glacial: Concepts and Terminology. *Quat. Sci. Rev.* 29: 2823-2827.

Seo, I., Y. Lee, C.M. Yoo, K. Hyeong. 2018. Migrations of the Kuroshio Extension in the northwest Pacific since the Last Glacial Maximum. *Palaeogeog., Palaeoclim., Palaeoeco.* 496: 323-331.

Serno, S. et al. 2014. Eolian dust input to the Subarctic North Pacific. *Earth Plan. Sci. Lett.* 387: 252-263.

Serno, S. et al. 2015. Comparing dust flux records from the Subarctic North Pacific and Greenland: Implications for atmospheric transport to Greenland and for the application of dust as a chronostratigraphic tool. *AGU Paleoc.* 10.1002/2014PA002748.

Shcherbina, A. Y., L.D. Talley., D.L. Rudnick. 2003. Direct Observations of North Pacific Ventilation: Brine Rejection in the Okhotsk Sea. *Science* 302: 1952-1955.

Shackleton, N.J., J. Backman, H. Zimmerman et al. 1984. Oxygen isotope calibration of the onset of ice-rafting in DSDP Site 552A: history of glaciation in the North Atlantic Region. *Nature* 307: 620-623.

Siddall, M. et al. 2003. Sea-level fluctuations during the last glacial cycle. *Nature* 423, 853-858.

Smith, V.C. et al. 2013. Identification and correlation of visible tephras in the Lake Suigetsu SG06 sedimentary archive, Japan: Chronostratigraphic markers for synchronising of east Asian/west Pacific Pacific palaeoclimatic records for 150ka. *Quat. Sci. Rev.* 61: 121-137.

Solomina, O., P.E. Calkin. 2003. Lichenometry as applied to moraines in Alaska, U.S.A., and Kamchatka, Russia. *Arctic, Antarctic, & Alp. Res.* 35: 129-143.

Stauch, G., L. Gualtieri. 2008. Late Quaternary glaciations in northeastern Russia. *J. of Quat. Sci.* 23: 545-558.

Stauch, G., F. Lehmkuhl. 2010. Quaternary glaciations in the Verkhoyansk Mountains, Northeast Siberia. *Quat. Res.* 74: 145-155.

Stuiver, M., Polach, H. A. 1977. Discussion; reporting of C-14 data. *Radiocarbon* 19: 355-363.

Stuiver, M et al. 2020. CALIB 8.2. http://calib.org. Accessed 05/09/2020.

St. John, K., S. Passchier, B. Tantillo et al. 2015. Microfeatures of modern sea-ice-rafted sediment and implications for paleo-sea-ice reconstructions. *Annals of Glaciology* 56(69): 83-93.

St. John, K.E.K., L.A. Krissek. 1999. Regional patterns of Pleistocene ice-rafted debris flux in the North Pacific. *Paleoceanography* 14: 653-662.

Swann, G.E.A. 2010. Salinity changes in the North West Pacific Ocean during the late Pliocene/early Quaternary from 2.73Ma to 2.52Ma. *E.P.S.L.* 297: 332-338.

Talley, L.D. 1991. An Okhotsk Sea water anomaly: implications for ventilation in the north Pacific. *Deep-Sea R.* 38: 8171-8190.

Thompson, P.R. 1981. Planktonic foraminifera in the western north Pacific during the past 150,000 years: comparison of modern and fossil assemblages. *Palaeogeog., Palaeoclim., Palaeoeco.* 35: 241-279.

Thompson, P.R., N.J. Shackleton. 1980. North Pacific palaeoceanography: Late Quaternary coiling variations of planktonic foraminifer *Neogloboquadrina pachyderma*. *Nature* 287: 829-833.

Tjallingii, R. 2006. Application and quality of X-ray fluorescence core scanning in reconstructing late Pleistocene NW African continental margin sedimentation patterns and paleoclimate variations. PhD Thesis. University of Bremen.

Uesawa, S., M. Nakagawa, A. Umetsu. 2016. Explosive eruptive history and temporal magmatic changes at Yotai Volcano during the last 50,000 year, southwest Hokkaido, Japan. *J. Volc. and Geotherm. Res.* 325: 27-44.

Vanin, N.S. 2013. An experience of using the Turner Angle for differentiating water structures in the northwest Pacific. *Russian Meteorol. & Hydrol.* 10: 688-693.

VanLaningham, S., N.G. Pisias, R.A. Duncan, P.D. Clift. 2009. Glacial-interglacial sediment transport from the Meiji Drift, northwest Pacific Ocean: Evidence for timing of Beringian outwashing. *Earth Plan. Sci. Lett.* 277: 64-72.

Van Meerbeeck, C.J., H. Renssen, D.M. Roche. 2009. How did Marine Isotope Stage 3 and Last Glacial Maximum climates differ? – Perspectives from equilibrium simulations. *Clim. Past.* 5: 33-51.

Von Huene, R., J. Crouch, E. Larson. 1976. Glacial advance in the Gulf of Alaska area implied by ice-rafted material. *Geol. Soc. of America Mem.* 145: 411-422.

Wadley, M.R., Bigg, G.R. 2000. Implementation of variable time stepping in an ocean general circulation model. *Ocean Model.* 1, 71-80.

Wagner, T.J.W., Stern, A.A., Dell, R.W., Eisenman, I. 2017. On the representation of capsizing in iceberg models. Ocean Model. 117: 88-96.

Wang, K-S., X-F. Shi, J.J. Zou et al. 2017. Sediment provenance variations in the southern Okhotsk Sea over the last 180 ka: Evidence from light and heavy minerals. *Palaeogeog., Palaeoclim., Palaeoeco.* 479: 61-70.

Wang, N., D. Jiang, X. Lang. 2018. Northern Westerlies during the Last Glacial Maximum: Results from CMIP5 Simulations. Journ. Clim. 31: 1135-1153.

Weltje, G.J., R. Tjallingii. 2008. Calibration of XRF core scanners for quantitative geochemical logging of sediment cores: Theory and application. *Earth. Plan. Sci. Lett.* 274: 423-438.

Weltje et al. 2015. Prediction of Geochemical Composition from XRF Core Scanner Data: A New Multivariate Approach Including Automatic Selection of Calibration Samples and Quantification of Uncertainties. *In* Croudace, I.W., R.G. Rothwell. *Micro-XRF studies of sediment cores.* Chapter 21. Springer.

Westerhold, T., U. Röhl, H.K. McCarren, J.C. Zachos. 2009. Latest on the absolute age of the Paleocene-Eocene Thermal Maximum (PETM): New insights from exact stratigraphic position of key ash layers + 19 and – 17. *Earth. Plan. Sci. Lett.* 287: 412-419.

Wiesner, M.G. et al. 2005. Grain size, areal thickness distribution and controls on sedimentation of the 1991 Mount Pinatubo tephra layer in the South China Sea. *Bull. Volc.* 67: 490-495.

Winter, D., J. Arney, S.W. Wise JR. 2005.Upper Miocene-Pleistocene Diatom Biostratigraphy in the Northwest Pacific, ODP Leg 191. *In* Sager, W.W., T. Kanazawa, C. Esculta, eds. Proc. ODP, Sci. Res., 191, 1-35.

XRF Core Scanner user manual version 2.0. (C) N.I.O.Z. & Avaatech 20/08/2007. https://epic.awi.de/id/eprint/37355/4/XRFCore-Scanner_user-manualV2.pdf. Lat accessed 28/09/2020.

Yamane, M. 2003. Late Quaternary variations in water mass in the Shatsky Rise area, northwest Pacific Ocean. *Marine Micropaleont.* 48: 205-223.

Yasuda, I. 2003. Hydrographic structure and variability in the Kuroshio-Oyashio Transition area. *J. of Oceanog.* 59: 389-402.

Yasuhara, M, A. Atushi, Y. Iba 2017. Past emergent phase of Shatsky Rise deep-marine igneous plateau. *Nature Scientific Reports* 7: 15423.

Yoneda et al. 2007. Radiocarbon marine reservoir ages in the western Pacific estimated by pre-bomb molluscan 743 shells. *Nuclear Instruments and Methods in Physics Research B* 259: 432-437.

Zamoruyev, V. 2004. Quaternary glaciation of north-eastern Asia. In Ehlers, J., P.L. Gibbard. (Eds.). *Quaternary Glaciations – Extent and Chronology, Part III: South America, Asia, Africa, Australia, Antarctica.* Elsevier, Amsterdam: pp. 321-323.

## Appendix 1: Weights table for ODP 1207A

Note: At depths where there are no weights, samples were not present.

| Depth (cm) | Sample weight (g) | >150µm (g) | 63-150µm (g) | <63µm (g) | <150µm (g) |
|---|---|---|---|---|---|
| 1 | 8.2195 | 0.2748 | 0.4072 | 7.5375 | |
| 2 | 4.683 | 0.1114 | | | 4.5716 |
| 3 | 4.8333 | 0.1187 | 0.1485 | 4.5661 | |
| 4 | 3.9929 | 0.1581 | | | 3.8348 |
| 5 | 3.7338 | 0.0766 | 0.1557 | 3.5015 | |
| 6 | 4.3822 | 0.139 | 0.1849 | 4.0583 | |
| 7 | 2.31 | 0.0573 | 0.0853 | 2.1674 | |
| 8 | 0.7188 | 0.0243 | | | 0.6945 |
| 9 | 2.6975 | 0.0694 | | | 2.6281 |
| 10 | 5.3343 | 0.1989 | 0.383 | 4.7524 | |
| 11 | | | | | |
| 12 | 4.1381 | 0.1075 | 0.1632 | 3.8674 | |
| 13 | 7.4964 | 0.2811 | 0.3476 | 6.8677 | |
| 14 | 6.7361 | 0.2214 | | | 6.5147 |
| 15 | 2.5461 | 0.071 | 0.1318 | 2.3433 | |
| 16 | 2.2418 | 0.0316 | 0.0819 | 2.1283 | |
| 17 | 2.4815 | 0.088 | | | 2.3935 |
| 18 | 2.9109 | 0.0667 | 0.1431 | 2.7011 | |
| 19 | 4.8923 | 0.1663 | | | 4.726 |
| 20 | 3.3497 | 0.1096 | 0.2641 | 2.976 | |
| 21 | 4.1743 | 0.0401 | 0.1784 | 3.9558 | |
| 22 | 4.9283 | 0.0667 | | | 4.8616 |
| 23 | 3.9492 | 0.0439 | 0.1084 | 3.7969 | |
| 24 | 3.8569 | 0.11 | 0.2405 | 3.5064 | |
| 25 | | | | | |
| 26 | | | | | |
| 27 | | | | | |
| 28 | 3.3932 | 0.2317 | | | 3.1615 |
| 29 | 5.4379 | 0.1623 | 0.2889 | 4.9867 | |
| 30 | 4.1678 | 0.1109 | 0.2231 | 3.8338 | |
| 31 | 4.2842 | 0.156 | | | 4.1282 |
| 32 | 4.3281 | 0.1336 | 0.1583 | 4.0362 | |
| 33 | 3.1805 | 0.0787 | | | 3.1018 |
| 34 | 3.5763 | 0.072 | 0.1974 | 3.3069 | |
| 35 | 4.1283 | 0.1528 | 0.2314 | 3.7441 | |
| 36 | 1.4244 | 0.0763 | | | 1.3481 |
| 37 | 1.9491 | 0.0599 | 0.0795 | 1.8097 | |
| 38 | 4.0251 | 0.167 | | | 3.8581 |
| 39 | | | | | |
| 40 | 2.1505 | 0.0852 | 0.1184 | 1.9469 | |

| | | | | | |
|---|---|---|---|---|---|
| 41 | 3.4076 | 0.0862 | 0.1494 | 3.172 | |
| 42 | 3.0853 | 0.0648 | 0.1428 | 2.8777 | |
| 43 | 2.0846 | 0.0534 | 0.0905 | 1.9407 | |
| 44 | 4.1744 | 0.1468 | | | 4.0276 |
| 45 | 4.4421 | 0.2154 | 0.2885 | 3.9382 | |
| 46 | 3.7963 | 0.1452 | 0.2872 | 3.3639 | |
| 47 | 2.1806 | 0.0995 | 0.1379 | 1.9432 | |
| 48 | 5.2002 | 0.2352 | | | 4.965 |
| 49 | 4.0182 | 0.2037 | 0.3399 | 3.4746 | |
| 50 | 4.1038 | 0.2265 | | | 3.8773 |
| 51 | 2.3183 | 0.1292 | 0.2166 | 1.9725 | |
| 52 | 3.3118 | 0.1152 | 0.1183 | 3.0783 | |
| 53 | 4.1537 | 0.2579 | | | 3.8958 |
| 54 | 5.4903 | 0.3101 | 0.2077 | 4.9725 | |
| 55 | 3.3634 | 0.3539 | 0.3057 | 2.7038 | |
| 56 | 3.3451 | 0.2319 | | | 3.1132 |
| 57 | 2.8527 | 0.177 | 0.1444 | 2.5313 | |
| 58 | 4.6755 | 0.3291 | | | 4.3464 |
| 59 | 3.0205 | 0.1232 | 0.1309 | 2.7664 | |
| 60 | 1.9184 | 0.0971 | 0.1388 | 1.6825 | |
| 61 | 4.0516 | 0.1637 | | | 3.8879 |
| 62 | 4.9128 | 0.1707 | 0.1517 | 4.5904 | |
| 63 | 4.1219 | 0.2227 | | | 3.8992 |
| 64 | 5.1902 | 0.2324 | 0.1084 | 4.8494 | |
| 65 | 1.1798 | 0.0836 | 0.1494 | 0.9468 | |
| 66 | 2.723 | 0.1475 | | | 2.5755 |
| 67 | 4.697 | 0.1657 | 0.1362 | 4.3951 | |
| 68 | 2.5854 | 0.1266 | | | 2.4588 |
| 69 | 3.8786 | 0.1093 | 0.1005 | 3.6688 | |
| 70 | 3.5667 | 0.2039 | 0.2874 | 3.0754 | |
| 71 | 2.8656 | 0.1926 | | | 2.673 |
| 72 | | | | | |
| 73 | 3.4409 | 0.146 | 0.0793 | 3.2156 | |
| 74 | 5.7344 | 0.3625 | | | 5.3719 |
| 75 | 2.2779 | 0.1991 | 0.1982 | 1.8806 | |
| 76 | 1.1676 | 0.0582 | 0.1259 | 0.9835 | |
| 77 | 2.8807 | 0.1363 | 0.0795 | 2.6649 | |
| 78 | 3.6316 | 0.2184 | | | 3.4132 |
| 79 | 3.0082 | 0.1648 | | | 2.8434 |
| 80 | 4.0081 | 0.2804 | 0.2781 | 3.4496 | |
| 81 | 3.9336 | 0.1768 | 0.1401 | 3.6167 | |
| 82 | 3.8086 | 0.1879 | 0.1334 | 3.4873 | |
| 83 | 4.4223 | 0.1992 | 0.2124 | 4.0107 | |
| 84 | | | | | |
| 85 | 3.7815 | 0.2771 | 0.2369 | 3.2675 | |
| 86 | 3.3225 | 0.1847 | | | 3.1378 |
| 87 | 3.2908 | 0.1566 | | | 3.1342 |
| 88 | 4.5627 | 0.1951 | 0.1619 | 4.2057 | |

| | | | | | |
|---|---|---|---|---|---|
| 89 | 4.9603 | 0.2474 | | | 4.7129 |
| 90 | 3.8173 | 0.2074 | 0.2229 | 3.387 | |
| 91 | 4.0902 | 0.1435 | 0.1091 | 3.8376 | |
| 92 | 4.2202 | 0.1417 | | | 4.0785 |
| 93 | 4.6448 | 0.179 | 0.1559 | 4.3099 | |
| 94 | 4.3355 | 0.1268 | | | 4.2087 |
| 95 | 3.7443 | 0.1124 | 0.1587 | 3.4732 | |
| 96 | 3.9221 | 0.089 | 0.0993 | 3.7338 | |
| 97 | 1.8402 | 0.0513 | | | 1.7889 |
| 98 | 4.6439 | 0.0953 | 0.0904 | 4.4582 | |
| 99 | 3.7461 | 0.1229 | | | 3.6232 |
| 100 | 3.5957 | 0.1587 | 0.1865 | 3.2505 | |
| 101 | 5.3898 | 0.2371 | 0.348 | 4.8047 | |
| 102 | 4.5532 | 0.184 | 0.1399 | 4.2293 | |
| 103 | 4.9198 | 0.2005 | | | 4.7193 |
| 104 | 5.7279 | 0.1264 | 0.1502 | 5.4513 | |
| 105 | 6.3031 | 0.2548 | 0.3254 | 5.7229 | |
| 106 | | 0.0933 | 0.0892 | | |
| 107 | 3.6262 | 0.1466 | | | 3.4796 |
| 108 | 3.4804 | 0.1397 | 0.1183 | 3.2224 | |
| 109 | | | | | |
| 110 | 3.9221 | 0.1196 | 0.1842 | 3.6183 | |
| 111 | 3.8024 | 0.0416 | 0.0907 | 3.6701 | |
| 112 | 5.1428 | 0.0528 | | | 5.09 |
| 113 | 3.3998 | 0.0326 | 0.072 | 3.2952 | |
| 114 | 3.8142 | 0.0863 | 0.1601 | 3.5678 | |
| 115 | 3.8479 | 0.0368 | 0.1268 | 3.6843 | |
| 116 | 2.2406 | 0.0243 | 0.0551 | 2.1612 | |
| 117 | 2.6229 | 0.0203 | | | 2.6026 |
| 118 | 2.3118 | 0.0147 | 0.0751 | 2.222 | |
| 119 | 4.2612 | 0.0733 | | | 4.1879 |
| 120 | 4.1158 | 0.0446 | 0.1209 | 3.9503 | |
| 121 | 4.8305 | 0.0909 | 0.1095 | 4.6301 | |
| 122 | 4.586 | 0.0788 | 0.1285 | 4.3787 | |
| 123 | 6.7798 | 0.0723 | | | 6.7075 |
| 124 | 4.8495 | 0.0381 | 0.132 | 4.6794 | |
| 125 | 3.7234 | 0.0271 | 0.1171 | 3.5792 | |
| 126 | 3.5448 | 0.0238 | 0.0991 | 3.4219 | |
| 127 | 4.5574 | 0.0548 | | | 4.5026 |
| 128 | 4.1299 | 0.025 | 0.1006 | 4.0043 | |
| 129 | 4.8809 | 0.0303 | | | 4.8506 |
| 130 | 5.2477 | 0.0398 | 0.1328 | 5.0751 | |
| 131 | 4.4482 | 0.0531 | 0.1215 | 4.2736 | |
| 132 | 5.3239 | 0.0594 | 0.1809 | 5.0836 | |
| 133 | 4.8157 | 0.0528 | | | 4.7629 |
| 134 | 4.011 | 0.0479 | 0.1322 | 3.8309 | |
| 135 | 5.8813 | 0.0577 | 0.2003 | 5.6233 | |
| 136 | 6.7854 | 0.1294 | 0.2528 | 6.4032 | |

| | | | | | |
|---|---|---|---|---|---|
| 137 | | 0.04 | | | 8.64 |
| 138 | | | | | |
| 139 | | | | | |
| 140 | | | | | |
| 141 | | | | | |
| 142 | | | | | |
| 143 | | | | | |
| 144 | | | | | |
| 145 | | | | | |
| 146 | | | | | |
| 147 | | | | | |
| 148 | | | | | |
| 149 | | | | | |
| 150 | | | | | |
| 151 | | 0.04 | | | 6.8 |
| 152 | | 0.08 | | | 6.23 |
| 153 | 7.4181 | 0.1681 | | | 7.25 |
| 154 | | 0.03 | | | 7.16 |
| 155 | 4.0601 | 0.076 | 0.2829 | 3.7012 | |
| 156 | 2.7122 | 0.0448 | 0.27 | 2.3974 | |
| 157 | 5.1711 | 0.1116 | | | 5.0595 |
| 158 | 5.98 | 0.03 | | | 5.95 |
| 159 | 6.9309 | 0.203 | | | 6.7279 |
| 160 | 5.3592 | 0.1399 | 0.6094 | 4.6099 | |
| 161 | 5 | 0.02 | | | 4.98 |
| 162 | 5.13 | 0.01 | | | 5.12 |
| 163 | 6.61 | 0.02 | | | 6.59 |
| 164 | 7.41 | 0.02 | | | 7.39 |
| 165 | 4.12 | 0.06 | | | 4.06 |
| 166 | 2.51 | 0.01 | | | 2.5 |
| 167 | 3.21 | 0.02 | | | 3.19 |
| 168 | 1.81 | 0.01 | | | 1.8 |
| 169 | 2.49 | 0.01 | | | 2.48 |
| 170 | 3.05 | 0.02 | | | 3.03 |
| 171 | 4.61 | 0.03 | | | 4.58 |
| 172 | 4.6564 | 0.0259 | 0.1816 | 4.4489 | |
| 173 | 5.2 | 0.02 | | | 5.18 |
| 174 | 3.725 | 0.1005 | | | 3.6245 |
| 175 | | | | | |
| 176 | 3.6305 | 0.0615 | | | 3.569 |
| 177 | 4.067 | 0.0813 | 0.1402 | 3.8455 | |
| 178 | | | | | |
| 179 | 3.2736 | 0.034 | | | 3.2396 |
| 180 | 5.66 | 0.04 | | | 5.62 |
| 181 | 5.9699 | 0.1141 | 0.2919 | 5.5639 | |
| 182 | 5.0232 | 0.0978 | 0.2035 | 4.7219 | |
| 183 | 3.847 | 0.1115 | | | 3.7355 |
| 184 | 4.9248 | 0.0901 | 0.2045 | 4.6302 | |

| | | | | | |
|---|---|---|---|---|---|
| 185 | 5.1 | 0.02 | | | 5.08 |
| 186 | 1.5952 | 0.0244 | | | 1.5708 |
| 187 | 3.3701 | 0.0723 | | | 3.2978 |
| 188 | 4.4866 | 0.0443 | 0.1836 | 4.2587 | |
| 189 | 3.8226 | 0.0789 | | | 3.7437 |
| 190 | 3.45 | 0.03 | | | 3.42 |
| 191 | 2.494 | 0.0443 | 0.0909 | 2.3588 | |
| 192 | 2.6638 | 0.0403 | 0.0975 | 2.526 | |
| 193 | 4.4939 | 0.0864 | | | 4.4075 |
| 194 | 6.0566 | 0.0786 | 0.2158 | 5.7622 | |
| 195 | 4.618 | 0.126 | | | 4.492 |
| 196 | 2.0647 | 0.118 | | | 1.9467 |
| 197 | 2.4292 | 0.0833 | 0.1502 | 2.1957 | |
| 198 | 4.8814 | 0.1616 | | | 4.7198 |
| 199 | 6.1159 | 0.2006 | 0.2621 | 5.6532 | |
| 200 | 6.1219 | 0.1399 | 0.6778 | 5.3042 | |
| 201 | 5.7268 | 0.1999 | | | 5.5269 |
| 202 | 5.503 | 0.1376 | 0.2035 | 5.1619 | |
| 203 | 5.5106 | 0.1939 | 0.2645 | 5.0522 | |
| 204 | 5.7638 | 0.2064 | | | 5.5574 |
| 205 | 5.0096 | 0.1683 | | | 4.8413 |
| 206 | 2.204 | 0.0584 | 0.092 | 2.0536 | |
| 207 | 4.2901 | 0.1155 | | | 4.1746 |
| 208 | 3.8123 | 0.041 | 0.1593 | 3.612 | |
| 209 | 4.6462 | 0.1045 | | | 4.5417 |
| 210 | 4.2808 | 0.1346 | | | 4.1462 |
| 211 | 6.4655 | 0.1565 | 0.2278 | 6.0812 | |
| 212 | 5.1293 | 0.1844 | 0.1986 | 4.7463 | |
| 213 | 4.3468 | 0.1579 | | | 4.1889 |
| 214 | 3.7303 | 0.1461 | 0.1647 | 3.4195 | |
| 215 | 5.6038 | 0.1935 | 0.2313 | 5.179 | |
| 216 | 4.8929 | 0.23 | 0.2061 | 4.4568 | |
| 217 | 6.1117 | 0.2726 | | | 5.8391 |
| 218 | 6.4517 | 0.2415 | 0.3639 | 5.8463 | |
| 219 | 7.7068 | 0.3653 | | | 7.3415 |
| 220 | 5.3514 | 0.3157 | 0.3347 | 4.701 | |
| 221 | 6.2641 | 0.3399 | 0.3512 | 5.573 | |
| 222 | 5.9734 | 0.2605 | | | 5.7129 |
| 223 | 7.8651 | 0.247 | 0.3024 | 7.3157 | |
| 224 | 5.8205 | 0.2628 | | | 5.5577 |
| 225 | 4.4944 | 0.2438 | | | 4.2506 |
| 226 | 2.2435 | 0.09 | 0.1073 | 2.0462 | |
| 227 | 4.282 | 0.1625 | | | 4.1195 |
| 228 | 6.4364 | 0.1927 | 0.2526 | 5.9911 | |
| 229 | 7.7395 | 0.3295 | | | 7.41 |
| 230 | 6.272 | 0.268 | 0.2282 | 5.7758 | |
| 231 | 8.0567 | 0.3053 | 0.2293 | 7.5221 | |
| 232 | 7.1613 | 0.2407 | 0.2164 | 6.7042 | |

| | | | | | |
|---|---|---|---|---|---|
| 233 | 7.3274 | 0.3106 | | | 7.0168 |
| 234 | 6.8989 | 0.2527 | 0.2103 | 6.4359 | |
| 235 | 7.6629 | 0.3662 | | | 7.2967 |
| 236 | 3.1806 | 0.1197 | | | 3.0609 |
| 237 | 4.9174 | 0.1657 | 0.2534 | 4.4983 | |
| 238 | 5.8683 | 0.1318 | | | 5.7365 |
| 239 | 6.9899 | 0.2542 | 0.2384 | 6.4973 | |
| 240 | 7.6471 | 0.3247 | 0.2299 | 7.0925 | |
| 241 | 3.9544 | 0.175 | | | 3.7794 |
| 242 | 3.8282 | 0.1061 | 0.1024 | 3.6197 | |
| 243 | 3.8028 | 0.1143 | | | 3.6885 |
| 244 | 5.8279 | 0.1731 | 0.2197 | 5.4351 | |
| 245 | 3.0361 | 0.1046 | | | 2.9315 |
| 246 | 4.3651 | 0.1811 | | | 4.184 |
| 247 | 5.5829 | 0.1919 | 0.2335 | 5.1575 | |
| 248 | 5.2145 | 0.1799 | | | 5.0346 |
| 249 | 5.1639 | 0.1751 | 0.1976 | 4.7912 | |
| 250 | 5.7698 | 0.3045 | | | 5.4653 |
| 251 | | | | | |
| 252 | 5.1342 | 0.334 | | | 4.8002 |
| 253 | 4.4394 | 0.2042 | 0.2999 | 3.9353 | |
| 254 | 4.7693 | 0.261 | | | 4.5083 |
| 255 | | | | | |
| 256 | | | | | |
| 257 | 4.276 | 0.2941 | 0.7658 | 3.2161 | |
| 258 | 4.7839 | 0.2391 | 0.3899 | 4.1549 | |
| 259 | 4.347 | 0.3002 | | | 4.0468 |
| 260 | | | | | |
| 261 | 5.1461 | 0.2549 | 0.2582 | 4.633 | |
| 262 | 5.7675 | 0.2099 | 0.3122 | 5.2454 | |
| 263 | 5.7454 | 0.2541 | | | 5.4913 |
| 264 | 3.4592 | 0.1416 | 0.1955 | 3.1221 | |
| 265 | 4.8089 | 0.2263 | | | 4.5826 |
| 266 | 5.2239 | 0.2922 | | | 4.9317 |
| 267 | | | | | |
| 268 | | | | | |
| 269 | | | | | |
| 270 | 4.4848 | 0.217 | 0.1827 | 4.0851 | |
| 271 | 5.0119 | 0.326 | | | 4.6859 |
| 272 | 5.2169 | 0.281 | 0.2309 | 4.705 | |
| 273 | 4.2135 | 0.2309 | | | 3.9826 |
| 274 | 4.7705 | 0.1278 | 0.2239 | 4.4188 | |
| 275 | 5.0974 | 0.3698 | | | 4.7276 |
| 276 | 4.7745 | 0.291 | | | 4.4835 |
| 277 | 4.0505 | 0.1686 | 0.266 | 3.6159 | |
| 278 | 5.7235 | 0.3508 | | | 5.3727 |
| 279 | 5.0487 | 0.2091 | 0.187 | 4.6526 | |
| 280 | 5.3045 | 0.2518 | 0.2665 | 4.7862 | |

| | | | | | |
|---|---|---|---|---|---|
| 281 | 6.3213 | 0.2492 | | | 6.0721 |
| 282 | | | | | |
| 283 | | | | | |
| 284 | 3.5638 | 0.0894 | 0.123 | 3.3514 | |
| 285 | 5.3364 | 0.1512 | 0.1331 | 5.0521 | |
| 286 | 5.3223 | 0.1918 | | | 5.1305 |
| 287 | 4.5676 | 0.1259 | 0.1083 | 4.3334 | |
| 288 | 6.2055 | 0.1987 | | | 6.0068 |
| 289 | 4.3381 | 0.1034 | 0.1126 | 4.1221 | |
| 290 | | | | | |
| 291 | 4.7965 | 0.2811 | | | 4.5154 |
| 292 | | | | | |
| 293 | | | | | |
| 294 | | | | | |
| 295 | | | | | |
| 296 | | | | | |
| 297 | | | | | |
| 298 | | | | | |
| 299 | | | | | |
| 300 | | | | | |

# Appendix 2: Aso-4 analytical data analysed from sample 16-17cm in ODP 1207A by V. Ponomareva and M. Portnyagin

## 2.1: Sample Information

| Sample# | Volcanic zone | Source | Eruption ID | Age | LAT / LONG | Sampling site # | Section location | Lab | Date EMP |
|---|---|---|---|---|---|---|---|---|---|
| ODP198-1207_1H2W_16-17 | Japan | Aso caldera | Aso-4 | ~87 ka | N 37.79055° E 162.750883° | ODP198-1207 | Pacific Ocean, Shatsky rise | GEOMAR | 7-Nov-15 |
| ODP198-1207_1H2W_16-17 | Japan | Aso caldera | Aso-4 | ~87 ka | N 37.79055° E 162.750883° | ODP198-1207 | Pacific Ocean, Shatsky rise | GEOMAR | 7-Nov-15 |
| ODP198-1207_1H2W_16-17 | Japan | Aso caldera | Aso-4 | ~87 ka | N 37.79055° E 162.750883° | ODP198-1207 | Pacific Ocean, Shatsky rise | GEOMAR | 7-Nov-15 |
| ODP198-1207_1H2W_16-17 | Japan | Aso caldera | Aso-4 | ~87 ka | N 37.79055° E 162.750883° | ODP198-1207 | Pacific Ocean, Shatsky rise | GEOMAR | 7-Nov-15 |
| ODP198-1207_1H2W_16-17 | Japan | Aso caldera | Aso-4 | ~87 ka | N 37.79055° E 162.750883° | ODP198-1207 | Pacific Ocean, Shatsky rise | GEOMAR | 7-Nov-15 |
| ODP198-1207_1H2W_16-17 | Japan | Aso caldera | Aso-4 | ~87 ka | N 37.79055° E 162.750883° | ODP198-1207 | Pacific Ocean, Shatsky rise | GEOMAR | 7-Nov-15 |
| ODP198-1207_1H2W_16-17 | Japan | Aso caldera | Aso-4 | ~87 ka | N 37.79055° E 162.750883° | ODP198-1207 | Pacific Ocean, Shatsky rise | GEOMAR | 7-Nov-15 |
| ODP198-1207_1H2W_16-17 | Japan | Aso caldera | Aso-4 | ~87 ka | N 37.79055° E 162.750883° | ODP198-1207 | Pacific Ocean, Shatsky rise | GEOMAR | 7-Nov-15 |
| ODP198-1207_1H2W_16-17 | Japan | Aso caldera | Aso-4 | ~87 ka | N 37.79055° E 162.750883° | ODP198-1207 | Pacific Ocean, Shatsky rise | GEOMAR | 7-Nov-15 |
| ODP198-1207_1H2W_16-17 | Japan | Aso caldera | Aso-4 | ~87 ka | N 37.79055° E 162.750883° | ODP198-1207 | Pacific Ocean, Shatsky rise | GEOMAR | 7-Nov-15 |
| ODP198-1207_1H2W_16-17 | Japan | Aso caldera | Aso-4 | ~87 ka | N 37.79055° E 162.750883° | ODP198-1207 | Pacific Ocean, Shatsky rise | GEOMAR | 7-Nov-15 |
| ODP198-1207_1H2W_16-17 | Japan | Aso caldera | Aso-4 | ~87 ka | N 37.79055° E 162.750883° | ODP198-1207 | Pacific Ocean, Shatsky rise | GEOMAR | 7-Nov-15 |
| ODP198-1207_1H2W_16-17 | Japan | Aso caldera | Aso-4 | ~87 ka | N 37.79055° E 162.750883° | ODP198-1207 | Pacific Ocean, Shatsky rise | GEOMAR | 7-Nov-15 |

## 2.2: Chemical element concentrations (%) in the Aso-4 tephra in ODP 1207A, 16-17cm, recorded by V. Ponomareva and M. Portnyagin.

| **SiO2** | **TiO2** | **Al2O3** | **FeO** | **MnO** | **MgO** | **CaO** | **Na2O** | **K2O** | **P2O5** | **F** | **SO3** | **Cl** | **Total** | **Original total** |
|---|---|---|---|---|---|---|---|---|---|---|---|---|---|---|
| 71.9714124 | 0.395372003 | 14.73865 | 1.481902 | 0.043331 | 0.3806162 | 1.14153 | 4.896147 | 4.634279 | 0.050411 | 0.0753903 | 0.058454 | 0.132501 | 100 | 96.69674371 |
| 70.4512868 | 0.446204276 | 15.5886 | 1.61228 | 0.198896 | 0.4855442 | 1.668955 | 4.7546758 | 4.375073 | 0.112702 | 0.0605929 | 0.089522 | 0.15567 | 100 | 95.22566667 |
| 70.9678497 | 0.437479847 | 15.26886 | 1.897503 | 0.080612 | 0.4841359 | 1.655228 | 4.6402077 | 4.254425 | 0.116736 | 0.0022913 | 0.055009 | 0.13966 | 100 | 96.01535183 |
| 71.8885012 | 0.438354867 | 14.70203 | 1.59895 | 0.172254 | 0.3995589 | 1.105667 | 4.4381657 | 5.035535 | 0.057664 | 0.0314505 | 0.007776 | 0.124098 | 100 | 96.65969145 |
| 71.6205054 | 0.404271069 | 15.01121 | 1.659199 | 0.077727 | 0.3591297 | 1.161602 | 4.919682 | 4.529847 | 0.041702 | 0.0788701 | 0.002033 | 0.134226 | 100 | 96.23416297 |
| 71.7466792 | 0.394294439 | 14.9779 | 1.50914 | 0.150476 | 0.3180028 | 1.120922 | 4.875113 | 4.632861 | 0.063478 | 0.0577227 | 0.022394 | 0.131021 | 100 | 95.62967546 |
| 70.3379903 | 0.471009978 | 15.45619 | 1.750196 | 0.120218 | 0.4387096 | 1.517178 | 5.0980201 | 4.460434 | 0.104502 | 0.0578672 | 0.066985 | 0.120699 | 100 | 95.90923392 |
| 70.7107169 | 0.484601691 | 15.04267 | 1.761372 | 0.089098 | 0.4719201 | 1.576268 | 5.2840342 | 4.252638 | 0.075537 | 0.0856361 | 0.051475 | 0.114036 | 100 | 98.20620388 |
| 71.5181304 | 0.427318197 | 15.01768 | 1.438671 | 0.119207 | 0.3305561 | 1.235856 | 4.8580479 | 4.808182 | 0.040667 | 0.0210302 | 0.046618 | 0.138035 | 100 | 93.19940573 |
| 72.5400901 | 0.347595793 | 14.37574 | 1.177058 | 0.119971 | 0.2506407 | 0.92755 | 4.7192814 | 5.253371 | 0.060421 | 0.0949553 | 0 | 0.133328 | 100 | 95.93985587 |
| 70.8567171 | 0.461281555 | 15.24889 | 1.732475 | 0.105662 | 0.4774677 | 1.524474 | 4.9840049 | 4.263424 | 0.065079 | 0.0798104 | 0.069602 | 0.131112 | 100 | 97.48105506 |
| 71.6869624 | 0.426662653 | 14.95848 | 1.480654 | 0.055488 | 0.3164857 | 1.179384 | 4.892024 | 4.714375 | 0.05152 | 0.0707804 | 0.028405 | 0.138776 | 100 | 96.77824056 |
| 71.2212263 | 0.485540779 | 15.16938 | 1.600904 | 0 | 0.4571432 | 1.388488 | 5.1826981 | 4.408793 | 0.057541 | 0.0282822 | 0 | 0 | 100 | 93.34493601 |

# Appendix 3: Weights table for DSDP 580.

Note: at depths where there are no weights or size fraction weights, the depth was either not sampled, or there was no sample present.

| Depth (cm) | Sample weight (g) | >150µm (g) | <63 µm (g) | 63-150µm (g) | <150 µm (g) |
|---:|---:|---:|---:|---:|---:|
| 1 | 2.0791 | 0.0053 | 2.0334 | 0.0404 | |
| 2 | | | | | |
| 3 | | | | | |
| 4 | | | | | |
| 5 | 1.6664 | 0.005 | | | 1.6614 |
| 6 | | | | | |
| 7 | | | | | |
| 8 | | | | | |
| 9 | | | | | |
| 10 | 2.1208 | 0.0106 | 2.0603 | 0.0499 | |
| 11 | | | | | |
| 12 | | | | | |
| 13 | | | | | |
| 14 | | | | | |
| 15 | | | | | |
| 16 | 2.281 | 0.0121 | | | 2.2689 |
| 17 | | | | | |
| 18 | | | | | |
| 19 | | | | | |
| 20 | | | | | |
| 21 | 3.9202 | 0.0073 | 3.7538 | 0.1591 | |
| 22 | | | | | |
| 23 | | | | | |
| 24 | | | | | |
| 25 | | | | | |
| 26 | 2.2412 | 0.0124 | | | 2.2288 |
| 27 | | | | | |
| 28 | | | | | |
| 29 | | | | | |
| 30 | 3.3824 | 0.0075 | 3.2829 | 0.092 | |
| 31 | | | | | |
| 32 | | | | | |
| 33 | | | | | |
| 34 | | | | | |
| 35 | 4.0389 | 0.0221 | | | 4.0168 |
| 36 | | | | | |
| 37 | | | | | |

| | | | | | |
|---|---|---|---|---|---|
| 38 | | | | | |
| 39 | | | | | |
| 40 | 3.7677 | 0.0275 | 3.5572 | 0.183 | |
| 41 | | | | | |
| 42 | | | | | |
| 43 | | | | | |
| 44 | | | | | |
| 45 | 5.1949 | 0.0565 | | | 5.1384 |
| 46 | | | | | |
| 47 | | | | | |
| 48 | | | | | |
| 49 | | | | | |
| 50 | 5.5346 | 0.0996 | 5.0165 | 0.4185 | |
| 51 | | | | | |
| 52 | | | | | |
| 53 | | | | | |
| 54 | | | | | |
| 55 | 3.5382 | 0.0936 | 3.1965 | 0.2481 | |
| 56 | | | | | |
| 57 | | | | | |
| 58 | | | | | |
| 59 | | | | | |
| 60 | 4.6951 | 0.4951 | | | 4.2 |
| 61 | | | | | |
| 62 | | | | | |
| 63 | | | | | |
| 64 | | | | | |
| 65 | 3.8846 | 0.9878 | 2.6259 | 0.2709 | |
| 66 | | | | | |
| 67 | | | | | |
| 68 | | | | | |
| 69 | | | | | |
| 70 | 3.1495 | 0.0835 | | | 3.066 |
| 71 | | | | | |
| 72 | | | | | |
| 73 | | | | | |
| 74 | | | | | |
| 75 | 3.3333 | 0.1314 | 3.1015 | 0.1004 | |
| 76 | | | | | |
| 77 | | | | | |
| 78 | | | | | |
| 79 | | | | | |
| 80 | 3.747 | 0.2155 | | | 3.5315 |
| 81 | | | | | |
| 82 | | | | | |
| 83 | | | | | |
| 84 | | | | | |
| 85 | 2.7946 | 0.1079 | 2.6095 | 0.0772 | |

|  |  |  |  |  |  |
|---|---|---|---|---|---|
| 86 |  |  |  |  |  |
| 87 |  |  |  |  |  |
| 88 |  |  |  |  |  |
| 89 |  |  |  |  |  |
| 90 | 2.6349 | 0.1428 | 2.4403 | 0.0518 |  |
| 91 |  |  |  |  |  |
| 92 |  |  |  |  |  |
| 93 |  |  |  |  |  |
| 94 |  |  |  |  |  |
| 95 | 2.7519 | 0.0416 |  |  | 2.7103 |
| 96 |  |  |  |  |  |
| 97 |  |  |  |  |  |
| 98 |  |  |  |  |  |
| 99 |  |  |  |  |  |
| 100 |  |  |  |  |  |
| 101 | 2.6335 | 0.0436 | 2.5285 | 0.0614 |  |
| 102 |  |  |  |  |  |
| 103 |  |  |  |  |  |
| 104 |  |  |  |  |  |
| 105 | 3.0874 | 0.1908 |  |  | 2.8966 |
| 106 |  |  |  |  |  |
| 107 |  |  |  |  |  |
| 108 |  |  |  |  |  |
| 109 |  |  |  |  |  |
| 110 | 3.8737 | 0.1878 | 3.5885 | 0.0974 |  |
| 111 |  |  |  |  |  |
| 112 |  |  |  |  |  |
| 113 |  |  |  |  |  |
| 114 |  |  |  |  |  |
| 115 | 2.9325 | 0.1031 | 2.7501 | 0.0793 |  |
| 116 |  |  |  |  |  |
| 117 |  |  |  |  |  |
| 118 |  |  |  |  |  |
| 119 |  |  |  |  |  |
| 120 | 4.2526 | 0.0751 |  |  | 4.1775 |
| 121 |  |  |  |  |  |
| 122 |  |  |  |  |  |
| 123 |  |  |  |  |  |
| 124 |  |  |  |  |  |
| 125 | 3.1342 | 0.0984 | 2.9616 | 0.0742 |  |
| 126 |  |  |  |  |  |
| 127 |  |  |  |  |  |
| 128 |  |  |  |  |  |
| 129 |  |  |  |  |  |
| 130 | 4.7543 | 0.1582 |  |  | 4.5961 |
| 131 |  |  |  |  |  |
| 132 |  |  |  |  |  |
| 133 |  |  |  |  |  |

| | | | | | |
|---|---|---|---|---|---|
| 134 | | | | | |
| 135 | 3.0041 | 0.0515 | 2.8746 | 0.078 | |
| 136 | | | | | |
| 137 | | | | | |
| 138 | | | | | |
| 139 | | | | | |
| 140 | 4.4938 | 0.0732 | | | 4.4206 |
| 141 | | | | | |
| 142 | | | | | |
| 143 | | | | | |
| 144 | | | | | |
| 145 | 3.3048 | 0.0223 | 3.2198 | 0.0627 | |
| 146 | | | | | |
| 147 | | | | | |
| 148 | | | | | |
| 149 | | | | | |
| 150 | | | | | |
| 151 | | | | | |
| 152 | | | | | |
| 153 | 2.1609 | | | | |
| 154 | | | | | |
| 155 | 2.6601 | | | | |
| 156 | | | | | |
| 157 | 1.4488 | | | | |
| 158 | | | | | |
| 159 | | | | | |
| 160 | | | | | |
| 161 | | | | | |
| 162 | | | | | |
| 163 | 3.4441 | | | | |
| 164 | | | | | |
| 165 | 2.9471 | 0.0192 | | | 2.9279 |
| 166 | | | | | |
| 167 | 2.4167 | | | | |
| 168 | | | | | |
| 169 | | | | | |
| 170 | | | | | |
| 171 | | | | | |
| 172 | | | | | |
| 173 | 3.7859 | | | | |
| 174 | | | | | |
| 175 | 3.6091 | 0.0238 | | | 3.5853 |
| 176 | | | | | |
| 177 | 3.1377 | | | | |
| 178 | | | | | |
| 179 | | | | | |
| 180 | | | | | |
| 181 | | | | | |

| | | | | | |
|---|---|---|---|---|---|
| 182 | | | | | |
| 183 | 4.662 | | | | |
| 184 | | | | | |
| 185 | 4.1973 | 0.0191 | | | 4.1782 |
| 186 | | | | | |
| 187 | 4.0923 | | | | |
| 188 | | | | | |
| 189 | | | | | |
| 190 | | | | | |
| 191 | | | | | |
| 192 | | | | | |
| 193 | 3.2281 | | | | |
| 194 | | | | | |
| 195 | 2.9355 | 0.0207 | | | 2.9148 |
| 196 | | | | | |
| 197 | | | | | |
| 198 | | | | | |
| 199 | | | | | |
| 200 | | | | | |
| 201 | | | | | |
| 202 | 3.8869 | | | | |
| 203 | 5.2403 | | | | |
| 204 | 4.1344 | | | | |
| 205 | 5.4542 | 0.0697 | | | 5.3845 |
| 206 | 4.8018 | | | | |
| 207 | 3.9703 | | | | |
| 208 | 2.7978 | | | | |
| 209 | 2.0312 | | | | |
| 210 | 1.9041 | | | | |
| 211 | | | | | |
| 212 | 5.1639 | | | | |
| 213 | 4.3198 | | | | |
| 214 | 5.5686 | | | | |
| 215 | 4.164 | 0.0559 | | | 4.1081 |
| 216 | 5.1459 | | | | |
| 217 | 4.7066 | | | | |
| 218 | 4.8336 | | | | |
| 219 | 4.8827 | | | | |
| 220 | 5.0444 | | | | |
| 221 | | | | | |
| 222 | 5.91 | | | | |
| 223 | 5.65 | 0.0924 | | | 5.5576 |
| 224 | 5.31 | | | | |
| 225 | 3.91 | 0.0324 | | | 3.8776 |
| 226 | 6.68 | | | | |
| 227 | 6.73 | 0.1365 | | | 6.5935 |
| 228 | 7.95 | | | | |
| 229 | 7.7 | | | | |

| | | | | | |
|---|---|---|---|---|---|
| 230 | 9.7 | | | | |
| 231 | 11.3 | | | | |
| 232 | 6.7 | | | | |
| 233 | 8.1 | | | | |
| 234 | 18.8 | | | | |
| 235 | 3.8 | | | | |
| 236 | 4.8 | | | | |
| 237 | | | | | |
| 238 | 9.57 | 0.16 | | | 9.41 |
| 239 | 4.81 | | | | |
| 240 | 4.48 | 0.0765 | | | 4.4035 |
| 241 | 3.5 | | | | |
| 242 | 3.15 | 0.1987 | | | 2.9513 |
| 243 | 2.73 | | | | |
| 244 | 4 | 0.1887 | | | 3.8113 |
| 245 | 2.84 | | | | |
| 246 | 1.82 | | | | |
| 247 | 4.32 | | | | |
| 248 | 3.33 | 0.0648 | | | 3.2652 |
| 249 | 4.59 | | | | |
| 250 | 4.19 | 0.0661 | | | 4.1239 |
| 251 | | | | | |
| 252 | 1.53 | 0.0285 | | | 1.5015 |
| 253 | | | | | |
| 254 | 3.4 | 0.1108 | | | 3.2892 |
| 255 | 3.47 | | | | |
| 256 | 2.57 | 0.0272 | | | 2.5428 |
| 257 | 3.13 | | | | |
| 258 | 2.94 | 0.0675 | | | 2.8725 |
| 259 | 2.05 | | | | |
| 260 | 3.03 | 0.0923 | | | 2.9377 |
| 261 | 3.1 | 0.0697 | | | 3.0303 |
| 262 | 2.53 | 0.0786 | | | 2.4514 |
| 263 | 3.13 | | | | |
| 264 | 2.87 | 0.0899 | | | 2.7801 |
| 265 | 1.93 | | | | |
| 266 | 2.83 | 0.0874 | | | 2.7426 |
| 267 | 3.52 | | | | |
| 268 | 3.76 | 0.1042 | | | 3.6558 |
| 269 | 3.5609 | | | | |
| 270 | 4.6556 | 0.1126 | | | 4.543 |
| 271 | | 0.0523 | | | -0.0523 |
| 272 | 4.0011 | | | | |
| 273 | 4.9282 | 0.052 | | | 4.8762 |
| 274 | 4.6022 | | | | |
| 275 | 4.3712 | 0.0758 | | | 4.2954 |
| 276 | 4.9689 | | | | |
| 277 | 4.3694 | 0.0399 | | | 4.3295 |

| | | | | | |
|---|---|---|---|---|---|
| 278 | 4.6163 | | | | |
| 279 | 3.0563 | 0.078 | | | 2.9783 |
| 280 | 4.8703 | | | | 4.8703 |
| 281 | | | | | |
| 282 | 7.715 | 0.0122 | | | 7.7028 |
| 283 | 5.2615 | | | | |
| 284 | 4.7622 | 0.0022 | | | 4.76 |
| 285 | 11.7926 | | | | |
| 286 | 9 | | | | |
| 287 | 8.6 | | | | |
| 288 | 3.6 | | | | |
| 289 | 2.2 | | | | |
| 290 | 3.5 | | | | |
| 291 | 3.2 | | | | |
| 292 | 3.5 | | | | |
| 293 | 3.5 | | | | |
| 294 | 4.4 | | | | |
| 295 | 5.4353 | | | | |
| 296 | 2.8245 | | | | |
| 297 | 2.2226 | | | | |
| 298 | | | | | |
| 299 | | | | | |
| 300 | | | | | |

# Appendix 4: Analytical data analysed from tephras in DSDP 580 by V. Ponomareva and M. Portnyagin

## 4.1: DSDP 580: 49-50cm Sample information

| Sample # | Volcanic zone | Source | Eruption ID | Age | LAT/LONG | Location | Lab | Date EMP |
|---|---|---|---|---|---|---|---|---|
| DSDP-86-580-1H1W_49-50 | Japan | Towada/Kurile Islands | ? | ? | N 41.6245° E 153.976° | NW Pacific | GEOMAR | 27-Mar-20 |
| DSDP-86-580-1H1W_49-50 | Japan | Towada/Kurile Islands | ? | ? | N 41.6245° E 153.976° | NW Pacific | GEOMAR | 27-Mar-20 |
| DSDP-86-580-1H1W_49-50 | Japan | Towada/Kurile Islands | ? | ? | N 41.6245° E 153.976° | NW Pacific | GEOMAR | 27-Mar-20 |
| DSDP-86-580-1H1W_49-50 | Japan | Towada/Kurile Islands | ? | ? | N 41.6245° E 153.976° | NW Pacific | GEOMAR | 27-Mar-20 |
| DSDP-86-580-1H1W_49-50 | Japan | Towada/Kurile Islands | ? | ? | N 41.6245° E 153.976° | NW Pacific | GEOMAR | 27-Mar-20 |
| DSDP-86-580-1H1W_49-50 | Japan | Towada/Kurile Islands | ? | ? | N 41.6245° E 153.976° | NW Pacific | GEOMAR | 27-Mar-20 |
| DSDP-86-580-1H1W_49-50 | Japan | Towada/Kurile Islands | ? | ? | N 41.6245° E 153.976° | NW Pacific | GEOMAR | 27-Mar-20 |
| DSDP-86-580-1H1W_49-50 | Japan | Towada/Kurile Islands | ? | ? | N 41.6245° E 153.976° | NW Pacific | GEOMAR | 27-Mar-20 |
| DSDP-86-580-1H1W_49-50 | Japan | Towada/Kurile Islands | ? | ? | N 41.6245° E 153.976° | NW Pacific | GEOMAR | 27-Mar-20 |
| DSDP-86-580-1H1W_49-50 | Japan | Towada/Kurile Islands | ? | ? | N 41.6245° E 153.976° | NW Pacific | GEOMAR | 27-Mar-20 |
| DSDP-86-580-1H1W_49-50 | Japan | Towada/Kurile Islands | ? | ? | N 41.6245° E 153.976° | NW Pacific | GEOMAR | 27-Mar-20 |
| DSDP-86-580-1H1W_49-50 | Japan | Towada/Kurile Islands | ? | ? | N 41.6245° E 153.976° | NW Pacific | GEOMAR | 27-Mar-20 |
| DSDP-86-580-1H1W_49-50 | Japan | Towada/Kurile Islands | ? | ? | N 41.6245° E 153.976° | NW Pacific | GEOMAR | 27-Mar-20 |
| DSDP-86-580-1H1W_49-50 | Japan | Towada/Kurile Islands | ? | ? | N 41.6245° E 153.976° | NW Pacific | GEOMAR | 27-Mar-20 |

| | | | | | | | | |
|---|---|---|---|---|---|---|---|---|
| DSDP-86-580-1H1W_49-50 | Japan | Towada/Kurile Islands | ? | ? | N 41.6245° E 153.976° | NW Pacific | GEOMAR | 27-Mar-20 |
| DSDP-86-580-1H1W_49-50 | Japan | Towada/Kurile Islands | ? | ? | N 41.6245° E 153.976° | NW Pacific | GEOMAR | 27-Mar-20 |
| DSDP-86-580-1H1W_49-50 | Japan | Towada/Kurile Islands | ? | ? | N 41.6245° E 153.976° | NW Pacific | GEOMAR | 27-Mar-20 |
| DSDP-86-580-1H1W_49-50 | Japan | Towada/Kurile Islands | ? | ? | N 41.6245° E 153.976° | NW Pacific | GEOMAR | 27-Mar-20 |
| DSDP-86-580-1H1W_49-50 | Japan | Towada/Kurile Islands | ? | ? | N 41.6245° E 153.976° | NW Pacific | GEOMAR | 27-Mar-20 |
| DSDP-86-580-1H1W_49-50 | Japan | Towada/Kurile Islands | ? | ? | N 41.6245° E 153.976° | NW Pacific | GEOMAR | 27-Mar-20 |
| DSDP-86-580-1H1W_49-50 | Japan | Towada/Kurile Islands | ? | ? | N 41.6245° E 153.976° | NW Pacific | GEOMAR | 27-Mar-20 |
| DSDP-86-580-1H1W_49-50 | Japan | Towada/Kurile Islands | ? | ? | N 41.6245° E 153.976° | NW Pacific | GEOMAR | 27-Mar-20 |
| DSDP-86-580-1H1W_49-50 | Japan | Towada/Kurile Islands | ? | ? | N 41.6245° E 153.976° | NW Pacific | GEOMAR | 27-Mar-20 |
| DSDP-86-580-1H1W_49-50 | Japan | Towada/Kurile Islands | ? | ? | N 41.6245° E 153.976° | NW Pacific | GEOMAR | 27-Mar-20 |
| DSDP-86-580-1H1W_49-50 | Japan | Towada/Kurile Islands | ? | ? | N 41.6245° E 153.976° | NW Pacific | GEOMAR | 27-Mar-20 |
| DSDP-86-580-1H1W_49-50 | Japan | Towada/Kurile Islands | ? | ? | N 41.6245° E 153.976° | NW Pacific | GEOMAR | 27-Mar-20 |
| DSDP-86-580-1H1W_49-50 | Japan | Towada/Kurile Islands | ? | ? | N 41.6245° E 153.976° | NW Pacific | GEOMAR | 27-Mar-20 |
| DSDP-86-580-1H1W_49-50 | Japan | Towada/Kurile Islands | ? | ? | N 41.6245° E 153.976° | NW Pacific | GEOMAR | 27-Mar-20 |

## 4.2: Chemical element abundance % for DSDP 580: 49-50cm tephra

| SiO2 | TiO2 | Al2O3 | FeOt | MnO | MgO | CaO | Na2O | K2O | P2O5 | F | SO3 | Cl |
|---|---|---|---|---|---|---|---|---|---|---|---|---|
| 77.26 | 0.29 | 12.49 | 1.49 | 0.12 | 0.33 | 1.86 | 4.55 | 1.35 | 0.00 | 0.12 | 0.01 | 0.12 |
| 76.66 | 0.31 | 12.71 | 1.68 | 0.03 | 0.42 | 2.05 | 4.63 | 1.26 | 0.01 | 0.12 | 0.01 | 0.11 |
| 78.17 | 0.28 | 12.13 | 1.27 | 0.02 | 0.32 | 1.83 | 3.91 | 1.75 | 0.06 | 0.00 | 0.02 | 0.24 |
| 77.86 | 0.24 | 12.03 | 1.55 | 0.06 | 0.30 | 1.78 | 4.07 | 1.73 | 0.02 | 0.06 | 0.02 | 0.27 |
| 77.80 | 0.30 | 12.12 | 1.43 | 0.03 | 0.28 | 1.89 | 4.27 | 1.60 | 0.00 | 0.01 | 0.02 | 0.24 |
| 78.05 | 0.26 | 11.87 | 1.59 | 0.11 | 0.34 | 1.69 | 3.94 | 1.80 | 0.01 | 0.08 | 0.01 | 0.26 |
| 77.68 | 0.31 | 12.42 | 1.55 | 0.08 | 0.33 | 2.02 | 4.23 | 1.26 | 0.02 | 0.02 | 0.00 | 0.10 |
| 76.83 | 0.32 | 12.82 | 1.64 | 0.11 | 0.33 | 1.97 | 4.44 | 1.28 | 0.00 | 0.13 | 0.01 | 0.12 |
| 74.36 | 0.50 | 12.99 | 2.61 | 0.09 | 0.54 | 2.54 | 3.96 | 2.01 | 0.06 | 0.11 | 0.02 | 0.20 |
| 75.27 | 0.40 | 13.44 | 1.84 | 0.15 | 0.46 | 2.49 | 4.56 | 1.19 | 0.00 | 0.07 | 0.01 | 0.11 |
| 76.77 | 0.32 | 12.65 | 1.57 | 0.02 | 0.40 | 1.98 | 4.82 | 1.28 | 0.06 | 0.00 | 0.01 | 0.11 |
| 75.13 | 0.48 | 13.11 | 2.24 | 0.10 | 0.57 | 2.56 | 4.37 | 1.16 | 0.09 | 0.10 | 0.00 | 0.10 |
| 77.27 | 0.28 | 12.59 | 1.53 | 0.07 | 0.34 | 1.96 | 4.51 | 1.28 | 0.00 | 0.06 | 0.00 | 0.11 |
| 72.98 | 0.45 | 14.21 | 2.49 | 0.10 | 0.77 | 3.25 | 4.32 | 1.11 | 0.11 | 0.07 | 0.03 | 0.11 |
| 74.96 | 0.42 | 13.49 | 2.03 | 0.13 | 0.57 | 2.51 | 4.56 | 1.15 | 0.04 | 0.02 | 0.01 | 0.12 |
| 78.07 | 0.25 | 11.96 | 1.68 | 0.07 | 0.24 | 1.72 | 3.95 | 1.72 | 0.01 | 0.06 | 0.00 | 0.27 |
| 74.37 | 0.38 | 13.65 | 1.89 | 0.12 | 0.49 | 2.44 | 5.18 | 1.27 | 0.07 | 0.00 | 0.04 | 0.11 |
| 77.69 | 0.29 | 12.22 | 1.47 | 0.07 | 0.33 | 1.82 | 4.09 | 1.74 | 0.01 | 0.02 | 0.00 | 0.25 |
| 70.98 | 0.64 | 14.14 | 3.37 | 0.17 | 0.92 | 3.78 | 5.07 | 0.69 | 0.11 | 0.00 | 0.02 | 0.10 |
| 77.68 | 0.28 | 12.08 | 1.49 | 0.08 | 0.30 | 1.70 | 4.15 | 1.86 | 0.01 | 0.10 | 0.03 | 0.24 |
| 77.85 | 0.30 | 12.06 | 1.41 | 0.11 | 0.31 | 1.81 | 4.04 | 1.75 | 0.01 | 0.11 | 0.01 | 0.23 |
| 76.75 | 0.27 | 12.79 | 1.51 | 0.08 | 0.30 | 2.03 | 4.28 | 1.69 | 0.04 | 0.00 | 0.01 | 0.26 |
| 77.90 | 0.24 | 12.38 | 1.44 | 0.08 | 0.35 | 1.87 | 4.37 | 1.22 | 0.02 | 0.00 | 0.01 | 0.11 |
| 72.90 | 0.48 | 14.20 | 2.44 | 0.14 | 0.72 | 3.04 | 4.79 | 1.09 | 0.04 | 0.00 | 0.08 | 0.09 |
| 74.97 | 0.39 | 13.59 | 1.89 | 0.14 | 0.54 | 2.40 | 4.54 | 1.22 | 0.03 | 0.14 | 0.04 | 0.10 |
| 75.29 | 0.39 | 13.29 | 1.98 | 0.06 | 0.48 | 2.37 | 4.66 | 1.17 | 0.06 | 0.11 | 0.01 | 0.12 |
| 73.14 | 0.47 | 14.07 | 2.42 | 0.10 | 0.77 | 3.20 | 4.46 | 1.08 | 0.12 | 0.03 | 0.05 | 0.09 |
| 77.63 | 0.27 | 11.98 | 1.71 | 0.09 | 0.30 | 1.70 | 4.13 | 1.80 | 0.07 | 0.06 | 0.03 | 0.23 |

### 4.3: DSDP 580: 64-65cm Sample information

| Sample# | Volcanic zone | Source | Eruption ID | Age | LAT/LONG | LOCATION | LAB | Date EMP |
|---|---|---|---|---|---|---|---|---|
| DSDP-86-580-1H1W_64-65 | Japan | Towada volcano | Towada Hachinohe | 15.7±0.2 b2k | N 41.6245° E 153.976° | NW Pacific | GEOMAR | 27-Mar-19 |
| DSDP-86-580-1H1W_64-65 | Japan | Towada volcano | Towada Hachinohe | 15.7±0.2 b2k | N 41.6245° E 153.976° | NW Pacific | GEOMAR | 27-Mar-19 |
| DSDP-86-580-1H1W_64-65 | Japan | Towada volcano | Towada Hachinohe | 15.7±0.2 b2k | N 41.6245° E 153.976° | NW Pacific | GEOMAR | 27-Mar-19 |
| DSDP-86-580-1H1W_64-65 | Japan | Towada volcano | Towada Hachinohe | 15.7±0.2 b2k | N 41.6245° E 153.976° | NW Pacific | GEOMAR | 27-Mar-19 |
| DSDP-86-580-1H1W_64-65 | Japan | Towada volcano | Towada Hachinohe | 15.7±0.2 b2k | N 41.6245° E 153.976° | NW Pacific | GEOMAR | 27-Mar-19 |
| DSDP-86-580-1H1W_64-65 | Japan | Towada volcano | Towada Hachinohe | 15.7±0.2 b2k | N 41.6245° E 153.976° | NW Pacific | GEOMAR | 27-Mar-19 |
| DSDP-86-580-1H1W_64-65 | Japan | Towada volcano | Towada Hachinohe | 15.7±0.2 b2k | N 41.6245° E 153.976° | NW Pacific | GEOMAR | 27-Mar-19 |
| DSDP-86-580-1H1W_64-65 | Japan | Towada volcano | Towada Hachinohe | 15.7±0.2 b2k | N 41.6245° E 153.976° | NW Pacific | GEOMAR | 27-Mar-19 |
| DSDP-86-580-1H1W_64-65 | Japan | Towada volcano | Towada Hachinohe | 15.7±0.2 b2k | N 41.6245° E 153.976° | NW Pacific | GEOMAR | 27-Mar-19 |
| DSDP-86-580-1H1W_64-65 | Japan | Towada volcano | Towada Hachinohe | 15.7±0.2 b2k | N 41.6245° E 153.976° | NW Pacific | GEOMAR | 27-Mar-19 |
| DSDP-86-580-1H1W_64-65 | Japan | Towada volcano | Towada Hachinohe | 15.7±0.2 b2k | N 41.6245° E 153.976° | NW Pacific | GEOMAR | 27-Mar-19 |
| DSDP-86-580-1H1W_64-65 | Japan | Towada volcano | Towada Hachinohe | 15.7±0.2 b2k | N 41.6245° E 153.976° | NW Pacific | GEOMAR | 27-Mar-19 |
| DSDP-86-580-1H1W_64-65 | Japan | Towada volcano | Towada Hachinohe | 15.7±0.2 b2k | N 41.6245° E 153.976° | NW Pacific | GEOMAR | 27-Mar-19 |
| DSDP-86-580-1H1W_64-65 | Japan | Towada volcano | Towada Hachinohe | 15.7±0.2 b2k | N 41.6245° E 153.976° | NW Pacific | GEOMAR | 27-Mar-19 |
| DSDP-86-580-1H1W_64-65 | Japan | Towada volcano | Towada Hachinohe | 15.7±0.2 b2k | N 41.6245° E 153.976° | NW Pacific | GEOMAR | 27-Mar-19 |

| SiO2 | TiO2 | Al2O3 | FeOt | MnO | MgO | CaO | Na2O | K2O | P2O5 | F | SO3 | Cl |
|---|---|---|---|---|---|---|---|---|---|---|---|---|
| 76.47 | 0.30 | 13.07 | 1.62 | 0.13 | 0.46 | 2.28 | 4.24 | 1.20 | 0.01 | 0.09 | 0.01 | 0.11 |
| 77.67 | 0.31 | 12.41 | 1.53 | 0.05 | 0.28 | 1.83 | 4.29 | 1.31 | 0.03 | 0.17 | 0.02 | 0.11 |
| 77.60 | 0.31 | 12.56 | 1.62 | 0.08 | 0.37 | 1.88 | 4.08 | 1.30 | 0.00 | 0.04 | 0.04 | 0.11 |
| 74.45 | 0.42 | 13.76 | 2.11 | 0.13 | 0.60 | 2.71 | 4.35 | 1.13 | 0.11 | 0.06 | 0.03 | 0.12 |
| 75.01 | 0.42 | 13.52 | 2.13 | 0.09 | 0.53 | 2.58 | 4.27 | 1.17 | 0.05 | 0.08 | 0.03 | 0.11 |
| 76.58 | 0.31 | 12.83 | 1.75 | 0.11 | 0.39 | 2.15 | 4.48 | 1.22 | 0.04 | 0.00 | 0.02 | 0.12 |
| 77.38 | 0.30 | 12.58 | 1.50 | 0.11 | 0.40 | 1.87 | 4.35 | 1.32 | 0.04 | 0.01 | 0.02 | 0.11 |
| 74.67 | 0.49 | 14.19 | 2.34 | 0.17 | 0.72 | 2.95 | 3.03 | 1.12 | 0.09 | 0.13 | 0.00 | 0.11 |
| 76.46 | 0.35 | 12.99 | 1.69 | 0.06 | 0.44 | 2.25 | 4.36 | 1.19 | 0.06 | 0.00 | 0.02 | 0.13 |
| 77.67 | 0.26 | 12.59 | 1.43 | 0.05 | 0.30 | 1.81 | 4.45 | 1.31 | 0.02 | 0.00 | 0.01 | 0.10 |
| 73.01 | 0.48 | 14.09 | 2.60 | 0.07 | 0.70 | 3.03 | 4.63 | 1.08 | 0.09 | 0.10 | 0.03 | 0.10 |
| 77.21 | 0.31 | 12.61 | 1.53 | 0.12 | 0.33 | 1.93 | 4.47 | 1.28 | 0.01 | 0.07 | 0.02 | 0.12 |
| 75.20 | 0.37 | 13.58 | 1.96 | 0.08 | 0.47 | 2.41 | 4.50 | 1.27 | 0.05 | 0.00 | 0.04 | 0.08 |
| 78.29 | 0.30 | 12.42 | 1.64 | 0.13 | 0.33 | 1.92 | 3.42 | 1.38 | 0.01 | 0.04 | 0.02 | 0.10 |
| 77.01 | 0.35 | 13.08 | 1.82 | 0.09 | 0.41 | 2.29 | 3.50 | 1.24 | 0.07 | 0.03 | 0.02 | 0.11 |
| 73.16 | 0.48 | 13.97 | 2.53 | 0.21 | 0.74 | 2.99 | 4.64 | 1.13 | 0.06 | 0.00 | 0.02 | 0.08 |
| 73.64 | 0.48 | 13.89 | 2.50 | 0.14 | 0.64 | 2.89 | 4.36 | 1.14 | 0.12 | 0.04 | 0.06 | 0.10 |

| | | | | | | | | |
|---|---|---|---|---|---|---|---|---|
| DSDP-86-580-1H1W_64-65 | Japan | Towada volcano | Towada Hachinohe | 15.7±0.2 b2k | N 41.6245° E 153.976° | NW Pacific | GEOMAR | 27-Mar-19 |
| DSDP-86-580-1H1W_64-65 | Japan | Towada volcano | Towada Hachinohe | 15.7±0.2 b2k | N 41.6245° E 153.976° | NW Pacific | GEOMAR | 27-Mar-19 |

### 4.4: Chemical element abundance % for DSDP 580: 64-65cm tephra (Towada Hachinohe)

### 4.5: DSDP 580: 234-235cm sample information

| Sample# | Volcanic zone | Source | Eruption ID | Age | LAT/LONG | LOCATION | LAB | Date EMP |
|---|---|---|---|---|---|---|---|---|
| IODP-86-580-1H2W_84-85 (234-235cm BSF) | Japan | Kutcharo caldera | ? | ? | N 41.6245 E 153.976 | NW Pacific | GEOMAR | 07-Nov-15 |
| IODP-86-580-1H2W_84-85 (234-235cm BSF) | Japan | Kutcharo caldera | ? | ? | N 41.6245 E 153.976 | NW Pacific | GEOMAR | 07-Nov-15 |
| IODP-86-580-1H2W_84-85 (234-235cm BSF) | Japan | Kutcharo caldera | ? | ? | N 41.6245 E 153.976 | NW Pacific | GEOMAR | 07-Nov-15 |
| IODP-86-580-1H2W_84-85 (234-235cm BSF) | Japan | Kutcharo caldera | ? | ? | N 41.6245 E 153.976 | NW Pacific | GEOMAR | 07-Nov-15 |
| IODP-86-580-1H2W_84-85 (234-235cm BSF) | Japan | Kutcharo caldera | ? | ? | N 41.6245 E 153.976 | NW Pacific | GEOMAR | 07-Nov-15 |
| IODP-86-580-1H2W_84-85 (234-235cm BSF) | Japan | Kutcharo caldera | ? | ? | N 41.6245 E 153.976 | NW Pacific | GEOMAR | 07-Nov-15 |
| IODP-86-580-1H2W_84-85 (234-235cm BSF) | Japan | Kutcharo caldera | ? | ? | N 41.6245 E 153.976 | NW Pacific | GEOMAR | 07-Nov-15 |
| IODP-86-580-1H2W_84-85 (234-235cm BSF) | Japan | Kutcharo caldera | ? | ? | N 41.6245 E 153.976 | NW Pacific | GEOMAR | 07-Nov-15 |
| IODP-86-580-1H2W_84-85 (234-235cm BSF) | Japan | Kutcharo caldera | ? | ? | N 41.6245 E 153.976 | NW Pacific | GEOMAR | 07-Nov-15 |
| IODP-86-580-1H2W_84-85 (234-235cm BSF) | Japan | Kutcharo caldera | ? | ? | N 41.6245 E 153.976 | NW Pacific | GEOMAR | 07-Nov-15 |
| IODP-86-580-1H2W_84-85 (234-235cm BSF) | Japan | Kutcharo caldera | ? | ? | N 41.6245 E 153.976 | NW Pacific | GEOMAR | 07-Nov-15 |
| IODP-86-580-1H2W_84-85 (234-235cm BSF) | Japan | Kutcharo caldera | ? | ? | N 41.6245 E 153.976 | NW Pacific | GEOMAR | 07-Nov-15 |
| IODP-86-580-1H2W_84-85 (234-235cm BSF) | Japan | Kutcharo caldera | ? | ? | N 41.6245 E 153.976 | NW Pacific | GEOMAR | 07-Nov-15 |
| IODP-86-580-1H2W_84-85 (234-235cm BSF) | Japan | Kutcharo caldera | ? | ? | N 41.6245 E 153.976 | NW Pacific | GEOMAR | 07-Nov-15 |
| IODP-86-580-1H2W_84-85 (234-235cm BSF) | Japan | Kutcharo caldera | ? | ? | N 41.6245 E 153.976 | NW Pacific | GEOMAR | 07-Nov-15 |
| IODP-86-580-1H2W_84-85 (234-235cm BSF) | Japan | Kutcharo caldera | ? | ? | N 41.6245 E 153.976 | NW Pacific | GEOMAR | 07-Nov-15 |
| IODP-86-580-1H2W_84-85 (234-235cm BSF) | Japan | Kutcharo caldera | ? | ? | N 41.6245 E 153.976 | NW Pacific | GEOMAR | 07-Nov-15 |
| IODP-86-580-1H2W_84-85 (234-235cm BSF) | Japan | Kutcharo caldera | ? | ? | N 41.6245 E 153.976 | NW Pacific | GEOMAR | 07-Nov-15 |

| | | | | | | | | |
|---|---|---|---|---|---|---|---|---|
| IODP-86-580-1H2W_84-85 (234-235cm BSF) | Japan | Kutcharo caldera | ? | ? | N 41.6245 E 153.976 | NW Pacific | GEOMAR | 07-Nov-15 |
| IODP-86-580-1H2W_84-85 (234-235cm BSF) | Japan | Kutcharo caldera | ? | ? | N 41.6245 E 153.976 | NW Pacific | GEOMAR | 07-Nov-15 |
| IODP-86-580-1H2W_84-85 (234-235cm BSF) | Japan | Kutcharo caldera | ? | ? | N 41.6245 E 153.976 | NW Pacific | GEOMAR | 07-Nov-15 |
| IODP-86-580-1H2W_84-85 (234-235cm BSF) | Japan | Kutcharo caldera | ? | ? | N 41.6245 E 153.976 | NW Pacific | GEOMAR | 07-Nov-15 |

## 4.6: Chemical element abundance % for DSDP 580: 234-235cm tephra

| SiO2 | TiO2 | Al2O3 | FeOt | MnO | MgO | CaO | Na2O | K2O | P2O5 | F | SO3 | Cl |
|---|---|---|---|---|---|---|---|---|---|---|---|---|
| 77.65 | 0.29 | 11.70 | 1.43 | 0.09 | 0.30 | 1.70 | 4.14 | 2.33 | 0.03 | 0.12 | 0.00 | 0.21 |
| 76.74 | 0.30 | 12.53 | 1.58 | 0.05 | 0.29 | 1.71 | 4.35 | 2.17 | 0.03 | 0.02 | 0.03 | 0.18 |
| 77.07 | 0.28 | 12.47 | 1.23 | 0.15 | 0.24 | 1.62 | 4.30 | 2.39 | 0.00 | 0.03 | 0.03 | 0.18 |
| 76.30 | 0.29 | 12.65 | 1.44 | 0.07 | 0.29 | 1.73 | 4.65 | 2.21 | 0.00 | 0.11 | 0.05 | 0.21 |
| 76.55 | 0.27 | 12.47 | 1.51 | 0.05 | 0.30 | 1.76 | 4.53 | 2.30 | 0.06 | 0.00 | 0.00 | 0.20 |
| 77.02 | 0.26 | 12.45 | 1.52 | 0.07 | 0.30 | 1.70 | 4.24 | 2.18 | 0.03 | 0.00 | 0.02 | 0.20 |
| 76.81 | 0.28 | 12.54 | 1.23 | 0.08 | 0.28 | 1.72 | 4.56 | 2.23 | 0.04 | 0.00 | 0.01 | 0.21 |
| 77.02 | 0.31 | 12.45 | 1.43 | 0.06 | 0.27 | 1.63 | 4.26 | 2.36 | 0.01 | 0.00 | 0.01 | 0.19 |
| 77.01 | 0.27 | 12.35 | 1.30 | 0.03 | 0.28 | 1.70 | 4.38 | 2.33 | 0.01 | 0.12 | 0.01 | 0.22 |
| 77.32 | 0.26 | 12.27 | 1.46 | 0.06 | 0.28 | 1.43 | 4.28 | 2.31 | 0.03 | 0.10 | 0.01 | 0.20 |
| 77.79 | 0.27 | 11.84 | 1.24 | 0.05 | 0.27 | 1.53 | 4.35 | 2.28 | 0.05 | 0.08 | 0.05 | 0.21 |
| 77.59 | 0.24 | 12.06 | 1.40 | 0.03 | 0.25 | 1.64 | 4.20 | 2.29 | 0.05 | 0.03 | 0.03 | 0.20 |
| 77.44 | 0.29 | 12.20 | 1.36 | 0.12 | 0.24 | 1.59 | 4.30 | 2.22 | 0.05 | 0.00 | 0.00 | 0.17 |
| 76.99 | 0.28 | 12.17 | 1.54 | 0.03 | 0.27 | 1.73 | 4.42 | 2.17 | 0.04 | 0.09 | 0.05 | 0.22 |
| 77.55 | 0.28 | 12.16 | 1.40 | 0.11 | 0.28 | 1.65 | 4.05 | 2.26 | 0.03 | 0.02 | 0.00 | 0.21 |
| 77.39 | 0.28 | 12.06 | 1.52 | 0.02 | 0.28 | 1.70 | 4.29 | 2.16 | 0.05 | 0.04 | 0.02 | 0.19 |
| 76.98 | 0.27 | 12.29 | 1.60 | 0.00 | 0.30 | 1.78 | 4.36 | 2.15 | 0.01 | 0.02 | 0.05 | 0.19 |
| 77.43 | 0.26 | 12.19 | 1.56 | 0.04 | 0.30 | 1.71 | 4.06 | 2.20 | 0.04 | 0.02 | 0.00 | 0.21 |
| 76.90 | 0.27 | 12.30 | 1.57 | 0.08 | 0.29 | 1.72 | 4.42 | 2.18 | 0.03 | 0.00 | 0.03 | 0.21 |
| 78.06 | 0.24 | 11.88 | 1.43 | 0.03 | 0.23 | 1.54 | 4.04 | 2.23 | 0.02 | 0.08 | 0.00 | 0.21 |
| 77.41 | 0.28 | 12.20 | 1.44 | 0.04 | 0.25 | 1.53 | 4.14 | 2.42 | 0.06 | 0.00 | 0.01 | 0.22 |
| 77.81 | 0.24 | 12.04 | 1.39 | 0.07 | 0.27 | 1.67 | 4.18 | 2.06 | 0.03 | 0.02 | 0.02 | 0.21 |

## 4.7: DSDP 580: 290-291cm sample information

| Sample# | Volcanic zone | Source | Eruption ID | Age | LAT/LONG | LOCATION | LAB | Date EMP |
|---|---|---|---|---|---|---|---|---|
| DSDP-86-580_1H2W_140-141 (290-291cm) | Japan | Kutcharo caldera | Kutcharo-Shoro (Kc-Sr) | 39.27-45.07 ka BP | N 41.6245 E 153.976 | NW Pacific | GEOMAR | 07-Nov-15 |
| DSDP-86-580_1H2W_140-141 (290-291cm) | Japan | Kutcharo caldera | Kutcharo-Shoro (Kc-Sr) | 39.27-45.07 ka BP | N 41.6245 E 153.976 | NW Pacific | GEOMAR | 07-Nov-15 |
| DSDP-86-580_1H2W_140-141 (290-291cm) | Japan | Kutcharo caldera | Kutcharo-Shoro (Kc-Sr) | 39.27-45.07 ka BP | N 41.6245 E 153.976 | NW Pacific | GEOMAR | 07-Nov-15 |
| DSDP-86-580_1H2W_140-141 (290-291cm) | Japan | Kutcharo caldera | Kutcharo-Shoro (Kc-Sr) | 39.27-45.07 ka BP | N 41.6245 E 153.976 | NW Pacific | GEOMAR | 07-Nov-15 |
| DSDP-86-580_1H2W_140-141 (290-291cm) | Japan | Kutcharo caldera | Kutcharo-Shoro (Kc-Sr) | 39.27-45.07 ka BP | N 41.6245 E 153.976 | NW Pacific | GEOMAR | 07-Nov-15 |
| DSDP-86-580_1H2W_140-141 (290-291cm) | Japan | Kutcharo caldera | Kutcharo-Shoro (Kc-Sr) | 39.27-45.07 ka BP | N 41.6245 E 153.976 | NW Pacific | GEOMAR | 07-Nov-15 |
| DSDP-86-580_1H2W_140-141 (290-291cm) | Japan | Kutcharo caldera | Kutcharo-Shoro (Kc-Sr) | 39.27-45.07 ka BP | N 41.6245 E 153.976 | NW Pacific | GEOMAR | 07-Nov-15 |
| DSDP-86-580_1H2W_140-141 (290-291cm) | Japan | Kutcharo caldera | Kutcharo-Shoro (Kc-Sr) | 39.27-45.07 ka BP | N 41.6245 E 153.976 | NW Pacific | GEOMAR | 07-Nov-15 |
| DSDP-86-580_1H2W_140-141 (290-291cm) | Japan | Kutcharo caldera | Kutcharo-Shoro (Kc-Sr) | 39.27-45.07 ka BP | N 41.6245 E 153.976 | NW Pacific | GEOMAR | 07-Nov-15 |
| DSDP-86-580_1H2W_140-141 (290-291cm) | Japan | Kutcharo caldera | Kutcharo-Shoro (Kc-Sr) | 39.27-45.07 ka BP | N 41.6245 E 153.976 | NW Pacific | GEOMAR | 07-Nov-15 |
| DSDP-86-580_1H2W_140-141 (290-291cm) | Japan | Kutcharo caldera | Kutcharo-Shoro (Kc-Sr) | 39.27-45.07 ka BP | N 41.6245 E 153.976 | NW Pacific | GEOMAR | 07-Nov-15 |

|  |  |  |  |  |  |  |  |  |
|---|---|---|---|---|---|---|---|---|
| DSDP-86-580_1H2W_140-141 (290-291cm) | Japan | Kutcharo caldera | Kutcharo-Shoro (Kc-Sr) | 39.27-45.07 ka BP | N 41.6245 E 153.976 | NW Pacific | GEOMAR | 07-Nov-15 |
| DSDP-86-580_1H2W_140-141 (290-291cm) | Japan | Kutcharo caldera | Kutcharo-Shoro (Kc-Sr) | 39.27-45.07 ka BP | N 41.6245 E 153.976 | NW Pacific | GEOMAR | 07-Nov-15 |
| DSDP-86-580_1H2W_140-141 (290-291cm) | Japan | Kutcharo caldera | Kutcharo-Shoro (Kc-Sr) | 39.27-45.07 ka BP | N 41.6245 E 153.976 | NW Pacific | GEOMAR | 07-Nov-15 |
| DSDP-86-580_1H2W_140-141 (290-291cm) | Japan | Kutcharo caldera | Kutcharo-Shoro (Kc-Sr) | 39.27-45.07 ka BP | N 41.6245 E 153.976 | NW Pacific | GEOMAR | 07-Nov-15 |
| DSDP-86-580_1H2W_140-141 (290-291cm) | Japan | Kutcharo caldera | Kutcharo-Shoro (Kc-Sr) | 39.27-45.07 ka BP | N 41.6245 E 153.976 | NW Pacific | GEOMAR | 07-Nov-15 |
| DSDP-86-580_1H2W_140-141 (290-291cm) | Japan | Kutcharo caldera | Kutcharo-Shoro (Kc-Sr) | 39.27-45.07 ka BP | N 41.6245 E 153.976 | NW Pacific | GEOMAR | 07-Nov-15 |
| DSDP-86-580_1H2W_140-141 (290-291cm) | Japan | Kutcharo caldera | Kutcharo-Shoro (Kc-Sr) | 39.27-45.07 ka BP | N 41.6245 E 153.976 | NW Pacific | GEOMAR | 07-Nov-15 |
| DSDP-86-580_1H2W_140-141 (290-291cm) | Japan | Kutcharo caldera | Kutcharo-Shoro (Kc-Sr) | 39.27-45.07 ka BP | N 41.6245 E 153.976 | NW Pacific | GEOMAR | 07-Nov-15 |
| DSDP-86-580_1H2W_140-141 (290-291cm) | Japan | Kutcharo caldera | Kutcharo-Shoro (Kc-Sr) | 39.27-45.07 ka BP | N 41.6245 E 153.976 | NW Pacific | GEOMAR | 07-Nov-15 |
| DSDP-86-580_1H2W_140-141 (290-291cm) | Japan | Kutcharo caldera | Kutcharo-Shoro (Kc-Sr) | 39.27-45.07 ka BP | N 41.6245 E 153.976 | NW Pacific | GEOMAR | 07-Nov-15 |
| DSDP-86-580_1H2W_140-141 (290-291cm) | Japan | Kutcharo caldera | Kutcharo-Shoro (Kc-Sr) | 39.27-45.07 ka BP | N 41.6245 E 153.976 | NW Pacific | GEOMAR | 07-Nov-15 |

## 4.8: Chemical element abundance % for DSDP 580: 290-291cm tephra (Kutcharo Shoro)

| SiO2 | TiO2 | Al2O3 | FeOt | MnO | MgO | CaO | Na2O | K2O | P2O5 | F | SO3 | Cl |
|---|---|---|---|---|---|---|---|---|---|---|---|---|
| 77.17 | 0.29 | 12.31 | 1.31 | 0.02 | 0.30 | 1.73 | 4.29 | 2.32 | 0.01 | 0.03 | 0.01 | 0.21 |
| 77.20 | 0.26 | 12.30 | 1.34 | 0.04 | 0.29 | 1.74 | 4.25 | 2.26 | 0.06 | 0.00 | 0.05 | 0.21 |
| 77.54 | 0.28 | 12.14 | 1.59 | 0.17 | 0.26 | 1.67 | 4.00 | 2.11 | 0.00 | 0.05 | 0.01 | 0.19 |
| 77.28 | 0.26 | 12.36 | 1.47 | 0.09 | 0.28 | 1.61 | 4.20 | 2.22 | 0.02 | 0.00 | 0.03 | 0.19 |
| 77.42 | 0.30 | 12.04 | 1.47 | 0.07 | 0.30 | 1.71 | 4.09 | 2.22 | 0.06 | 0.07 | 0.05 | 0.21 |
| 77.18 | 0.29 | 12.31 | 1.50 | 0.05 | 0.26 | 1.63 | 4.28 | 2.22 | 0.05 | 0.02 | 0.03 | 0.20 |
| 77.61 | 0.27 | 12.24 | 1.33 | 0.10 | 0.29 | 1.67 | 4.07 | 2.17 | 0.06 | 0.00 | 0.00 | 0.19 |
| 77.46 | 0.30 | 12.10 | 1.35 | 0.12 | 0.30 | 1.71 | 4.21 | 2.20 | 0.04 | 0.00 | 0.00 | 0.22 |
| 77.90 | 0.26 | 11.79 | 1.30 | 0.01 | 0.28 | 1.68 | 4.34 | 2.16 | 0.02 | 0.02 | 0.01 | 0.20 |
| 77.29 | 0.30 | 12.05 | 1.52 | 0.01 | 0.25 | 1.74 | 4.32 | 2.26 | 0.03 | 0.02 | 0.00 | 0.22 |
| 77.99 | 0.25 | 11.86 | 1.38 | 0.13 | 0.27 | 1.52 | 4.04 | 2.21 | 0.05 | 0.04 | 0.03 | 0.24 |
| 77.21 | 0.27 | 12.53 | 1.33 | 0.00 | 0.27 | 1.63 | 4.23 | 2.21 | 0.07 | 0.00 | 0.03 | 0.22 |
| 77.79 | 0.27 | 12.16 | 1.33 | 0.02 | 0.30 | 1.64 | 3.94 | 2.28 | 0.03 | 0.01 | 0.03 | 0.20 |
| 77.50 | 0.27 | 12.11 | 1.46 | 0.08 | 0.30 | 1.70 | 4.10 | 2.20 | 0.01 | 0.04 | 0.03 | 0.19 |
| 77.19 | 0.30 | 12.30 | 1.41 | 0.10 | 0.29 | 1.71 | 4.26 | 2.14 | 0.04 | 0.02 | 0.04 | 0.19 |
| 77.60 | 0.28 | 12.23 | 1.32 | 0.04 | 0.32 | 1.63 | 4.06 | 2.24 | 0.01 | 0.03 | 0.03 | 0.20 |
| 77.19 | 0.26 | 12.01 | 1.43 | 0.09 | 0.30 | 1.68 | 4.48 | 2.31 | 0.03 | 0.00 | 0.01 | 0.20 |
| 77.03 | 0.31 | 12.24 | 1.53 | 0.07 | 0.32 | 1.66 | 4.29 | 2.25 | 0.05 | 0.00 | 0.04 | 0.21 |
| 77.06 | 0.28 | 12.36 | 1.43 | 0.11 | 0.28 | 1.72 | 4.32 | 2.21 | 0.01 | 0.02 | 0.00 | 0.19 |
| 77.54 | 0.29 | 12.09 | 1.45 | 0.08 | 0.30 | 1.72 | 4.16 | 2.09 | 0.03 | 0.04 | 0.03 | 0.20 |
| 78.01 | 0.25 | 11.81 | 1.33 | 0.03 | 0.27 | 1.51 | 4.32 | 2.23 | 0.04 | 0.00 | 0.01 | 0.19 |
| 77.50 | 0.26 | 12.06 | 1.37 | 0.06 | 0.26 | 1.70 | 4.26 | 2.20 | 0.04 | 0.08 | 0.00 | 0.19 |

# Appendix 5: Updated age model for DSDP 580 based on a best-fit model of the dates of Koizumi, (1994) and the tephrochronology of Chapter 5

| Depth (cm) | Age |
|---|---|
| 1 | 3985.69 |
| 2 | 4123.88 |
| 3 | 4262.07 |
| 4 | 4400.26 |
| 5 | 4538.45 |
| 6 | 4676.64 |
| 7 | 4814.83 |
| 8 | 4953.02 |
| 9 | 5091.21 |
| 10 | 5229.4 |
| 11 | 5367.59 |
| 12 | 5505.78 |
| 13 | 5643.97 |
| 14 | 5782.16 |
| 15 | 5920.35 |
| 16 | 6058.54 |
| 17 | 6196.73 |
| 18 | 6334.92 |
| 19 | 6473.11 |
| 20 | 6611.3 |
| 21 | 6749.49 |
| 22 | 6887.68 |
| 23 | 7025.87 |
| 24 | 7164.06 |
| 25 | 7302.25 |
| 26 | 7440.44 |
| 27 | 7578.63 |
| 28 | 7716.82 |
| 29 | 7855.01 |
| 30 | 7993.2 |
| 31 | 8131.39 |
| 32 | 8269.58 |
| 33 | 8407.77 |
| 34 | 8545.96 |
| 35 | 8684.15 |
| 36 | 8822.34 |
| 37 | 8960.53 |
| 38 | 9098.72 |
| 39 | 9236.91 |
| 40 | 9375.1 |
| 41 | 9513.29 |
| 42 | 9651.48 |
| 43 | 9789.67 |
| 44 | 9927.86 |
| 45 | 10066.05 |
| 46 | 10204.24 |
| 47 | 10342.43 |
| 48 | 10480.62 |

| | |
|---:|---:|
| 49 | 10618.81 |
| 50 | 10757 |
| 51 | 10895.19 |
| 52 | 11033.38 |
| 53 | 11171.57 |
| 54 | 11309.76 |
| 55 | 11447.95 |
| 56 | 11586.14 |
| 57 | 11724.33 |
| 58 | 11862.52 |
| 59 | 12000.71 |
| 60 | 12138.9 |
| 61 | 12277.09 |
| 62 | 12415.28 |
| 63 | 12553.47 |
| 64 | 12691.66 |
| 65 | 12829.85 |
| 66 | 12968.04 |
| 67 | 13106.23 |
| 68 | 13244.42 |
| 69 | 13382.61 |
| 70 | 13520.8 |
| 71 | 13658.99 |
| 72 | 13797.18 |
| 73 | 13935.37 |
| 74 | 14073.56 |
| 75 | 14211.75 |
| 76 | 14349.94 |
| 77 | 14488.13 |
| 78 | 14626.32 |
| 79 | 14764.51 |
| 80 | 14902.7 |
| 81 | 15040.89 |
| 82 | 15179.08 |
| 83 | 15317.27 |
| 84 | 15455.46 |
| 85 | 15593.65 |
| 86 | 15731.84 |
| 87 | 15870.03 |
| 88 | 16008.22 |
| 89 | 16146.41 |
| 90 | 16284.6 |
| 91 | 16422.79 |
| 92 | 16560.98 |
| 93 | 16699.17 |
| 94 | 16837.36 |
| 95 | 16975.55 |
| 96 | 17113.74 |
| 97 | 17251.93 |
| 98 | 17390.12 |
| 99 | 17528.31 |
| 100 | 17666.5 |
| 101 | 17804.69 |
| 102 | 17942.88 |
| 103 | 18081.07 |

| | |
|---|---|
| 104 | 18219.26 |
| 105 | 18357.45 |
| 106 | 18495.64 |
| 107 | 18633.83 |
| 108 | 18772.02 |
| 109 | 18910.21 |
| 110 | 19048.4 |
| 111 | 19186.59 |
| 112 | 19324.78 |
| 113 | 19462.97 |
| 114 | 19601.16 |
| 115 | 19739.35 |
| 116 | 19877.54 |
| 117 | 20015.73 |
| 118 | 20153.92 |
| 119 | 20292.11 |
| 120 | 20430.3 |
| 121 | 20568.49 |
| 122 | 20706.68 |
| 123 | 20844.87 |
| 124 | 20983.06 |
| 125 | 21121.25 |
| 126 | 21259.44 |
| 127 | 21397.63 |
| 128 | 21535.82 |
| 129 | 21674.01 |
| 130 | 21812.2 |
| 131 | 21950.39 |
| 132 | 22088.58 |
| 133 | 22226.77 |
| 134 | 22364.96 |
| 135 | 22503.15 |
| 136 | 22641.34 |
| 137 | 22779.53 |
| 138 | 22917.72 |
| 139 | 23055.91 |
| 140 | 23194.1 |
| 141 | 23332.29 |
| 142 | 23470.48 |
| 143 | 23608.67 |
| 144 | 23746.86 |
| 145 | 23885.05 |
| 146 | 24023.24 |
| 147 | 24161.43 |
| 148 | 24299.62 |
| 149 | 24437.81 |
| 150 | 24576 |
| 151 | 24714.19 |
| 152 | 24852.38 |
| 153 | 24990.57 |
| 154 | 25128.76 |
| 155 | 25266.95 |
| 156 | 25405.14 |
| 157 | 25543.33 |
| 158 | 25681.52 |

| | |
|---:|---:|
| 159 | 25819.71 |
| 160 | 25957.9 |
| 161 | 26096.09 |
| 162 | 26234.28 |
| 163 | 26372.47 |
| 164 | 26510.66 |
| 165 | 26648.85 |
| 166 | 26787.04 |
| 167 | 26925.23 |
| 168 | 27063.42 |
| 169 | 27201.61 |
| 170 | 27339.8 |
| 171 | 27477.99 |
| 172 | 27616.18 |
| 173 | 27754.37 |
| 174 | 27892.56 |
| 175 | 28030.75 |
| 176 | 28168.94 |
| 177 | 28307.13 |
| 178 | 28445.32 |
| 179 | 28583.51 |
| 180 | 28721.7 |
| 181 | 28859.89 |
| 182 | 28998.08 |
| 183 | 29136.27 |
| 184 | 29274.46 |
| 185 | 29412.65 |
| 186 | 29550.84 |
| 187 | 29689.03 |
| 188 | 29827.22 |
| 189 | 29965.41 |
| 190 | 30103.6 |
| 191 | 30241.79 |
| 192 | 30379.98 |
| 193 | 30518.17 |
| 194 | 30656.36 |
| 195 | 30794.55 |
| 196 | 30932.74 |
| 197 | 31070.93 |
| 198 | 31209.12 |
| 199 | 31347.31 |
| 200 | 31485.5 |
| 201 | 31623.69 |
| 202 | 31761.88 |
| 203 | 31900.07 |
| 204 | 32038.26 |
| 205 | 32176.45 |
| 206 | 32314.64 |
| 207 | 32452.83 |
| 208 | 32591.02 |
| 209 | 32729.21 |
| 210 | 32867.4 |
| 211 | 33005.59 |
| 212 | 33143.78 |
| 213 | 33281.97 |

| | |
|---:|---:|
| 214 | 33420.16 |
| 215 | 33558.35 |
| 216 | 33696.54 |
| 217 | 33834.73 |
| 218 | 33972.92 |
| 219 | 34111.11 |
| 220 | 34249.3 |
| 221 | 34387.49 |
| 222 | 34525.68 |
| 223 | 34663.87 |
| 224 | 34802.06 |
| 225 | 34940.25 |
| 226 | 35078.44 |
| 227 | 35216.63 |
| 228 | 35354.82 |
| 229 | 35493.01 |
| 230 | 35631.2 |
| 231 | 35769.39 |
| 232 | 35907.58 |
| 233 | 36045.77 |
| 234 | 36183.96 |
| 235 | 36322.15 |
| 236 | 36460.34 |
| 237 | 36598.53 |
| 238 | 36736.72 |
| 239 | 36874.91 |
| 240 | 37013.1 |
| 241 | 37151.29 |
| 242 | 37289.48 |
| 243 | 37427.67 |
| 244 | 37565.86 |
| 245 | 37704.05 |
| 246 | 37842.24 |
| 247 | 37980.43 |
| 248 | 38118.62 |
| 249 | 38256.81 |
| 250 | 38395 |
| 251 | 38533.19 |
| 252 | 38671.38 |
| 253 | 38809.57 |
| 254 | 38947.76 |
| 255 | 39085.95 |
| 256 | 39224.14 |
| 257 | 39362.33 |
| 258 | 39500.52 |
| 259 | 39638.71 |
| 260 | 39776.9 |
| 261 | 39915.09 |
| 262 | 40053.28 |
| 263 | 40191.47 |
| 264 | 40329.66 |
| 265 | 40467.85 |
| 266 | 40606.04 |
| 267 | 40744.23 |
| 268 | 40882.42 |

| | |
|---:|---:|
| 269 | 41020.61 |
| 270 | 41158.8 |
| 271 | 41296.99 |
| 272 | 41435.18 |
| 273 | 41573.37 |
| 274 | 41711.56 |
| 275 | 41849.75 |
| 276 | 41987.94 |
| 277 | 42126.13 |
| 278 | 42264.32 |
| 279 | 42402.51 |
| 280 | 42540.7 |
| 281 | 42678.89 |
| 282 | 42817.08 |
| 283 | 42955.27 |
| 284 | 43093.46 |
| 285 | 43231.65 |
| 286 | 43369.84 |
| 287 | 43508.03 |
| 288 | 43646.22 |
| 289 | 43784.41 |
| 290 | 43922.6 |
| 291 | 44060.79 |
| 292 | 44198.98 |
| 293 | 44337.17 |
| 294 | 44475.36 |
| 295 | 44613.55 |
| 296 | 44751.74 |
| 297 | 44889.93 |
| 298 | 45028.12 |
| 299 | 45166.31 |
| 300 | 45304.5 |

# Appendix 6: Estimated terminus width (km), coordinates and estimated flux (km$^3$ yr$^{-1}$) of possible palaeo-ice streams in NE Siberia under “maximal” flux conditions, used for model iceberg seeding.

| Terminus width (km) | Latitude (º) | Longitude (º) | Flux (km$^3$ yr$^{-1}$) |
|---|---|---|---|
| 124 | 62.038 | 177.24 | 40 |
| 106 | 61.695 | 175.698 | 25 |
| 146 | 60.92 | 173.416 | 48 |
| 109 | 60.202 | 168.775 | 30 |
| 126 | 60.185 | 171.453 | 40 |
| 75 | 60.107 | 167.639 | 18 |
| 105 | 59.66 | 163.994 | 25 |
| 63 | 59.495 | 165.243 | 15 |
| 25 | 59.468 | 159.378 | 4 |
| 12 | 58.795 | 157.518 | 1 |
| 140 | 58.368 | 162.623 | 45 |
| 25 | 57.258 | 162.859 | 4 |
| 19 | 56.09 | 155.07 | 2 |
| 31 | 56.047 | 162.432 | 5 |
| 73 | 55.437 | 162.042 | 20 |
| 35 | 54.907 | 155.03 | 5 |
| 47 | 54.411 | 160.722 | 10 |
| 107 | 53.747 | 160.041 | 25 |
| 105 | 53.033 | 155.947 | 25 |
| 70 | 52.68 | 158.704 | 20 |
| 85 | 51.58 | 158.016 | 22 |
| 128 | 51.485 | 156.279 | 40 |
| 39 | 51.087 | 157.207 | 7 |
| * | 58.5 | 153 | 48 |
| * | 58.5 | 147 | 48 |
| * | 45.1 | 150.5 | 10 |
| * | 44.5 | 148.5 | 10 |
| * | 51.3 | -130 | 300 |
| * | 54.5 | -134 | 500 |
| * | 58.5 | -139 | 150 |
| * | 59.5 | -146.5 | 150 |
| * | 58 | -150 | 75 |
| * | 56 | -155 | 50 |

Note: Those on the Kamchatka/Koryak coast were based on published data, DEM and satellite image analysis (see Chapter 7). The last 10 were chosen to allow model icebergs to be seeded from possible glacial marine termini along the northern coast of the Sea of Okhotsk, and from the Kurile Islands. These were chosen to maximise potential fluxes from sites with some evidence from satellite images of a likely marine or near coastal glacial history (hence there is no terminus estimate).